

Internal electric fields and electrode effects in ferroelectric thin films for piezoelectric energy harvesting

THÈSE N° 8074 (2017)

PRÉSENTÉE LE 24 NOVEMBRE 2017
À LA FACULTÉ DES SCIENCES ET TECHNIQUES DE L'INGÉNIEUR
LABORATOIRE DE CÉRAMIQUE
PROGRAMME DOCTORAL EN SCIENCE ET GÉNIE DES MATÉRIAUX

ÉCOLE POLYTECHNIQUE FÉDÉRALE DE LAUSANNE

POUR L'OBTENTION DU GRADE DE DOCTEUR ÈS SCIENCES

PAR

Robin NIGON

acceptée sur proposition du jury:

Dr L. Weber, président du jury
Prof. P. Muralt, directeur de thèse
Dr. M. Maglione, rapporteur
Dr E. Defay, rapporteur
Prof. D. Damjanovic, rapporteur



ÉCOLE POLYTECHNIQUE
FÉDÉRALE DE LAUSANNE

Suisse
2017

Man can give nothing to his fellow-men but himself.
— August Schlegel

To my parents.



Acknowledgements

I would like to thank Professor Paul Muralt, for offering me the opportunity to do my PhD thesis with his group, and for his constant support and scientific expertise throughout the thesis years. Much less would have been achieved if it were not for his supervision.

I acknowledge the support of the Swiss National Science Foundation for funding this thesis work under the contract number 200021_150108.

I would like to thank Professor Nava Setter for giving access to the Ceramics Laboratory rich facilities. I am very grateful to Professors Dragan Damjanovic and Alexander Tagantsev who were always available and patient enough to answer my questions, and helped me greatly in my understanding of the difficult physics of ferroelectricity and piezoelectricity.

Many colleagues from the Ceramics laboratory unfortunately left before my work was complete, but their technical support and great experience were nonetheless very precious to me. I gratefully acknowledge their help and friendship, and in particular that of Arnaud Crassous, Tomas Sluka, Igor Stolichnov and Kaushik Vaideeswaran. I would like to thank Enrico Colla, Lino Olivetta and Yuko Kagata for their constant availability and helpfulness.

I would not have been successful in my work without the support of my seniors in Paul's group on all matters of experimental work, material behavior and fabrication: Andrea Mazzalai, Davide Balma, and Ramin Matloub for his constant availability, help and friendship. I am very much indebted to Nachiappan Chidambaram who taught me all the precursor solution preparation, the sol-gel processing and the microfabrication work. There would be no sample to analyze without his kind and thorough teaching.

I would like to thank my current colleagues from Paul's group: Xiao Di, Mahmoud Hadad, Stefan Mertin, Fazel Parsapour, Vladimir Pashchenko, Cosmin Sandu, for their kindness and their help for the lab's daily life. The contribution of Cosmin Sandu for all the TEM imaging in this work is gratefully acknowledged. Sina Hashemizadeh, Mahmoud Hadad, and Elmira Shahrabi are sincerely thanked for their friendly and supportive company during the last months. Their presence made the last difficulties feel much lighter.

Acknowledgements

I would like to thank the staff of the EPFL Center of MicroNanotechnology (CMi) for their valuable support and their work to keep the cleanroom facilities in excellent condition.

I would like to acknowledge the contributions of the master students who have worked with me on several aspects of this thesis work: Taiki Nishiumi, Johnathan Ponard, Jarla Thiesbrummel, and in particular Trygve M. Ræder, with whom the systematic investigations into the interdigitated electrode system started. His outstanding contribution is present in nearly all the chapters of this thesis.

I would like to thank Cuong H. Nguyen for his fruitful collaboration. He brought much improvement into the proper understanding of the interdigitated electrode system, and our discussions always left me with a clearer picture of the situation.

I am very grateful for the help of Iaroslav Gaponenko from Prof. Paruch's Group at the University of Geneva, who welcomed me in his lab and provided precious assistance on PFM imaging.

I would like to thank Franz Fengler and Dr. Uwe Schröder for interesting discussions on novel hafnia-based ferroelectrics. They made me discover many new aspects of the field which I would otherwise have unduly overlooked.

I would like to thank Kaitlin Howell, Janina Löffler and Hadrien O. Michaud who kindly accepted to review parts of the manuscript. Their precious comments greatly improved the quality of the final text.

I would like to thank my friends, from Lausanne and beyond, for accompanying me through all the highs and lows of the thesis work.

Last but not least, I am thanking my family, and in particular my parents Pascal and Françoise and my sister Alice, for their constant support and their love, and for being there for me at all times.

Lausanne, 3 November 2017

Robin Nigon

Abstract

The continuing decrease of power requirements of electronic circuits offers the potential to deploy wireless systems as embedded sensors for cars or industrial tools, and implanted medical devices. Harvesting ambient vibrations by an appropriate energy harvesting (EH) device allows to avoid an undesirable battery replacement. At the scale of micro-electromechanical systems, where severe size constraints must be met, microfabricated EH devices with piezoelectric thin films offer the best energy density. Ferroelectric lead zirconate titanate (PZT) thin films with interdigitated electrode (IDE) appear as the most promising device design for this purpose.

Accurate characterization of the thin film response is necessary to determine the PZT composition and doping, the electrode geometry, and the stack design for maximum EH efficiency. Unfortunately, there is no rigorous description of the physical behavior of the IDE system to date. One goal of this thesis was thus to provide a better understanding of the experimental observations made by previous researchers. In addition, only a limited PZT composition and doping range has been investigated in this configuration. It was the second goal of this thesis to widen this range in order to determine the combination that yields the best EH efficiency. Finally, the risk of partial or total depoling over the device lifetime is always present in ferroelectric materials. The phenomena of aging and self-poling are of great interest to ensure proper retention of the poled state and, thus, the reliability of the harvesting device. Neither of the two are well understood. It was the third goal of this thesis to investigate the aging behavior and methods to promote self-poling.

In this thesis work, we have have proposed a description of the physical behavior of the IDE system, and we have developed an analytical model for extracting the effective material properties from standard characterization measurements, which is well supported by both finite element (FE) simulations and experimental data. We found that if the substrate is conductive enough, a parasitic capacitance is present in parallel to the material response. We have provided a method to subtract the contribution of the parasitic capacitance, which has an accuracy of better than 4 % in a wide range of IDE geometries as determined by FE simulations.

We have investigated the performances of doped PZT thin films with IDE for several combinations of dopant and composition. We have improved an existing fabrication route to obtain textured PZT films on an insulating MgO layer. We found that dopants systematically reduced the piezoelectric response and retention capability, and increased the dielectric constant. All three are detrimental for EH. Undoped compositions should be chosen.

Abstract

We have studied methods to improve the stability of the poled state through aging and self-poling. Introducing the latter into the IDE configuration did not provide sufficiently strong effects to be of practical interest. On the contrary, the aging process may allow to tune the extrinsic contributions to the dielectric and piezoelectric response. It is likely caused by polarization discontinuities at grain boundaries. Further work is needed for fully optimizing this phenomenon.

Finally, from the previous investigations, we could deduce and propose golden rules for the design of IDE structures, and discuss typical applications where they are advantageous.

Key words: *energy harvesting, MEMS, piezoelectric thin film, ferroelectric thin film, lead zirconate titanate, interdigitated electrodes*

Résumé

La diminution continue des besoins en puissance des circuits électroniques permet le déploiement de systèmes sans fil tels que des capteurs, incorporés dans des voitures ou des équipements industriels, ou des appareils médicaux implantés. La récupération de l'énergie des vibrations ambiantes par un appareil de récupération d'énergie permet d'éviter des remplacements de batterie indésirables. A l'échelle des microsystèmes électromécaniques, pour lesquels de rigoureuses contraintes de taille doivent être respectées, les récupérateurs d'énergie avec couche mince piézoélectrique offrent la densité d'énergie la plus élevée. Le zirconate titanate de plomb (PZT), matériau ferroélectrique, sous forme de couche mince avec électrodes interdigitales (EID), apparaît comme le design le plus prometteur pour accomplir cet objectif.

La caractérisation précise de la réponse du matériau en couche mince est nécessaire pour déterminer la composition et le dopage du PZT, la géométrie des EID, et l'architecture des couches successives qui maximisent l'efficacité de la récupération d'énergie. Malheureusement, il n'existe à ce jour aucune description rigoureuse du comportement physique du système avec EID. L'un des objectifs de ce travail de thèse était donc d'offrir une meilleure compréhension des résultats expérimentaux obtenus par de précédentes études. De plus, seul un nombre restreint de compositions et de dopages ont été étudiés dans cette configuration. Le second objectif de ce travail de thèse était donc d'étendre ce champ d'investigation, afin de déterminer quelle combinaison de composition et de dopage maximise l'efficacité de la récupération d'énergie. Enfin, le risque de dépolarisation partielle ou totale au cours de la durée de vie du système est un risque intrinsèque aux matériaux ferroélectriques. Les phénomènes de vieillissement et d'autopolarisation sont d'un grand intérêt pour assurer la permanence de l'état polarisé, et ainsi la fiabilité du récupérateur d'énergie. Aucun de ces deux phénomènes n'est bien compris. Ainsi, le troisième objectif de ce travail de thèse était d'étudier le phénomène de vieillissement et de déterminer des méthodes pour provoquer l'autopolarisation du matériau.

Dans ce travail de thèse, nous avons proposé une description du comportement physique du système avec EID, et nous avons développé un modèle analytique qui permet d'extraire des mesures de caractérisation standard les propriétés effectives du matériau. Nos conclusions sont en accord avec les résultats expérimentaux et les simulations par éléments finis. Nous avons découvert que, si le substrat est suffisamment conducteur, une capacité parasite est présente en parallèle de la réponse électrique du matériau. Nous avons fourni une méthode pour soustraire la contribution de cette capacité parasite, qui a une précision meilleure que 4 %

Résumé

pour un large champ de géométrie des EID d'après des résultats de simulations par éléments finis.

Nous avons étudié les performances de couches minces de PZT dopées, avec EID, pour plusieurs combinaisons de composition et de dopant. Nous avons amélioré un procédé de fabrication existant, qui permet désormais de faire croître des films minces texturés de PZT sur une couche isolante de MgO. Nous avons observé que les dopants réduisent systématiquement la réponse piézoélectrique et les capacités de rétention du matériau, et qu'ils augmentent la constante diélectrique. Ces trois propriétés sont néfastes pour la récupération d'énergie. Il est donc nécessaire d'employer des compositions sans dopage.

Nous avons étudié des méthodes pour améliorer la stabilité de l'état polarisé par l'intermédiaire des phénomènes de vieillissement et d'autopolarisation. Nous avons pu provoquer ce dernier dans la configuration avec EID, mais les effets observés ne sont pas assez prononcés pour être d'un quelconque intérêt pratique. Au contraire, le phénomène de vieillissement pourrait permettre d'ajuster les contributions extrinsèques aux réponses diélectrique et piézoélectrique. Il est vraisemblablement dû à la discontinuité de polarisation qui existe à l'emplacement des joints de grain. Des investigations supplémentaires sont nécessaires afin d'exploiter pleinement ce phénomène.

Enfin, d'après les études précédentes, nous avons pu déduire et proposer des règles d'or pour la conception de structures avec EID, ainsi que discuter des applications possibles où l'usage de ces structures est avantageux.

Mots clefs : *récupération d'énergie, MEMS, couche mince piézoélectrique, couche mince ferroélectrique, zirconate titanate de plomb, électrodes interdigitales*

Contents

Acknowledgements	i
Abstract (English/Français)	iii
1 Introduction	1
1.1 Constitutive equations of piezoelectricity	1
1.1.1 Tensor description	1
1.1.2 The matrix notation	4
1.1.3 Crystal symmetry	6
1.1.4 Standard notations for piezoelectricity	7
1.2 Ferroelectricity	8
1.3 Lead zirconate titanate	11
1.4 PZT thin films for MEMS	13
1.4.1 PZT thin films by CSD	16
1.5 Piezoelectric energy harvesting	17
1.5.1 Motivations	17
1.5.2 Principle of operation	19
1.5.3 PEH for MEMS applications	22
1.6 Aims of the work	30
2 Characterization methods for ferroelectric thin films	33
2.1 Standard characterization measurements	33
2.2 Piezoelectric coefficient in converse mode	36
2.2.1 Cantilever bending geometry	37
2.2.2 Parallel plate electrodes	37
2.2.3 Interdigitated electrodes	38
2.3 Piezoelectric coefficient in direct mode	39
2.3.1 Setup description and cantilever bending geometry	39
2.3.2 Parallel plate electrodes	40
2.3.3 Interdigitated electrodes	41
3 Physical behavior of ferroelectric thin films with IDE and characterization methodology	43
3.1 Introduction	43

Contents

3.2	The simple formula	44
3.3	The Gevorgian formula for the capacitance of IDE capacitors	45
3.4	The partial capacitance method for multilayers	47
3.5	Simplification of the Gevorgian procedure for specific geometries	48
3.6	The Igreja formula for the capacitance of IDE capacitors	49
3.7	Simplification of the Igreja procedure for specific geometries	50
3.8	Comparison with finite element simulation	51
3.9	Electric field reduction	52
3.10	Parasitic capacitance	56
3.10.1	Origin and estimates	56
3.10.2	Evaluation	59
3.10.3	Influence on PV and CV loops	62
3.11	Effective surface	63
3.12	Maximum reachable polarization	66
3.13	Experimental verification	67
3.13.1	Simple model	68
3.13.2	Gevorgian model	70
3.13.3	Igreja model	73
3.14	Displacement measurements in converse mode	75
3.15	Discussion on the gap dependence of the IDE properties	77
3.16	Conclusion	79
4	Doped PZT thin films with interdigitated electrodes	81
4.1	Introduction	81
4.2	Sample fabrication	81
4.3	Film microstructure	84
4.4	Electrical and piezoelectric response characterization	95
4.4.1	Effect of annealing	96
4.4.2	Effect of doping for the tetragonal composition	98
4.4.3	Effect of doping for the MPB composition	104
4.4.4	Comparison between the IDE and the PPE configurations	105
4.5	Conclusion	110
5	Aging and imprint in PZT thin films with IDE	113
5.1	Introduction	113
5.2	Harmonic analysis of the polarization response	117
5.2.1	Description of the harmonic response	118
5.2.2	Intrinsic and extrinsic contributions	119
5.2.3	Subswitching driving fields	121
5.2.4	Switching driving fields	130
5.3	Aging mechanisms	131
5.4	Goals of this chapter	137
5.5	Methods	138

5.6	Experimental results	141
5.6.1	General observations and UV light exposure	141
5.6.2	Rate of imprint	146
5.6.3	Subswitching dielectric spectroscopy	154
5.7	Conclusion	156
6	PZT thin films with asymmetric electrodes	159
6.1	Introduction	159
6.2	Sample fabrication	160
6.3	Results	162
6.3.1	IDE structures	162
6.3.2	PPE structures	164
6.3.3	Discussion	164
6.4	Introduction of self-poling into the IDE system	166
6.4.1	Fabrication	167
6.4.2	Results	167
6.4.3	Discussion	169
6.5	Conclusion	172
7	Applications and design rules for PZT thin films with IDE	175
7.1	Introduction	175
7.2	Applications for PZT thin films with IDE	175
7.3	Design rules	178
7.4	Conclusion	179
8	Conclusion and outlook	181
A	PZT thin films by CSD	185
B	Piezoelectric coefficient for the cantilever beam architecture	187
B.1	Piezoelectric coefficient in converse mode	187
B.1.1	Cantilever bending geometry	188
B.1.2	Parallel plate electrodes	189
B.1.3	Interdigitated electrodes	192
B.2	Piezoelectric coefficient in direct mode	195
B.2.1	Setup description and cantilever bending geometry	195
B.2.2	Parallel plate electrodes	197
B.2.3	Interdigitated electrodes	200
C	Conformal mapping and elliptic functions	205
C.1	Conformal mapping	205
C.1.1	Definition	205
C.1.2	Conformal transplants and boundary-value problems	206
C.1.3	The Schwartz-Christoffel transformation	206

Contents

C.2 Elliptic functions	208
C.2.1 Motivations	208
C.2.2 Jacobi elliptic and theta functions	208
D Derivation of the simplified Gevorgian model	211
D.1 Simplification of k	211
D.2 Simplification of $K(k)$ and $K(k')$	213
E Derivation of the simplified Igreja model	217
F Derivation of the maximum reachable polarization	221
E1 Tetragonal (100)	222
E2 Tetragonal (110)	223
E3 Tetragonal (111)	224
E4 Rhombohedral (100)	225
E5 Rhombohedral (110)	226
E6 Rhombohedral (111)	228
G Dielectric spectroscopy	229
G.1 Experimental setup	229
G.2 Derivation of the polarization harmonics	230
Bibliography	235
Curriculum Vitae	251

1 Introduction

In this chapter, we will present the piezoelectric effect and the ferroelectric effect. The piezoelectric properties of a body are described with a set of constitutive equations which allow to deal with the anisotropic properties inherent to the existence of piezoelectricity. The principal features of the physical behavior of ferroelectric crystals will be presented. We will then briefly introduce lead zirconate titanate (PZT), which is the ferroelectric material on which our work is focused. We will present the principal features of PZT for its use as a thin film in microsystems. One such microsystem is an energy harvester, whose purpose is the scavenging of ambient mechanical energy sources to power wireless low power systems. We will show how piezoelectric energy harvesting is a very promising approach at the MEMS scale. We will present the principles of operation of such systems, and illustrate them with a short review of published devices. We will then present what is the best route for improvement, and finally conclude by exposing the aims for this PhD work and the outline of the thesis.

1.1 Constitutive equations of piezoelectricity

1.1.1 Tensor description

A crystal can be described by two sets of tensors: matter tensors and field tensors [1]. Matter tensors refer to properties that are intrinsic to the crystal being considered, such as its dielectric permittivity. Field tensors refer to external actions that act upon the crystal; examples include the electric field or the mechanical stress. The tensor formalism is rendered necessary by the anisotropic nature of crystal properties in general, and offers a convenient way to obtain any of these properties along an arbitrary direction thanks to transformation rules. Typically a small set of tensor variables, combining matter and field tensors, are sufficient to describe the state of the crystal under an external action. In addition, the situation often allows to consider that changes are small enough so that the crystal response can be approximated, with good accuracy, as a linear response. This is the case when elastic behavior is assumed; the elements of the stress tensor σ and those of the strain tensor ϵ are then related to each other by the

Chapter 1. Introduction

following equivalent equations:

$$\epsilon_{ij} = s_{ijkl} \sigma_{kl} \quad (1.1a)$$

$$\sigma_{ij} = c_{ijkl} \epsilon_{kl} \quad (1.1b)$$

where $i, j = 1, 2, 3$ for all equations written in the tensor notation. Throughout the text, we will also use the convention of summation for repeated indices. Hence for example for $i = j = 1$:

$$\epsilon_{11} = s_{11kl} \sigma_{kl} = \sum_{k=1}^3 \sum_{l=1}^3 s_{11kl} \sigma_{kl} \quad (1.2)$$

σ and ϵ are second-rank tensors and s and c are fourth-rank tensors. s is the compliance tensor and c is the stiffness tensor, and $s = c^{-1}$ (meaning their product yields the unity fourth-rank tensor). σ and ϵ are field tensors and their elements can take any value for a given crystal, and are not necessarily the same for all the points in the crystal, *i. e.* they are not necessarily homogeneous; on the contrary, s and c are matter tensors and once the coordinate system is chosen, their elements are fixed for a given crystal and are the same at any point in the crystal — under the assumption that they do not depend on σ nor on ϵ . In other words, they are a material property.

Matter tensors relate the value of field tensors within the crystal. A small change in temperature dT (zero-rank tensor *i. e.* scalar value), electric field dE (first-rank tensor) or stress $d\sigma$ imposed on the crystal will induce a small change in entropy dS (scalar), dielectric displacement dD (first-rank tensor) or strain $d\epsilon$, respectively, according to the following equations:

$$dS = \frac{C}{T} dT \quad (1.3a)$$

$$dD_i = \epsilon_0 dE_i + \epsilon_0 \chi_{ij} dE_j \quad (1.3b)$$

$$d\epsilon_{ij} = s_{ijkl} d\sigma_{kl} \quad (1.3c)$$

C is the heat capacity, ϵ_0 the dielectric permittivity of vacuum, χ the dielectric susceptibility tensor of the crystal (rank-two tensor). The polarization tensor P (first-rank) of the crystal is defined as:

$$P_i = \epsilon_0 \chi_{ij} E_j \quad (1.4)$$

And we can write:

$$D_i = \epsilon_0 E_i + P_i \quad (1.5)$$

$$D_i = \kappa_{ij} E_j \quad (1.6)$$

where the $\kappa_{ij} = \epsilon_0(\delta_{ij} + \chi_{ij})$ are the elements of the dielectric permittivity tensor κ (rank-two tensor) and δ_{ij} is Kronecker's symbol. The elements of the dielectric constant tensor (rank-two tensor) are given by κ_{ij}/ϵ_0 . P has the unit of an electrical dipole moment per unit volume, or

of a charge per unit area. If an electric field is applied orthogonal to a slate-shaped crystal, then a charge $\mathbf{P} \cdot \mathbf{S}$ will appear on one of the slate surfaces S , and a charge $-\mathbf{P} \cdot \mathbf{S}$ will appear on the other. Here bold letters denote vector variables (which is an equivalent way of describing first-rank tensors), and $\mathbf{S} = S\mathbf{n}$ where \mathbf{n} is the unit vector normal to the surface S and pointing outward.

The previous relations constitute the so-called principal effects. There exist so-called coupled effects as well, relating field tensors of different ranks with one another. One of them is the direct piezoelectric effect, from the Greek word $\pi\iota\epsilon\zeta\epsilon\iota\nu$ meaning “to press”. It quantifies the polarization change dP caused by the application of a stress $d\sigma$ thanks to the piezoelectric tensor d (rank-three tensor):

$$dP_i = d_{ijk} d\sigma_{jk} \quad (1.7)$$

The converse piezoelectric effect quantifies the strain change $d\epsilon$ caused by the application of an electric field dE . It can be shown that the same tensor d quantifies this effect, and we have:

$$d\epsilon_{ij} = d_{kij} dE_k \quad (1.8)$$

Note that unlike equation 1.7, in equation 1.8 the sum on the right-hand side is along the first subscript of d . The d_{ijk} are called the piezoelectric coefficients. Figure 1.1 shows the direct and coupled effects connecting the field tensors for mechanical, electrical and thermal properties.

If we write all the equations for all the coupled effects, we find that only 3 variables among T , S , E , D , σ and ϵ are in fact independent, and that the principal effects and coupled effects equations can be used to write the thermodynamical equations of state of the crystal as a function of these 3 variables [1]. The 3 independent variables are usually chosen so that they closely represent experimental conditions. The matter tensors then naturally appear as partial derivatives with reference to one (or more) of the independent variable, while the remaining independent variables are held constant; and similarly to the direct and converse piezoelectric effects being quantified by the same tensor, a reduced number of matter tensors is found to link various couples of field tensors. Because they can be regarded as partial derivatives, the matter tensor values will usually depend on the experimental conditions; the variable(s) held constant are then specified as a superscript of the tensor element. In integrated form, choosing (σ, E, T) as the 3 independent variables and choosing 0 as integration constant for σ and E , we can write, following Nye [1]:

$$\epsilon_{ij} = s_{ijkl}^{E,T} \sigma_{kl} + d_{kij}^T E_k + \alpha_{ij}^E \Delta T \quad (1.9a)$$

$$D_i = d_{ijk}^T \sigma_{jk} + \kappa_{ij}^{\sigma,T} E_j + p_i^\sigma \Delta T \quad (1.9b)$$

$$\Delta S = \alpha_{ij}^E \sigma_{ij} + p_i^\sigma E_i + \frac{C^{\sigma,E}}{T} \Delta T \quad (1.9c)$$

The α_{ij} are the thermal expansion coefficients and the p_i are the pyroelectric coefficients.

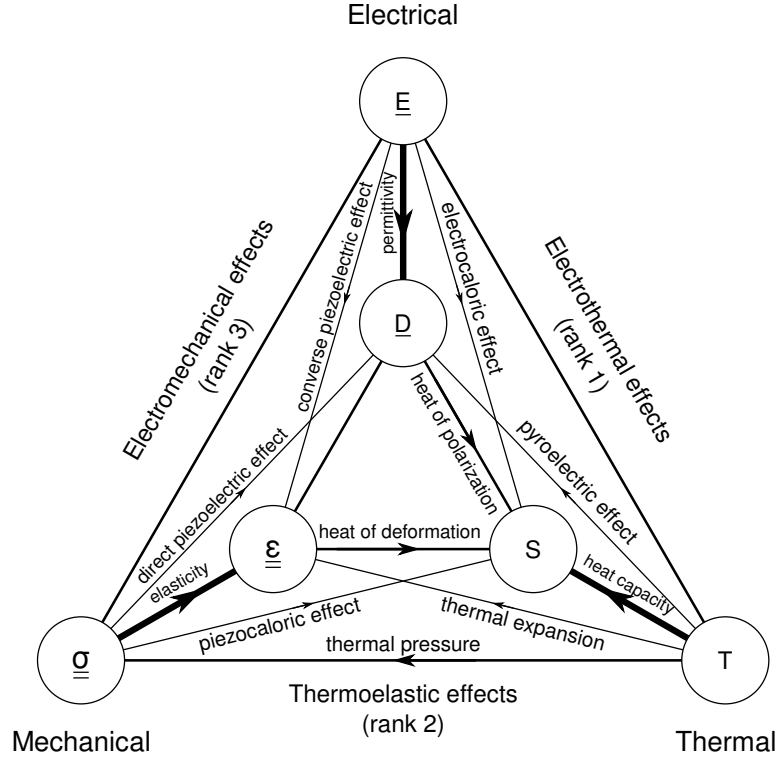


Figure 1.1 – Diagram showing direct and coupled effects, after Nye [1]. The lines connecting σ and E and ϵ and D are associated with the piezoelectric coefficient e (see section 1.1.2). The line connecting E and T is associated with $-t$, where t is the heat of polarization coefficient. The rank of the matter tensors for each side is specified in brackets. The rank of the field tensors is denoted by the number of bars below the symbol.

1.1.2 The matrix notation

Physical arguments or construction rules result in the stress and strain tensors being symmetrical tensors, *i. e.* $\sigma_{ij} = \sigma_{ji}$ and $\epsilon_{ij} = \epsilon_{ji}$ for $i, j = 1, 2, 3$. This can be extended to the other matter tensors in the following way:

$$\alpha_{ij} = \alpha_{ji} \quad (1.10a) \quad s_{ijkl} = s_{ijlk} = s_{jikl} \quad (1.11a)$$

$$d_{ijk} = d_{ikj} \quad (1.10b) \quad c_{ijkl} = c_{ijlk} = c_{jikl} \quad (1.11b)$$

This allows to use the so-called matrix notation or Voigt notation, which makes the relations of equations 1.9a to 1.9c less cumbersome to manipulate. The stress tensor is written as:

$$\begin{pmatrix} \sigma_{11} & \sigma_{12} & \sigma_{13} \\ \sigma_{12} & \sigma_{22} & \sigma_{23} \\ \sigma_{13} & \sigma_{23} & \sigma_{33} \end{pmatrix} = \begin{pmatrix} \sigma_1 & \sigma_6 & \sigma_5 \\ \sigma_6 & \sigma_2 & \sigma_4 \\ \sigma_5 & \sigma_4 & \sigma_3 \end{pmatrix} = \begin{pmatrix} \sigma_1 \\ \sigma_2 \\ \vdots \\ \sigma_6 \end{pmatrix} \quad (1.12)$$

1.1. Constitutive equations of piezoelectricity

The stress tensor σ is now written as a vector where the longitudinal components receive the single index $i = 1, 2, 3$, and the shear components receive the single index $j = 4, 5, 6$. This is extended to the other tensors in the following way : the couples 11, 22 and 33 are replaced by the single index 1, 2, 3 respectively; the couples 12 or 21, 13 or 31, and 23 or 32 are replaced by the single index 4, 5, 6, respectively. This is summarized in table 1.1.

Table 1.1 – Rule of correspondence between tensor and matrix notations.

Tensor notation	11	22	33	23 or 32	13 or 31	12 or 21
Matrix notation	1	2	3	4	5	6

This rule is sufficient for the stress tensor σ and the elastic stiffness tensor c . However for the strain, thermal expansion, piezoelectric coefficient and elastic compliance tensors, the new components are given by the following equations in addition to the previous rule:

$$\epsilon_m = \epsilon_{ij} \quad \text{for } m = 1, 2, 3 \quad (1.13a) \quad d_{im} = d_{ijk} \quad \text{for } m = 1, 2, 3 \quad (1.14a)$$

$$\epsilon_m = 2\epsilon_{ij} \quad \text{for } m = 4, 5, 6 \quad (1.13b) \quad d_{im} = 2d_{ijk} \quad \text{for } m = 4, 5, 6 \quad (1.14b)$$

$$\alpha_m = \alpha_{ij} \quad \text{for } m = 1, 2, 3 \quad (1.13c) \quad s_{mn} = s_{ijkl} \quad \text{for } m = 1, 2, 3 \quad (1.14c)$$

$$\alpha_m = 2\alpha_{ij} \quad \text{for } m = 4, 5, 6 \quad (1.13d) \quad s_{mn} = 2s_{ijkl} \quad \text{for } m \text{ or } n = 4, 5, 6 \quad (1.14d)$$

$$s_{mn} = 4s_{ijkl} \quad \text{for both } m, n = 4, 5, 6 \quad (1.14e)$$

The dielectric permittivity and pyroelectricity tensors are unchanged. Note that the piezoelectric coefficient matrix d is a rectangular matrix with 3 rows and 6 columns. In this way, all variables from equations 1.9a to 1.9c are now either vectors or matrices and can be written out on a sheet of paper for hand calculation using matrix product rules:

$$\epsilon_i = s_{ij}^{E,T} \sigma_j + d_{ji}^T E_j + \alpha_i^E \Delta T \quad (1.15a)$$

$$D_i = d_{ij}^T \sigma_j + \kappa_{ij}^{\sigma,T} E_j + p_i^\sigma \Delta T \quad (1.15b)$$

$$\Delta S = \alpha_i^E \sigma_i + p_i^\sigma E_i + \frac{C^{\sigma,E}}{T} \Delta T \quad (1.15c)$$

where $i, j = 1 \dots 6$ for all equations written in the matrix notation. Note that in equation 1.15a the transposed piezoelectric coefficient matrix ${}^t d$ is used. In this form, the matrices do not obey the tensor transformation rules. If the coordinate frame is changed, the original tensors must be transformed, and the new matrices obtained from the transformed tensors.

In practice, it is sometimes more convenient to write equations 1.15a and 1.15b in terms of other variables. Under isothermal conditions, omitting the superscript T , they are given by, both in tensor or matrix notation [2]:

$$\epsilon = s^D \sigma + g D \quad (1.16a) \quad \sigma = c^E \epsilon - e E \quad (1.17a)$$

$$E = -g \sigma + \beta^\sigma D \quad (1.16b) \quad D = e \epsilon + \kappa^E E \quad (1.17b)$$

$$\sigma = c^D \epsilon - h D \quad (1.18a)$$

$$E = -h \epsilon + \beta^E D \quad (1.18b)$$

where $\beta = \kappa^{-1}$ (this is true both in matrix and tensor notation) and the various piezoelectric coefficient tensors d , g , e and h are related to each other by the following equations in tensor notation:

$$d = \kappa^\sigma g = e s^E \quad (1.19a)$$

$$g = \beta^\sigma d = h s^D \quad (1.19b)$$

$$e = \kappa^E h = d c^E \quad (1.19c)$$

$$h = \beta^E e = g c^D \quad (1.19d)$$

These equations are also valid in matrix notation [2]. Note that the exponent, *i. e.* the boundary conditions, is not the same depending on which set of variables is used. The consequence is that the physical properties of a piezoelectric material depend on the boundary conditions, as we already mentioned before. It is therefore crucial, to properly estimate the material properties, to choose the set of variables and equations which describes the experimental conditions the most accurately.

1.1.3 Crystal symmetry

The symmetry of the crystal imposes constraints on the number of elements of the matter tensors which are independent or non-zero. The higher the symmetry, the less the number of non-zero or independent coefficients. An important particular case for piezoelectricity is centrosymmetry. If a centrosymmetric crystal is put under stress, a charge should appear on its surface according to the direct piezoelectric effect. If the crystal is now rotated by 180° about its center of symmetry, an opposite charge should appear; however since the crystal is centrosymmetric, this charge should also be the same as before. Therefore, the appearing charge is zero and all the piezoelectric coefficients are actually zero. Centrosymmetric crystals do not show any piezoelectric coupling. This is also true for the point group 432, even though it is not centrosymmetric.

The symmetry classes 4mm (tetragonal), 6mm (hexagonal) and ∞m (poled, randomly oriented polycrystalline materials) are often encountered in practical situations. By convention, axis 3 is often used as the polar axis; the following tensors of interest are, for those symmetry classes,

in matrix notation [1, 2]:

$$\kappa = \begin{pmatrix} \kappa_{11} & 0 & 0 \\ 0 & \kappa_{11} & 0 \\ 0 & 0 & \kappa_{33} \end{pmatrix} \quad (1.20a)$$

$$d = \begin{pmatrix} 0 & 0 & 0 & 0 & d_{15} & 0 \\ 0 & 0 & 0 & d_{15} & 0 & 0 \\ d_{13} & d_{13} & d_{33} & 0 & 0 & 0 \end{pmatrix} \quad (1.20b)$$

$$s = \begin{pmatrix} s_{11} & s_{12} & s_{13} & 0 & 0 & 0 \\ s_{12} & s_{11} & s_{13} & 0 & 0 & 0 \\ s_{13} & s_{13} & s_{33} & 0 & 0 & 0 \\ 0 & 0 & 0 & s_{44} & 0 & 0 \\ 0 & 0 & 0 & 0 & s_{44} & 0 \\ 0 & 0 & 0 & 0 & 0 & s_{66} \end{pmatrix} \quad (1.20c)$$

For the symmetry classes 6mm and ∞m , s_{66} is not independent and is given by $2(s_{11} - s_{12})$.

The elastic stiffness matrix c and the piezoelectric e coefficient matrix will be useful in a number of measurements and are given below for the same symmetry classes [2, 3]:

$$e = \begin{pmatrix} 0 & 0 & 0 & 0 & e_{15} & 0 \\ 0 & 0 & 0 & e_{15} & 0 & 0 \\ e_{13} & e_{13} & e_{33} & 0 & 0 & 0 \end{pmatrix} \quad (1.21a)$$

$$c = \begin{pmatrix} c_{11} & c_{12} & c_{13} & 0 & 0 & 0 \\ c_{12} & c_{11} & c_{13} & 0 & 0 & 0 \\ c_{13} & c_{13} & c_{33} & 0 & 0 & 0 \\ 0 & 0 & 0 & c_{44} & 0 & 0 \\ 0 & 0 & 0 & 0 & c_{44} & 0 \\ 0 & 0 & 0 & 0 & 0 & c_{66} \end{pmatrix} \quad (1.21b)$$

For the symmetry classes 6mm and ∞m , c_{66} is not independent and is given by $1/2(c_{11} - c_{12})$. The e coefficients are obtained from equation 1.19d [2]:

$$e_{31} = d_{31}(c_{11}^E + c_{12}^E) + d_{33}c_{13}^E \quad (1.22a)$$

$$e_{33} = 2d_{31}c_{13}^E + d_{33}c_{33}^E \quad (1.22b)$$

$$e_{15} = d_{15}c_{44}^E \quad (1.22c)$$

1.1.4 Standard notations for piezoelectricity

The notations used above are the common notations for the fields of crystallography, thermodynamics or continuum mechanics. However some of these notations conflict when usages from other fields are brought together : for instance, the dielectric permittivity is often written

as ε in material science, very close to the notation for the strain ϵ adopted in this section. For this reason, in the rest of the text, we will sometimes follow the notation of the IEEE Standard on Piezoelectricity [4], where the notable differences with the above are:

1. The strain is noted S .
2. The stress is noted T .
3. The dielectric constant is noted ε .

The intended meaning shall be sufficiently clear whenever a different notation is employed. In publications on piezoelectricity, the strain is also sometimes written ξ .

1.2 Ferroelectricity

As we saw in the previous section, materials from a crystal class which is not centrosymmetric and does not belong to point group 432 may be piezoelectric. One such material is quartz. The symmetry of the quartz single crystal allows piezoelectricity to exist. However, a compound made of polycrystalline quartz in which the grains have a random orientation, such as a quartz ceramic, would display a global spherical symmetry. The spherical symmetry possesses centrosymmetry; therefore, such a compound would not be piezoelectric. Physically speaking, the random orientation of the crystallites implies that under the action of a stress or an electric field, the responses of the crystallites will compensate each other, so that the net macroscopic effect is zero.

Fortunately, piezoelectricity is not restricted to single crystals. Polycrystalline materials composed of piezoelectric grains may be used if the orientation of the grains is not random, and not centrosymmetric. Ordered growth along a specific crystalline direction is realized for thin films possessing a texture, *i. e.* a predominant out-of-plane orientation. This allows the use of piezoelectricity in micro-electromechanical systems (MEMS). AlN is an important technological example, since it is widely used as the oscillating element in radio-frequency (RF) filters [5]. AlN is in addition a polar material: It exhibits a permanent electrical dipole moment within the unit cell; its direction is called the polar axis.

The direction of the permanent dipole moment of an AlN crystal cannot be changed. For this reason, an AlN ceramic would not be piezoelectric either, because the grains are randomly oriented. Materials possessing a permanent electrical dipole moment are called pyroelectric. If the direction of the dipole moment can be changed by the application of a sufficiently large electric field, *i. e.* if its direction can be reversed, then the material is said to be ferroelectric. A ferroelectric ceramic can be piezoelectric: after applying a strong enough electric field, the misaligned permanent dipoles are reoriented to point towards the direction of the electric field — as much as they are allowed to by the symmetry of the crystallite. This process is called poling and is schematically shown in Figure 1.2. A poled ferroelectric ceramic possesses

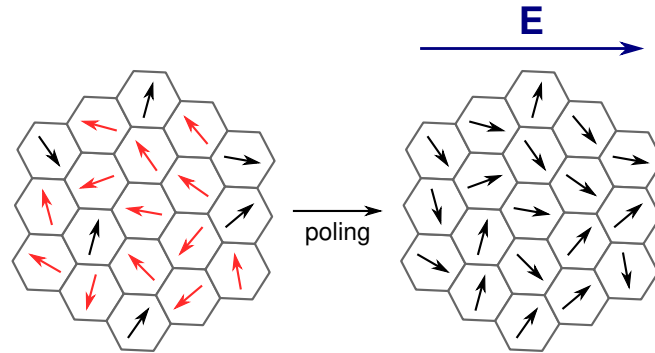


Figure 1.2 – Schematic picture of the poling process. The dipole moment of each hexagonal crystallite is shown by an arrow, which is red when there is a component which goes against the poling field. When the poling field is applied, the red arrows switch by 180° and are now aligned with the direction of the external field.

a conic symmetry ∞m , and there is a net macroscopic dipole moment pointing towards a unique direction: this material is thus piezoelectric. Note that it is also ferroelectric, since the net macroscopic dipole moment may be reversed by reversing the direction of the electric field. The existence of a net dipole moment makes it also pyroelectric. Hence, each material class is a subclass of the others, as pictured in Figure 1.3.

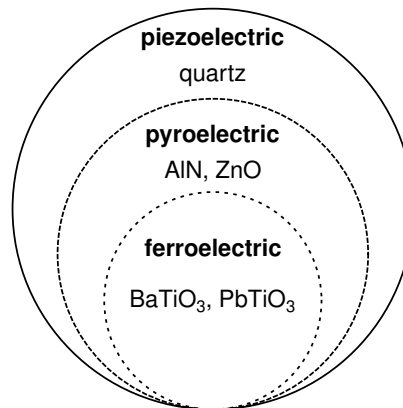


Figure 1.3 – Subclasses of piezoelectric materials. Some representative materials are indicated for each class.

The magnitude of the net dipole moment obtained after the poling process can be estimated by measuring the surface charge which has appeared on the material surface orthogonal to the direction of the poling electric field. This value is called the polarization; it also has the unit of a dipole moment per volume. Its value is generally given in $\mu\text{C}/\text{cm}^2$. By analogy, the microscopic dipole moment is generally referred to as the polarization, although the formal definition of polarization is more complex [6].

In ferroelectric materials, the new direction of the dipole moments is retained after the electric field is removed : The polarization shows a hysteretic behavior. Typically, ferroelectric mate-

materials possess a number of stable polar states at room temperature, and the dipole moment of the unit cell can be reoriented along any of them under the action of an appropriately directed electric field of sufficient magnitude. As a consequence, a ferroelectric crystal may be split into various regions with homogeneous dipole moment orientation. Such regions are called domains, and the boundary between them are called domain walls. If the crystal displays several domains, it is said to be in a polydomain state. Under the action of an electric field of sufficient magnitude, it is possible to align the polarization along the same direction everywhere in the crystal, which then consists of only one domain: It is said to be in a single domain or monodomain state. Many ferroelectric materials possess a high symmetry paraelectric phase at high temperatures which is non-ferroelectric [7]; the ferroelectric phase appears when the material is cooled down below a phase transition temperature called the Curie temperature. When this critical temperature is reached, the crystal will spontaneously split into domains in order to minimize the electrostatic energy (by avoiding the creation of charged surfaces) and the elastic energy (by orientating the polar axis so as to relieve existing stresses). As a consequence, as-fabricated samples, even single crystals, are generally not piezoelectric and must be poled to exhibit a piezoelectric response. Therefore, there are two disorders which poling will cancel: the polycrystalline disorder within the sample, and the polydomain disorder within each crystallite.

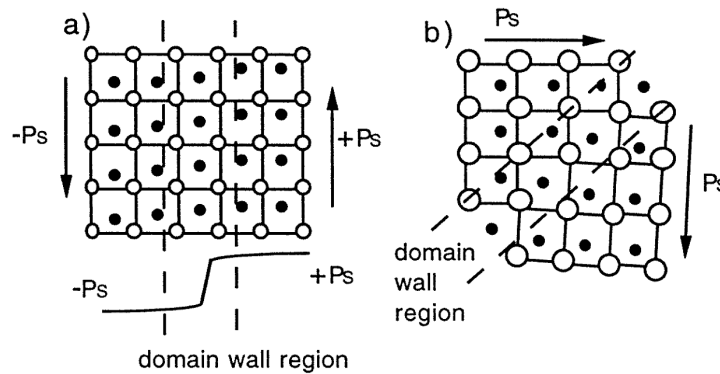


Figure 1.4 – Schematic illustration of the electrical and mechanical compatibility rules in a ferroelectric with a tetragonal unit cell for a 180°-domain wall in (a) and a 90° domain wall in (b). The polarization is directed along the long axis of the tetragonal unit cell. From Damjanovic [8].

Domain walls are named after the angle between the polarization directions of the two domains they separate. Two classes of domain walls can be distinguished. 180° domain walls are ferroelectric domain walls and spontaneously appear to minimize the electrostatic energy. They can be moved by the application of an electric field, but not by the application of a stress [8]. Non-180° domain walls are ferroelectric-ferroelastic domain walls. They can minimize both the electrostatic energy and the elastic energy of the crystal [8]. They will respond to both an electric field and a stress. Domain walls have specific orientations with respect to the domains they separate, to ensure both electrical compatibility (the domain wall is not charged)

and mechanical compatibility (between adjacent unit cells with a different polar axis). This is schematically shown in Fig. 1.4. At the first order, the motion of 180° domain walls contributes to the dielectric response of the crystal only, whereas the motion of non- 180° domain walls contributes to both the dielectric and piezoelectric response. In a polycrystalline sample, many internal stresses may exist after fabrication, so that the crystallites will spontaneously split into both ferroelectric and ferroelastic domains in order to minimize the total electrostatic and elastic energy [9]. An optical microscope image of the resulting domain pattern for a ceramic sample is shown in Fig. 1.5. The inset shows how the domains are arranged: In this case, all the boundaries between domains of different orientations are 90° domain walls.

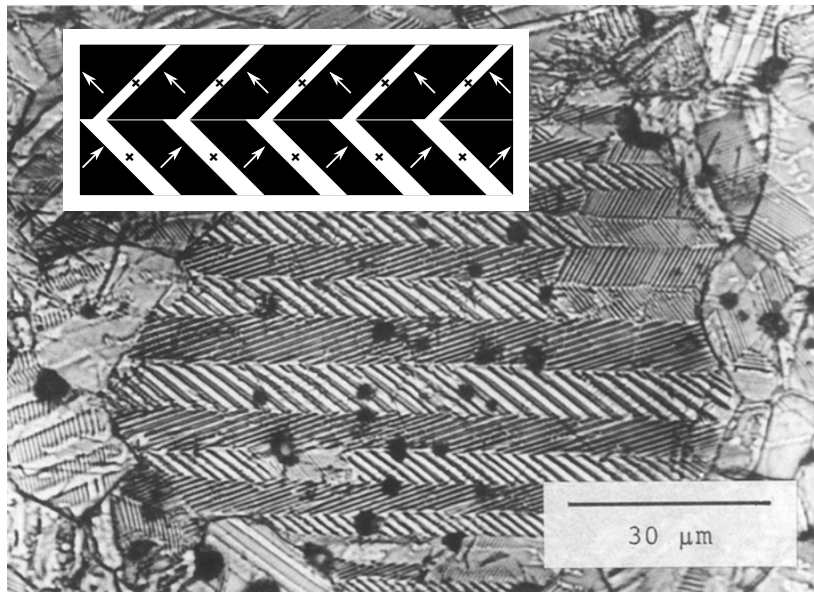


Figure 1.5 – Domain pattern inside ferroelectric BaTiO_3 ceramic grains. The ceramic was cut, polished and etched to reveal this pattern. The complex intertwining of 90° domain walls indicates domain splitting for stress relief. The contrast in this optical micrograph picture is given by the change of refractive index for different domain orientations. The inset [10] shows how the polarization vector is arranged. From Arlt [9].

1.3 Lead zirconate titanate

Lead zirconate titanate $\text{PbZr}_x\text{Ti}_{1-x}\text{O}_3$ (PZT) is a solid solution of PbTiO_3 (PTO) and PbZrO_3 (PZO) which is ferroelectric at room temperature for $x < 0.95$ [11]. This material is used both in ceramics [12] and thin film form [13] for its large piezoelectric coupling coefficients, and its tunability of properties by aliovalent doping makes it well-suited for a variety of applications, such as precision actuators or ultrasonic power generators [12]. It has a perovskite structure, where Pb atoms occupy the A-sites and Ti or Zr atoms occupy the B-sites, as pictured in Fig. 1.6 (a) and (b) for PTO. It has a paraelectric cubic phase at high temperature, which becomes tetragonal for Ti-rich compositions and rhombohedral for Zr-rich compositions below the

Curie temperature T_C [11]. Both phases are ferroelectric but do not have the same polar axis: For the tetragonal structure, the polar axis is situated along the long axis of the tetragonal unit cell, while for the rhombohedral phase, it is situated along the elongated body diagonal of the unit cell. The phase diagram of PZT is shown in Figure 1.6 (c). The compositional phase transition happens at $x \approx 0.52$, which is called the morphotropic phase boundary (MPB). A number of material properties, including the piezoelectric response, are peaking at this composition [14].

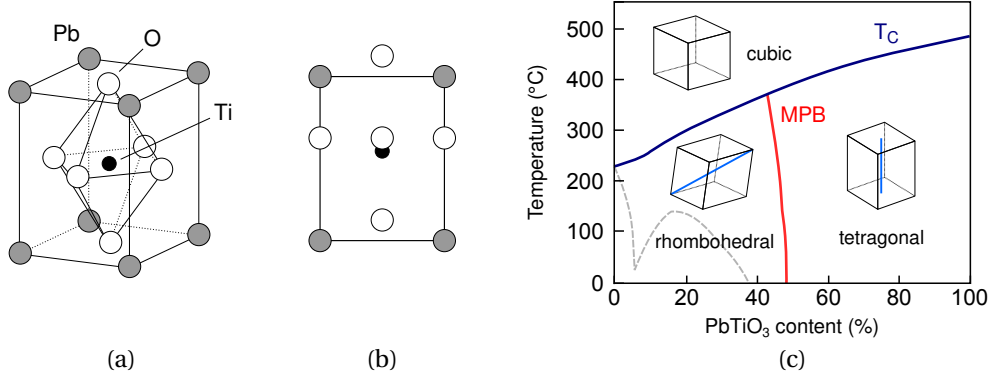


Figure 1.6 – (a): Unit cell for PbTiO₃ in the tetragonal phase. (b): Tetragonal unit cell with displacement of O and Ti atoms with reference to Pb atoms [15]. The tetragonal strain and the atomic displacements are exaggerated for clarity. (c): Phase diagram of PZT. The polar axis of the ferroelectric phases is shown in blue. The dashed line indicates the phase transition to the rhombohedral low temperature phase (above 5 at.% PTO content) or to the orthorhombic antiferroelectric low temperature phase (below 5 at.% PTO content). From Jaffe *et al.* [11].

The thermodynamics of the ferroelectric properties of PZT can be described by the Landau-Ginsburg-Devonshire phenomenology [7]. The full set of thermodynamic coefficients for the entire phase diagram of PZT was determined and discussed by Haun and coworkers in a series of papers [16–20]. This provides a framework to explain the origin of the change of properties induced by varying the $Zr/(Zr+Ti)$ ratio. The enhanced properties at the MPB were thus explained by a large transverse and anisotropic susceptibility of the polar axis at this composition [21]. These coefficients are also used to estimate the theoretical maximum for piezoelectric coefficients in thin films [22], for which properties differ significantly from that of bulk ceramics, so that direct comparison is often not relevant.

The overall response of PZT samples greatly depends on the domain wall contributions [21]. For the dielectric or the piezoelectric response, the response r may be written as:

$$r = r_{\text{int}} + r_{\text{ext}} \quad (1.23)$$

where r_{int} denotes the lattice contribution and r_{ext} the domain wall contribution. r_{ext} can be comparable or larger in magnitude to the intrinsic contribution [23] and its magnitude can be tuned by the addition of dopants [12]. The domain wall contribution to the overall response, as well as the influence of the most common types of dopants, are discussed in more

details in chapter 5, where we show how it is possible to take advantage of them to improve the performance of piezoelectric energy harvesting devices with PZT thin films.

1.4 PZT thin films for MEMS

The great interest in MEMS lies in the opportunity to offer more diverse functionalities to microfabricated chips by the addition of mechanical components [13]. Piezoelectric thin films are attractive materials for MEMS, since they display an electromechanical coupling which is intrinsic to the material; this allows straightforward downscaling and simple architectures for resonant structures in addition to low power requirements [24]. PZT thin films are the material of choice if the desired output is a force, a displacement amplitude, or a large output power, whereas AlN is preferred if the size of the output voltage or if the power efficiency are more important [25]. PZT has been employed for a variety of applications including micromotors [26], IR-detection arrays [27], photoacoustic gas sensors [22], ultrasonic transducers [28], ink-jet printing heads [29], microscanners for various optical applications [30], non-volatile memory storage [31], or energy harvesting [32].

PZT can be deposited by all the major techniques: physical vapor deposition (PVD), metal-organic chemical vapor deposition (MOCVD), pulsed laser deposition (PLD) and chemical solution deposition (CSD or sol-gel) [25]. A precise control of stoichiometry is required to avoid the appearance of competing, non-ferroelectric phases which are more tolerant to off-stoichiometric compositions than the perovskite phase [33].

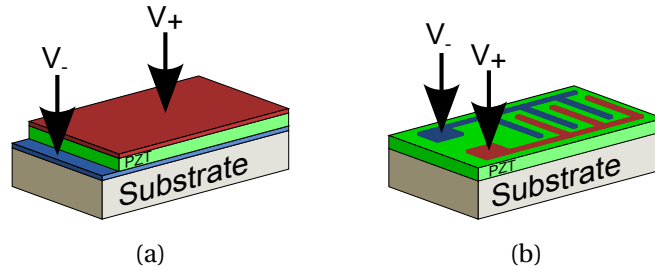


Figure 1.7 – (a): parallel plate electrode configuration. (b): interdigitated electrode configuration.

The integration of PZT is not straightforward, since PZT cannot be grown directly on Si and requires high processing temperatures [33]. To address the former, an adequate set of buffer layers preventing interdiffusion must be used, typically Ti/SiO₂/Si [33]. The high processing temperature means that the bottom electrode must be a noble metal or a conductive oxide to prevent oxidation during processing, if the parallel plate electrode configuration (PPE) is used (Fig. 1.7 (a)); Pt, RuO₂ or SrTiO₃ are commonly used [33]. Growth of PZT on insulating layers for use with interdigitated electrodes (IDE) (Fig. 1.7 (b)) is not yet fully mastered, and ZrO₂ [34] as well as MgO [35] have been proposed to prevent lead interdiffusion or to promote textured growth. The following enumeration compares the features of the PPE and IDE designs:

PPE configuration:

- Low voltage output in direct mode
- Low driving voltage in converse mode
- Tensile stress generated in the film
- Transverse piezoelectric coefficient
- Lower polarization retention and larger losses
- Well-established process route

IDE configuration:

- High voltage output in direct mode
- High driving voltage in converse mode
- Compressive stress generated in the film
- Longitudinal piezoelectric coefficient
- Better polarization retention and lower losses
- Process route not fully established

As mentioned, the interest in PZT thin films for MEMS lies in the large force or displacement output they can provide; reports therefore usually focus on the determination of the piezoelectric coefficients, which are a good indication of the performances in this case. In the PPE configuration for use in a cantilever beam, the piezoelectric coefficient of interest is an effective transverse coefficient called $e_{31,f}$. It is different from the piezoelectric coefficient e_{31} because the PZT thin film is clamped by the substrate [36] — it is actually larger in absolute value. This coefficient is often reported as a measure of the piezoelectric response of piezoelectric thin films, because it is relatively straightforward to measure [37]. The cantilever architecture is well representative of practical situations, since many MEMS devices are based on the bending of flexural structures by the stress generated in the active piezoelectric layer [38], so that thin film characterization is often performed with this type of device. In particular, this is an architecture very similar to piezoelectric energy harvesting devices with piezoelectric thin films (see section 1.5), so that the literature values for $e_{31,f}$ can be directly used to estimate the film performance for energy harvesting. This is an important point for the device design: The high cost of MEMS processing means that it is very desirable to optimize all the design parameters with test structures before reaching the prototyping phase. Accurate characterization of the thin film performances is therefore valuable, since it allows to determine the proper material fabrication route for optimal performances.

$e_{31,f}$ may be measured in two ways: either with the direct piezoelectric effect after poling [39] (often called “direct mode” measurement), or with the converse piezoelectric effect [40] (called “converse mode” measurement). Several techniques exist for the direct effect $e_{31,f}$ measurement, including cantilever bending [39], four-point bending [41] and the wafer flexure technique [42]. Although the cantilever bending technique is more complex, due to the inhomogeneous strain imposed on the bending beam [43], it allows to measure both direct and converse $e_{31,f}$ on the same sample, so that the influence of the boundary conditions on the film properties can be readily evaluated. This is valuable for complex architectures such as the IDE configuration, which is better suited for energy harvesting applications than the PPE configuration (see section 1.5).

In converse mode, the cantilever is typically clamped at one end and the tip excursion is measured by interferometry by shining a laser beam onto a dedicated reflector at the tip, or with a photonic sensor placed at the same location [40]. The excursion then allows the determination of $e_{31,f}$. There is, unfortunately, no common standard for the measurement of

the converse $e_{31,f}$ coefficient [40]. It shows a pronounced dependence on the electric field and on the prehistory, so that, as discussed by Mazzalai and coworkers [40], it is best to report the full $e_{31,f}$ vs. field curve for an accurate assessment of the performances. Other groups simply use the peak-to-peak tip displacement without providing this curve [37]. In direct mode, the value of $e_{31,f}$ also depends on the poling conditions and the thickness of the film [44] as well as on the static strain imposed on the sample during the measurement [39]. In all cases, the frequency of the oscillating strain or voltage must be away from the cantilever resonance, where $e_{31,f}$ is peaking [37, 40] and is thus not representative of the properties of the film.

For the IDE configuration, effective coefficients were proposed by Chidambaram and coworkers: e_{IDE} for direct mode [43] and $e_{33,if}$ for converse mode measurements [35]. Note that these coefficients are positive whereas $e_{31,f}$ is negative; this is because a negative (compressive) stress σ is generated in the PZT film with the IDE configuration, and $\sigma = -e_{33,if}E$ where E is the electric field. e_{IDE} and $e_{33,if}$ can be considered equal with good accuracy, as is shown in appendix B. In the IDE configuration, the Poisson's ratio of the substrate is included in the definition of e_{IDE} (but not in the approximation $e_{IDE} = e_{33,if}$), so that comparison with the PPE case for direct mode should be done by defining $e_{PPE} = e_{31,f}(1 - \nu_s)$, where ν_s is the Poisson's ratio of the substrate [43, 45]. The IDE coefficients can be evaluated with the same techniques used to obtain $e_{31,f}$.

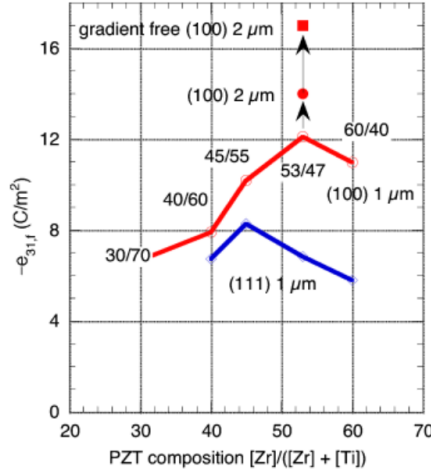


Figure 1.8 – Effective transverse piezoelectric coefficient $e_{31,f}$ of PZT thin films as a function of the $Zr/(Ti+Zr)$ ratio for the {100} and {111} texture. From Muralt [13].

In the PPE configuration, the performances depend greatly on the composition and on the film texture [13], as shown in Fig. 1.8. The significant drop of $e_{31,f}$ when the texture differ from {100} is the reason why texture control is very desirable for PZT thin films. In the IDE configuration, no such study on texture is available, but the texture will determine the maximum reachable polarization after poling [45]; low polarization is detrimental for the value of $e_{33,if}$. Note that in chapter 3, we provide values for the maximum reachable polarization which are more accurate than the ones given in Ref. [45]. A number of reported $e_{31,f}$, $e_{33,if}$ and e_{IDE} values are

Table 1.2 – Reported $e_{31,f}$ and $e_{33,if}$ (converse mode) or e_{IDE} (direct mode) values. Negative values are $e_{31,f}$ values and positive values are $e_{33,if}$ or e_{IDE} values.

Reference	e value (C/m ²)	Mode	Deposition route	Year
Ref. [44]	−13	direct	sol-gel	2003
Ref. [46]	−15	direct	sol-gel	2007
Ref. [47]	−18	direct	sol-gel	2007
Ref. [41]	−12	direct	sol-gel	2007
Ref. [42]	−6	direct	sol-gel	2012
Ref. [45]	−11	direct	sol-gel	2013
Ref. [48]	−23	converse	RF-sputtered	2014
Ref. [35]	−15	converse	sol-gel	2015
Ref. [37]	−15	converse	RF-sputtered	2015
Ref. [45]	15	direct	sol-gel	2013
Ref. [35]	15	converse	sol-gel	2015

shown in Table 1.2. In all cases, the films had the MPB composition. There is no clear trend, but recent publications usually reach at least 15 C/m² in absolute value for either of these coefficients; this value can therefore be considered as state-of-the-art. Note that all the values were rounded to the nearest integer for clarity.

1.4.1 PZT thin films by CSD

As we saw above, CSD or sol-gel has a large predominance in the literature. Indeed, this is an inexpensive method which allows to easily work with various compositions and dopants, by the preparation of the appropriate precursors using simple chemical methods. Sol-gel PZT films are very dense [13], and as seen in Table 1.2, state-of-the-art piezoelectric response may be obtained. Even though the single-target RF sputtering route is also mentioned in Table 1.2, it offers little flexibility since a new target must be prepared whenever a different composition is desired. It is possible to vary the composition of sputtered films with a single tool by co-sputtering from 3 metal targets [23]; but this technique is seldom reported in the recent literature, and it anyhow requires all the equipments needed to operate a vacuum chamber dedicated to sputtering, whereas for the sol-gel method, only a chemical bench and an annealing tool are necessary. CSD therefore provides an ideal testbed for fundamental research as well as for prototyping [49].

Sol-gel deposited PZT thin films are typically dense and smooth with columnar grains [44], and have a similar microstructure for growth on Pt or MgO [35]. Texture control is realized by the use of an appropriate seed layer [25]: PTO is generally used for {100} growth and a thin TiO₂ seed layer is chosen for {111} growth, resulting in more than 90 % of the film volume having the desired orientation for a large range of Ti/(Ti+Zr) ratio [50]. PTO has also been used as a seed layer to obtain {100} films on MgO [35], albeit with limited reproducibility [51].

If only one precursor solution is used for all spinning steps, the final film shows a gradient of composition within each crystallized layer [44]. It is possible to reduce the dispersion around the nominal composition from ± 12 at.% to ± 2.5 at.% by using a set of 4 solutions with graded compositions opposing the natural Zr/(Zr+Ti) gradient, as shown by Calame and Muralt [47]; this is the so-called gradient-free route. This results in a 20 %-larger $e_{31, f}$ as compared to a film fabricated with the one-composition route, for a nominal composition at the MPB. This is the highest $e_{31, f}$ value for sol-gel PZT shown in Table 1.2. This route requires the preparation of more precursor solutions (4 instead of 2), and is therefore more expensive to pursue, so that the one-composition route remains sometimes preferred despite the non-maximal performance it provides.

In this work, we have exclusively used the gradient-free route to exclude any possible effect due to the presence of a composition gradient. A few more details on this deposition technique are given in appendix A.

1.5 Piezoelectric energy harvesting

1.5.1 Motivations

Energy harvesting broadly defines the scavenging of ambient energy sources for specific purposes. Watermills and windmills are centuries-old examples of energy harvesting systems which have been used by many cultures. The industrial age has brought in large-scale application of the same principle in the form of the renewable energy sources exploited for the supply of the power grid — such as wind, tide, or sunlight energy.

At a much smaller scale, the continuing decrease in the power requirements of electronic circuits offers the potential for the deployment of wireless systems in a variety of situations [52]. As an example, we mention structural health monitoring of large civil infrastructures, which is particularly interesting to better understand their behavior under test loads or real loads [53, 54]. Thermal effects and wind interactions with suspension bridges remain not fully understood [54] and require on-site monitoring for proper assessment of their impact on the structure. Wired sensors distributed over the structure offer a reliable way for data collection, but such systems are very expensive to install and to maintain, leading to insufficient node density and the continuing necessity for human inspection [53]. Because they are cheaper to install and do not require maintenance, wireless monitoring devices are attracting a lot of attention in the structural health monitoring community. Equipped with on-board chips, they can perform local data treatment and take decisions based on the outcome, with the prospect of turning the monitoring of the structure into a completely automated process [53]. In order to fully attain this maintenance-free situation, it is highly desirable that the monitoring node includes its own power source in the form of an energy harvesting device. Ambient sources of energy available for harvesting, apart from sunlight, include the vibration of the bridge structure induced by the traffic [55] and wind energy [56]. In this case, the lifetime of the

device would be limited by the lifetime of its internal components only, virtually removing the need for on-site human intervention entirely. Wireless sensor nodes (WSN) are not restricted to the monitoring of large civil infrastructures, but can also be applied as embedded sensors on cars, airplanes, or industrial tools. Another potential application is the powering of low-power equipment, such as lamplights or low power integrated circuits, whenever wiring is costly or unpractical. WSN have power requirements of the order of $100\mu\text{W}$ [52], and the decreasing need for power requirement combined with increasing refinement in energy harvesting technology creates the prospect of large-scale production of such autonomous wireless systems in the near future.

Another important area of interest concerns implanted medical devices (IMD). Here battery replacement sometimes means invasive surgery on a patient already suffering from a condition, with all the risks this implies. Autonomous powering of such systems, provided that the general lifetime of the equipment is sufficiently long, could remove the necessity for device maintenance, whatever the form it takes, for the entire lifetime of the patient. Ambient energy sources that can be harvested in the human body are numerous, and include temperature gradients, joint rotation, deformation of tissues, and others [57]. In the following, we will discuss energy harvesting with WSN or IMD as the targeted applications.

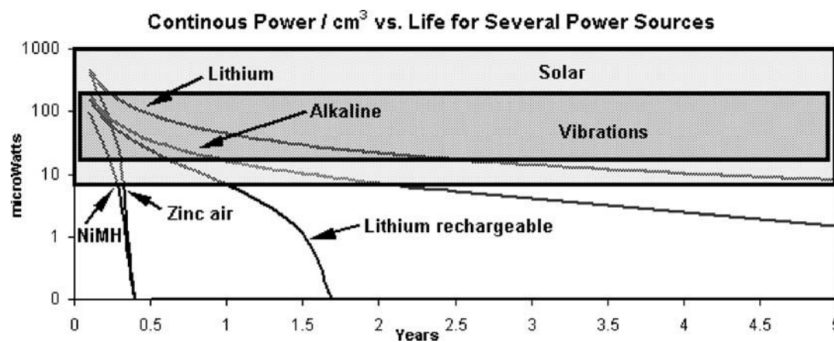


Figure 1.9 – Power density of solar and ambient vibrations compared to conventional battery technology (for a single charge). From Ref. [58].

Roundy *et al.* have shown that, if sunlight is not available, harvesting ambient vibrations is a serious alternative to conventional batteries whenever the WSN lifetime exceeds several years [58]. Indeed, for a single charge, the power density of batteries decreases with time, so that they ultimately must be recharged or replaced; on the contrary, ambient vibrations provide a large and constant power density, as shown in Fig. 1.9. The authors analyzed the power spectra of several possible vibration sources and investigated the merits of electrostatic and piezoelectric energy harvesting as a powering solution.

Piezoelectric energy harvesters (PEH) refer to energy harvesting systems whose working principle rely on the deformation of piezoelectric materials. They can be used for low or very low scale energy production, from the mW range down to the μW range. For vibration energy harvesting in this power range, two other methods are also available : electrostatic energy

Table 1.3 – Theoretical maximum energy density for three principles of vibration energy harvesting. From Ref. [62].

Principle	Energy density (mJ/cm ³)	Figure of merit	Assumptions
Piezoelectric	35.4	$(1/2)\sigma^2 k^2 / 2c$	PZT 5H
Electromagnetic	24.8	$(1/2)B^2 / \mu_0$	$B = 0.25 \text{ T}$
Electrostatic	4	$(1/2)\epsilon_0 E^2$	$E = 3 \times 10^7 \text{ V/m}$

harvesting [58, 59], where the distance between two electrodes separated by a dielectric is varied; and electromagnetic harvesters [60, 61], where the relative movement of a coil in a magnetic field causes current to flow in the coil. Roundy and Wright [62] have compared the energy density provided by these three approaches. The result is shown in Table 1.3. They were obtained with typical values for the physical parameters involved : σ is the stress, k is the piezoelectric coupling coefficient, c is the elastic constant relevant to the system configuration, B is the magnetic field, μ_0 the permeability of vacuum, E the electric field, and ϵ_0 the permittivity of vacuum. We observe that piezoelectric energy harvesters offer the highest energy density of the three, which is advantageous for WSN and IMD, where size is often a critical factor. With the constant advances in device miniaturization, piezoelectric energy harvesting has therefore attracted much more attention than the other two approaches in recent years [63].

In the following, we will describe in more details the working principle for vibration-based piezoelectric energy harvesters, a configuration which is often adopted in the literature.

1.5.2 Principle of operation

Figure 1.10 (a) shows a bimorph cantilever beam with seismic mass, which is a typical configuration of many PEH designs, because it has the lowest stiffness for a given size, and yields a large average strain for a given force [58]. The seismic mass is coupled to the external vibration source by the beam and moves up and down as a consequence. The mechanical properties can be adjusted by inserting a shim between the two piezoelectric layers. The presence of a shim is actually necessary in the unimorph configuration, so that the neutral axis is not situated within the piezoelectric layer; this would result in self-compensating charge generation because both compressive and tensile strains will exist in the polar material.

In first approximation, this system can be modeled by the equivalent mechanical system shown in Fig. 1.10 (b) [58]. The system has a mass M and its position $z(t)$ is inertially coupled to the external vibration source having function $y(t)$. The stiffness k represents the stiffness of the oscillating structure, while the damping coefficients b_e and b_m represent the piezoelectric damping (converting mechanical energy into electrical energy through the direct piezoelectric effect and taking it away from the system, *i. e.* this is the harvesting term) and the mechanical damping (mostly air in typical situations), respectively.

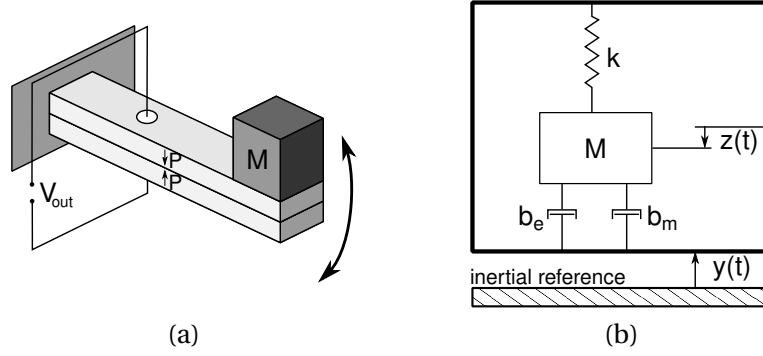


Figure 1.10 – (a): bimorph cantilever beam with seismic mass, composed of two layers of piezoelectric material with opposite polarization. The series connection of the two layers is shown; parallel connection is also possible. (b): equivalent mechanical systems for the cantilever beam in (a).

The equation of movement of the mass M is:

$$M\ddot{z} + (b_e + b_m)\dot{z} + kz = -M\ddot{y} \quad (1.24)$$

The resonance frequency is $\omega_0/2\pi$, where $\omega_0 = \sqrt{k/M}$. At resonance, the harvested power P is given by [60]:

$$P = \frac{M\zeta_e A^2}{4\omega_0(\zeta_e + \zeta_m)^2} \quad (1.25)$$

where $\zeta_e = b_e/(2M\omega_0)$ and $\zeta_m = b_m/(2M\omega_0)$ are normalized damping factors, and $A = Y\omega_0^2$ is the input acceleration amplitude, $Y > 0$ being the displacement amplitude of the source vibration.

This equation shows that designs operating with a large mass and at low frequencies are the most efficient. Typical frequency spectra of ambient vibrations show a high power density peak at some frequency below 200 Hz [58], to which, therefore, the harvester should ideally be tuned. A large value of ζ_m is detrimental for the output power, because most of the harvested energy is then dissipated mechanically and not by the piezoelectric material. The optimum output power is obtained for $\zeta_e = \zeta_m$ and the relative damping should thus also be optimized by the chosen design. An expression for ζ_e was derived analytically by Roundy and coworkers [58] with beam theory and piezoelectric constitutive equations, yielding:

$$\zeta_e = \frac{\omega_0 k_{31}^2}{\sqrt{\omega_0^2 + (RC)^{-2}}} \quad (1.26)$$

$$k_{31}^2 = \frac{E_p d_{31}^2}{\varepsilon_p} \quad (1.27)$$

where k_{31}^2 is the coupling coefficient for the piezoelectric transverse mode, E_p and ε_p are

respectively the Young's modulus and dielectric constant of the piezoelectric material, C is the capacitance of the piezoelectric layers, and R is the load resistance. The performance of the PEH depends both on the piezoelectric material and on the load circuit: There is an optimal load R for which we can achieve the condition $\zeta_e = \zeta_m$ for optimal output power. In addition, regarding the piezoelectric material itself, the transverse piezoelectric coefficient d_{31} should be large while the dielectric constant ϵ_p should be small for maximal electrical damping, *i. e.* maximal conversion of the input mechanical power into output electrical power.

The model of Fig. 1.10 (b) is only an approximation, however; these equations were originally introduced by Williams and Yates [60] for electromagnetic harvesters and they do not describe the electromechanical damping accurately [64]. For instance, the physical properties of the piezoelectric material will vary depending on the electrical boundary conditions, *i. e.* the load resistance; this effect is not addressed by this model. Erturk and Inman proposed more accurate equations for the unimorph and bimorph configurations in two later publications [65, 66]. However this analytical approach is rather complex, and finite element (FE) modeling can prove to be simpler and more helpful for the designing process [48]. Nevertheless, Eq. 1.25 captures the essential trade-offs of the PEH system, and can be used for an initial designing phase.

For piezoelectric thin films, the figure of merit for the harvesting performance is the product of the effective piezoelectric coefficients eh [43]:

- $e_{\text{PPE}}h_{\text{PPE}}$ for PPE, where $e_{\text{PPE}} = (1 - \nu_s)e_{31, \text{f}}$ and $h_{\text{PPE}} = (1 - \nu_s)h_{31, \text{f}}$, where ν_s is the Poisson's ratio of the substrate;
- $e_{\text{IDE}}h_{\text{IDE}}(1 - \eta)$ for IDE, where $\eta = b/(a + b)$ is the metalization ratio, b the electrode finger width and a the IDE gap.

The product eh has the unit of an energy density. The h coefficient is measured in direct mode in open circuit conditions (see chapter 2). It can be approximated as $h \approx e/\epsilon_0\epsilon_p$, where ϵ_p is the dielectric constant of the piezoelectric layer; so that the product eh may be obtained as:

$$eh \approx \frac{e^2}{\epsilon_0\epsilon_p} \quad (1.28)$$

If a full device is fabricated, the effective electromechanical coupling coefficient k_{eff}^2 can be estimated with the knowledge of the resonance and antiresonance frequencies f_r and f_a , which can be obtained by driving the device with a frequency sweep and recording the impedance. It quantifies the amount of mechanical energy transformed into electrical energy by the piezoelectric transducer. It is given by [32]:

$$k_{\text{eff}}^2 = \frac{2(f_a - f_r)}{f_r} \quad (1.29)$$

Table 1.4 – Acceleration and low frequency peak position for selected sources. 1 g is taken as 9.81 ms^{-2} . From Ref. [58].

Vibration source	Acceleration (g)	Freq. of power density peak (Hz)
Car engine compartment	1.2	200
Base of 3-axis machine tool	1	70
Clothes dryer	0.36	121

1.5.3 PEH for MEMS applications

One of the difficulties in using vibration-based energy harvesting for micro-electromechanical systems (MEMS), is that the seismic mass is necessarily limited by the small dimensions of the device. According to Eq. 1.25, since the output power is proportional to the mass for a given acceleration, it is crucial to attempt to match the resonance frequency of the system with the highest power density peak of the ambient vibration spectrum. For the same reason, such PEH should be used only when sufficient accelerations are present, due to the A^2 dependence of the output power. Table 1.4 shows a selection of sources where microscale PEH could be employed due to their high acceleration value. The frequency peak is at maximum located at a few hundreds of Hz. All the other examples provided by Roundy *et al.* [58] have the highest power density peak lower than 125 Hz. Extracting power from slow oscillations with a vibration-based device demands excellent performance, since the acceleration level for such sources is generally low, because of the acceleration dependence on the square of the frequency.

For a cantilever system with a proof mass whose dimensions are much smaller than the cantilever length, the resonance frequency is proportional to $\sqrt{K/(M_e + M)}$, where M is the proof mass, and K and M_e are respectively the effective stiffness and effective mass of the cantilever, and are given by [67]:

$$K = \frac{3Dw}{L^3} \quad (1.30)$$

$$D = \frac{E_{\text{eff}}h^3}{12} \quad (1.31)$$

$$M_e = 0.236mwL \quad (1.32)$$

where L , w and h are the length, width and height of the cantilever, respectively, E_{eff} is the effective Young's modulus of the cantilever, and m is the mass per unit width. D is the bending modulus per unit width. Therefore, for a fixed proof mass M , the main route for lowering the resonance frequency is to reduce the effective cantilever stiffness. This can be achieved by using mechanically compliant materials and by diminishing the cantilever height to length ratio h/L . Since piezoelectric ceramics are rather stiff, softer underlayers can be used, and the ratio between the thickness of the underlayer and the thickness of the piezoelectric layer should be optimized — a thinner piezoelectric ceramic layer will be more compliant, but also

generate less power. Increasing L may be prevented by size constraints, but reducing h is relatively simple with regular microfabrication techniques, and for this reason many cantilever designs are suspended like the one shown in Fig. 1.11 and fabricated by Jeon *et al.* [68]. For such structures, the residual stress of the active layer and underlayers should be properly controlled for optimal operation. The authors used dry etching to release the structures. The active layer is a $0.5\text{ }\mu\text{m}$ -thick sol-gel PZT thin film with the MPB composition. The authors did not use a proof mass, resulting in a high fundamental resonance frequency of 13.9 kHz and an output power of $1\text{ }\mu\text{W}$ for the optimal load after rectification, for an acceleration of about 10 g.

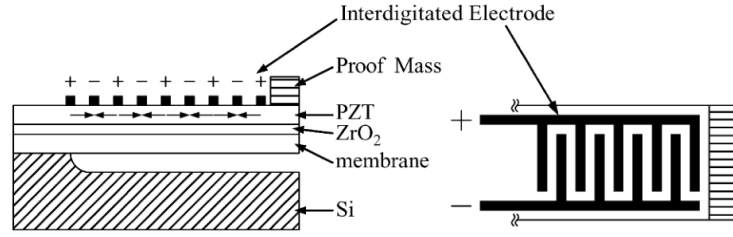


Figure 1.11 – Thin cantilever structures from Jeon *et al.* [68].

A similar device, this time with a proof mass, using a $2\text{ }\mu\text{m}$ -thick sol-gel PZT thin film, was later fabricated by Muralt *et al.* [32]. The Si from the wafer was used as the seismic mass, and an optimized PZT/Si thickness ratio, combined with the growth of a SiO_2 underlayer for PZT stress compensation, resulted in a coupling constant of 5 % and an output power per acceleration and unit area of $220\text{ }\mu\text{W}/\text{cm}^2/\text{g}$. The resonance frequency was 855 Hz and $1\text{ }\mu\text{W}$ was obtained at an acceleration of 1.5 g, with an output voltage of about 1.4 V. The output voltage is of importance because the AC voltage output of a PEH generally needs to be rectified, since many microelectronic circuits are powered with DC voltage. The efficiency of the rectifier quickly drops below a threshold voltage of about 0.5 V [32]. For this reason, the IDE configuration used by Ref. [68] and [32] is often chosen when materials with a large dielectric constant like PZT are used, since the finger spacing can be adjusted to several times the film thickness, reducing the capacitance of the device as compared to the parallel plate (PPE) configuration. The PEH converts mechanical power into electrical power through the direct piezoelectric effect, and therefore generates charges; for a given amount of charge, the output voltage will be larger if the capacitance is lower, according to the relation $Q = CV$. In addition, the IDE configuration uses the longitudinal piezoelectric coefficient instead of the transverse coefficient, which should increase the figure of merit for the PEH [43]. A larger poling voltage is however required, and the film volume situated below the electrode fingers is not active [35], so that, for a given device size, designs with larger finger widths have a reduced power output.

Along PZT thin films, AlN thin films are also often used in PEH [63]. The reason for this is twofold. The first reason is an easier integration with the CMOS process. A high thermal budget is needed for the deposition of PZT thin films, usually above $500\text{--}600\text{ }^\circ\text{C}$ either by sputtering or sol-gel, due to the high energy required to crystallize the ferroelectric perovskite

phase. In addition, safety measures must be taken to protect the workers from the toxicity of Pb and to avoid cross-contamination. No such precautions are needed with AlN, which can be deposited by sputtering at temperatures down to 300 °C, a much more acceptable thermal budget. The second reason is that, even though the transverse piezoelectric coefficient of AlN is 10 times less than that of PZT, its dielectric constant is about a hundred times lower; thus a similar coupling coefficient is obtained (see Eq. 1.27), but with the benefit of a large decrease of the capacitance of the device, providing higher voltage output for a similar design. Note that, since AlN is a pyroelectric material, grown with the polar axis out of the plane, it cannot be used in the IDE configuration but only in the PPE configuration. Sc-doped AlN films show higher transverse piezoelectric coefficients than undoped films [69] and could be a promising candidate for future PEH, provided that the doping does not increase the dielectric constant nor the dielectric losses too much.

The lower coupling of AlN cantilevers can be compensated by the reduction of the mechanical damping coefficient thanks to vacuum packaging, as reported by Elfrink *et al.* [70] and Defosseux and coworkers [71]. Elfrink *et al.* [70] observed a 4-fold increase and a narrowing of the power output resonance peak when testing their device under vacuum. The resonance frequency was close to 600 Hz. They could power a small temperature-reading WSN mounted on a shaker with an acceleration of 0.64 g at 353 Hz. Unfortunately, the slow leaking of air into the package means that the vacuum condition cannot be maintained over time. Defosseux and coworkers [71] employed a tapered cantilever design, enlarging near the clamped end in a rounded fashion to distribute the bending stress over a larger area. Their device had a resonance frequency at 214 Hz and a power output of 0.6 μ W at 0.15 g of acceleration under vacuum, compared to about 0.25 μ W at the same acceleration but under air. Higher accelerations did not provide higher outputs because the packaging limited the excursion of the device, in order to prevent mechanical failure from large strains. 2.2 V output voltage were reached at 0.25 g. Note that due to their high Q factors, such devices display narrow resonance peaks, and are therefore restricted to situations with a well-defined vibration resonance frequency which does not vary with time. This is typically the case for industrial equipments.

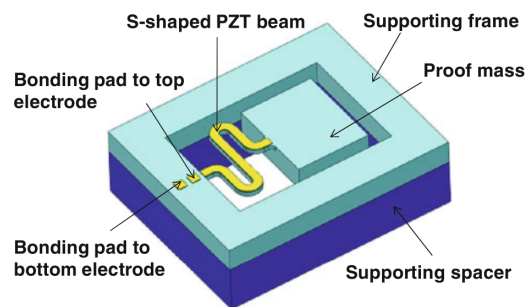


Figure 1.12 – S-shaped cantilever structure from Liu *et al.* [72].

Reducing the stiffness of the PEH structure can also be achieved by using an architecture other than the cantilever design. Liu and coworkers designed a meandering cantilever connected

to a proof mass to reduce the stiffness of the structure [72], as pictured in Fig. 1.12. This design allowed them to decrease the resonance frequency down to 27 Hz. The active layer is a 2.5 μm -thick sol-gel PZT thin film with the MPB composition. They tested only very low accelerations of a few 0.01 g and report an output power of the order of the nW with an output RMS voltage of 40 mV.

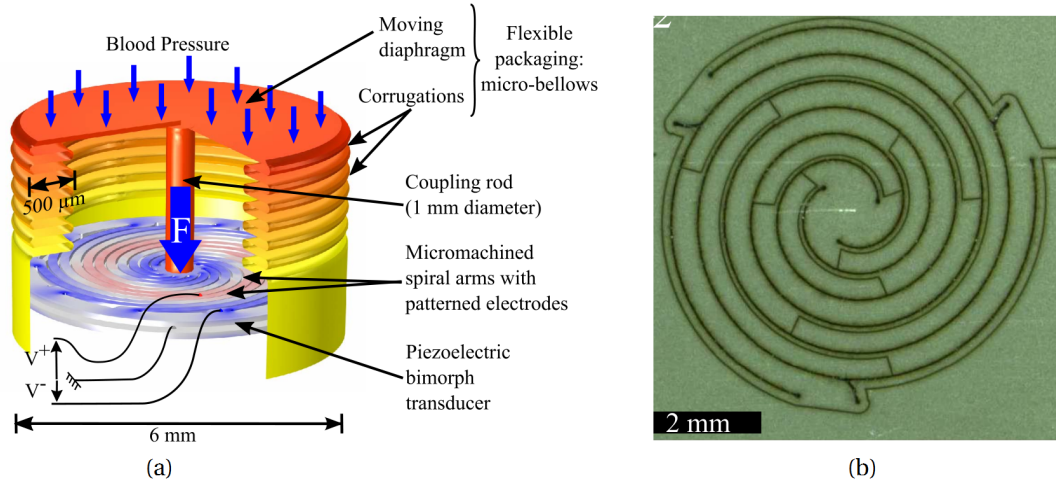


Figure 1.13 – (a): Picture of the full device designed by Deterre and coworkers. (b) : Optical microscope image of the fabricated spiral bimorph. From Deterre *et al.* [73].

A related design was recently proposed by Deterre *et al.* [73] for harvesting the blood pressure change in the heart ventricles occurring at every heart beat. This is a very low frequency situation of between 1 Hz and 3 Hz. They used a sealed package with a cylindrical, 10 μm -thick corrugated metal casing, which is compressed due to the pressure change, and transmits a strain to a spiral-like cantilever bimorph with thin PZT ceramic sheets of 130 μm thickness. The situation is shown in Fig. 1.13 (a). This is an example of a direct-force generator, where a transducer generates power by opposing the movement of a proof mass acted upon by an external force, as opposed to the inertial generators so far discussed. The spiral has multiple arms, as displayed in Fig. 1.13 (b), to effectively occupy the limited space offered by the packaging case, which must fit inside a heart ventricle. Because the spiral arm experiences both bending and torsion, the sign of the stress during deformation must be estimated by FE modeling to pattern the electrodes in such a way that regions with opposite signs of stress are not in electrical contact — this would cancel out their contribution to the harvested power. The PZT bimorph is patterned into the spiral shape with femto-second laser micromachining. The same technique is used to pattern the electrodes. The device is designed to operate away from resonance, in a quasi-static fashion. With an optimal resistive load, an output power of 22 nW was obtained at a frequency of 1.5 Hz and a force amplitude of 180 mN; that is an energy of 33 μJ per cycle. The open circuit output voltage was 1.5 V. Such a design does not seem very promising as a vibration energy harvesting device, however. If we replace the mobile case by a seismic mass, about 18 g would be required to produce the same power output at an acceleration of 1 g. This means about 2 cm^3 of stainless steel (of density around 8 g/cm^3),

which is a rather large volume if size constraints must be respected. Higher density materials should be used; using tungsten for instance (of density near 20 g/cm^3), the necessary volume is reduced to less than 1 cm^3 .

If tuning to one of the power density peak of the vibration source is not practical — for instance because of an intermittent or variable source — excursion-based systems can be used when the resonance frequency of the device is much larger than the source frequency [74]. At every cycle of the source frequency, the PEH experiences an excursion from its equilibrium position and is then left free to oscillate at its natural resonance frequency until the next cycle, as pictured in Fig. 1.14. This is the so-called frequency up-conversion technique [75]. In this free oscillation regime, electrical and mechanical damping are directly competing: The higher of the two will dissipate most of the elastic energy stored in the system during the excursion phase. Therefore, in such devices, the electrical damping must be made as large as possible. Pozzi and Zhu [75] used a bimorph cantilever made of two $125 \mu\text{m}$ -thick sheets of ceramic PZT 5H with a free length of 26 mm for tests with a plucking plectrum. For the largest deflection before release they tested, the energy dissipated in the load resistor of $25 \text{ k}\Omega$ after complete damping of the free oscillations was $40 \mu\text{J}$. Even though there exists an optimal plucking frequency at which a maximum average power can be delivered, their system was designed for the energy harvesting of human motion, where the frequency of the targeted activity is expected to be quite variable.

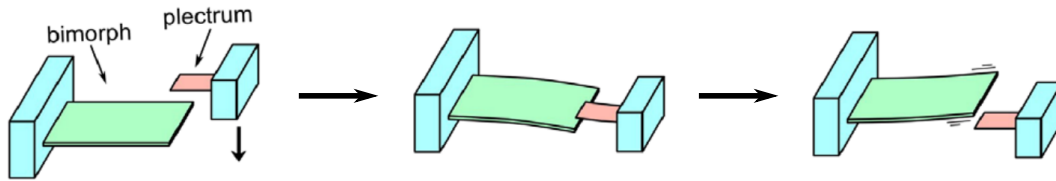


Figure 1.14 – Principle of operation for the excursion-based PEH devices. Time goes from left to right. From Ref. [75].

Similar devices with PZT and $\text{Al}_{1-x}\text{Sc}_x\text{N}$ thin films were investigated by Mazzalai and Muralt [48]. They used a cantilever beam configuration with seismic mass, like for vibration energy harvesters, with IDE for the PZT thin films and PPE for the $\text{Al}_{1-x}\text{Sc}_x\text{N}$ film. In this case, the magnitude of the initial deflection is limited by the failure stress of the layers. The cantilevers were 7 mm long and could deliver up to $0.75 \mu\text{J}$ after 40 ms of free oscillations, for a $50 \mu\text{m}$ -thick sample. The best coupling coefficient of 2.8 % was obtained for a $10 \mu\text{m}$ -thick cantilever, with a maximum peak-to-peak voltage of 18 V, which is excellent for rectification. This sample had a resonance frequency of 81 Hz and could, therefore, equally be used as a vibration PEH. The best $\text{Al}_{1-x}\text{Sc}_x\text{N}$ -based device tested had slightly lower peak-to-peak voltage at 15 V but a significantly lower coupling coefficient of 0.72 %, and a similar resonance frequency. Both of those samples harvested about the same amount of energy after 200 ms, at about $0.35 \mu\text{J}$. This shows the potential of the IDE configuration for PZT-based PEH, combining high coupling coefficients while allowing large output voltages as well.

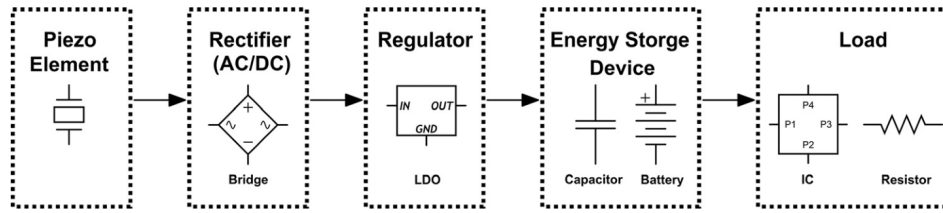


Figure 1.15 – Typical electrical circuit for the formatting of the PEH power output. From Ref. [74].

Proper output power management is very important for the performance of the full device [74]. The electrical output of a PEH cannot generally be used as such and must be rectified for DC powering. In addition, the voltage is generally too high for most microelectronic applications; therefore, a voltage regulator must be used. The latter has the additional advantage that it can also address the sometimes intermittent nature of the source. The low power output of harvesters often impose low duty cycle operations for WSN applications, such as wireless transmitters which require a large peak power. For this reason, the harvested energy must be stored, either *via* a rechargeable battery, or a capacitor with sufficiently large capacitance for supplying the whole device operation energy. The latter solution is preferred if a high power density is required. Fig. 1.15 pictures the typical pathway for power formatting of the PEH output.

As an example of a complete WSN, a bridge health monitoring node, which we designed in collaboration with Anthony Beaumont under the supervision of Dr. Danick Briand from LMTS Laboratory at EPFL, is shown in Fig. 1.16. It harvests the vibration of the bridge structure caused by the passing vehicles. This design uses only commercially available off-the-shelf components and contains:

1. A PEH array with PZT ceramic bimorphs;
2. A voltage regulator which includes a rectifier;
3. Capacitors for energy storage at the input and output of the voltage regulator;
4. A micro-controller for sensor and energy management;
5. Four types of environmental sensors : a temperature sensor, an accelerometer, a linear displacement sensor and a strain sensor;
6. A transceiver for wireless communication between the node and the base station.

This is a low duty cycle design measuring and emitting about every 30 min. This active period lasts for only a few seconds. At the capacitor situated at the output of the voltage regulator, there is a DC bus of 3.3 V, which provides electrical power to the micro-controller, the wireless transceiver, the digital sensor (accelerometer) and to the sensor power switch. The switch then distributes the power to the individual sensors selected by the micro-controller, and each sensor in return provides its data signals (analog or digital) to the micro-controller. The voltage regulator and the switch are equipped with digital inputs and outputs connected to

Table 1.5 – Power consumption of the bridge monitoring WSN during the sleep period. The power requirement of the full circuit is $64\text{ }\mu\text{W}$ after rectification.

Power sink	Fraction of harvested power
Power loss in rectifier	20 %
Quiescent power of the voltage regulator	8 %
Capacitors leakage	34 %
Sleep mode power consumption	16 %
Energy accumulation for the active period	22 %

the micro-controller for the energy management. The wireless transceiver and accelerator sensor are equipped with digital serial ports connected to the micro-controller for both energy management and data signal transfer.

During the sleep period, energy is accumulated in the supercapacitor, situated at the input of the voltage regulator, by the harvesting action of the PEH array. The voltage regulator continuously transfers sleep power to the output during this phase. The sleep period lasts until enough energy is accumulated at the input capacitor so that 3.3 V can be maintained at the output of the voltage regulator for the entire duration of the measuring and transmission phase.

Table 1.5 shows how the harvested power is consumed by the full circuit during the sleep period. Since we must accumulate energy for a long time from a low power source, much of the harvested energy is lost in the leakage of the capacitors. The rectifier is also a significant source of loss. The proposed system is not optimized, but it nonetheless shows the great impact that circuit design and component selection have on the overall performance of a PEH-powered device.

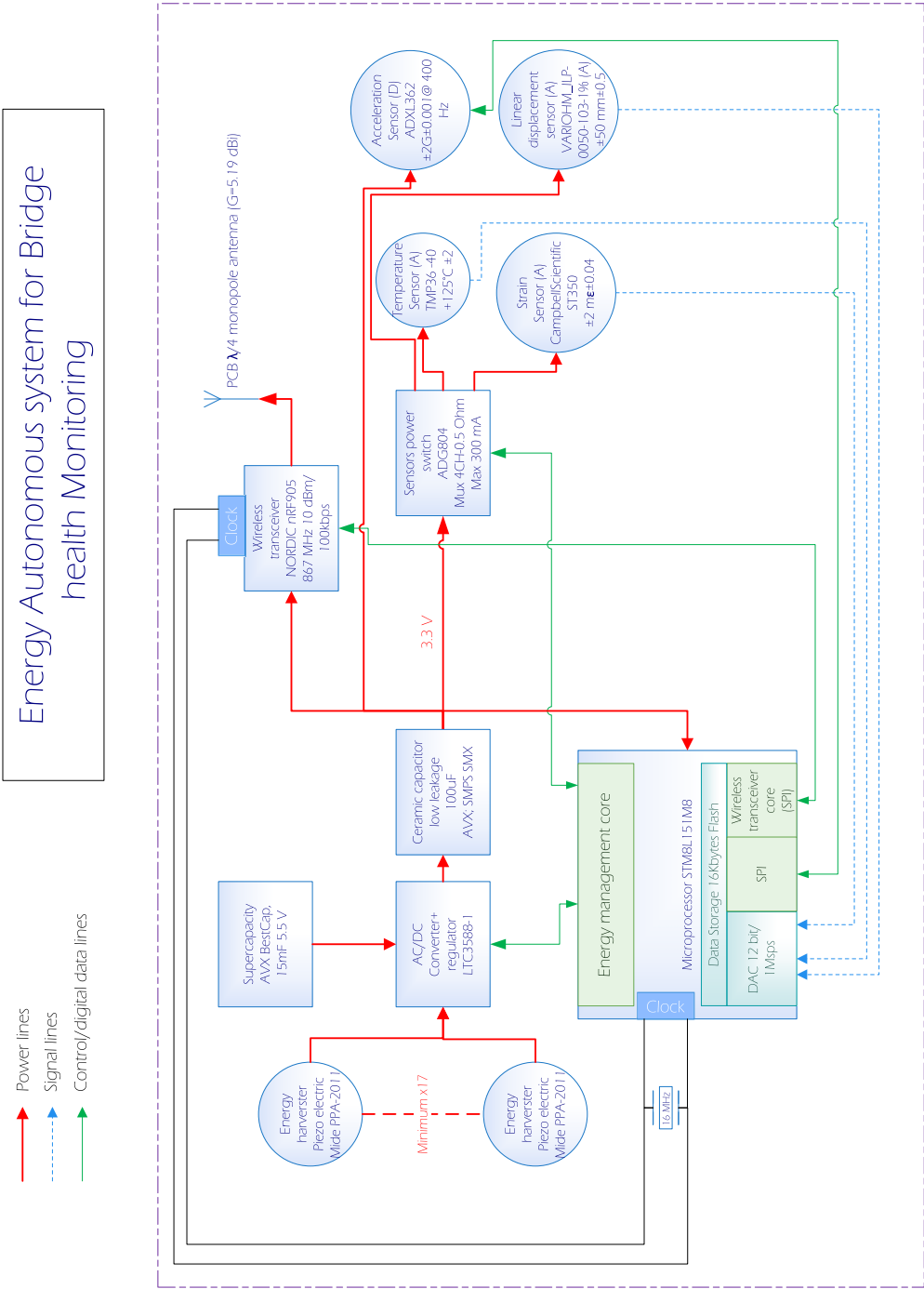


Figure 1.16 – Block-diagram of the bridge monitoring WSN. Courtesy A. Beaumont.

In conclusion, the field of PEH is very broad. A number of diverse and interesting solutions are being explored in order to take advantage of the many ambient sources of energy which could allow the ubiquitous deployment of multi-functional, low power integrated circuits. Good performances were obtained with the devices of Elfrink *et al.* [70], Defosseux *et al.* [71] and Mazzalai and Muralt [48]. The demonstrator of Elfrink *et al.* [70] shows how it is possible to power an actual WSN with a piezoelectric thin film-based PEH. The strategy to lower the mechanical damping coefficient where no margin of progress is available for the electrical damping, as is the case with AlN thin films for which the performances are already mature, appears successful. However, air leak into the vacuum package shows that this strategy still suffers from reliability issues. On the contrary, increasing the electrical damping to reach the value of the mechanical damping seems more promising. This was actually achieved by Mazzalai and Muralt [48], and, combined with the large voltage output and the low resonance frequency of their devices, shows the potential of cantilever-based PEH with PZT thin films in the IDE configuration. This system has a complexity comparable to that of the systems of Elfrink *et al.* [70] and Defosseux *et al.* [71], but without the need for packaging, reducing cost, increasing reliability and facilitating integration into a larger device; at the expense, however, of a higher thermal budget and the use of a material which is more complex to fabricate. Nonetheless, from the performance point of view, PZT thin films with IDE structures seem the most promising approach for the improvement of PEH with piezoelectric thin films.

1.6 Aims of the work

We have seen how the large voltage response of PZT thin films with the IDE configuration is beneficial for PEH operations, as it combines the best of both worlds: the large piezoelectric coefficients of PZT and the large voltage output of AlN. Even though vacuum packaging allows to bring down the mechanical damping coefficient so that AlN-based PEH may reach high performances, this technique is not yet reliable due the slow leakage of air into the package. The alternative route, *i. e.* increasing the electrical damping coefficient to attain parity with the mechanical damping coefficient, without the need for any packaging, appears more promising; in this situation, PZT is the material of choice. There is little interest, however, in pursuing research into the PPE configuration for PEH with PZT thin films. Indeed, in addition to the larger voltage output, the IDE configuration also offers a better polarization stability of the poled state and lower dielectric losses [45]. The former is of primary importance, because it ensures the reliability of the PEH device, which is a very critical point as it is the power source of the entire microsystem.

The high cost of MEMS processing means that it is very desirable to optimize the material performance with test structures before reaching the prototyping phase. Accurate characterization of the thin film response is necessary to determine the proper fabrication route, composition and doping for maximum harvesting efficiency and voltage output. Unfortunately, IDE structure characterization is not straightforward, because of the inhomogeneous electric field: When the structures are biased, neither the direction nor the intensity of the

electric field is uniform inside the film [35]. A number of corrections have been proposed in previous works by Chidambaram *et al.* [35, 45] to address this point. However, these previous approaches are incomplete: They do not explain the observed scaling of the coercive field with the IDE gap distance; they assume an effective surface to obtain the polarization value from the current integration by analogy with an equivalent PPE configuration, without providing theoretical support for this approximation; finally, a significant dependence of the dielectric constant on the gap distance is still present. There is no clear understanding for these experimental observations. No rigorous description of the physical behavior of the IDE system is available to date. This is very detrimental for the device design, since improper interpretation of the characterization results may lead to suboptimal material design and device architecture.

In addition, a systematic characterization of the IDE system is lacking. Previous studies by Chidambaram *et al.* [35, 43, 45] have focused on undoped films with the MPB composition. Scanning a wider portion of the composition range and introducing dopants could reveal more appropriate combinations to achieve higher output power for PEH.

Finally, even if the IDE design already displays good retention capabilities, it is still desirable to reduce the risk of depoling as much as possible. In this regard, the phenomena of aging and self-poling deserve some attention, since they both provide improved stability of the poled state. Unfortunately, neither of them is well understood, and, to our knowledge, they have not been studied for the IDE configuration yet. Understanding the underlying mechanisms of each could make it possible to improve the device reliability even more.

In light of this discussion, this PhD thesis work is organized in six chapters. Chapter 2 will briefly introduce the standard techniques for ferroelectric thin film characterization which will be used throughout the work. Chapter 3 addresses the physical behavior of PZT thin films with IDE; it provides a physical description of the IDE system which explains the experimental observations, and presents analytical formulas which make it possible to accurately extract the effective material properties from standard characterization measurements, for a range of geometries useful for PEH. Chapter 4 presents the results of systematic characterization of PZT thin films with IDE for various combinations of composition and dopant; it determines the best combinations for PEH and discusses the relative advantages of the other combinations. In chapter 5, we review the literature available on the topic of aging in ferroelectric compounds with a focus on PZT, and we introduce less standard measurement techniques which are precious for investigating this phenomenon; we then present the results of our own investigations, and the benefits that aging can bring for PEH. Chapter 6 studies the possibility of introducing self-poling into the IDE system, with the desire to improve the stability of the poled state to ensure the reliability of the harvesting operation. Finally, from the results of the previous chapters, chapter 7 shortly outlines design rules for the optimal performance of IDE systems, and discusses the most interesting applications for this configuration.

2 Characterization methods for ferroelectric thin films

In this section, we will review the standard characterization techniques for a ferroelectric thin film with a cantilever architecture, both in the IDE and PPE configuration. Due to the hysteretic behavior of ferroelectric materials, typical characterization involves recording the film response to a bipolar excitation. This provides so-called loops when the response is plotted *vs.* the electric field. Polarization, capacitance, losses, and cantilever tip displacement are recorded. The latter gives access, on the basis of theoretical models describing the cantilever bending, to the ferroelectric film stress and to the piezoelectric coefficient. We will first review the two characterization regimes, and we will then present the equations to extract the piezoelectric coefficient from the tip displacement measurement in converse and direct mode.

2.1 Standard characterization measurements

Two regimes are used for characterization: the large-signal measurement and the small-signal measurement. In the large-signal measurement, a triangle wave is applied to the sample and the response is recorded continuously. In the small-signal regime, a small oscillating voltage of high frequency (typically 1 kHz) is applied on top of a DC voltage (or a low frequency triangle wave). The DC voltage is varied in a step-by-step fashion, and the sample response at the frequency of the small signal is recorded at each step. The two types of driving signals are schematically shown in Fig. 2.1.

Large signal measurements are used to obtain the polarization. A virtual ground is used to record the polarization current induced in the sample by the cycling voltage. In the absence of leakage currents, the polarization is obtained by integration of the current loop:

$$\frac{1}{A} \int_0^{t_0} i(t) dt = P(V(t_0)) - P(V(0)) \quad (2.1)$$

where t_0 is the time at which the polarization is calculated, $P(t_0) = P(V(t_0))$ is the polarization and A is the area of the sample. Since $P(V(0))$ is not known, a convention must be used. In this

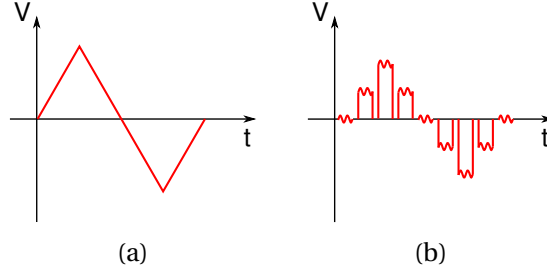


Figure 2.1 – (a): voltage signal for large-signal measurements. (b): voltage signal for small-signal measurements.

work, we set the integration constant so that $P(V_{\max}) = -P(-V_{\max})$. This gives a polarization *vs.* voltage or *vs.* field loop (PV loop). The displacement of the cantilever tip is recorded at the same time, setting the initial position as the reference position. The stress is then extracted from this measurement, yielding a stress-field loop.

In the small-signal regime, the capacitance and losses of the samples are recorded at each DC voltage step. This gives a capacitance *vs.* DC voltage or *vs.* DC field loop (CV loop) and a loss *vs.* field loop. The oscillation amplitude of the tip at the frequency of the small signal is recorded at each DC voltage step; the piezoelectric coefficient is extracted from this measurement, yielding a small-signal coefficient *vs.* field loop.

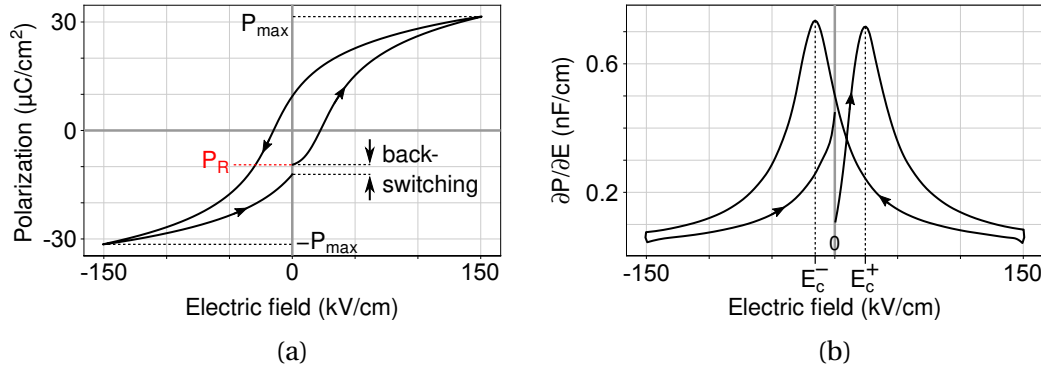


Figure 2.2 – (a): typical PV loop from a Nb-doped PZT 53/47 PPE sample. (b): $\partial P / \partial E$ curve of the PV loop in (a). Arrows indicate the loop direction.

The PV loop may be open or closed; Fig. 2.2 shows a typical open PV loop. Closed PV loops are obtained when applying a continuous AC voltage to the film and recording the current response, for instance thanks to a charge amplifier connected to an oscilloscope. Open PV loops are obtained by integration of the current response when applying a single period of the AC signal. Typically, two triangle waves are sent in a sequence and the current is recorded for the second wave only. Because of the hysteretic behavior of the polarization, the film is initially in the polarization state imposed upon by the first triangle wave, *i. e.* the negative polarization state. The polarization then increases while domains switch polarization one after the other, until reaching the saturating polarization P_{\max} ; then, the polarization starts

to decrease when the field decreases. This is because some domains spontaneously switch back. The combination of back-switching and actual switching brings the polarization to the saturating negative value $-P_{\max}$, which then decreases in absolute value while the field is brought back to zero. The initial polarization at zero field is called remanent polarization P_R ; it is different from the polarization obtained at the end of the measurement because of the back-switching. For this reason, the loop is open: there is a gap between the initial and final polarization value. Typically, the two triangle waves are sent 1 s apart, so that this gap can be used as a standard measure of the retention capability of the sample. The coercive field, *i. e.* the electric field causing polarization reversal, is obtained at the maximum of the $\partial P/\partial E$ curve. There is one coercive field for switching from the negative to the positive polarization state, E_c^+ , and one coercive field for switching from the positive to the negative polarization state, E_c^- . If $E_c^+ \neq E_c^-$, the PV loop is said to show a field offset or voltage offset. Since closed loops are obtained by cycling the sample continuously, it is not possible to directly estimate the retention capability of the sample with a closed loop. For this reason, in this work, we performed open loop only.

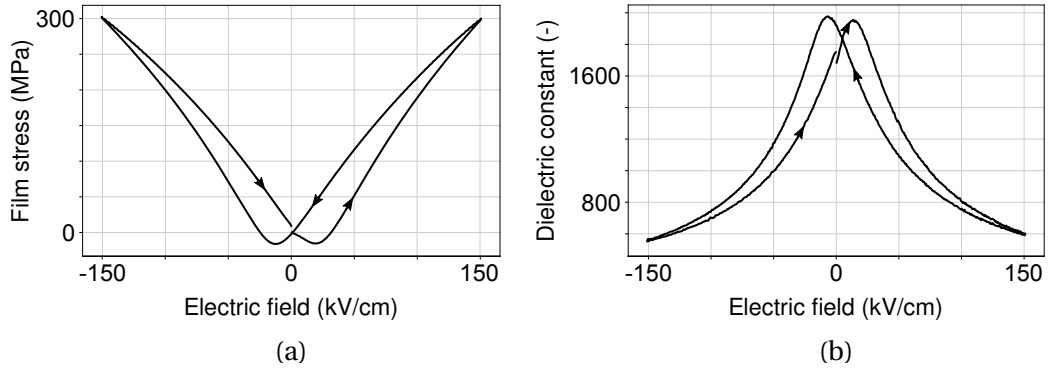


Figure 2.3 – (a): typical stress-field loop from a Nb-doped PZT 53/47 PPE sample; (b): typical CV loop of the same sample. Arrows indicate the loop direction.

Fig. 2.3 left shows a typical large-signal stress-field loop, also called “butterfly loop” due to its characteristic shape. Like for the PV loop, it may be open or closed. After poling by the cycling field (*i. e.* after reaching saturation), the sample roughly behaves as a piezoelectric sample, *i. e.* the stress is approximately proportional to the electric field; however, as soon as the coercive field for the other polarity is reached, the polarization reverses and the sign of the response as well, which means that only one type of stress may be obtained: tensile for the PPE configuration, or compressive for the IDE configuration.

Fig. 2.3 right shows a typical CV loop. The value at zero field is larger than the value at large field due to the larger number of domain walls present, which are generated by the back-switching. The dielectric constant peaks at the coercive fields, where the domain wall density reaches a maximum. Similarly, the losses peak at this field as well. With good accuracy, the lattice does not contribute to the losses, so that they are representative of the current number of domain walls. In the PPE configuration, the dielectric constant of the ferroelectric film ϵ_f is

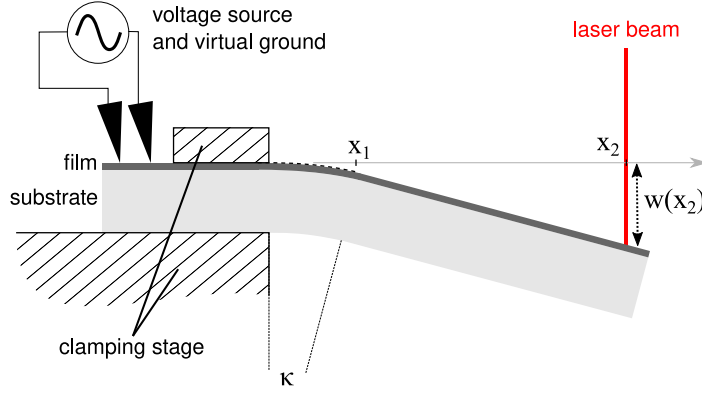


Figure 2.4 – Configuration of the clamping stage. The dimensions are not to scale. The cantilever tip excursion $w(x_2)$ is exaggerated for clarity. Samples with IDE will bend downward as pictured; samples with PPE will bend upward.

readily obtained as:

$$\epsilon_f = \frac{C}{\epsilon_0} \frac{t_f}{A} \quad (2.2)$$

where C is the measured capacitance, ϵ_0 is the permittivity of vacuum, t_f is the ferroelectric film thickness and A is the capacitor area. The calculation of ϵ_f from the value of C in the IDE case will be treated in chapter 3.

2.2 Piezoelectric coefficient in converse mode

Figure 2.4 pictures a typical configuration for the converse mode measurement of a cantilever beam with IDE. The cantilever is clamped at the start of the interdigitation zone, which is the active zone. When the electrodes are biased, compressive stress builds up between the IDE fingers, which bends the substrate downward. Note that, because of polarization reversal, only compressive stress can be obtained whenever the applied voltage exceeds the coercive voltage. In a PPE cantilever, tensile stress would be developed and the beam would bend upward. The curvature of the active zone is amplified by the slope of the cantilever in the inactive zone. The cantilever tip excursion is measured by interferometry by shining a laser beam onto a dedicated reflector at the sample end, or with a photonic sensor positioned at the same location [40].

The full derivation of how to obtain the piezoelectric coefficients from the tip displacement is given in appendix B, where the previous approaches from Mazzalai *et al.* [40] and Chidambaram *et al.* [35] are presented and discussed; in this section, only the final results are shown for brevity.

2.2.1 Cantilever bending geometry

The origin of lengths is set at the start of the unclamped zone, which coincides with the start of the active area. Constant curvature is assumed in the active area (extending from 0 to x_1), caused by the stress in the PZT film from the converse piezoelectric effect; and zero curvature in the inactive area (which extends from x_1 to the end of the cantilever). $w(x)$ is the (small) excursion of the point at coordinate x . The laser spot shines onto the point of coordinate x_2 . The situation is pictured in Figure 2.4. In the PPE configuration, a tensile stress will appear in the film upon biasing, causing the cantilever to bend upward instead of downward as pictured. Downward bending will happen in the IDE configuration, where a compressive stress is developed instead. κ is the curvature of the active zone: $\kappa = 1/R$ where R is the radius of curvature. It is linked to the tip excursion by:

$$\frac{1}{R} = \kappa = \frac{2w(x_2)}{x_1(2x_2 - x_1)} \quad (2.3)$$

Therefore, measuring the tip excursion and knowing the sample geometry gives access to the curvature of the active region. The latter, in turn, can be related to the ferroelectric film stress. The PPE and IDE cases must be treated separately and are presented below.

2.2.2 Parallel plate electrodes

This case is treated by Mazzalai and coworkers [40]. If we write as c_f the electrode width to cantilever width ratio $c_f = w_{el}/w_{ca}$, or electrode coverage factor, the film equi-biaxial stress σ_f in the active zone is obtained by :

$$\sigma_f = \frac{1}{6R} \frac{E_s t_s^2}{(1 - \nu_s) c_f t_f} ((1 - \nu_s)(1 - c_f) + c_f) \quad (2.4)$$

where E_s and ν_s are Young's modulus and Poisson's ratio of the substrate, respectively, t_f is the ferroelectric film thickness and t_s is the substrate thickness.

Thanks to equation 2.3 we can link the tip displacement and the film stress as follows:

$$\sigma_f = \frac{1}{3} \frac{E_s t_s^2}{(1 - \nu_s) c_f t_f} ((1 - \nu_s)(1 - c_f) + c_f) \frac{w(x_2)}{x_1(2x_2 - x_1)} \quad (2.5)$$

Single crystal Si wafers are not isotropic materials. Hence, in equation 2.5, orientational Young's modulus and Poisson's ratio must be used. Our cantilever long axis is along the Si [110] direction (parallel to the main flat) and the orthogonal axis is along the $[\bar{1}10]$ direction, hence we should use $E_s = 169$ GPa and $\nu_s = 0.064$ [40, 76].

Dividing by the electric field strength in the out-of-plane direction $E_3 = V/t_f$, where V is the bias across the parallel plate electrodes, we obtain the effective transverse piezoelectric

coefficient $e_{31, f}$ [40]:

$$e_{31, f} = -\frac{1}{3} \frac{E_s t_s^2}{V(1 - \nu_s) c_f} ((1 - \nu_s)(1 - c_f) + c_f) \frac{w(x_2)}{x_1(2x_2 - x_1)} \quad (2.6)$$

This latter formula is used to obtain $e_{31, f}$ from small-signal measurements; V is then the small-signal amplitude and $w(x_2)$ the tip displacement amplitude. For large signal measurements, one should rather calculate σ_f from equation 2.5 and then use $e_{31, f} = d\sigma_f/dE_3$ as discussed by Mazzalai and coworkers [40], to capture both the field and history-dependence of $e_{31, f}$ in ferroelectric thin films. $e_{31, f}$ is negative and is obtained from the material properties as follows [39]:

$$e_{31, f} = e_{31} - e_{33} \frac{c_{13}^E}{c_{33}^E} = \frac{d_{31}}{s_{11}^E + s_{12}^E} \quad (2.7)$$

2.2.3 Interdigitated electrodes

This case is treated by Chidambaram *et al.* [35]. Here, we must first determine the equation for the stress between the IDE fingers, and then propose a model for the bending of the interdigitation zone. The stress between the IDE fingers σ_3 is uniaxial in first approximation [35]. We show in appendix B that this approximation is accurate. We thus have:

$$\sigma_3 = \frac{1}{6R} \frac{E_s t_s^2}{t_f} \quad (2.8)$$

Now we must link the curvature within the gap to the cantilever tip displacement. The regions below the electrode fingers are inactive and as such, show no stress [35]. a is the gap distance and b the finger width, and $\eta = b/(a+b)$ the metalization ratio. We assume that the Si substrate shows a constant, averaged curvature within the interdigitation zone, given by $(1 - \eta)/R$ [35]. Assuming uniaxial stress in the substrate outside of the interdigitation zone, we obtain, with the same notations as before [35]:

$$\sigma_3 = \frac{w(x_2)}{3x_1(2x_2 - x_1)(1 - \eta)} \frac{E_s t_s^2}{c_f t_f} \quad (2.9)$$

Lastly, dividing by the electric field within the gap region $E_3 = V/a$, we find $e_{33, if}$ as a function of the tip displacement :

$$e_{33, if} = -\frac{w(x_2)}{3x_1(2x_2 - x_1)(1 - \eta)} \frac{a E_s t_s^2}{V c_f t_f} \quad (2.10)$$

where $e_{33, if} > 0$ is an effective piezoelectric coefficient describing the cantilever bending in the IDE case, like $e_{31, f}$ for the PPE case. It includes a mixture of longitudinal and transverse

2.3. Piezoelectric coefficient in direct mode

Table 2.1 – Effective piezoelectric coefficients for standard PZT ceramic grades.

PZT grade	e_{31} (C/m ²)	e_{33} (C/m ²)	$e_{31,f}$ (C/m ²)	$e_{33,if}$ (C/m ²)
PZT-4	−5.2	15.1	−15	17.9
PZT-5H	−6.55	23.3	−23.3	27.7

piezoelectric coefficients and is given by [35]:

$$e_{33,if} = e_{33} - \frac{c_{13}^E}{c_{11}^E} e_{31} \quad (2.11)$$

As will be seen in chapter 3, it is more accurate to write $E_3 = V/(a + \Delta a)$ where $a + \Delta a$ is an effective gap for electrical properties. In this case we have:

$$e_{33,if} = -\frac{w(x_2)}{3x_1(2x_2 - x_1)(1 - \eta)} \frac{(a + \Delta a)E_s t_s^2}{V c_f t_f} \quad (2.12)$$

Table 2.1 shows the values of the effective piezoelectric coefficients for two common commercial PZT ceramic grades. We have $e_{33,if} > e_{33}$ and $|e_{31,f}| > |e_{31}|$. This means that the film clamping improves the piezoelectric response in the IDE case, which is also true in the PPE case as was shown by Muralt [36], although the improvement is less pronounced for IDE. We expect a larger piezoelectric response in the IDE configuration, since $e_{33,if} > |e_{31,f}|$.

2.3 Piezoelectric coefficient in direct mode

2.3.1 Setup description and cantilever bending geometry

For measuring the transverse piezoelectric coefficient through the direct piezoelectric effect, a setup first proposed by Dubois and Muralt [39] is used. In this setup, a cantilever beam is clamped at one end and a piezoelectric actuator applies an alternating displacement on the beam other end. The setup is pictured in Figure 2.5. Since the piezoelectric film is much thinner than the substrate, it is assumed to experience the same strain as that induced at the surface of the bent substrate. The electrodes are connected either to a charge amplifier to collect the piezoelectric charges generated by the oscillating strain — the piezoelectric film is then in closed-circuit condition, since the charge amplifier input behaves as a virtual ground; or to a voltage amplifier to measure the voltage difference induced by the oscillating strain — the open-circuit condition is then realized in the film. An oscilloscope is used to record the peak-to-peak variation of the charge (resp. the voltage). This allows to obtain the effective e and h coefficients, respectively.

We set $x = 0$ at the clamping position and $x = l > 0$ at the point where the actuator is in contact with the substrate at zero excursion. The actuator peak-to-peak displacement is written as

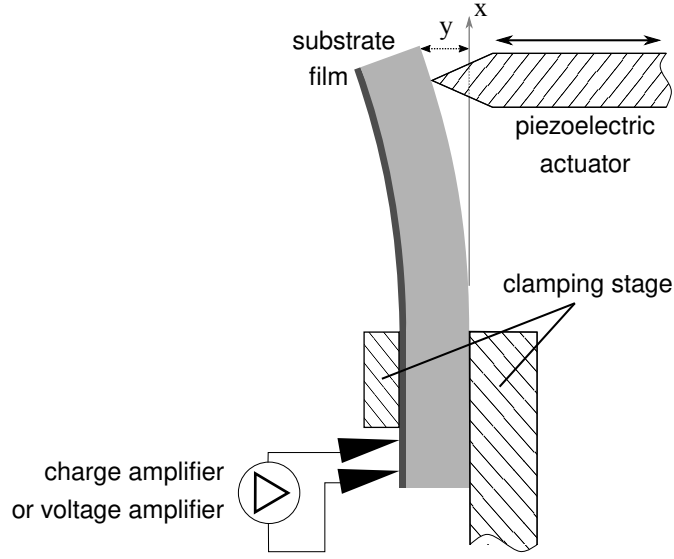


Figure 2.5 – Configuration of the clamping stage for direct transverse piezoelectric effect measurements. The dimensions are not to scale. The cantilever excursion y is exaggerated for clarity. The piezoelectric actuator moves back and forth as indicated by arrows, causing a small excursion oscillation around an average excursion value.

Δy_{act} , imposed on the cantilever beam at $x = l$. The active zone starts at $x = 0$. The full derivation of the coefficients is given in appendix B; here, only the final results are presented.

2.3.2 Parallel plate electrodes

This case is treated by Dubois and Muralet [39]. Let d be the length of the top electrode along the x direction. As before we name w_{el} the (rectangular) top electrode width. $e_{31, f}$ is given as function of the sample geometry, peak-to-peak actuator displacement and recorded peak-to-peak charge signal ΔQ as follows:

$$e_{31, f} = - \frac{2l^3 \Delta Q}{3\Delta y_{\text{act}} t_s (1 - \nu_s) w_{\text{el}} d \left(l - \frac{d}{2} \right)} \quad (2.13)$$

And $h_{31, f}$ is obtained from the measured peak-to-peak voltage ΔV by:

$$h_{31, f} = \frac{2l^3 \Delta V}{3\Delta y_{\text{act}} t_s (1 - \nu_s) t_f \left(l - \frac{d}{2} \right)} \quad (2.14)$$

2.3.3 Interdigitated electrodes

This case is treated by Chidambaram *et al.* [43]. We must define, unlike for the PPE case, a new effective piezoelectric coefficient e_{IDE} :

$$e_{\text{IDE}} = e_{31} \left(\frac{\nu_s c_{12}^E - c_{13}^E}{c_{11}^E} - \nu_s \right) + e_{33} \quad (2.15)$$

Note that e_{IDE} is not a material parameter but depends on the Poisson's ratio of the substrate. We show in appendix B that it can be approximated by e_{33} , if with good accuracy.

With the same notations as before, e_{IDE} is given by [43]:

$$e_{\text{IDE}} = - \frac{2l^3 \Delta Q}{3\Delta y_{\text{act}} t_s w_{\text{el}} t_f N_g \left(l - \frac{d}{2} \right)} \quad (2.16)$$

where N_g is the number of IDE gaps and $d = N_g(a + b)$ is the length of the interdigitation zone.

The open circuit coefficient is also a new coefficient, defined as:

$$h_{\text{IDE}} = h_{31} \left(\frac{\nu_s c_{12}^D - c_{13}^D}{c_{11}^D} - \nu_s \right) + h_{33} \quad (2.17)$$

With the same notations as before, we have:

$$h_{\text{IDE}} = \frac{2l^3 \Delta V}{3\Delta y_{\text{act}} t_s a \left(l - \frac{d}{2} \right)} \quad (2.18)$$

As will be seen in chapter 3, it is more accurate to use an effective gap value of $a + \Delta a$. The formula then becomes :

$$h_{\text{IDE}} = \frac{2l^3 \Delta V}{3\Delta y_{\text{act}} t_s (a + \Delta a) \left(l - \frac{d}{2} \right)} \quad (2.19)$$

3 Physical behavior of ferroelectric thin films with IDE and characterization methodology

3.1 Introduction

The interdigitated electrode (IDE) configuration allows for a large voltage response [32], which is important when using ferroelectric thin films with high dielectric constants such as $\text{PbZr}_x\text{Ti}_{1-x}\text{O}_3$ (PZT). It offers a number of further advantages : better polarization stability at small fields due to less polarization back-switching [45], a lower hysteresis in the unipolar mode [35], and lower dielectric losses [45]. There is therefore a large interest to improve characterization of such devices. The main difficulty to characterize ferroelectric properties in ferroelectric films with IDE lies in the inhomogeneous and curved electric field, resulting in much more complex patterns than in the PPE case. When the structures are biased, neither the direction nor the intensity of the electric field is uniform inside the film [35]. For this reason, a number of corrections are required if one wants to extract the material properties from standard measurements [35, 45, 77]. There are particularly questions about the interpretation of a ferroelectric loop. How is the polarization derived from the charges captured by the ID electrodes? And how should one correct the electric field to obtain the real coercive field?

In this chapter, we first review the previous approaches to this problem. There is the simple model assuming that the electrodes traverse the ferroelectric thin film, approximating the IDE with parallel plate capacitors that are connected in parallel. This model underestimates the dielectric constant [45]. Much better agreement with expected dielectric constants is obtained by applying a conformal mapping transformation approach following Gevorgian and coworkers [78] or Igreja and Dias [79]. However, this approach does not give an answer on how one has to transform electric fields, and to the question of how polarization charges are transmitted to the interdigitated electrodes. We will show that for typical geometries — with a film thickness smaller than the electrode gap — one can simplify the expressions of Gevorgian's and Igreja's methods to extract the dielectric constant, and that the electric field between the fingers can be considered as homogeneous, depending on the gap distance and the ferroelectric film thickness only. We also calculate the effective area that should be

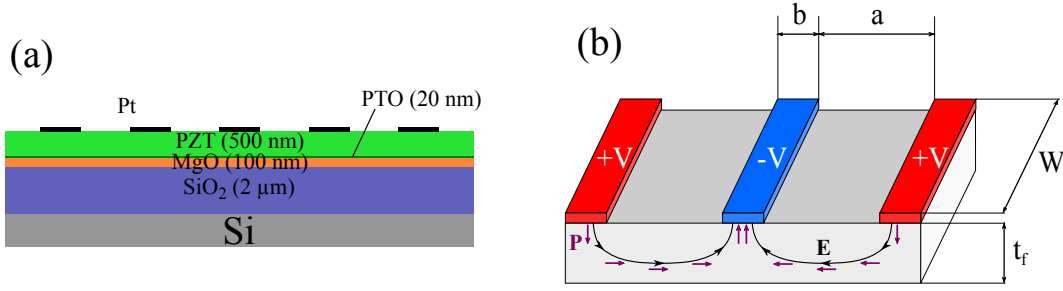


Figure 3.1 – (a) : Stack design of the samples used in this study. (b) : Geometry of the interdigitation zone and definition of the geometrical quantities. The electric field lines, as well as the local polarization vector, which will attempt to align with the local direction of the electric field, are shown to illustrate the expected behavior of the ferroelectric film.

used to obtain the polarization from switching current measurements; and we show that the Si substrate — though separated through 2 μm of SiO₂ and only weakly doped — adds a parasitic capacitance that should be removed. Our corrections result in polarization versus field (PV) and permittivity versus field (CV) loops that overlap for a large value range of IDE gaps, showing that they must be close to intrinsic material values.

Figure 3.1 (b) defines the geometrical quantities used to describe the IDE structure. a is the finger distance or gap, b is the finger width, W is the finger length (only considering the distance over which fingers of opposite polarity are facing each other), N is the number of fingers for each electrode (thus $2N$ is the total number of fingers), and t_f is the ferroelectric film thickness. V is the potential difference applied across the IDE capacitor. Our PZT films are grown on a 100-nm-thick MgO layer on Si substrate with 2 μm wet oxide to provide electrical insulation, as pictured in Figure 3.1 (a). The detailed fabrication route can be found in a previous publication [35].

This chapter is adapted from the following publications :

- A) R Nigon, TM Raeder, and P Muralt. Characterization methodology for lead zirconate titanate thin films with interdigitated electrode structures. *Journal of Applied Physics*, 121(20):204101, 2017
- B) CH Nguyen, R Nigon, TM Ræder, U Hanke, E Halvorsen, and P Muralt. Extraction of properties of ferroelectric thin films in interdigitated electrode systems. In preparation

3.2 The simple formula

The simplest approximation for a mathematical description is to assume that the electrode fingers extend all the way down to the bottom of the ferroelectric film [45, 82], as depicted in Figure 3.2. In this case the IDE structure is equivalent to $2N - 1$ PPE capacitors in parallel, of

3.3. The Gevorgian formula for the capacitance of IDE capacitors

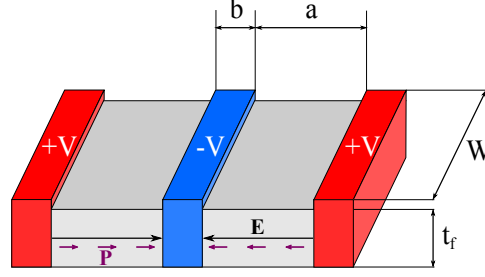


Figure 3.2 – Illustration of the assumptions made with the simple model for the behavior of IDE structures. The IDE capacitor behaves like $2N - 1$ PPE capacitors in parallel.

thickness a and of surface $W t_f$. The total capacitance then becomes:

$$C = \epsilon_f \epsilon_0 \frac{(2N - 1) W t_f}{a} \quad (3.1)$$

In this approximation, the electric field inside the ferroelectric film is uniform, lying in the film plane, orthogonal to the fingers, and given by $E = V/a$. Therefore, cycling the capacitor with a triangular voltage signal and measuring the output current gives the polarization P after integration in absence of leakage currents :

$$\int_0^{t_0} i(t) dt = (P(V(t_0)) - P(V(0))) (2N - 1) W t_f \quad (3.2)$$

Note that in this approximation, the finger width b has no influence on the behavior.

3.3 The Gevorgian formula for the capacitance of IDE capacitors

A more accurate approach was proposed by Chidambaram *et al.* [45]. The simple model was maintained to quantify the PV loop. For the extraction of the dielectric constant from the CV loop, however, a dedicated formula was applied based on the works of Gevorgian *et al.* [78] and Vendik *et al.* [83], who treated the problem to calculate the capacitance of an interdigitated structure on a multilayered dielectric stack in case of homogeneous dielectric properties in each layer. Their calculations involve a conformal mapping method with a Schwartz–Christoffel transformation, turning the IDE structure into an equivalent PPE structure of thickness and surface related to the IDE geometry through transformation functions. They use the partial capacitance method for multilayered stacks (see section 3.4). Gevorgian and coworkers also consider the stray field at the end of the IDE fingers, as well as the stray fields for the first and last finger of the interdigitation zone. Chidambaram *et al.* [45] reversed the formula given by Gevorgian *et al.* to extract the dielectric constant of the ferroelectric layer from a capacitance measurement. This method is expected to yield a more accurate result than that given by equation 3.1. Their approach neglects the presence of underlayers

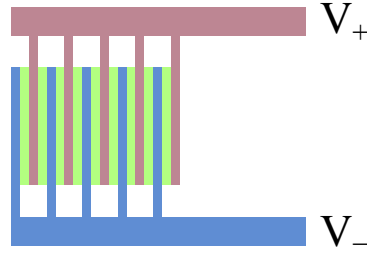


Figure 3.3 – Drawing of IDE structures. The area overlaid in green is the one considered for the calculation of the capacitance.

below the PZT film and considers only the capacitance due to the volume of the film present below and between fingers (in green in Figure 3.3). They omitted the contribution from stray fields at the tip of the fingers and at each end of the interdigitation zone, which is justified when the finger length is much larger than any other dimension (close to 1 mm, whereas the dimensions of the gap and the finger width are within the range 1–20 μm in our devices) and when the number of fingers is large ($2N = 100$ or 200 in our case). Applying Gevorgian's model, the PZT film is assumed to be a dielectric material with isotropic and homogeneous dielectric properties throughout the film. The presence of domain walls and any dielectric anisotropy, common in ferroelectrics and which gives a different dielectric constant along and orthogonal to the polar axis, is therefore ignored. This is a reasonable approximation at large fields, where it is expected that the polarization vector is aligned with the field lines everywhere inside the PZT film, especially if the film has the morphotropic phase boundary (MPB) composition. At switching and subswitching fields, or with compositions away from the MPB, this approximation will be less accurate.

Under all these assumptions, and applying Gevorgian's derivation, the capacitance C of the ferroelectric film with IDE structures is obtained by the following equations [78]:

$$C = \frac{1}{2} \epsilon_f \epsilon_0 \frac{K(k)}{K(k')} (2N - 1) W \quad (3.3a)$$

$$K(k) = \int_0^1 \frac{dt}{\sqrt{(1-t^2)(1-k^2 t^2)}} \quad (3.3b)$$

$$k = \frac{\sinh\left(\frac{\pi b}{4t_f}\right)}{\sinh\left(\frac{\pi(a+b)}{4t_f}\right)} \times \sqrt{\frac{\cosh^2\left(\frac{\pi(a+b)}{4t_f}\right) + \sinh^2\left(\frac{\pi(a+b)}{4t_f}\right)}{\cosh^2\left(\frac{\pi b}{4t_f}\right) + \sinh^2\left(\frac{\pi(a+b)}{4t_f}\right)}} \quad (3.3c)$$

$$k' = \sqrt{1 - k^2} \quad (3.3d)$$

K is the complete elliptical integral of the first kind and accepts arguments $k \in [0, 1]$, and $K(k) \xrightarrow[k \rightarrow 1]{} +\infty$. Elliptical integrals appear in the Schwartz-Christoffel transformation used to obtain the equivalent length in a parallel plate configuration of the curved electric field lines of the IDE system. These integrals were given this name in the seventeenth century as mathematicians of the time used them to evaluate arc lengths of ellipses [84]. The argument k then corresponds to the eccentricity of the ellipse, which is 0 for a circle and approaches 1 for very elongated ellipses. Appendix C shortly presents the use of conformal mapping techniques to solve Laplace's equation in boundary-value problems.

Chidambaram *et al.* have used the parameter α , given by [45]:

$$\alpha = \frac{C_{\text{simple}}}{C_{\text{Gevorgian}}} \quad (3.4a)$$

$$= \frac{2t_f K(k')}{a K(k)} \quad (3.4b)$$

α quantifies the divergence of the two procedures as a function of the IDE geometry. The cited work [45] details the dependences of α : As expected, it is close to 1 for large a/t_f ratios, and increases for decreasing a and increasing t_f , as the geometry becomes more and more distant from the simple model geometry. α also has a moderate dependence on b , increasing slightly with decreasing b . To compare the accuracy of different models for various geometries, it is more convenient to use the value $1/\alpha$, which is proportional to the capacitance of the model being considered.

3.4 The partial capacitance method for multilayers

As discussed in the work of Gevorgian and coworkers [78], the previous formula can be used to calculate the capacitance of a multi-layered IDE capacitor using the so-called partial capacitance method. This method is simply an application of the superposition principle. For a two-layer IDE capacitor, the capacitance of the stack C_{tot} is given by:

$$C_{\text{tot}} = C_G(a, b, t_1, \varepsilon_1) + C_G(a, b, t_1 + t_2, \varepsilon_2) - C_G(a, b, t_1, \varepsilon_2) \quad (3.5)$$

where t_1 , t_2 and ε_1 , ε_2 are respectively the thickness and the dielectric constant of the top layer and the bottom layer, respectively, and C_G is the function of the IDE geometry that gives the capacitance using the Gevorgian formula (we omitted the dependence on N and W for brevity). We can also write:

$$C_{\text{tot}} = C_G(a, b, t_1, \varepsilon_1 - \varepsilon_2) + C_G(a, b, t_1 + t_2, \varepsilon_2) \quad (3.6)$$

The subtraction comes from the fact that in $C_G(a, b, t_1 + t_2, \varepsilon_2)$, we have an extra contribution of $C_G(a, b, t_1, \varepsilon_2)$ which must be removed to obtain the contribution of the underlayer only.

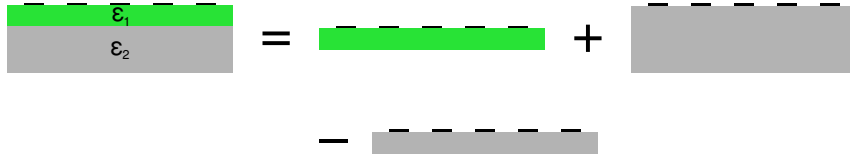


Figure 3.4 – Schematic illustration of the partial capacitance method for multilayers.

The process is schematically illustrated in Figure 3.4.

In a similar way, the capacitance of an arbitrary stack can be obtained, as well as the capacitance due to air on top of the IDE structures by using the formula with a dielectric constant of 1; and also for buried IDE structures.

3.5 Simplification of the Gevorgian procedure for specific geometries

In the regime where $a, b \gg t_f$, k is very close to zero. This feature can greatly simplify the evaluation of k and $K(k)$. The complete derivation is given in appendix D. We find that the elliptic integral ratio is given by, in the first order for $a, b \gg t_f$:

$$\frac{K(k)}{K(k')} = \frac{2t_f}{a + \Delta a} \quad (3.7)$$

where we wrote :

$$\Delta a = \frac{4\ln(2\sqrt{2})}{\pi} t_f \quad (3.8a)$$

$$\approx 1.324 t_f \quad (3.8b)$$

The capacitance of the ferroelectric film with IDE structures is then obtained thanks to equation 3.3a:

$$C = \epsilon_f \epsilon_0 \frac{(2N-1) W t_f}{a + \Delta a} \quad (3.9)$$

This is similar to equation 3.1 giving the capacitance for the simple model, but replacing the finger distance a by an effective finger distance $a + \Delta a$, where $\Delta a > 0$ is proportional to t_f as

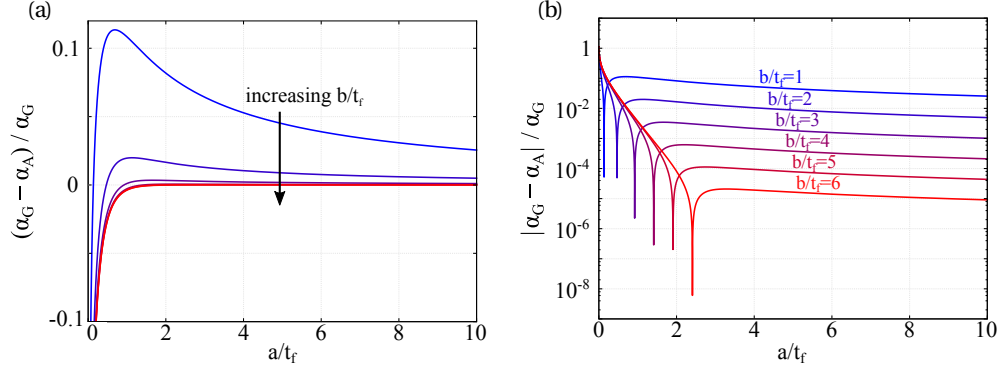


Figure 3.5 – $(\alpha_G - \alpha_A)/\alpha_G$ as a function of a/t_f for several values of b/t_f , in linear scale in (a) and in logarithmic scale in (b). The color code is given in (b).

seen from equation 3.8a. It follows that in this case, the factor α is given by:

$$\alpha = \frac{a + \Delta a}{a} \quad (3.10)$$

It is remarkable that, in the regime of interest, there is no dependence on the finger width b , and that Δa is simply proportional to the film thickness t_f .

Figure 3.5 shows the value of $(\alpha_G - \alpha_A)/\alpha_G$ — where α_G is computed exactly from equation 3.4b, and α_A is given by equation 3.10 — as a function of a/t_f for several values of b/t_f . The approximation is very accurate even for relatively small values of a/t_f and b/t_f , because of the negative exponential dependence of A and B on a/t_f and b/t_f , respectively. The approximation is better than 1% for $a > t_f$ and $b > 3t_f$, and also for $b > 2t_f$ if $a > 4t_f$. Outside of this zone, the approximation will be poorer, in particular for $b \leq 2t_f$.

3.6 The Igreja formula for the capacitance of IDE capacitors

Igreja and Dias [79] also propose a method involving a Schwartz-Christoffel transformation to calculate the capacitance of an IDE capacitor with underlayers. The total capacitance for the IDE structure is given by, if $2N > 3$:

$$C = \frac{1}{2} C_I (2N - 3) W + 2 \frac{C_I C_E}{C_I + C_E} \quad (3.11)$$

C_I is the capacitance per unit finger length for one finger located in the interior of the interdigitation zone, and C_E is the capacitance per unit finger length for one finger situated at the end of the interdigitation zone. C_I and C_E are expressed with elliptic and hyperbolic functions as follows:

Chapter 3. Physical behavior of ferroelectric thin films with IDE and characterization methodology

$$C_I = \varepsilon_f \varepsilon_0 \frac{K(k_I)}{K(k'_I)} \quad (3.12a)$$

$$C_E = \varepsilon_f \varepsilon_0 \frac{K(k_E)}{K(k'_E)} \quad (3.13a)$$

$$k_I = t_2 \sqrt{\frac{t_4^2 - 1}{t_4^2 - t_2^2}} \quad (3.12b)$$

$$k_E = \frac{1}{t_3} \sqrt{\frac{t_5^2 - t_3^2}{t_5^2 - 1}} \quad (3.13b)$$

$$k'_I = \sqrt{1 - k_I^2} \quad (3.12c)$$

$$k'_E = \sqrt{1 - k_E^2} \quad (3.13c)$$

$$t_2 = \operatorname{sn}(K(k) \eta, k) \quad (3.12d)$$

$$t_3 = \cosh\left(\frac{\pi(1-\eta)}{8r}\right) \quad (3.13d)$$

$$t_4 = \frac{1}{k} \quad (3.12e)$$

$$t_5 = \cosh\left(\frac{\pi(1+\eta)}{8r}\right) \quad (3.13e)$$

$$k = \frac{\vartheta_2(0, q)^2}{\vartheta_3(0, q)^2} \quad (3.12f)$$

$$q = \exp(-4\pi r) \quad (3.12g)$$

Here sn is the sine amplitude Jacobi elliptic function, and ϑ_2 and ϑ_3 are Jacobi theta functions. q is called the nome — which must satisfy $|q| < 1$ — and k is the modulus. $\eta = 2b/\lambda$ is the metallization ratio and $r = t_f/\lambda$ is the thickness-to-period ratio, where $\lambda = 2(a+b)$ is the IDE period. See appendix C for definitions of elliptic and theta functions and a brief explanation of why these functions enter the calculations.

Like for the Gevorgian formula, the formula for multilayered stacks or buried IDE structures is obtained with the partial capacitance method.

3.7 Simplification of the Igreja procedure for specific geometries

Like for the Gevorgian formula, it is possible to simplify C_I in the regime where $a, b \gg t_f$. The complete derivation is given in appendix E. The capacitance C of the ferroelectric film with IDE structures is then given by, assuming that $C_E = C_I$ for simplicity:

$$C = \varepsilon_f \varepsilon_0 \frac{(2N-1) W t_f}{a + \Delta a} \quad (3.14)$$

where we wrote :

$$\Delta a = \frac{4 \ln(2)}{\pi} t_f \quad (3.15a)$$

$$\approx 0.883 t_f \quad (3.15b)$$

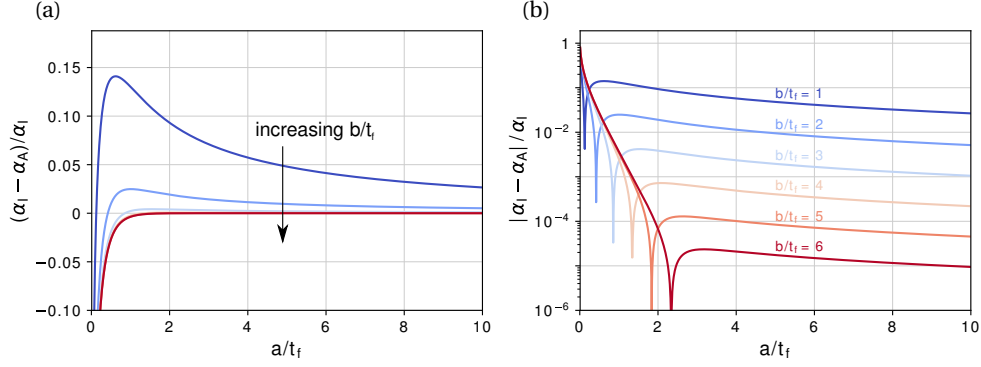


Figure 3.6 – $(\alpha_I - \alpha_A)/\alpha_I$ as a function of a/t_f for several values of b/t_f , in linear scale in (a) and in logarithmic scale in (b). The color code is given in (b).

Equation 3.15a is remarkably close to Equation 3.8a obtained after simplification of the Gevorgian formula; they differ only by a factor $\sqrt{2}$ in the logarithm.

Figure 3.6 shows the value of $(\alpha_I - \alpha_A)/\alpha_I$ — where α_I is computed exactly from equation 3.12a, and α_A is given by equation 3.10 using equation 3.15a for Δa — as a function of a/t_f for several values of b/t_f . The approximation shows nearly identical behavior to that of the Gevorgian model shown in Figure 3.5. The approximation is better than 1% for $a > t_f$ and $b > 3t_f$, and also for $b > 2t_f$ if $a > 4t_f$. Outside of this zone, the approximation will be poorer, in particular for $b \leq 2t_f$.

3.8 Comparison with finite element simulation

To evaluate the accuracy of each approach, we developed a finite element (FE) model with the software Comsol for comparison. Full details on the FE model are given in section 3.9. We have modeled a two-dimensional portion of the interdigitation zone containing two fingers, with a geometry close to that of our samples : A 500 nm-thick layer of dielectric material of dielectric constant 1000 on top of a 2 μm -thick layer of dielectric material with dielectric constant of 4.2 — the built-in value for SiO_2 in Comsol — with periodic boundary conditions on each side and zero charge at the top and bottom interfaces. We have obtained the capacitance using a so-called “terminal” interface provided by the software. a varied between 2.5 μm and 20 μm and b was held constant at 5 μm . Figure 3.7 shows the capacitance per unit length obtained with the FE model, and calculated with the exact Gevorgian and Igreja analytical formulas (using C_I for the Igreja formula). The same procedure with $b = 2.5 \mu\text{m}$ yielded almost identical values, showing again the fact that for sufficiently large a/t_f and b/t_f ratios, the capacitance is independent of b .

We observe that the Gevorgian analytical formula systematically underestimates the FEM capacitance, while the Igreja formula provides very good agreement. The discrepancy between

Chapter 3. Physical behavior of ferroelectric thin films with IDE and characterization methodology

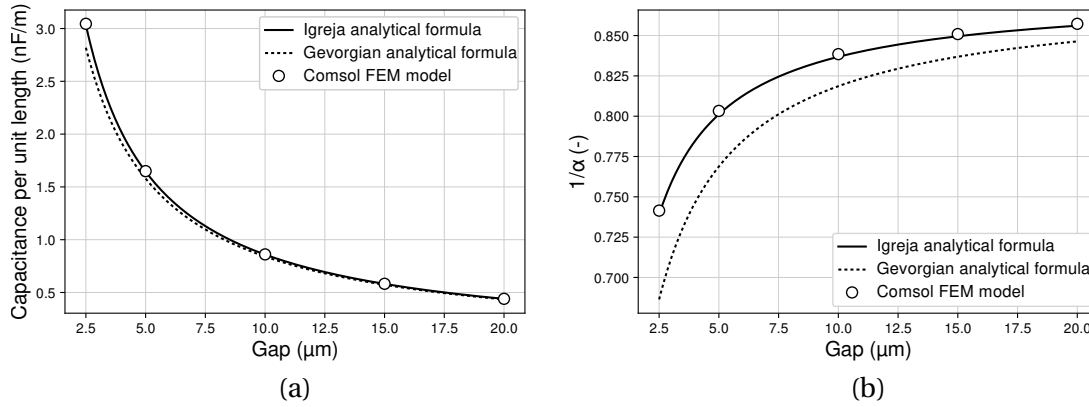


Figure 3.7 – Comparison between the Gevorgian and Igreja analytical formulas, and the FEM model. (a) : capacitance per unit length values; (b) : values normalized to C_{simple} for each gap.

the Gevorgian formula and the FE model increases for decreasing gap values. We observe a similar, but much less pronounced, dependence for the Igreja formula, which even for the smallest gap investigated, remains very close to the FE value. The reason for the discrepancy between the two analytical models is not clear. Gevorgian and coworkers do not use the same sequence of conformal mapping transformations as Igreja and Dias, who also observe that the Gevorgian formula underestimates the capacitance, and who did not find a more satisfying explanation [79].

We thus conclude that the Igreja formula provides the better accuracy for the purpose of extracting the dielectric constant from capacitance-voltage measurement. This will be experimentally verified in section 3.13.

3.9 Electric field reduction

Equations 3.9 and 3.14 suggest that, in the geometry regime where the approximations derived in section 3.5 and section 3.7 are accurate, the ferroelectric film with IDE structures is equivalent to a PPE capacitor with surface $(2N - 1) W t_f$ and thickness $a + \Delta a$. The length $a + \Delta a$ would represent the average length of the field lines joining fingers of opposite polarity, where Δa is proportional to the film thickness t_f . This situation is illustrated in Figure 3.8. In the regime where the previously derived simplification is applicable, the system behaves as if the field lines could be split into two parts : a straight line of length a running within the gap through the bulk of the film, and two curved lines of length $\Delta a/2$ joining the straight line to each electrode. The fact that there is no dependence on the finger width b means that the electrode charges are concentrated at the edges of the fingers. When a is changed, the geometry of the *curved* part of the field lines is *not* changed. However when t_f is increased while a is kept constant, the length of the curved part increases on average since some of the field lines are then located further away from the fingers. Δa is independent from the electrode spacing a because the size and shape of the curved regions are independent of

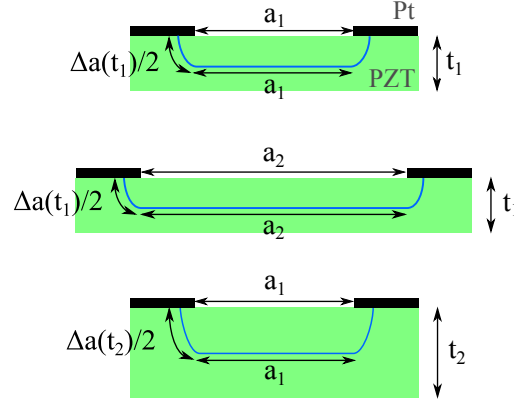


Figure 3.8 – Schematic drawing a ferroelectric film with IDE structures for different combinations of finger distance and film thickness. A field line running through the middle height of the film is indicated in blue in each picture. The two top pictures have the same thickness but different gaps; the top and bottom pictures have the same gap but different thicknesses. The total length of the blue field line is the sum of its straight portion of length a_i and its two curved portions, each of length $\Delta a(t_i)/2$.

a. This qualitatively explains the observed dependencies of the expressions derived in the previous sections.

Such effective capacitor gap of $a + \Delta a$ implies that the effective electric field inside the gap amounts to $V/(a + \Delta a)$, which can be notably smaller than V/a and this even for large a/t_f ratio. An electric field smaller than V/a was already observed in FE simulations previously published [35]. The reduced electric field picture is supported by the fact that, in ferroelectric films with IDE structures, the coercive field as extracted from the PV loops scales with the IDE gap, with a proportionality factor equal to α [45]. Indeed, the ferroelectric properties of the film should not depend on the finger distance, and thus, the coercive field should be the same for all samples.

We have performed FE modelling with the software Comsol to calculate the electric field, and to compare it with the effective field defined above. We modelled the interdigitation zone of the IDE system for a three-layer-stack of dielectric materials : The top one of thickness $t_f = 0.5 \mu\text{m}$ or $1 \mu\text{m}$ with dielectric constant of 1000 or 300 representing PZT, the middle one of thickness $0.1 \mu\text{m}$ and dielectric constant 10 representing MgO [85], and the bottom one of thickness $2 \mu\text{m}$ with dielectric constant 4.2 (the built-in value in Comsol) representing SiO₂. The situation is pictured in Figure 3.9. A positive voltage V was applied to the electrodes on the sides, such as $V/a = 100 \text{ kV/cm}$ for all a , while the middle electrode was grounded. Periodic boundary conditions were applied to the side of the layers. The top surface of the PZT layer was kept uncharged, and the bottom of the SiO₂ layer was set as a floating potential. This is because the RC constant of the circuit formed by the two series capacitors of PZT-MgO-SiO₂ connected through the resistance formed by the Si substrate, which exhibits a conductivity of the order of $10 \Omega \cdot \text{cm}$ on average, is several orders of magnitude smaller than the period of

Chapter 3. Physical behavior of ferroelectric thin films with IDE and characterization methodology

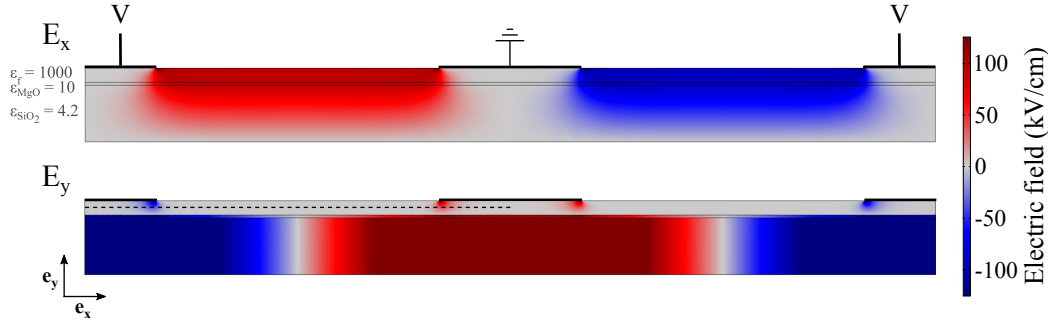


Figure 3.9 – Simulation result for $V = 100\text{V}$, $b = 5\mu\text{m}$ and $a = 10\mu\text{m}$. The x coordinate of the electric field is shown on the top while the y coordinate is shown on the bottom. The dashed line in the E_y plot shows the middle line along which we have plotted E_x in Figure 3.10. Note that a periodic boundary condition was applied, so that the right and left edges of the model are identical: Each half electrode belongs to the same electrode finger.

the triangular signal applied to measure the PV loop. The consequences of this feature are discussed in more details in section 3.10.

We plotted the x coordinate of the electric field E_x along lines located at the bottom, middle and top of the PZT layer, situated at $0.01t_f$, $0.5t_f$ and $0.99t_f$ above the bottom of the layer, respectively. The lines start at the middle of the finger of positive polarity and stop at the middle of the grounded finger. The middle line is depicted in Figure 3.9 as a dashed line. The results for $b = 5\mu\text{m}$ and two different a values are shown in Figure 3.10. We also show the $V/(a + \Delta a)$ value as a dashed line when Δa is computed with equation 3.8a (Gevorgian model), and as a dash-dotted line when it is computed with equation 3.15a (Igreja model). For large gaps, E_x decreases towards midgap, where it reaches a local minimum. For small gaps, E_x is nearly constant throughout the gap distance. For all gaps E_y is almost zero within the gap as can be seen in Figure 3.9. We observe a field concentration zone near the finger edge, while both E_x and E_y are nearly zero below the fingers, confirming earlier work [35]. The decrease of E_x in the middle of the gap for larger values of a is the result of the conduction through silicon. Indeed, the capacitance through the gap must be larger than the capacitance between the electrodes and the floating silicon “electrode” for getting a large E_x value. For our geometry, this means $a \ll t_{\text{SiO}_2}\epsilon_f/\epsilon_{\text{SiO}_2} = 150\mu\text{m}$. When we remove the floating silicon in our model, E_x is indeed calculated to be constant across the gap for all values of a , as shown in Figure 3.10. In all cases, $V/(a + \Delta a)$, when computed with equation 3.15a (Igreja), is found to be a good approximation on average for the electric field between the fingers, while the computation with equation 3.8a (Gevorgian) underestimates the electric field for small gaps, in line with the underestimation of the capacitance, also more pronounced for small gaps, reported in section 3.8. For the value range of $1\mu\text{m} \leq a \leq 20\mu\text{m}$ realized in our samples, E_x can be considered to be homogeneous and close to $V/(a + \Delta a)$ in first approximation.

Figure 3.11 shows the value of E_x at mid-film (mid-height of the PZT film) and midgap for various simulation conditions. In all cases E_x was the same at the top, middle and bottom of

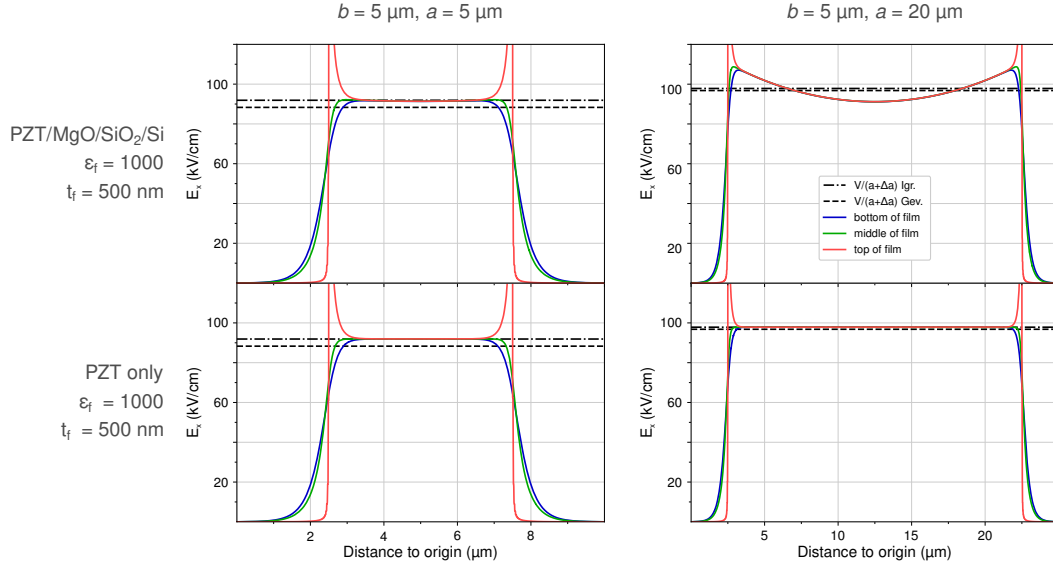


Figure 3.10 – Line scans data from FE model (FEM) simulations for $b = 5 \mu\text{m}$, with $a = 5 \mu\text{m}$ on the left charts and $a = 20 \mu\text{m}$ on the right charts. The top charts show the case when PZT has an MgO/SiO₂/Si underlayer while the bottom charts show the case when the PZT layer is taken alone in vacuum. In all cases V was chosen such as $V/a = 100 \text{ kV/cm}$.

the film. Using $b = 2.5 \mu\text{m}$ instead of $b = 5 \mu\text{m}$ has no influence on the value of E_x at midgap for $t_f = 0.5 \mu\text{m}$ (Fig. 3.11 (a)), while it occasionned a drop of less than 0.5 kV/cm for $t_f = 1 \mu\text{m}$, which is less than 1% (Fig. 3.11 (b)). This is in agreement with the previous finding that b has little influence on the properties if the ratio b/t_f is sufficiently large. Working with a smaller b/t_f ratio will increase the inhomogeneity of the electric field : E_x will decrease when closer to the bottom of the PZT layer, and E_y below the fingers will become non-zero in a larger zone.

Figure 3.11 (a) shows that for a fixed V/a ratio the electric field at mid-film and midgap shows a maximum for medium gap values and decreases when the gap increases and decreases. We already discussed the former case. For the latter case, this is due to the fact that $V/(a + \Delta a)$ becomes an increasingly smaller fraction of V/a as a decreases, since Δa is not dependent on a . Taking $\epsilon_f = 300$ greatly reduced the field at mid-film and midgap for large a values, while it has a small influence for low gaps (Fig. 3.11 (a)); the maximum field is shifted towards a lower gap value. A similar, but less pronounced dependence is observed in Figure 3.11 (b) for $t_f = 1 \mu\text{m}$.

$V/(a + \Delta a)$, computed with the Igreja formula, is observed to be an overestimate for large gaps and an increasingly good estimate for lower gaps, as seen in Figure 3.11 (c) and (d). Since the Igreja formula does not take the floating bottom interface into account, it is not able to capture the decrease of the electric field at mid-film and mid-gap for larger gap values. The same can be said of the $V/(a + \Delta a)$ value computed with the Gevorgian model; it is found to be an overestimate of the actual electric field for large gaps and an underestimate for low gaps,

Chapter 3. Physical behavior of ferroelectric thin films with IDE and characterization methodology

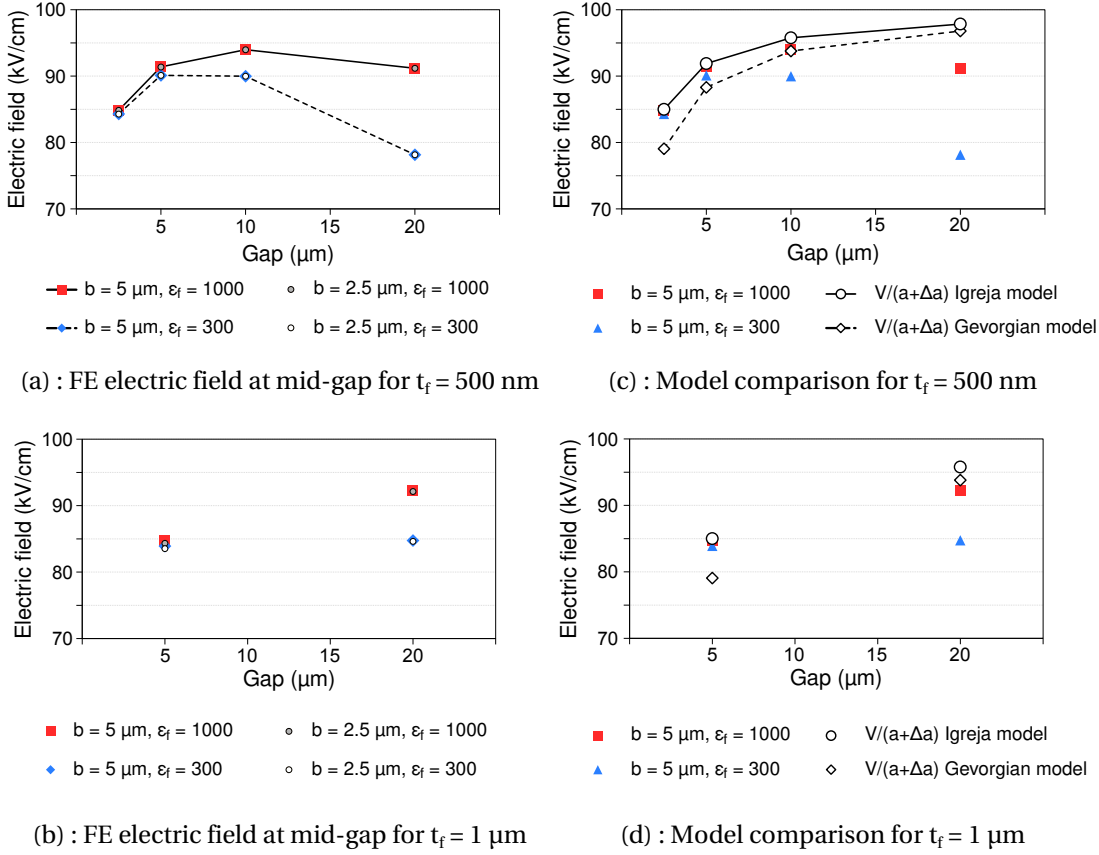


Figure 3.11 – E_x at mid-film and midgap from FEM simulations for gap values. (a) : comparison between $b = 5\mu\text{m}$ and $2.5\mu\text{m}$ for $t_f = 500$ nm. (b) : comparison between $b = 5\mu\text{m}$ and $2.5\mu\text{m}$ for $t_f = 1\mu\text{m}$. (c) : comparison with analytical models for $t_f = 500$ nm. (d) : comparison with analytical models for $t_f = 1\mu\text{m}$. The data for $b = 5\mu\text{m}$ is the same in all charts for a given t_f .

while being a good estimate for intermediate gaps. For both formulas the estimate is better if $\varepsilon_f = 1000$, because this situation is closer to the case when no floating bottom interface is present. Conversely, both estimates perform the worst at large gaps with $\varepsilon_f = 300$.

3.10 Parasitic capacitance

3.10.1 Origin and estimates

Because the Si substrate behaves as a floating electrode, it not only influences the electric field, but leads in addition to a parasitic capacitance in combination with the large electrode structures (contact pads and bus lines) outside of the interdigitation zone, as depicted in Figure 3.12. Similarly, as suggested from the E_y plot from the FE simulation shown in Figure 3.9, each finger will also act as a capacitor parallel to the part of the PZT film situated within the IDE gap. The equivalent circuit for the interdigitation zone is pictured in Figure 3.13 (a).

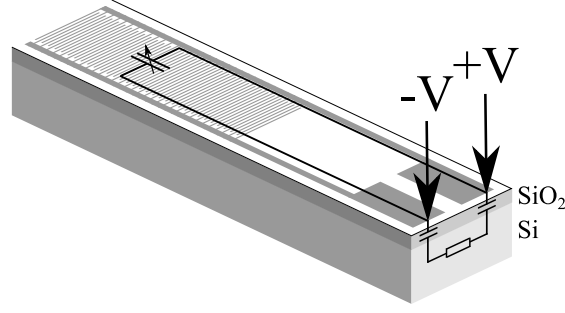
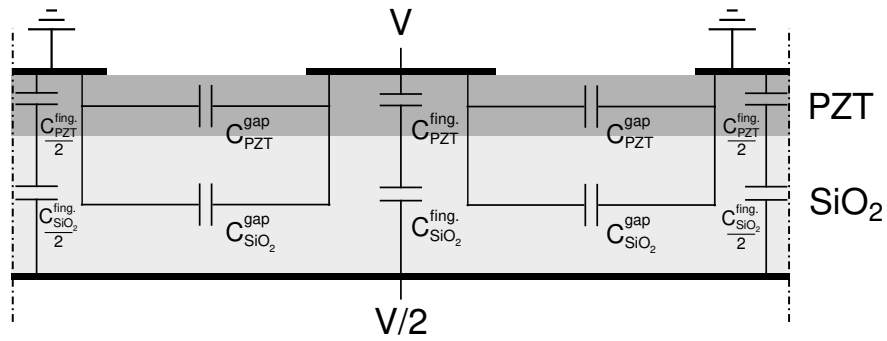


Figure 3.12 – Schematic drawing showing the equivalent electric circuit on top of the IDE structures. The electrical contact is represented by two arrows.

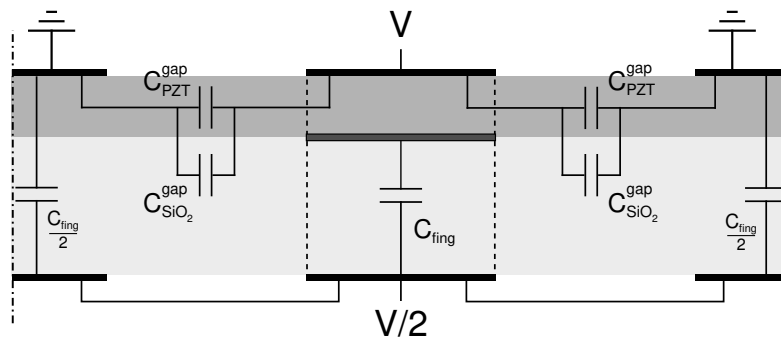
The parasitic capacitance outside of the interdigitation zone $C_{\text{par}}^{\text{str.}}$ can be measured by cleaving away the interdigitation zone, and contacting the contact pads to measure the impedance of the remaining structures. Knowing the area covered by the structures gives an experimental capacitance per area value, which can then be used to evaluate the parasitic capacitance for the complete device, and for all geometries. The inclusion of the parasitic capacitance due to the fingers in the interdigitation zone $C_{\text{par}}^{\text{fing.}}$ is discussed below. Both capacitances can also be estimated from the dielectric constant of the underlying layers, with the Si substrate acting as a resistance connecting two identical PZT/MgO/SiO₂ stacks in series — however, we found that this did not yield an accurate evaluation. Our PZT films with IDE structures typically have a relatively small capacitance of a few tens to a few hundreds of pF (depending on the geometry); the total parasitic capacitance was calculated and measured to be of the order of 10 pF (here also depending on the geometry), therefore contributing to a noticeable extent to the PV and CV loop measurements in some cases.

The frequency dependence of the parasitic capacitance needs also to be discussed to determine the limiting frequency below which the Si substrate must be considered as a conductor at some floating potential. Our Si substrates have a resistivity around $\rho_{\text{Si}} = 10 \Omega \cdot \text{cm}$. Assuming a conductive channel below the PZT film of length a and depth d both of the order of $10 \mu\text{m}$, being as wide as the finger length W , the resistance of the Si substrate between the fingers can be estimated as $R = 100 \Omega$. The capacitance between finger and silicon is evaluated as 0.1 pF. The resulting RC time constant within the interdigitation zone is thus of the order of 10 ps, corresponding to a frequency of roughly 10 GHz. This is very far from the Hz to kHz frequencies usually used for PV and CV loop measurements. We cleaved away the interdigitation zone to find out the time constant of the parasitic circuit made by the rest of the structure (bus lines and contact pads). We found a capacitance resonance at 30 MHz, again much beyond the frequency range used for electrical characterization of our samples.

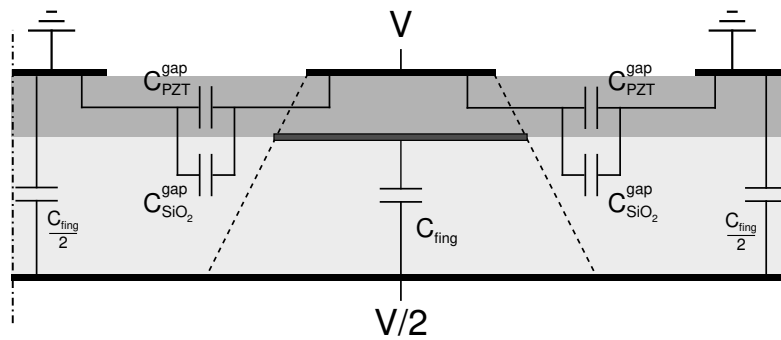
Chapter 3. Physical behavior of ferroelectric thin films with IDE and characterization methodology



(a) : equivalent circuit for the general situation



(b) : equivalent circuit for the empirical model



(c) : equivalent circuit for the conformal mapping model

Figure 3.13 – Equivalent circuit to the layers in the interdigitation zone. We omitted the MgO layer for simplicity. (a) : equivalent circuit of the general situation. (b) : equivalent circuit within the empirical parallel plate model approximation. (c) : equivalent circuit with the conformal mapping approach.

3.10.2 Evaluation

As discussed, $C_{\text{par}}^{\text{str.}}$ is readily evaluated as a function of the bus bar length by cleaving the structures at various distances from the contact pads, removing the interdigitation zone in the process, and measuring the capacitance with an impedance-meter. We conducted this evaluation for several wafers and always found a linear dependence of $C_{\text{par}}^{\text{str.}}$ on the bus bar length, as well as variations of $C_{\text{par}}^{\text{str.}} / A_{\text{str.}}$ of less than 1 % across wafers, where $A_{\text{str.}}$ is the area of the remaining structures.

The effect of the parasitic capacitance of the fingers $C_{\text{par}}^{\text{fing.}}$ due to the silicon substrate is included in the FEM calculations. In order to compare these results with the analytical models, we need to include $C_{\text{par}}^{\text{fing.}}$ in the latter. Two approaches have been developed for this purpose : an empirical approach and a conformal mapping approach, which are discussed below.

Empirical approach

In the empirical approach, we assume that each finger forms a parallel plate capacitor of surface bW and thickness t_{SiO_2} . The situation is pictured in Figure 3.13 (b). The capacitance per unit electrode area is evaluated from the capacitance of the cleaved structures $C_{\text{par}}^{\text{str.}}$, whose area $A_{\text{str.}}$ is measured with an optical microscope. The capacitance $C_{\text{par}}^{\text{fing.}}$ is then given by:

$$C_{\text{par}}^{\text{fing.}} = 2NbW \frac{C_{\text{par}}^{\text{str.}}}{A_{\text{str.}}} \quad (3.16)$$

Here $A_{\text{str.}}$ is the area of both sides of the IDE.

Conformal mapping approach

This second approach employs conformal mapping to obtain an analytical formula for the finger-to-substrate capacitance. This approach was proposed by C. H. Nguyen in a collaboration work [81].

Cattaneo [86] uses conformal mapping to provide analytical formulas to obtain the strip-to-ground capacitance for a single dielectric layer with IDE electrodes and a bottom electrode, where the IDE are biased and the bottom electrode is grounded. It cannot be used directly for our geometry because we have a multilayered stack. However, since the layers are all connected in series and the capacitance of the SiO_2 layer is much less than that of either the PZT or the MgO layers, we can neglect both the latter ones in first approximation. Since the IDE fingers are not in direct contact with the SiO_2 layer, we must use an effective IDE gap and finger width to evaluate the capacitance with the Cattaneo formula. C. H. Nguyen proposes to use the effective finger width $b_{\text{eff}} = b + at_f / (t_f + t_{\text{SiO}_2})$, obtained geometrically as the intersection between the top of the SiO_2 layer and the line connecting the finger edge to the Si substrate at mid-gap, neglecting the MgO layer, as pictured in Figure 3.13 (c). The

Chapter 3. Physical behavior of ferroelectric thin films with IDE and characterization methodology

effective gap is then given by $a_{\text{eff}} = a + b - b_{\text{eff}}$.

The finger-to-ground capacitance per unit length C_{fing} is then evaluated thanks to the following relations given by Cattaneo [86]:

$$C_{\text{fing}} = 2\epsilon_f \epsilon_0 \frac{K(k_2)}{K(k'_2)} \quad (3.17a)$$

$$k_2 = k_1 \text{sn}(K(k_1) \eta_{\text{eff}}, k_1) \quad (3.17b)$$

$$k'_2 = \sqrt{1 - k_1^2} \quad (3.17c)$$

$$k_1 = \frac{\vartheta_2(0, q)^2}{\vartheta_3(0, q)^2} \quad (3.17d)$$

$$q = \exp(-4\pi r_{\text{SiO}_2}) \quad (3.17e)$$

where $\eta_{\text{eff}} = b_{\text{eff}}/(a + b)$ is the effective metallization ratio, and $r_{\text{SiO}_2} = t_{\text{SiO}_2}/\lambda$ is the SiO₂ layer thickness-to-period ratio, where $\lambda = 2(a + b)$. Note that by construction, using the effective values b_{eff} and a_{eff} does not change the value of the half period $a + b$, nor that of the period $2(a + b)$ of the IDE geometry.

For our configuration, since two fingers are always connected in series through the conductive Si substrate, the parasitic finger capacitance per unit length and per pair of two half fingers is $C_{\text{fing}}/4$, therefore for $2N$ fingers of active length W will have the total capacitance $C_{\text{par}}^{\text{fing}}$ given by:

$$C_{\text{par}}^{\text{fing}} = 2NW \frac{C_{\text{fing}}}{4} \quad (3.18)$$

Comparison of the various approaches with FE modelling

Figure 3.14 compares various analytical models with FEM results. The capacitance in the FEM model C_{FEM} has been obtained by integration of the energy density $\mathbf{D} \cdot \mathbf{E}/2$ over the volume Ω occupied by the various dielectric materials, and equating with the total energy stored $U = C_{\text{FEM}} V^2/2$, where V is the voltage difference across the electrodes:

$$C_{\text{FEM}} = \frac{1}{V^2} \int_{\Omega} \mathbf{D} \cdot \mathbf{E} d\Omega \quad (3.19)$$

This is to minimize the error due to the singularities at the edge of the electrode fingers. The FEM model assumed a dielectric constant of 1000 and a thickness of 580 nm for PZT, and a thickness of 2 μm and a dielectric constant of 4.2 for SiO₂. b was kept constant at 6 μm while the gap a was varied. These dimensions were chosen since they are close to that of the samples used for the experimental verification of section 3.13.

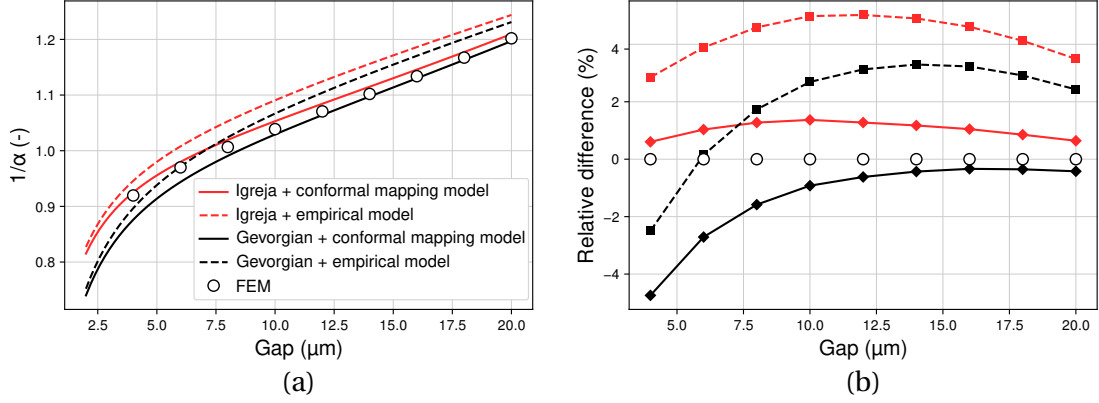


Figure 3.14 – Calculated capacitance per unit finger length for a PZT layer thickness of 580 nm, of finger width $b = 6\mu\text{m}$, of dielectric constant 1000, on a $2\mu\text{m}$ -thick underlayer of SiO_2 with dielectric constant 4.2 with floating potential at the bottom, for various gaps and various models. (a) : the capacitance normalized to the simple capacitance of the same geometry. (b) : the relative difference to the FEM result. The line style and color code is the same as in (a).

Figure 3.14 (a) and (b) show that the empirical PPE model for the finger parasitic capacitance always performs worse than the conformal mapping model, in conjunction with either the Gevorgian or the Igreja formula to obtain the capacitance of the gap region. Although for large gaps, the Gevorgian formula in conjunction with the conformal mapping model is closer to the FEM result, the Igreja formula in conjunction with the conformal mapping model is nearly independent of the gap and closer than 2 % to the FEM results for the entire range of gaps investigated (Fig. 3.14 (b)). The Gevorgian model with the conformal mapping model is always an underestimate and this underestimation is more pronounced for lower gap values. This is likely a consequence of the fact that the Gevorgian model underestimates the gap capacitance for all gaps, and even more so for smaller gaps, as we have seen before. On the contrary, we found earlier that the Igreja formula was a good estimate for the gap capacitance. This suggests that the proposed conformal mapping model is a slight, nearly gap-independent overestimate of the actual parasitic capacitance of the fingers. This gap-independence is a very desirable feature, since any significant gap-dependence of the PZT dielectric constant extracted with this model can then be readily attributed to the material behavior. Figure 3.15 shows the ratio of the Igreja formula with the conformal mapping model to the capacitance estimated by FE modelling for a wide range of IDE geometries, for a $2\mu\text{m}$ -thick underlayer of SiO_2 and constant $b = 6\mu\text{m}$. The maximum error is less than 4 %, showing the very good accuracy of this model.

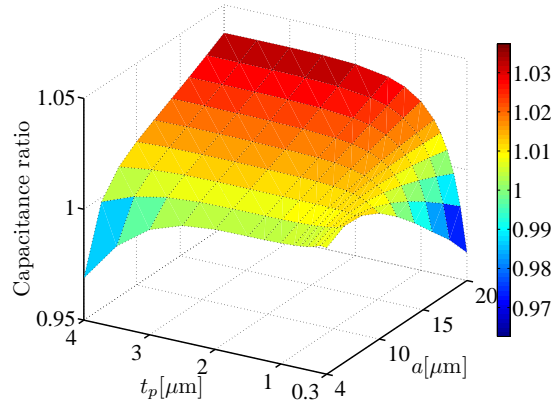


Figure 3.15 – Ratio of the Igreja formula with the conformal mapping model to the capacitance estimated by FE modelling, for a varying PZT thickness t_p and IDE gap a . The thickness of the SiO_2 layer is constant at $2\text{ }\mu\text{m}$, and the finger width b is fixed at $b = 6\text{ }\mu\text{m}$. Courtesy C. H. Nguyen.

3.10.3 Influence on PV and CV loops

The parasitic capacitance $C_{\text{par}} = C_{\text{par}}^{\text{str.}} + C_{\text{par}}^{\text{fing.}}$ will contribute to the charges Q_{measured} collected by the measurement apparatus when recording PV loops, as given by the following formula:

$$Q_{\text{measured}} = Q_{\text{ferroelectric film}} + VC_{\text{par}} \quad (3.20)$$

where V is the voltage applied to the IDE structures and $Q_{\text{ferroelectric film}}$ the charges due to the ferroelectric film polarization change upon application of V . For this reason, the measured polarization P_{measured} must be corrected in the following way to obtain the true polarization P_{true} of the ferroelectric film :

$$P_{\text{true}} = P_{\text{measured}} - \frac{VC_{\text{par}}}{A} \quad (3.21)$$

where $A = (2N - 1)Wt_f$ is the area of the IDE capacitor according to the simple model used to extract the polarization from the integrated current, as described in Equation 3.2.

Similarly, C_{par} should be subtracted to the measured capacitance to obtain the true capacitance and, hence, the true dielectric constant of the ferroelectric film:

$$C_{\text{true}} = C_{\text{measured}} - C_{\text{par}} \quad (3.22)$$

The simple model, the Gevorgian formula or the Igreja formula can then be used to yield the dielectric constant of the film from the value of C_{true} .

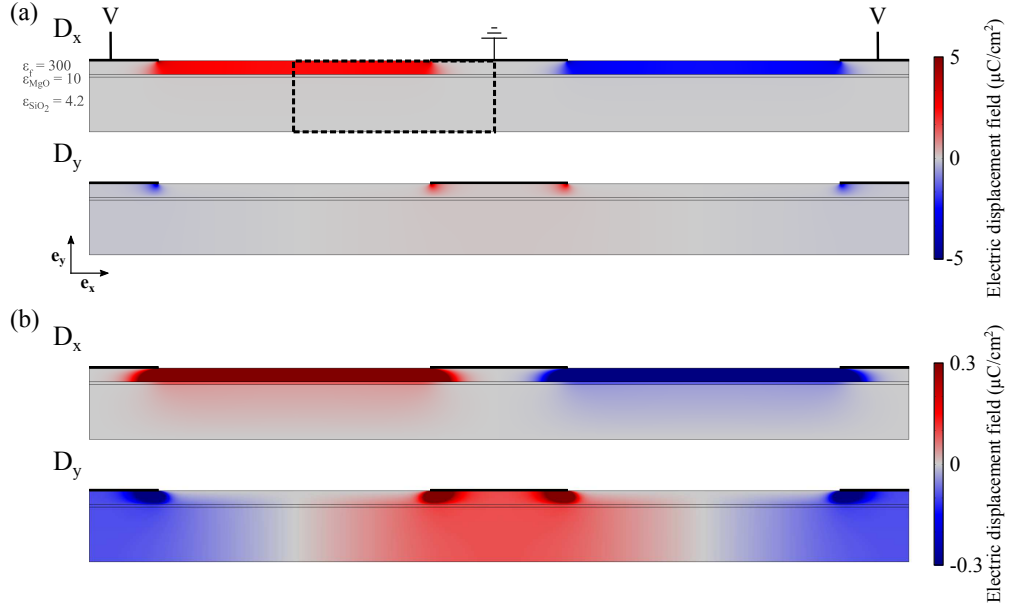


Figure 3.16 – Simulation result for $b = 5 \mu\text{m}$ and $a = 10 \mu\text{m}$. V is set to 100V and ε_f to 300. The x coordinate of the electric displacement field is shown on the top while the y coordinate is shown on the bottom in both (a) and (b). Both (a) and (b) show the same simulation result, but with different color scales.

3.11 Effective surface

In section 3.2 we estimated the polarization using an effective surface given by $A = (2N - 1) W t_f$. In this section, we will show that this is the value that should indeed be used. This is firstly suggested by the FEM simulation in Figure 3.16 showing the \mathbf{D} field for a similar situation as the electric field displayed in Figure 3.9 (the bold font denotes a vector variable). We observe that the \mathbf{D} field is mainly contained within the PZT layer and between the electrode fingers, and is about two orders of magnitude lower in the MgO and SiO₂ layers.

Secondly, it is supported by the relevant Maxwell equation integrated over an appropriate volume and applying the Gauss theorem:

$$\iiint \text{div} \mathbf{D} dV = \iiint \rho_{\text{free}} dV \quad (3.23)$$

$$\oint \mathbf{D} \cdot d\mathbf{S} = Q_{\text{free}} \quad (3.24)$$

where Q_{free} is the net free charge enclosed in the volume, and $d\mathbf{S}$ is the infinitesimal surface vector locally orthogonal to the boundary of the volume and pointing outward.

In our situation, the problem is 2-dimensional as \mathbf{D} is always in the x - y plane orthogonal to the direction z of the fingers (in the approximation of infinitely long fingers). The volume

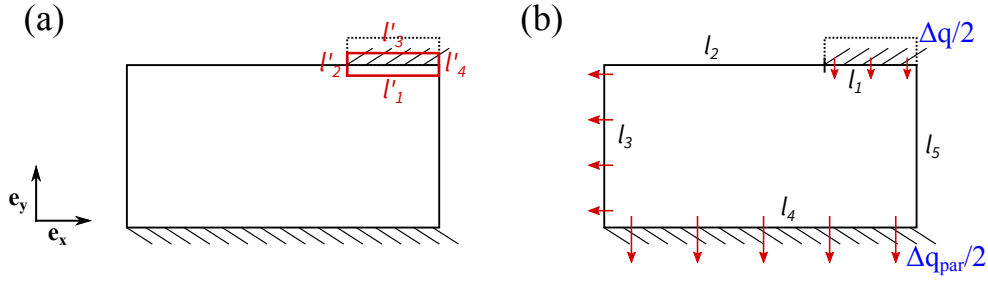


Figure 3.17 – (a) : Close-up view of the area enclosed in the thick dashed line, with a Gauss rectangle divided in 4 segments of length l_i . The half electrode is shown as a dotted silhouette. The hatches show the electrode parts. (b) : Close-up view of the area enclosed in the thick dashed line, divided in five segments of length l_i . The half electrode is shown as a dotted silhouette. The hatches show the electrode parts. The charge that each electrode bear is indicated in blue. The D field flux is schematically shown with red arrows.

integral can be replaced by a surface integral, and the contour integral becomes a line integral.

For symmetry reasons, we consider only the zone enclosed in a thick dashed line in Figure 3.16. A schematic close-up view of this area is shown in Figure 3.17. First, we apply the Gauss theorem in the red rectangle shown in Figure 3.17, which contains the film-electrode interface. If Δq is the change of charge integrated over the cross-section (x and y) of one electrode finger (Δq is therefore a charge per unit length in the z direction) for a change of voltage ΔV , we have:

$$\int_{\mathcal{C}} \Delta \mathbf{D} \cdot d\mathbf{l}' = \sum_{i=1}^4 \int_{\mathcal{C}_i} \Delta \mathbf{D} \cdot d\mathbf{l}'_i = \frac{\Delta q}{2} \quad (3.25)$$

where \mathcal{C} is the contour of the red zone shown in Figure 3.17, \mathbf{D} the electric displacement in the material along this contour, and $d\mathbf{l}'$ the infinitesimal normalized vector locally orthogonal to \mathcal{C} and pointing towards the outside of the red zone. There is no \mathbf{D} field inside the metal electrode, hence $\int_{\mathcal{C}_3} \Delta \mathbf{D} \cdot d\mathbf{l}'_3 = 0$. In addition, we can take \mathcal{C}_2 and \mathcal{C}_4 arbitrarily small. Therefore we can write that, for \mathcal{C}_1 very close to the film-electrode interface, we have:

$$\int_{\mathcal{C}_1} \Delta \mathbf{D} \cdot d\mathbf{l}'_1 = \frac{\Delta q}{2} \quad (3.26)$$

Now we apply the same consideration onto the complete problem, choosing the zone of the ferroelectric film enclosed in the thick dashed line shown in Figure 3.16. The border of the considered zone can be split in 5 segments as shown in Figure 3.17 (b). There are no free charges inside the PZT, MgO and SiO_2 since they are dielectric materials, so we have:

$$\int_{\mathcal{C}} \Delta \mathbf{D} \cdot d\mathbf{l} = \sum_{i=1}^5 \int_{\mathcal{C}_i} \Delta \mathbf{D} \cdot d\mathbf{l}_i = 0 \quad (3.27)$$

with similar notation as before and \mathcal{C}_1 , \mathcal{C}_2 and \mathcal{C}_4 arbitrarily close the neighbouring interface.

Within the PZT layer, we can write $\Delta \mathbf{D} = \Delta \mathbf{P}$ where \mathbf{P} is the local spontaneous polarization (which is electric field dependent), neglecting as customary the term $\epsilon_g \Delta \mathbf{E}$, where ϵ_g denotes a background contribution [87, 88] that is estimated to be around 10 [89].

Since \mathcal{C}_5 is situated on a plane of symmetry, the electric field along this path is purely along \mathbf{e}_y ; since $d\mathbf{l}_5 \propto \mathbf{e}_x$, we have $\mathbf{D} \cdot d\mathbf{l}_5 = 0$ in the SiO_2 and MgO layers, and $\int_{\mathcal{C}_5} \Delta \mathbf{D} \cdot d\mathbf{l}_5 = \int_{\mathcal{C}_5} \Delta P_x(y) dy$ within the PZT layer. Because the electric field is along \mathbf{e}_y , P_x should not change (the PZT is unpoled in this direction) and hence $\int_{\mathcal{C}_5} \mathbf{D} \cdot d\mathbf{l}_5 = 0$. On the surface of PZT between the electrodes, $\mathbf{E} \propto \mathbf{e}_x$ holds along \mathcal{C}_2 , and $d\mathbf{l}_2 \propto \mathbf{e}_y$; hence we also have $\int_{\mathcal{C}_2} \Delta \mathbf{D} \cdot d\mathbf{l}_2 = \int_{\mathcal{C}_2} \Delta P_y(x) dx = 0$.

From equation 3.26, since $d\mathbf{l}_1 = -d\mathbf{l}'_1$, we have $\int_{\mathcal{C}_1} \Delta \mathbf{D} \cdot d\mathbf{l}_1 = -\Delta q/2$. We can write that $\int_{\mathcal{C}_4} \Delta \mathbf{D} \cdot d\mathbf{l}_4 = -\Delta q_{\text{par}}/2$ where Δq_{par} is the change of charge on the Si floating electrode for one spatial period of the IDE structure, per unit length along the z direction, for a change of voltage ΔV .

Therefore since $d\mathbf{l}_3 \propto -\mathbf{e}_x$:

$$\begin{aligned} 0 = & -\frac{\Delta q}{2} - \int_{t_{\text{SiO}_2} + t_{\text{MgO}}}^{t_{\text{SiO}_2} + t_{\text{MgO}} + t_f} \Delta P_x^{\text{mid-gap PZT}}(y) dy \\ & - \int_{t_{\text{SiO}_2}}^{t_{\text{SiO}_2} + t_{\text{MgO}}} \Delta D_x^{\text{mid-gap MgO}}(y) dy \\ & - \int_0^{t_{\text{SiO}_2}} \Delta D_x^{\text{mid-gap SiO}_2}(y) dy - \frac{\Delta q_{\text{par}}}{2} \end{aligned} \quad (3.28)$$

The sum of the $\Delta \mathbf{D}$ field inside the MgO layer at mid-gap corresponds to the field lines directly connecting both electrodes fingers and passing through the PZT and then the MgO layers. Similarly the sum of the $\Delta \mathbf{D}$ field inside the SiO_2 layer corresponds to field lines going through PZT, MgO and then SiO_2 before reaching the other electrode. $\Delta q_{\text{par}}/2$ corresponds to the field lines connecting the electrode fingers of opposite polarity *via* the floating Si substrate. Since the dielectric constants of MgO and SiO_2 are much smaller than that of single domain PZT (which at its smallest should be close to 300, for large electric field values), the sum of the $\Delta \mathbf{D}$ field inside these layers can be neglected in the previous equation. This is also confirmed by the FE simulation result shown in Figure 3.16. Note that in our coordinate system $P_x^{\text{mid-gap PZT}}(y)$ is negative when pointing outward of the volume. We can now write:

$$\frac{\Delta q}{2} = -t_f \Delta \langle P_x \rangle_{\text{thickness}} - \frac{\Delta q_{\text{par}}}{2} \quad (3.29)$$

where $\langle \cdot \rangle$ denotes averaging. Thus the charges on the electrode finger compensate for the in-plane polarization in the PZT film at midgap and for the parasitic capacitance due to the Si substrate. Since the finger length W is much larger than any other dimension, border effects at the finger tips can be neglected, and we can sum along the finger length and multiply by the

Chapter 3. Physical behavior of ferroelectric thin films with IDE and characterization methodology

number of finger half-pairs $2N - 1$:

$$\frac{(2N - 1) W \Delta q}{2} = - (2N - 1) W t_f \Delta \langle P_x \rangle_{\text{midgap surface}} - \frac{(2N - 1) W \Delta q_{\text{par}}}{2} \quad (3.30)$$

$$\frac{\Delta Q_{\text{meas}}^{\text{fingers}}}{A} = - \Delta \langle P_x \rangle_{\text{midgap surface}} - \frac{C_{\text{par}}^{\text{fing.}} \Delta V}{A} \quad (3.31)$$

where $A = (2N - 1) W t_f$ is the effective surface used for the simple model as in equation 3.2. For the total charge change of the complete device, the parasitic contribution from the bus lines and contact pads must be taken into account as well.

Thus we find that, once the contribution from the parasitic capacitance from the Si substrate is removed, the change of charge on the electrode fingers compensate exactly for the change of net polarization projected on the plane at mid-gap orthogonal to the electric field direction. This is similar to the parallel plate case. Since, as we found in section 3.9, the electric field at mid-gap is very homogeneous within the PZT film for t_f much smaller than a and b , the IDE sample can be accurately represented, as far as the electrical properties are concerned, by an equivalent PPE capacitor of area $A = (2N - 1) W t_f$ and thickness T such as the electric field at mid-gap is given by $E = V / T$. In the approximation presented in section 3.9 this distance is given by $T = a + \Delta a$, where Δa is obtained either with the Gevorgian or the Igreja formula. If t_f becomes comparable to a and b , the previous derivation for the effective surface still holds, but the electric field will not be homogeneous over the mid-gap plane, and it is therefore expected that the electrical behavior will depart from that of a PZT film with parallel plate electrodes — notably, the polarization switching is expected to be spread over a wider voltage range, since different regions of the PZT film will experience a different electric field for the same applied voltage.

3.12 Maximum reachable polarization

Table 3.1 shows the maximum reachable polarization after poling of a PZT thin film with IDE structures, for different grain orientations and crystalline structures. For a given distribution of orientations, one needs to take the weighed average using weights corresponding to the proportion of each grain orientation. So-called “hard” and “soft” MPB correspond to two different methods for obtaining the maximum reachable polarization for that composition : In the “hard” MPB approach we consider that 50% of the grains are tetragonal and the remaining 50% are rhombohedral, hence the maximum reachable polarization is the average of the two values for a given orientation; in the “soft” MPB approach, we consider that each grain takes the best phase (tetragonal or rhombohedral) to maximize $\mathbf{P} \cdot \mathbf{E}$. This value was obtained by computer calculations. The values for each orientation of the tetragonal and rhombohedral phases are determined explicitly in appendix F, and confirmed by computer calculations. The

Table 3.1 – Maximum polarization after poling for various grain orientations and crystalline structures for PZT with IDE.

Texture	Tetragonal	Rhombohedral	“Hard” MPB	“Soft” MPB
{100}	$0.90P_s$	$0.74P_s$	$0.82P_s$	$0.91P_s$
{110}	$0.78P_s$	$0.89P_s$	$0.835P_s$	$0.95P_s$
{111}	$0.78P_s$	$0.90P_s$	$0.84P_s$	$0.90P_s$

method was refined with respect to an earlier publication [45] giving now precise results.

The orientation to achieve the largest polarization after poling depends on the phase : It is {100} for tetragonal compositions; {111} for rhombohedral compositions; {111} for “hard” MPB compositions; and {110} for “soft” MPB compositions. However, whatever the model used, the maximum reachable polarization for the MPB composition shows only a weak dependence on the film texture. This means that for PZT MPB films with IDE, texture control is not necessarily required, which can give some flexibility for device fabrication.

3.13 Experimental verification

In the previous sections we have presented a number of corrections and features that need to be taken into account for obtaining the true ferroelectric properties of a ferroelectric film with IDE structures : the use of the Gevorgian or of the Igreja model to extract the dielectric constant of the film from impedance measurements, which can be used in a simplified form when t_f is many times smaller than both a and b ; the removal of the parasitic capacitance contribution to the PV and the CV loops; and the correction of the electric field governing at mid-gap between the electrode fingers. We also showed that dielectric and polarization properties at mid-gap are the ones that influence most the observed capacitance and polarization properties. In this section we will show how these features fit with observations on ferroelectric films with IDE structures.

For the following measurements we used a single 580-nm-thick sol-gel PZT film with the MPB composition, deposited with the gradient-free route, similarly to a previous publication [35]. IDE structures with various gaps a and finger widths b in the μm range were patterned on the top surface of the PZT film, and then the wafer was diced into $1.5\text{ mm} \times 15\text{ mm}$ cantilevers. The finger length was $980\text{ }\mu\text{m}$ and the number of fingers $2N$ either 100 or 200. The chosen PZT film thickness leads to $\Delta a \approx 0.76\text{ }\mu\text{m}$ with the Gevorgian formula and $\Delta a \approx 0.51\text{ }\mu\text{m}$ with the Igreja formula. Before measuring, all samples were annealed together in a rapid thermal annealing tool for 10 min at $550\text{ }^\circ\text{C}$ under 100 sccm of O_2 flow. Since the PV and CV loops are quite sensitive to the history of the samples, each set of measurements was accomplished at identical conditions and prehistories. The aixACCT[®] TF2000 setup was used for the measurements. The large signal measurements (PV loop) were recorded with a triangle wave at 20 Hz, preceded by an identical wave with a 1 s waiting time in between. The small-signal measurements (CV and

piezoelectric coefficient *vs.* field loop) were recorded with a triangle wave at a frequency of 100 mHz as the large signal, and a sine wave at 1 kHz and amplitude of 5 kV/cm as the small signal.

3.13.1 Simple model

First we have measured PV and CV loops on a set of samples with varying finger distances a and fixed finger width b (a nominally constant value for b on the photolithography design resulted in $b = 6.5$ to $6.8 \mu\text{m}$ for this series of samples), using a maximum voltage V_{max} given by $V_{\text{max}} = aE_{\text{max}}$ where $E_{\text{max}} = 150 \text{ kV/cm}$. Figure 3.18 (b) shows the PV loops derived according to the simple model. We observe that, similar to the previously cited work [45], the apparent coercive field depends on the finger distance; and that the slope of the saturated branches of the PV loops increases with increasing gap. The step of the dielectric constant curves between low- and large-gap samples in Figure 3.18 (a) corresponds to a change in the number of electrode fingers (200 for low-gap samples, 100 for large-gap samples). Removing the contribution from the parasitic capacitance with the empirical model, and rescaling the x-axis as $E = V / (a + \Delta a)$ (Gevorgian model), yields a set of PV loops with much better overlap (Figure 3.18 (d)). The coercive fields are hardly distinguishable, and the saturated branches have almost equal slopes, showing somewhat lower polarization values for large gaps. The latter is in agreement with the FE simulation results yielding mid-gap fields that are lower than the $V / (a + \Delta a)$ value, as presented in section 3.9. For the CV loops the simple model results in an increased dielectric constant for larger gap values (Figure 3.18 (a)). After removal of the parasitic capacitance with the empirical model, applying the single layer Gevorgian formula to extract the dielectric constant from the capacitance, and rescaling of the electric field axis with the same model, a much better overlap of the curves for the various geometries is obtained: The dielectric constant dependence on the finger distance is very much reduced, and the step of dielectric constant observed in Figure 3.18 (a) has disappeared. Still, the coercive field (peak position) seems to increase slightly with larger gap (Figure 3.18 (c)). Also a small dependence of the dielectric constant on the finger distance is still present. This is in part due to fact that the smaller gap samples are less saturated, because the maximum field they experienced, now given by $V_{\text{max}} / (a + \Delta a) < 150 \text{ kV/cm}$, is smaller. In addition, as was shown in section 3.10, it is expected that the accuracy of this method is still somewhat gap-dependent, which can also contribute to the observed discrepancy.

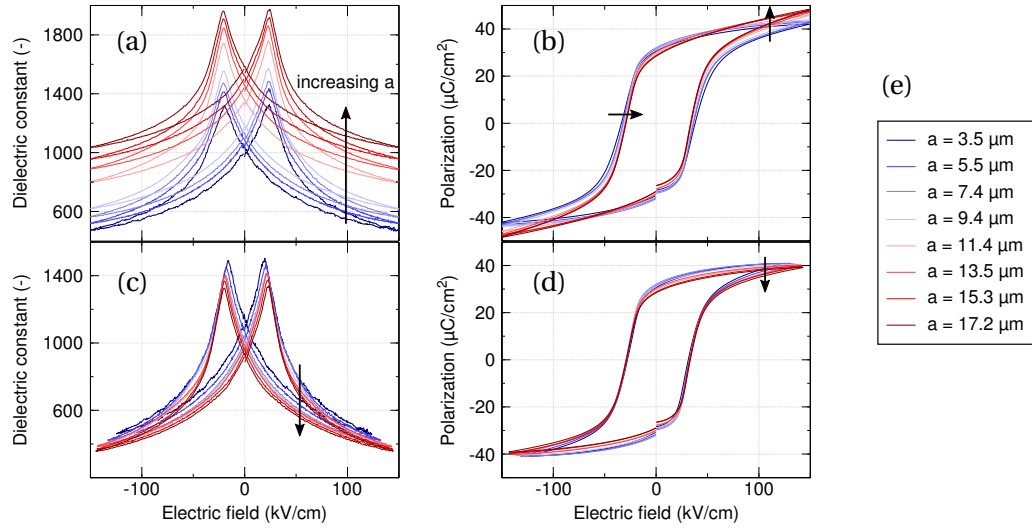


Figure 3.18 – (a) and (b) : as-measured CV and PV loops, respectively. The dielectric constant in (a) has been obtained using the simple model. (c) and (d) : CV and PV loops, respectively, corrected for the parasitic capacitance (empirical model) and the electric field reduction (Gevorgian formula). The dielectric constant in (c) has been obtained using the single layer Gevorgian formula. (e) : finger distances for each curve. Note that, after rescaling the x-axis, the maximum electric field is $V_{\text{max}} / (a + \Delta a)$ and is therefore gap-dependent, since V_{max} was chosen proportional to a .

Chapter 3. Physical behavior of ferroelectric thin films with IDE and characterization methodology

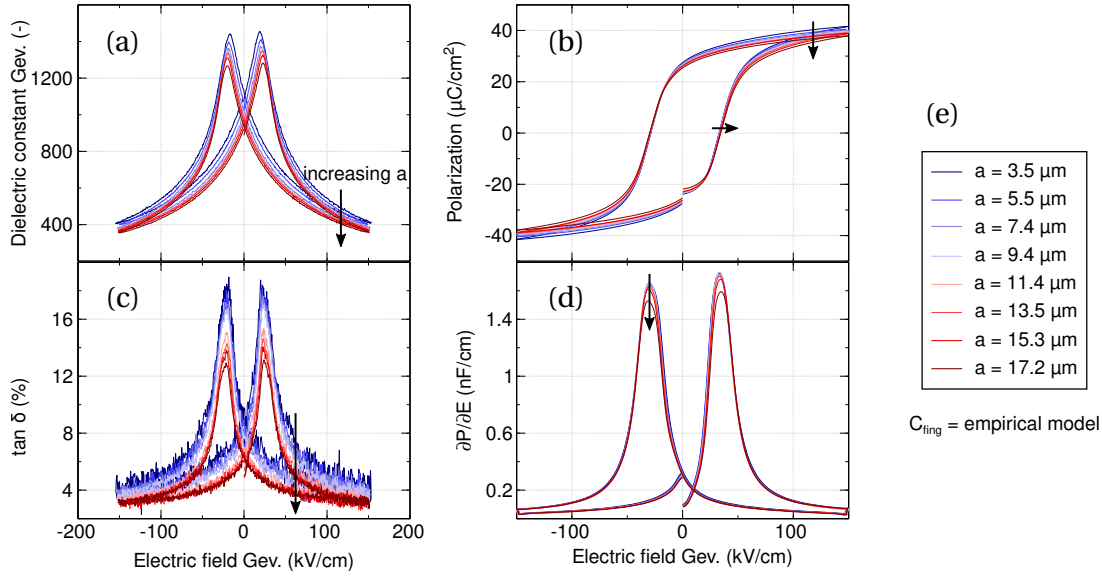


Figure 3.19 – (a) and (b) : CV and PV loops, respectively, cycled at a maximum voltage V_{\max} such as $V_{\max} = E_{\max} / (a + \Delta a)$ where $E_{\max} = 150 \text{ kV/cm}$ and Δa is given by the Gevorgian formula. Both types of loops have been corrected for parasitic capacitance (empirical model) and the x-axis field is given by $V / (a + \Delta a)$ (Gevorgian). The dielectric constant was obtained with the single layer Gevorgian formula. (c) shows the losses and (d) the derivative of the PV loops, both with x-axis given by $V / (a + \Delta a)$ (Gevorgian). (e) : finger distances for each curve and finger capacitance model used.

3.13.2 Gevorgian model

To fully assess the accuracy of the corrections, we have then cycled the same set of samples (after annealing them again as described above) using a maximum voltage V_{\max} given by $V_{\max} = (a + \Delta a) E_{\max}$ where $E_{\max} = 150 \text{ kV/cm}$ and Δa is given by the Gevorgian formula. The resulting PV loops are shown in Figure 3.19. The field axis shows $V / (a + \Delta a)$ (Gevorgian formula) and the parasitic capacitance (empirical model) has been subtracted. We can see that, as expected, the PV loops overlap already quite well. A small reduction of the coercive field is observed for decreasing gap values, which is attributed to the gap-dependent inaccuracy of approaching the mid-gap electric field by $V / (a + \Delta a)$ (Gevorgian) as discussed before. Figure 3.19 (d) shows that the slopes of the saturated branches of the PV loops are nearly equal for all gap values, which suggests that all the parasitic capacitance sources have been accurately corrected for. The saturated polarization is slightly larger for smaller gaps as before, for which we can advance the same arguments as before.

Figure 3.19 (a) shows the CV loops corrected for all parasitic capacitances (empirical model), extracted using the single layer Gevorgian formula, and with the field axis showing $V / (a + \Delta a)$ (Gevorgian). The same dependence of the coercive field on the gap as for the PV loops is observed. As above we notice that the dielectric constant still shows some dependence on the gap value. This dependence is less pronounced for intermediate gap values. This is consistent

with the trend we have witnessed in section 3.10, where we observed that the Gevorgian formula is less gap-dependent in this range.

The losses (Figure 3.19 (c)) are considerably larger for smaller gaps. The increase is much more pronounced than in the dielectric constant. We do not have a theory for the correction of the loss tangent. Formally, we can introduce a complex permittivity into the conformal mapping transformation. As the permittivity appears always in a linear way, real and imaginary parts transform with the same multiplication factor. This means that $\tan \delta$ does not change upon this transformation and should be measured correctly. The larger noise for small gaps is caused by the much smaller applied AC voltage that was also scaled with the gap distance to obtain identical electric field amplitudes. If the apparent increased permittivity at smaller gaps is real, we expect also larger losses for small gaps, because dielectric losses usually depend on a power higher than 1 on the dielectric constant [90]. Parasitic contributions due to the Si substrate are not contributing significantly to the losses. Resistive losses are expected to occur at much higher frequencies than the small signal frequency of 1 kHz, since the observed RC time constant is very short. Also, the $2\text{ }\mu\text{m}$ -thick SiO_2 layer grown by wet oxidation of the Si substrate, which makes the greater part of the parasitic capacitance, is expected to display losses less than 10 % of the losses measured for the PZT film. Since C_{par} makes up 10 % of the total capacitance of the device, as a rough approximation, this means that the contribution of the parasitic capacitance should amount to about 1 % of the values shown in Figure 3.19 (c), with the rest coming from the PZT film. This does not account for the differences observed for different gap values. A more likely explanation is the drop of electric field within the gap for larger gaps, as discussed previously. Even if the small signal voltage amplitude V_{ss} was scaled with the gap value such as $V_{\text{ss}} / (a + \Delta a) = 5\text{ kV/cm}$, we saw in section 3.9 that this formula is underestimating (resp. overestimating) the real electric field within the gap for small gap values (resp. for large gap values). Lower small signal amplitudes will cause less irreversible movement of domain walls, which qualitatively explains why the losses appear lower with increasing gap.

Chapter 3. Physical behavior of ferroelectric thin films with IDE and characterization methodology

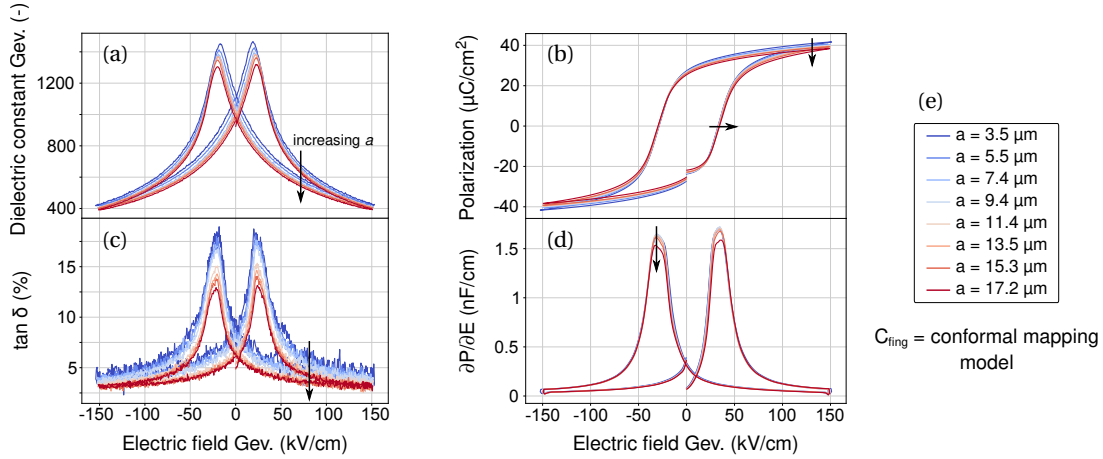


Figure 3.20 – (a) and (b) : CV and PV loops, respectively, cycled at a maximum voltage V_{max} such as $V_{\text{max}} = E_{\text{max}} / (a + \Delta a)$ where $E_{\text{max}} = 150 \text{ kV/cm}$ and Δa is given by the Gevorgian formula. Both types of loops have been corrected for parasitic capacitance (conformal mapping model) and the x-axis field is given by $V / (a + \Delta a)$ (Gevorgian). The dielectric constant was obtained with the single layer Gevorgian formula. (c) shows the losses and (d) the derivative of the PV loops, both with x-axis given by $V / (a + \Delta a)$ (Gevorgian). (e) : finger distances for each curve and finger capacitance model used.

Figure 3.20 shows the same data as in Figure 3.19 but using the conformal mapping model for the finger parasitic capacitance instead of the empirical model. This further improves the overlap of the CV loops as seen in Figure 3.20 (a). This is as expected, since we saw in section 3.10 that using the conformal mapping model reduces the gap-dependence with the Gevorgian formula, in particular for large gaps. However there is a large dispersion for small gaps, where the gap-dependence of the model is more pronounced. The loops in (b) and (d) (PV loops and their derivative) remain relatively unchanged; this shows that they are less sensitive to the model used for removing the finger parasitic capacitance. The CV loops are better indicators for the accuracy of the analytical model.

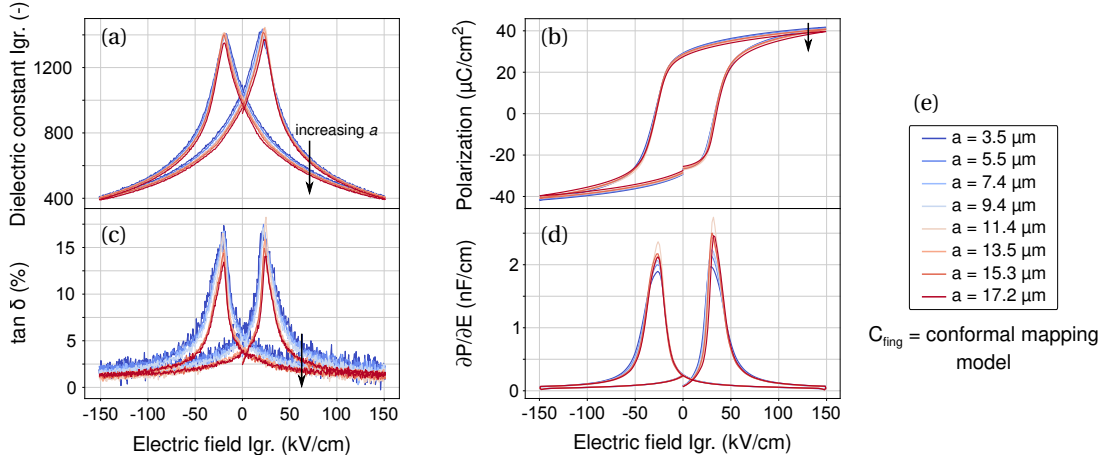


Figure 3.21 – (a) and (b) : CV and PV loops, respectively, cycled at a maximum voltage V_{max} such as $V_{\text{max}} = E_{\text{max}} / (a + \Delta a)$ where $E_{\text{max}} = 150 \text{ kV/cm}$ and Δa is given by the Igreja formula. Both types of loops have been corrected for parasitic capacitance (conformal mapping model) and the x-axis field is given by $V / (a + \Delta a)$ (Igreja). The dielectric constant was obtained with the Igreja formula. (c) shows the losses and (d) the derivative of the PV loops, both with x-axis given by $V / (a + \Delta a)$ (Igreja). (e) : finger distances for each curve and finger capacitance model used.

3.13.3 Igreja model

Finally, we have cycled the same set of samples (after one more annealing) using a maximum voltage V_{max} given by $V_{\text{max}} = (a + \Delta a) E_{\text{max}}$ where $E_{\text{max}} = 150 \text{ kV/cm}$ and Δa is given by the Igreja formula. The PV loops are shown in Figure 3.21 (b). The field axis shows $V / (a + \Delta a)$ (Igreja formula) and the parasitic capacitance (conformal mapping) has been subtracted. The PV loops overlap slightly better than before. The coercive field is now nearly gap-independent. The saturated branches of the PV loops are virtually equal for all gap values (Figure 3.21 (d)), while the maximum slope is highest for intermediate gap values. The saturated polarization is still slightly larger for smaller gaps, as before.

Figure 3.21 (a) shows the CV loops corrected for all parasitic capacitances (conformal mapping), extracted using the Igreja formula, and with the field axis showing $V / (a + \Delta a)$ (Igreja). Even though the dielectric constant still shows some dependence on the gap value, this is the best overlap for all models investigated; the dielectric constant has very little dispersion at large fields and at the peak of the loops (except for the largest gap for the latter case). This is a great improvement over the simple model shown in Figure 3.18 (a).

Chapter 3. Physical behavior of ferroelectric thin films with IDE and characterization methodology

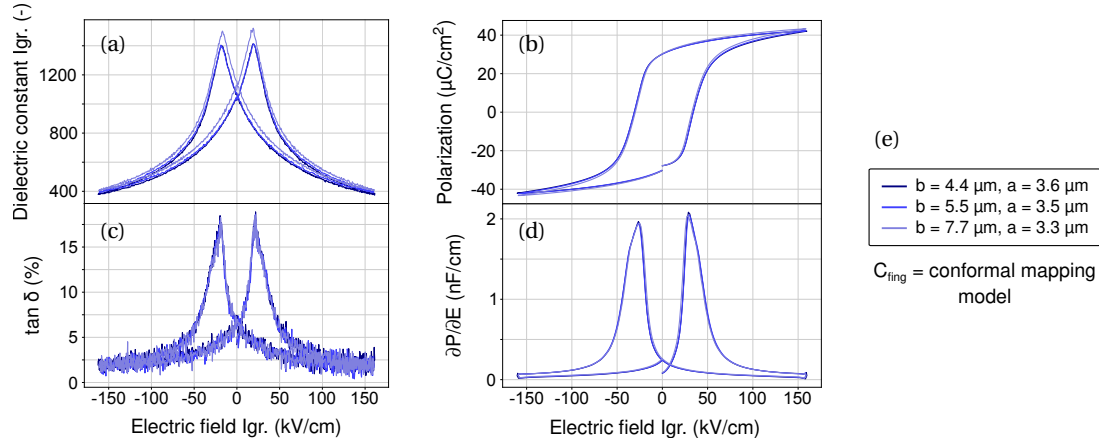


Figure 3.22 – (a) and (b) : CV and PV loops, respectively, cycled at a maximum voltage V_{max} such as $V_{\text{max}} = E_{\text{max}} / (a + \Delta a)$ where $E_{\text{max}} = 150 \text{ kV/cm}$ and Δa is given by the Igreja formula. Both types of loops have been corrected for parasitic capacitance (conformal mapping model) and the x-axis field is given by $V / (a + \Delta a)$ (Igreja). The dielectric constant was obtained with the Igreja formula. (c) shows the losses and (d) the derivative of the PV loops, both with x-axis given by $V / (a + \Delta a)$ (Igreja). (e) : finger width b and gap a for each curve and finger capacitance model used.

Figure 3.22 shows the same as Figure 3.21 but with another set of samples having nearly the same gap and different finger widths. The curves for the samples having $b = 4.4 \mu\text{m}$ and $b = 5.5 \mu\text{m}$ overlap perfectly, while those for the sample with $b = 7.7 \mu\text{m}$ display a slight deviation. The latter sample has a smaller gap than both of the former, and the observed deviation follows the trend discussed before for decreasing gap. In addition, the two smaller finger widths are closer to each other than each is to the largest finger width. This could be a sign that the formula we used to estimate the parasitic capacitance of the fingers has a limited validity range for various values of b . In section 3.10 we only investigated the gap dependence of the formula.

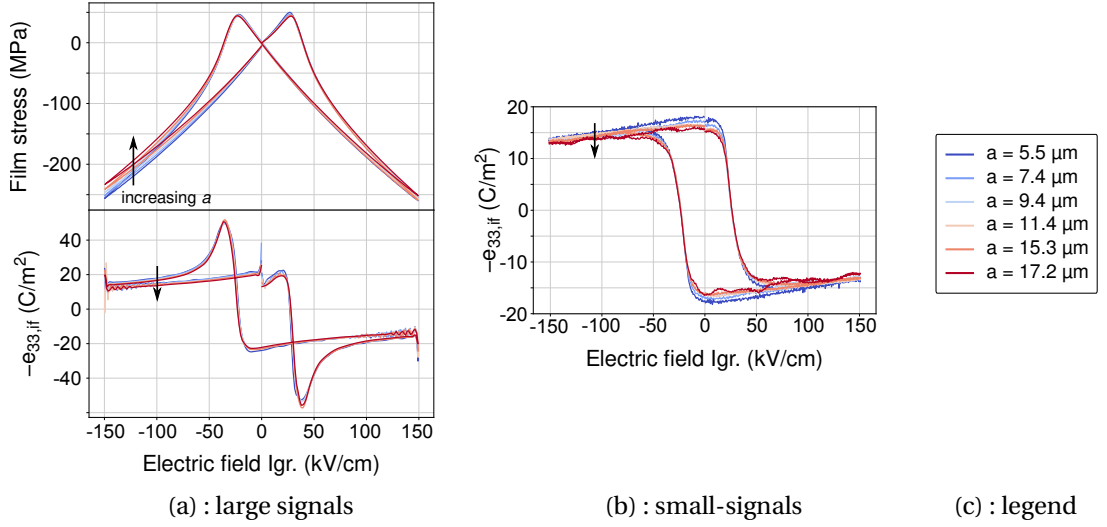


Figure 3.23 – (a) : large signal displacement measurements, cycling at a maximum voltage V_{\max} such as $V_{\max} = E_{\max} / (a + \Delta a)$ where $E_{\max} = 150 \text{ kV/cm}$ and Δa is given by the Igreja formula. The x-axis field is given by $V / (a + \Delta a)$ (Igreja). The film stress and the $e_{33,if}$ coefficients have been obtained considering that only the gap region is active. (b) : small signal displacement measurement in the same conditions as in (a). (c) : gap for each curve.

3.14 Displacement measurements in converse mode

As described in chapter 2, a single laser beam interferometer is used to measure the cantilever tip excursion in order to extract the stress in the ferroelectric film. The cantilever is clamped at the start of the interdigitation zone, which is the active zone. When the electrodes are biased, compressive stress builds up between the IDE fingers, which bends the substrate downward. The deflection is then amplified by the slope of the cantilever in the inactive zone. The same set of samples as in the previous section was used.

Figure 3.23 (a) and (b) shows the large and small signal displacement measurements, respectively, from which we have extracted the film stress (in (a)) and the piezoelectric coefficient $e_{33,if}$ (in (a) and (b)), using equation 2.10 from chapter 2, and using the Igreja electric field as the field in the active region. Note that, since the number of gaps is 199, it is equivalent to use either of the geometrical factors g_1 or g_2 introduced in appendix B. Therefore, our values should correspond to the real material coefficient $\widehat{e_{33,if}}$ of Chidambaram and coworkers [35]. This indeed yields a very good overlap of the various curves in all cases. In particular, the coercive field is the same for all samples in Figure 3.23 (b). The slope of the small-signal curve on the return branch can be attributed to the increase of the dielectric constant on the return branch of the CV loop (Figure 3.21 (a)). The perfect overlap of the forward and return branches at high fields for the small signal measurements suggests that the domain pattern evolves in an anhysteretic fashion beyond a threshold field: indeed, the slope remains quite constant until the field drops to less than 10 kV/cm in absolute value. This constant slope all the way to nearly 0 bias is also evident on the return branch of the large-signal $e_{33,if}$ in Figure 3.23 (a),

Chapter 3. Physical behavior of ferroelectric thin films with IDE and characterization methodology

which is also close to the forward branch at high fields, displaying little hysteresis in this range.

For both large and small signal measurements, we observe that the piezoelectric response is larger for smaller gaps. This is particularly noticeable at remanence in Figure 3.23 (b): the remanent value is $e_{33, \text{if}} = 17 \text{ C/m}^2$ for $a = 5.5 \mu\text{m}$ and 15 C/m^2 for $a = 17.2 \mu\text{m}$. That is more than 10 % difference. This effect is less pronounced at high fields. This remanent value is excellent and much larger than what can usually be obtained with the parallel plate configuration; this will be commented in more details in chapter 4.

Note that the dispersion of the film stress and $e_{33, \text{if}}$ values cannot be attributed to the variability of the clamping conditions in converse mode measurements, provided that the tip excursion remains of the order of the μm . Indeed, if the electrodes start after the end of the clamp, there could in theory be some bending due to the clamping acting on the beam. This is actually also true even if the clamping ends exactly where electrodes start. We are concerned with vertical forces causing a reaction from the clamp. The force generated by the piezoelectric actuation can be written as $F = \sigma_f t_f$; σ_f is obtained with the Stoney formula as described in appendix B. The straight part of the beam makes a small angle θ with the horizontal; θ is given with good approximation by $w(x_2)/(x_2 - x_1)$, because it is indeed quite small: writing $w(x_2) = 1 \mu\text{m}$ and $x_2 - x_1 = 5 \text{ mm}$, this ratio is 5×10^{-3} . The vertical component of the force is then lower than $F_{\perp} = F \sin \theta \approx \sigma_f t_f \theta$. The clamp will react with a force of equal strength and opposite direction. This creates a bending moment of the order of $M = F_{\perp} x_{\text{mid}}$ where x_{mid} is the distance from the clamp to the middle of the active zone. This bending moment may compete with or add to the bending moment of the substrate caused by the piezoelectric actuation. The latter is of the order of $F \cos \theta t_s \approx \sigma_f t_f t_s$, where t_s is the substrate thickness. Hence the ratio of the clamp moment to the piezoelectric moment is given by $\theta x_{\text{mid}}/t_s = w(x_2)x_{\text{mid}}/(x_2 - x_1)t_s$. This is the same order of magnitude as $w(x_2)/t_s$, which is less than 1 % for piezoelectric films on cantilever with full wafer thickness. Note that this estimate is obtained with the same assumptions as for the derivation of the Stoney formula; in particular, it is not valid for the thin substrate case (*i. e.* if the thickness of the piezoelectric film is an appreciable fraction of the total thickness of the cantilever).

Hence, as long as the clamp does not cover a portion of the active zone, the force situation is not changed. The only source of error which remains is the misestimation of the distances between the laser spot and each of the active zone extremities. These distances enter in the $e_{31, \text{f}}$ and $e_{33, \text{if}}$ formulas in a linear or inverse way. Since the structure geometry is known from the photolithography mask (or shadow mask) design, or, in any case, can be measured with an optical microscope, the only source of variability originating from the mounting of the samples lies with the positioning of the laser spot — as long as the active zone is fully unclamped. The laser spot must be centered on a circular reflector of diameter $600 \mu\text{m}$. We estimate that we can position it within $100 \mu\text{m}$ of the actual reflector center. Since the distance between the center of this reflector and the start of the active zone is 9.5 mm , this amounts to about 2 % error for x_2 . This is less than the observed variations of dielectric constant and $e_{33, \text{if}}$ with the IDE gap. Besides, the observed gap-dependence is consistent across the 6 samples

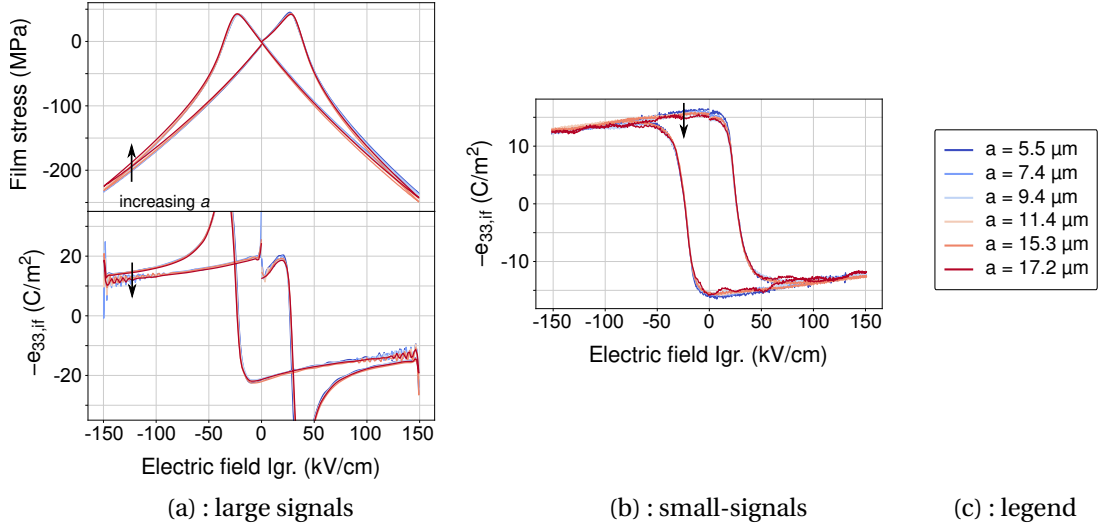


Figure 3.24 – (a) : large signal displacement measurements, cycling at a maximum voltage V_{\max} such as $V_{\max} = E_{\max} / (a + \Delta a)$ where $E_{\max} = 150 \text{ kV/cm}$ and Δa is given by the Igreja formula. The x-axis field is given by $V / (a + \Delta a)$ (Igreja). The film stress and the $e_{33,if}$ coefficients have been obtained considering that the active region has a length of $a + \Delta a$, where Δa is given by the Igreja formula. (b) : small signal displacement measurement in the same conditions as in (a). (c) : gap for each curve.

we measured, which seems too systematic to be due to some external variability. A more likely cause is either a gap-dependence stemming from some inaccuracy in the geometric model we used, or a gap-dependent material response.

Fig. 3.24 shows the same data as in Fig. 3.23, but considering that the active region is not contained within each gap, but extends over a distance of $a + \Delta a$, where Δa is given by the Igreja model. Since we interpreted the simplified Igreja formula as an indication that the electric field lines have a length $a + \Delta a$, it is reasonable to assume that the active region in converse mode extends over the same distance. We observe that the overlap is improved in this case, but that a small gap-dependence remains.

3.15 Discussion on the gap dependence of the IDE properties

In the previous sections we have noticed a small dependence of the IDE properties on the IDE gap. Since we saw in section 3.10 that the Igreja formula with the conformal mapping model for the finger capacitance is very weakly gap-dependent (about 1 % in Fig. 3.14), the gap-dependence of the dielectric constant observed in Fig. 3.21, which is larger than that, can be attributed to the material response. Similarly, with the reasonable assumption that the active zone between two IDE fingers extends over the distance $a + \Delta a$, where Δa is given by the Igreja model, $e_{33,if}$ in Fig. 3.24 still shows some gap dependence. Therefore it is likely that the gap dependence of the saturated polarization in Fig. 3.21 (b) is also the consequence of

Chapter 3. Physical behavior of ferroelectric thin films with IDE and characterization methodology

a gap-dependent material response. The trend is as follows : higher dielectric constant for small gaps, higher switchable polarization for small gaps, and higher piezoelectric response for small gaps.

All the samples were fabricated with the same PZT film and are taken from the same region of the wafer. The sol-gel process employed for the PZT film deposition yields a very good film uniformity. In addition, a non-uniform film would not display a gap-dependent trend as we observe, but rather a dispersion of values around an average. Thus we must conclude that either the field condition or the mechanical conditions within the film, or both, show some variation when the gap is varied. Figure 3.9 shows that there exists a field concentration zone near the electrode finger edge with non-zero vertical electric field, meaning that the electric field cannot be considered to be in the plane of the film inside this region. FE simulations show that the size of this region is gap-independent (for the range of gaps realized in our samples). This means that the volume of PZT enclosed by this region will be a larger fraction of the active PZT volume (the PZT volume situated within the gap) for small gaps than for large gaps, hence contributing to the measured properties to a larger extent for small gaps.

We still have to explain why the contribution of this zone gives larger permittivity, switchable polarization, and piezoelectric response than the bulk of the active volume. The variations of the electric field in this zone could imply a contribution from ϵ_{\perp} to the film properties, and in PZT we have $\epsilon_{\perp} > \epsilon_{\parallel}$, in particular at the MPB composition [20]. This would contribute to the permittivity, but also to the piezoresponse, because of the transverse instability of the polar axis at the MPB giving enhanced response away from the polar axis direction [21]. Since this additional volume is poled in addition to the active volume defined by the effective area times the effective gap $A_{\text{eff}}(a + \Delta a)$, its relative weight on the switchable polarization will be slightly larger for small gaps, slightly increasing the apparent saturating polarization. A similar study performed away from the MPB composition could give more precision as to the existence of such an effect.

Another possibility is that the dead zones below the electrode fingers behave as mechanical buffers, reducing the active zone mechanical clamping for small gaps for which the a/b ratio is smaller. This is consistent with the increased dielectric constant for small gaps, since $\epsilon_f^S < \epsilon_f^T$, but not with the larger piezoelectric response for small gaps, since relieving the clamping condition should reduce e_{33} , if as seen in chapter 2. Further FE modeling work should be undertaken to assess the existence and magnitude of such an effect, which should include the electromechanical coupling of the PZT layer unlike in our FE model, with the appropriate mechanical boundary conditions. Such a work is currently in progress within a collaboration work [81].

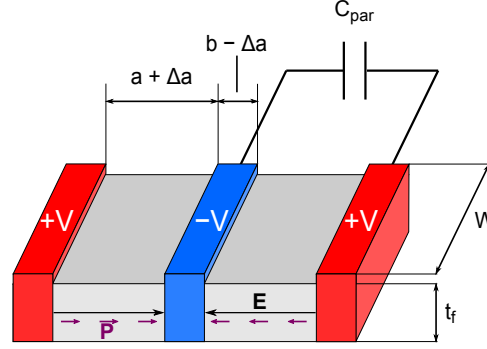


Figure 3.25 – Equivalent IDE model. C_{par} is calculated as explained in the text.

3.16 Conclusion

In conclusion, we showed that ferroelectric films with IDE structures are subject to a number of artefacts in standard characterization measurements. Except for a small volume fraction along the electrode edges, the electric field experienced by the film is always lower than V/a , where a is the finger distance and V the voltage applied to the sample. In addition, the presence of the Si substrate — even when separated by a thick silicon oxide film — causes a parasitic capacitance to exist in parallel with the ferroelectric film. These two features should be corrected for to obtain the true material properties. In this chapter, we developed a correction procedure for this purpose. Several procedures were proposed and tested. We found that the conformal transformation sequence elaborated by Igreja *et al.* [79] leads to a better overlap of the ferroelectric characterization loops than the ones worked out by Gevorgian *et al.* [78], and that the parasitic effect of the SiO_2 underlayer within the interdigitation zone is best described by the conformal mapping model of Cattaneo [86]. We thus extended the understanding of the conformal mapping transformation from a sole calculation of the effective dielectric constant, to a apprehension of the electric field governing the IDE capacitor. We obtained very satisfying agreements of CV and PV curves for a number of different gaps and finger widths in a typical range of useful IDE geometries for energy harvesting ($a > t_f$). We have shown that the polarization derived after the correction procedure is the average value present at mid-gap between the fingers, and that the coercive field scales well with the effective field we propose from the conformal mapping transformations. Therefore, our results show that the IDE sample can be treated as equivalent to the simple IDE model presented in section 3.2, but replacing the gap distance by $a + \Delta a$ (where Δa is obtained with the Igreja model), with a parasitic capacitance C_{par} connected in parallel, as pictured in Fig. 3.25. The theoretical evaluation of the maximal achievable polarization was revisited, and it has been found that more than 74% of the polarization align with the in-plane electric field, whatever the texture or the PZT composition may be.

We also addressed limiting situations. If a and b get closer to t_f , deviations from the expected behavior can occur. These deviations are due to the fact that the electric field becomes then much less homogeneous inside the ferroelectric film. Also, if a becomes much larger than

Chapter 3. Physical behavior of ferroelectric thin films with IDE and characterization methodology

$(\epsilon_f/\epsilon_{\text{SiO}_2}) t_{\text{SiO}_2}$, each finger will behave as a lone PPE capacitor and there will be no field within the gap between the fingers. This effect is caused by the conducting Si substrate behaving as a floating electrode. Therefore, for proper operation and easier characterization, the ratio a/t_f should be neither too small nor too large. For the moment, the exact electric field at mid-gap in the presence of a SiO_2 underlayer on top of a conductive Si substrate can only be obtained with FE simulations. A recent publication by Dias and Igreja [91] proposes an recursive image method to obtain the electric potential and electric field for IDE capacitors. Even though it is rather complex, this method could be adapted to our situation to provide an analytical formula for the electric field at midgap. This would give accurate knowledge of the film properties even for a large a/t_f ratio, which is beneficial since this corresponds to a larger fraction of active PZT volume; and in particular, it would give the precise voltage value required for the sufficient poling of structures with this geometry.

The models used in this work are postulating homogeneous dielectric properties. However, the CV loop shows us that this cannot be the case, since the electric field is not homogeneous. The combination of inhomogeneous electric fields along with the ferroelectric properties (including domains) makes the film response very complex to analyze. Further efforts are needed in this respect to fully understand the behavior of IDE systems, particularly for gaps close to the film thickness. Recent FE simulation results that we have obtained in collaboration with C. H. Nguyen show that, if the inhomogeneity of the dielectric constant due to the inhomogeneous electric field within the sample is taken into account, the overall capacitance of the device at a given voltage value is the same at that obtained with the effective dielectric constant derived from the conformal mapping transformation at the same voltage. The effective dielectric constant then corresponds to an equivalent average value. This result will be discussed in detail in our article in preparation [81].

The phenomenology of ferroelectric materials provides an interesting way for verifying analytical models for capacitance and electric fields. The strong dependence of their properties on the current electric field, and the switching response at precisely the coercive field, offer a testbed against which model predictions can be evaluated, by comparing the expected response of the same film in various configurations: if the model is accurate, the recorded hysteresis loops should overlap.

4 Doped PZT thin films with interdigitated electrodes

4.1 Introduction

A systematic characterization of IDE samples is lacking. We have provided a body of experiments for various electrode geometries in the previous chapter; in this chapter, we will provide the characterization results for 5 different combinations of PZT compositions and dopings, to get a better picture of the behavior of PZT thin films with the IDE configuration, and to determine the compositions and dopings which yield the best performance. The optimized fabrication route that we employed will be presented. We will also compare the performance of an IDE sample and a PPE sample of the same PZT composition and doping.

4.2 Sample fabrication

For the characterization of the performances of PZT thin films with IDE, with various composition and dopants, we have grown thin films following the sol-gel processing route developed by Chidambaram and coworkers [35, 43, 45]. The microstructure of the obtained films will be described in details below; it is similar to that published in Ref. [35].

We used either Nb or Fe as dopants, to obtain compositions of the form $\text{Pb}(\text{Zr}_x\text{Ti}_{1-x})_{1-y}\text{Me}_y\text{O}_3$, where Me is Fe or Nb. For Fe, we set $y = 0.01$, and for Nb, $y = 0.02$, that is 1 at.% doping for Fe and 2 at.% doping for Nb. Undoped, Fe-doped and Nb-doped PZT thin films with the 43/57 Zr/Ti nominal composition were prepared; this composition has the tetragonal phase. We also made undoped and Nb-doped PZT thin films with the 53/47 Zr/Ti nominal composition, which is the MPB composition [44]. We will later designate the doped films in the form Me:PZT $x/1 - x$, where Me is Fe or Nb, and x is the Zr/(Ti+Zr) ratio; if no dopant is specified, we mean to speak about the undoped film.

We prepared the precursor solutions with a 2-methoxyethanol route adapted from Blum and Gurkovich [92]. The solution preparation procedure is described in detail in Chidambaram's PhD thesis [93]. For each composition, doped and undoped, 4 solutions were prepared with

the Zr/(Zr+Ti) stoichiometric ratio following the gradient-free route developed by Calame and Muralt [47], which limits deviations from the nominal composition along the growth direction to within ± 2.5 at.%. Each precursor solution is spun and pyrolyzed in a sequence going from solution 1 to solution 4, and a crystallization step in a rapid thermal annealing tool (RTA), at 650 °C for 1 min in air under 100 sccm of oxygen flow, is performed after the 4-spinning sequence is complete. This results in a crystallized film thickness of about 250 nm; the sequence is repeated to obtain thicker films. All solutions have 10 at.% lead excess to compensate for lead loss during the RTA step, except solution 4 which was prepared with 30 at.% lead excess. For all films, a 20 nm-thick lead titanate PbTiO_3 (PTO) seed layer prepared with 30 at.% lead excess is used to facilitate the nucleation of the perovskite phase and to promote textured growth. This layer is crystallized in the RTA tool, under the same conditions as above, after only 1 spinning and pyrolysis. We used the following precursors for the preparation of the solutions, all purchased from Sigma-Aldrich®:

- For Pb : lead (II) acetate tri-hydrate
- For Ti : titanium (IV) isopropoxide
- For Zr : zirconium (IV) propoxide
- For Nb : niobium (V) ethoxide
- For Fe : iron (III) nitrate non-ahydrate

The stoichiometry was controlled by weight.

We used full-wafer thickness devices for characterization. This has the advantage that all samples are immediately compatible with our existing setups and equipments, while at the same time allowing for simple microprocessing procedures and short fabrication time. We used slightly doped, single-side polished 100 mm single crystal $\langle 100 \rangle$ Si wafers as substrate, with 2 μm wet oxide for electrical insulation from the Si substrate. The conductivity of the Si was either 15–25 $\Omega\text{ cm}$ or 0.1–100 $\Omega\text{ cm}$. This conductivity difference has no influence on the contribution of the parasitic capacitance at the frequencies encountered in our measurements, as discussed in chapter 3. The wafer thickness was measured with a mechanical profilometer and was between 523 μm and 536 μm for the IDE samples, and was 388 μm for the PPE samples. The PPE samples were kindly provided to us by Dr. Ramin Matloub.

A 100 nm-thick MgO buffer layer was e-beam evaporated onto the wafers. This layer serves to promote the $\{100\}$ PTO growth as well as a diffusion barrier to prevent lead interdiffusion at the high temperature of crystallization [35]. Unlike sol-gel PZT growth on $\{111\}$ Pt bottom electrodes, for which an overwhelmingly dominant $\{100\}$ texture is routinely achieved with the appropriate seed layer [50], the texture control provided by the MgO layer is not fully reproducible and is very sensitive to the ambient moisture: Indeed, MgO readily reacts with water to form magnesium hydroxide [94]. After evaporation, the wafers are exposed to ambient air during their transfer between the evaporator to the room where we proceed to the spin-coating of the PTO seed layer immediately afterwards. Although the room is equipped with a dehumidifier, good texture control for all the wafers of a given batch could not always

be obtained — note that since we proceed to the PTO deposition one wafer at a time, some wafers are exposed to air during a longer time. During the transfer, the wafers are transported in a sealed wafer box; we found that adding a large quantity of silica gel beads inside this box improves the number of wafers with the {100} PZT texture for a given batch. We managed to obtain almost full texture control for all wafers in a given batch for MgO depositions performed during the winter months, when the ambient air is naturally very dry. If the same route is used for sputter deposition of PZT, the best situation is to proceed to PZT growth directly after the MgO evaporation without breaking the vacuum in between. This is unfortunately not possible for sol-gel processing which takes place in air. In this case therefore, it is recommended that the sol-gel equipment be situated in the same room as, or as near as possible to, the evaporator and that the ambient humidity in this room be made extremely low. This is also beneficial if the precursor solutions were prepared with the 2-methoxyethanol route, since such solutions are sensitive to moisture as well.



Figure 4.1 – Schematic of the fabrication steps.

Immediately after MgO evaporation, a 20 nm-thick PTO seed layer is deposited by sol-gel and crystallized in the RTA tool as described above. We found that this PTO layer is stable for at least several weeks, with the PZT layer deposited on top at a later time reproducing its texture as expected. Finally, the PZT layers were deposited. Two RTA steps were performed to obtain a film thickness of around 550 nm (that is a total of 8 spinning steps).

The interdigitated top electrodes were patterned by photolithography and lift-off to avoid any damage to the PZT surface, which can lead to surface conduction or electrical breakdown upon biasing. Sputtered Pt was used as the electrode material. Although evaporation is the PVD technique of choice for lift-off processing, evaporated Pt does not adhere well on our sol-gel PZT surfaces [51], whereas sputtered Pt provided good adhesion and was therefore preferred. A number of IDE structures with various gap distances and finger widths were patterned on the PZT film and then diced to obtain elongated cantilevers 15 mm long and 1.5 mm wide. The active area corresponds to the interdigitation zone and occupies only a fraction of the total cantilever surface, namely a few mm in length and 1 mm in width. The fabrications steps are summarized in Figure 4.1. Figure 4.2 shows an optical microscope view of a finished cantilever.

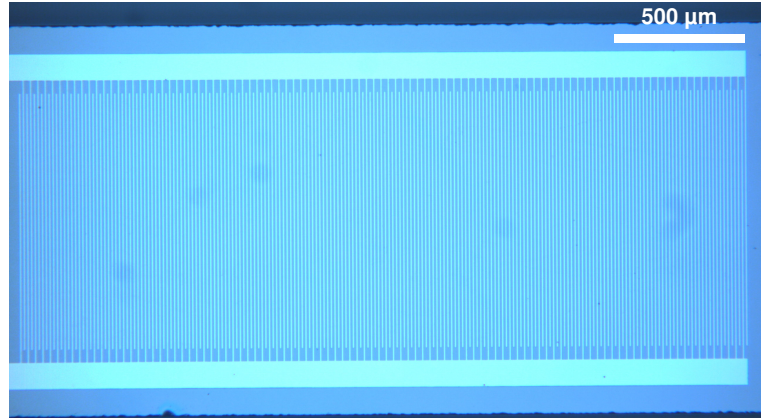


Figure 4.2 – Optical microscope image of the interdigitation zone after dicing.

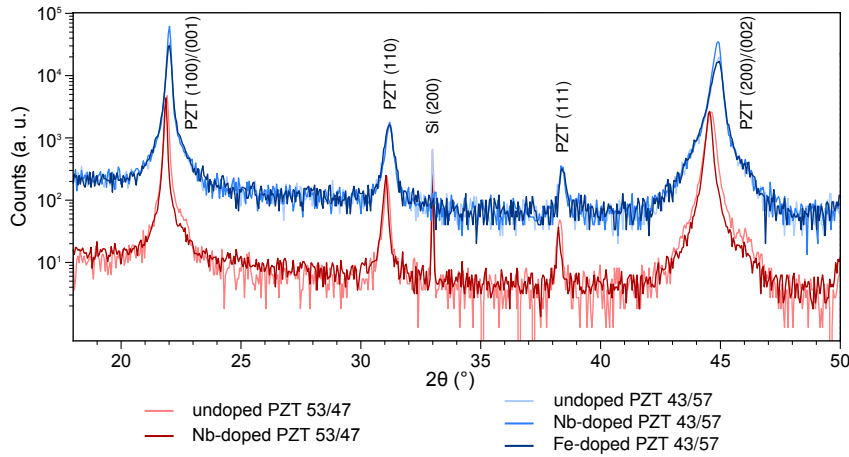


Figure 4.3 – XRD scans of the investigated IDE films. The Si (200) peak is present because of the film stress after sol-gel processing.

4.3 Film microstructure

Figure 4.3 shows the XRD scans of the fabricated films. The Si {200} peak at 33° is visible due to non-zero stress present in the PZT films after sol-gel processing. All the layers are fully in the perovskite phase. We note the slight shift of the PZT peaks to lower 2θ angles for the films with the 53/47 composition. The scans overlap very well for a given composition, showing good reproducibility of the deposition process. All films have more than 90 % of the crystallites with the {100} direction out-of-plane. The computed textures for each film were obtained from XRD peak integration (neglecting orientations other than those shown in Figure 4.3) normalized to the intensity of the corresponding orientation and are shown in table 4.1. The intensity for each direction was obtained from published powder diffraction data [95], taking the powder diffraction intensity for the {100}/{001} peak as the sum of the intensities of each separate peak as found in the cited reference.

Table 4.1 – Volume fraction of crystallites for each out-of-plane orientation.

Orientation	PZT 53/47	Nb:PZT 53/47	PZT 43/57	Nb:PZT 43/57	Fe:PZT 43/57
{100}/{001}	93 %	93 %	93 %	95 %	93 %
{110}	5 %	6 %	6 %	4 %	6 %
{111}	2 %	1 %	1 %	1 %	1 %

Scanning electron microscope (SEM) images shown in Figure 4.4 (a) to (e) reveal similar surface features and grain sizes for all films — the scale is the same in Figure 4.4 (a) to (e). The undoped and Fe-doped PZT 43/57 films display a significant surface porosity in the form of pores present at the junctions of several grain boundaries, and sometimes within grains as well, whereas they are much less frequent for the other films. Atomic force microscopy (AFM) scans reveal an otherwise very smooth surface, with a roughness root mean square typically comprised between 2 and 3.5 nm. The cross-section view in Figure 4.4 (f) shows a dense film with columnar grains, as expected for this processing route. The cross-section SEM images were similar for all films.

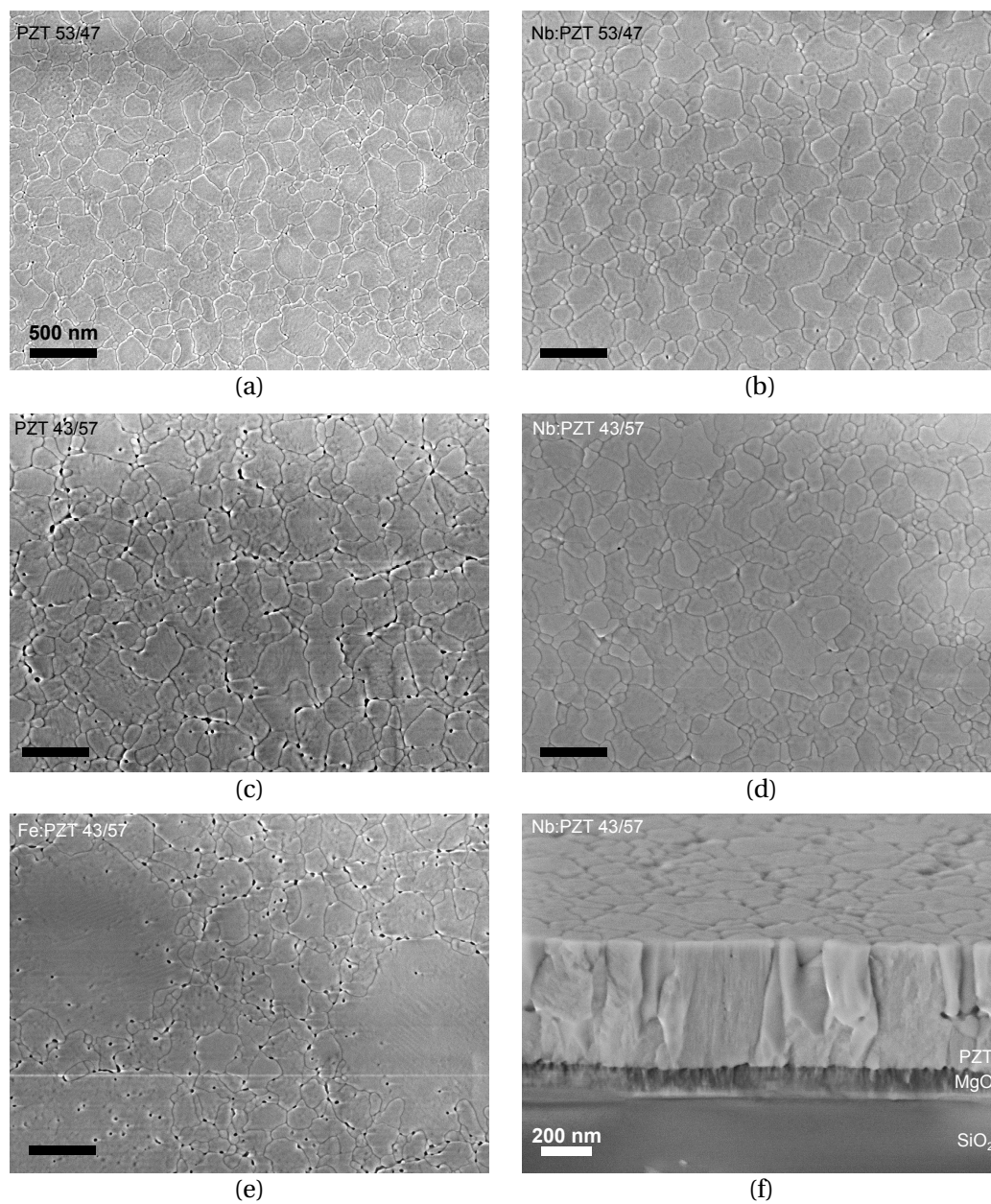


Figure 4.4 – SEM images of the surface of the films under study ((a) to (e)) and SEM image of one of the film cross-section in (f). The scale bar is the same from (a) to (e). Some domains can be distinguished in the big grains in (e).

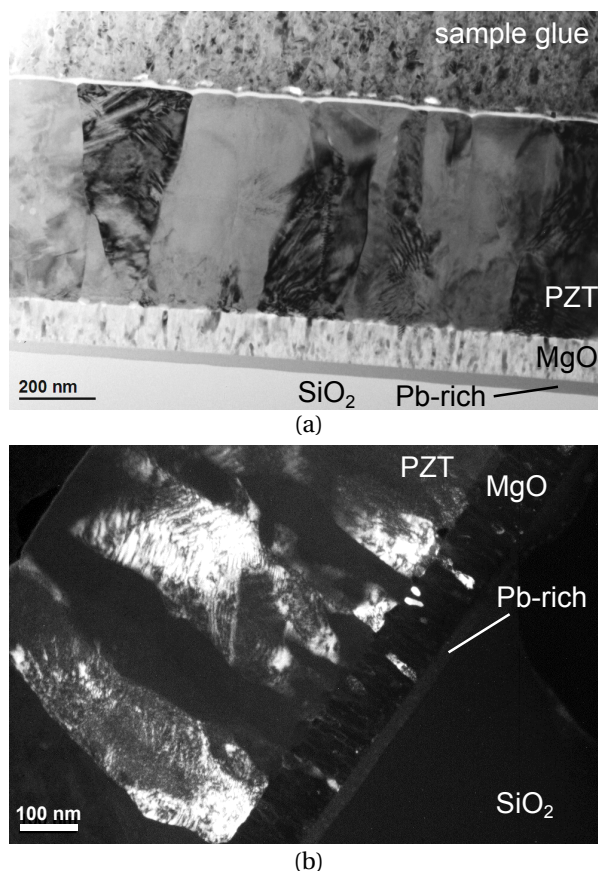


Figure 4.5 – Typical bright field (a) and dark field (b) TEM image of the films under study. Some needle-shaped domains making a 45° angle with the film surface can be seen in the top half of the darker grain on the left of the bright field image.

Some of the films were also characterized with transmission electron microscopy (TEM). All the images obtained by TEM were recorded by Dr. Cosmin Sandu. Figures 4.5 (a) and (b) show typical bright field and dark field images of the films, respectively. Here again we notice the dense, columnar PZT growth. We also observe that the MgO layer is composed of crystallites much smaller than the PZT grains, which appear not to always extend across the whole thickness of the film. Between the MgO and SiO₂ layers is an amorphous Pb-rich region, as revealed by energy dispersive X-ray spectroscopy (EDX) mapping of the thinned sample in Figure 4.6. The Ti K- α radiation intensity curve shows a small slope within the MgO layer, below the PTO layer situated at about 0.17 μm from the origin of lengths, in Figure 4.6 (d), reaching about zero at the bottom of the MgO film. On the contrary, the Pb K- α radiation intensity is constant within the MgO layer. This suggests that, at the crystallization anneal temperature of 650 °C, the steady state for diffusion was reached for Pb: Two Pb flows of equal strength, but opposite direction, result in an equilibrium, constant Pb atomic concentration within the MgO layer. On the contrary, since the Ti signal varies in intensity within the MgO layer, there is presumably a net flow of Ti atoms towards the SiO₂ layer, whose rate is limited

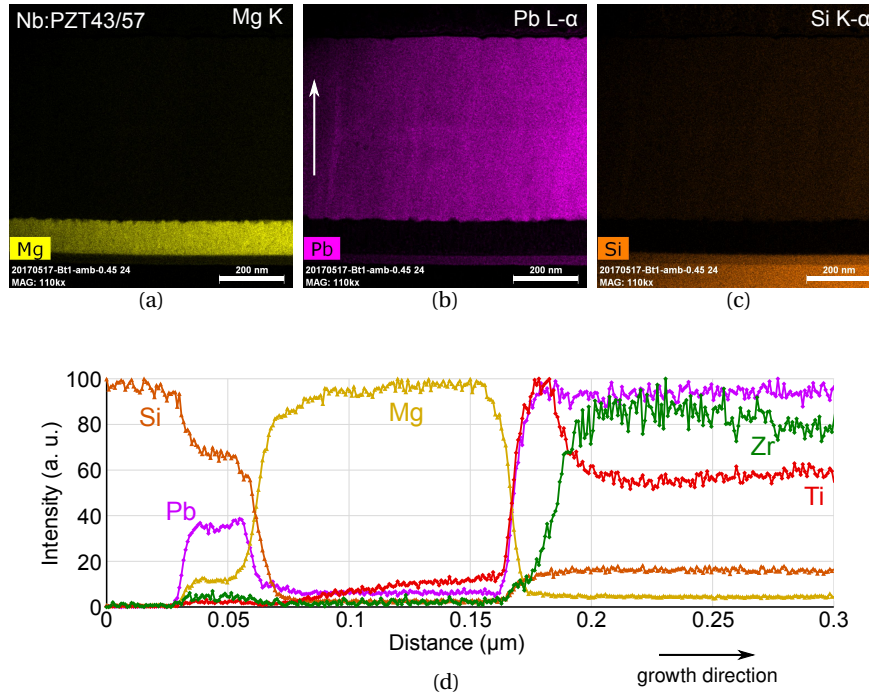


Figure 4.6 – EDX maps for Mg (a), Pb (b) and Si (c) for the Nb-doped PZT43/57 film. An arrow indicates the PZT growth direction in (b) and (d). (d) shows the integrated X-ray peak intensity *vs.* the distance along the growth direction starting from a point near the bottom of the image. The Si signal within the PZT layer is an artefact due to the proximity of the Si K- α peak with one low-energy Pb peak. The K- α line was used for Ti and Zr.

by the processing temperature, so that equilibrium cannot be reached within the anneal time of 2 times 1 min (two RTA steps were performed for crystallization). This shows that the MgO layer is actually not suitable as a diffusion barrier for Pb. The Zr and Si signals are both nearly 0 within the MgO layer, showing that they are efficiently prevented from diffusing. The Si signal within the PZT layer is an artefact due to the proximity of the Si K- α peak with one low-energy Pb peak.

Selected area electron diffraction (SAED) was performed in a selected zone containing a portion of both the PZT and the MgO layer. The resulting diffraction pattern is shown in Figure 4.7. It is similar to the one described in Ref. [35]. We observe a well defined growth direction for PZT which corresponds to the {100} set of planes — two directions with a small tilt are actually observed. The many small MgO crystallites are randomly oriented and yield a powder-like diffraction pattern, with many small dots arranged on concentric rings corresponding to the sequence of the crystal planes with the rocksalt structure [96]. This suggests that the {100}/{001} PZT texture is not promoted by a particular set of planes of the MgO structure, and in particular is not due to a favorable epitaxial arrangement of the TiO₂ planes or the PbO planes on the MgO top surface. The final texture of the PZT film reproduces the texture of the PTO seed layer: {100}-textured (resp. random) PTO yields {100}-textured (resp. random)

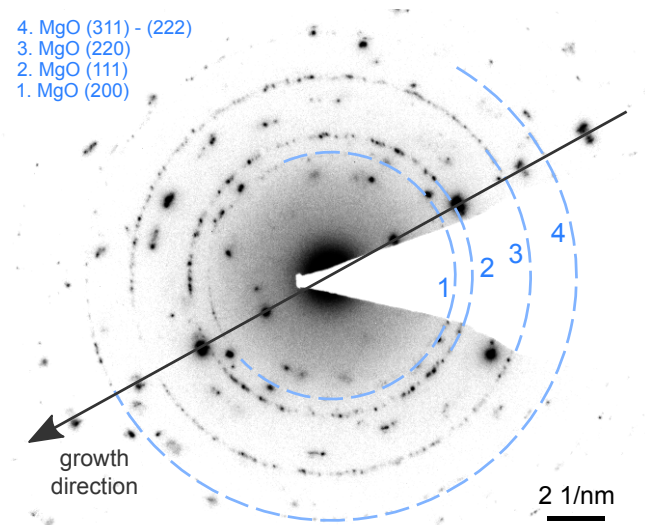


Figure 4.7 – SAED of a zone containing both PZT and MgO grains. The growth direction is indicated with an arrow. The blue dashed lines are guide to the eye to spot the ring-like diffraction pattern of MgO. Each ring is numbered and the corresponding set of planes is indicated in the top left corner.

PZT films. Therefore, to understand this behavior, one has to understand the reason for {100}-textured PTO growth on a random MgO underlayer. The SAED was taken at the bottom of the film, where EDX maps show that the PTO seed layer is only partly incorporated into the final PZT film; as a consequence, the diffraction pattern should correspond to nearly pure PTO. We see in Figure 4.7 that the (111) inter-plane distance of MgO corresponds to two times the (100) inter-plane distance in PTO. It is not clear whether this fact can promote any texture. In particular, moisture contamination should not influence the orientation of MgO crystallites, and yet it results in random growth. A more likely explanation is that the as-deposited MgO surface is very smooth and inert, and this promotes the growth of the lowest energy surface, which is {100} for PTO in lead-rich conditions [97] (the PTO precursor solution is prepared with 30 at.% Pb excess). Reaction of the MgO surface with moisture could slowly introduce some roughness, after which no particular orientation is favored, resulting in random growth.

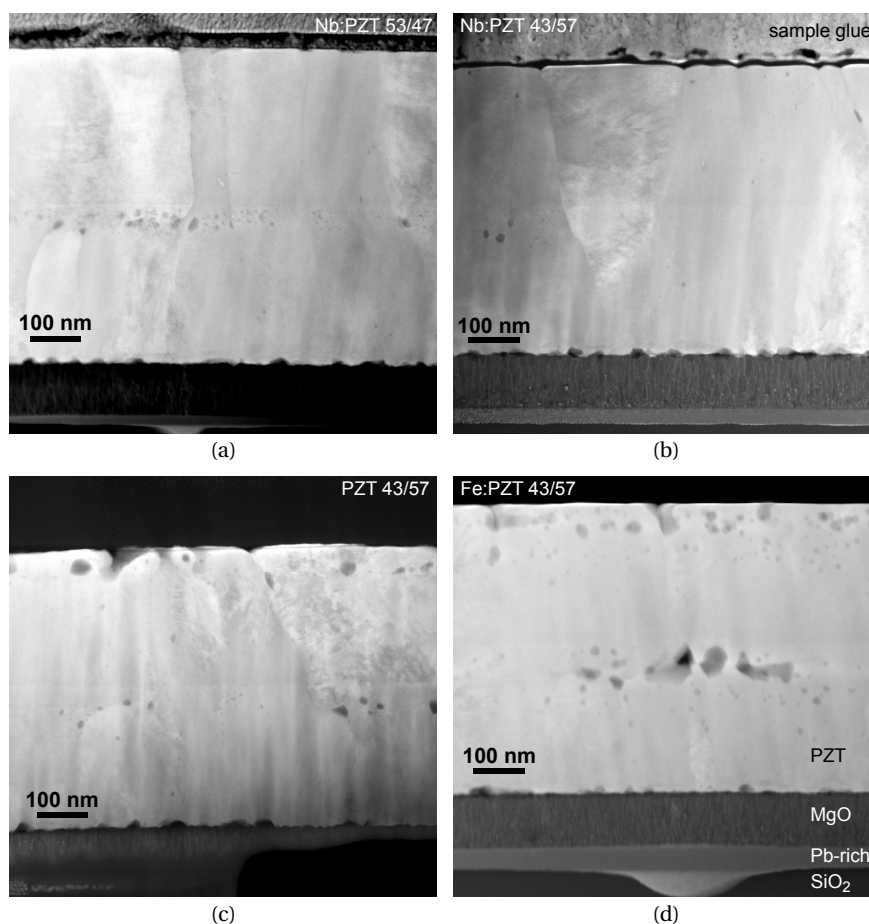


Figure 4.8 – HAADF images of the various films under study. (c) was taken close to the thin side and the MgO and SiO₂ layers end at the middle of the image.

High angle annular dark field (HAADF) images were also recorded and are shown in Figure 4.8. HAADF provides an atomic number contrast; heavier elements appear brighter. This feature is very helpful to evaluate the density of the layer, in addition to the chemical contrast. The Pb-rich layer between MgO and SiO₂ is well visible in Figure 4.8 as brighter than the layers on either side, which is consistent with the fact that Pb is by far the heaviest element in the picture. Similarly, brighter veins are visible within the MgO layer in all images, which could mark the diffusion channels for Pb interdiffusion during the crystallization anneal. The white dots visible in the Pb-rich region in (b) are the result of local crystallization caused by the prolonged exposure to the focused electron beam of the scanning TEM (STEM) imaging mode.

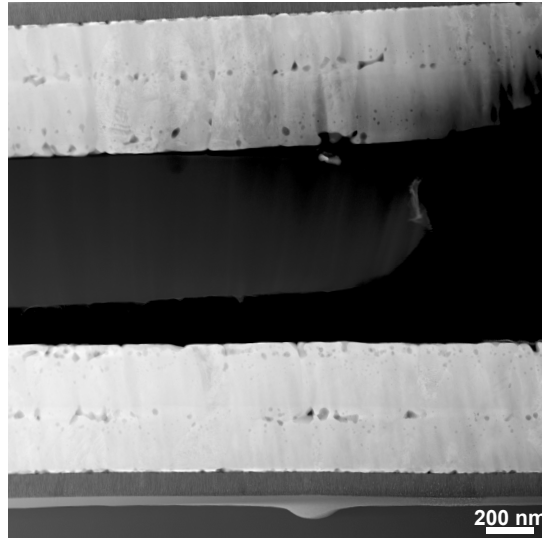


Figure 4.9 – Low magnification view of the thinned sample of the Fe-doped PZT 43/57 film. The two TEM thin samples are visible on the same image. The close-up view of Figure 4.8 (d) is in the middle of the bottom sample.

All layers show good density except at the surface or at the interface marking the junction between the two RTA steps. Some porosity is present there, and its extent seems to scale according to the porosity observed at the surface of the films : It is particularly pronounced for the Fe-doped PZT 43/57 film (Figure 4.8 (d) and Figure 4.9) and almost absent in the Nb-doped PZT 43/57 film (Figure 4.8 (b)). This suggests that the surface porosity of the films, whatever its cause, is present at the surface of each crystallized layer and cannot be completely canceled by recrystallization during the second crystallization anneal.

The sol-gel gradient-free route should compensate for the faster incorporation of Ti ions in the crystallizing layer. Figure 4.10 shows the EDX map for Pb, Ti and Zr for two different films. They illustrate the two kinds of typical behavior we observed in all the films. The first kind is shown in Figure 4.10 (a) to (c) for the Nb-doped PZT 53/47 film. For this sample we observe a nearly constant Zr/Ti ratio, as verified by the value of the intensity ratio shown in Figure 4.10 (c) which should be proportional to the ratio of the spatial concentration of the two elements. In this case the graded compositions of the precursor solutions used for spin-coating allowed for a virtual suppression of the composition gradient within the PZT layer. The second kind is shown in Figure 4.10 (d) to (f). In this case the natural gradient is overcompensated and the bottom of each RTA layer is slightly Zr-richer than the top. The reason for the presence of two behaviors is not known. The precursor solutions are prepared with a careful control of their stoichiometry. It is possible that the nominal composition (53/47 or 43/57) plays a role and that the general formula given by Calame and Muralt [47] should be adapted depending on the targeted composition. The spin-coating process itself could also be a source of deviation: Since the precursor solutions are dispensed by hand on the wafer, it is not possible to deposit exactly the same volume of solution with a similar surface coverage at each spinning step. However, the similarity between the two RTA layers for both films suggests good reproducibility nonetheless; the high spinning rate of 3000 r.p.m. for 40 s possibly cancels to a large extent the influence of the variations in volume and coverage introduced before spinning.

For all films, we observe a peak in Zr concentration followed by a peak in Ti concentration (counting distance along the growth direction) at the interface between the two RTA steps. This is surprising given the fact that the bottom of the gel is Ti-poor in the gradient-free route. The cations should not be mobile in the perovskite lattice at the crystallization temperature of 650 °C. However, the formation of a Pb-rich layer within the SiO₂ underlayer shows that some interdiffusion does happen. Since the top of the crystallized film should be significantly Ti-richer than the bottom of the amorphous gel with which it is in physical contact, it is possible that over a very short distance, at the onset of nucleation, some recrystallization takes place, and that Ti cations are preferentially incorporated. In this scenario, both diffusion and easier Ti-incorporation would contribute to the effect. The crystallization process then continues as usual, and in the remaining volume, the counter-gradient introduced in the gel compensates well for the faster Ti-incorporation in the perovskite lattice, as expected. This would locally make the top of the first RTA layer Ti-poor, and the bottom of the second RTA layer Ti rich, as compared to the surrounding volume — which is what we observe. The same effect was observed in an undoped 1 μm-thick PZT film with the 43/57 nominal composition, at the junction between each RTA layers (4 RTA steps were performed in total). This scenario is supported by the observation that the PTO seed layer is, in a similar way, partially incorporated into the rest of the film, as revealed by the sharp, and overlapping, Zr and Ti intensity gradients at the bottom of the film in Fig. 4.10 (c) and (f).

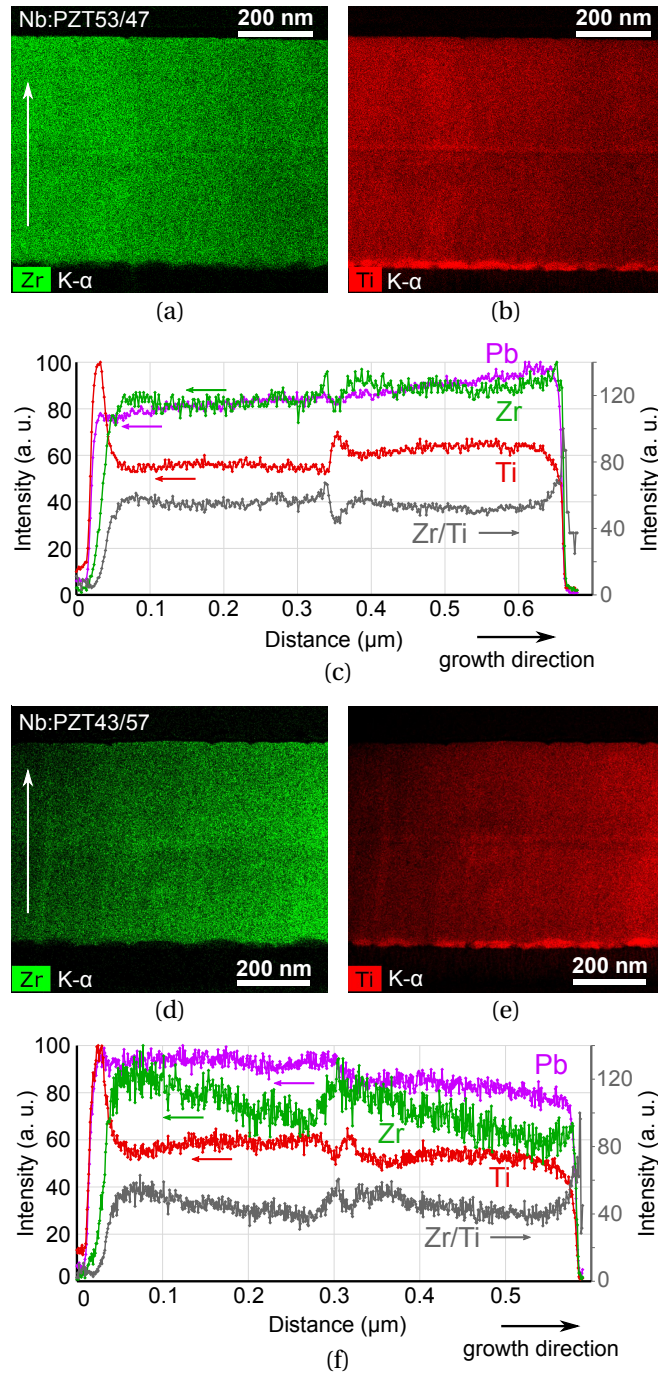


Figure 4.10 – (a), (b), (d) and (e) show the EDX map for Pb, Ti and Zr for two of the films under study. (c) and (f) show the radiation intensity normalized to 100 for each element as well as their ratio, which should be proportional to the ratio of the atomic concentration. An arrow indicates the growth direction in (a), (c), (d) and (f). For both (c) and (f), the origin of length is chosen slightly below the PTO seed layer. The L- α line was used for Pb.

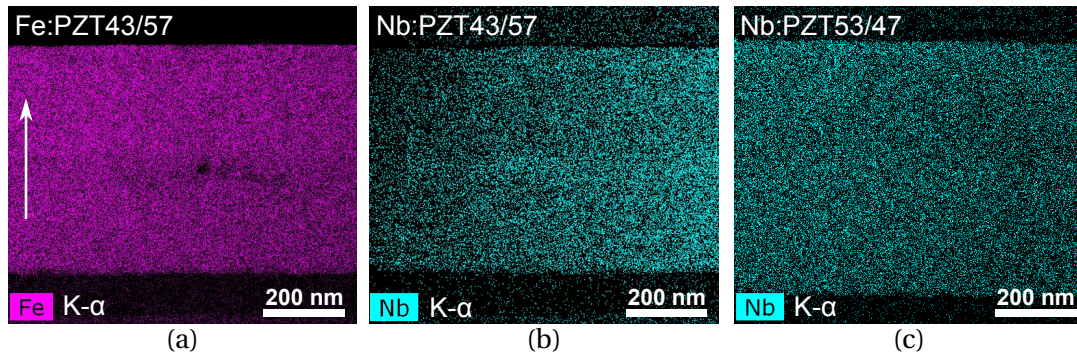


Figure 4.11 – EDX maps for Fe in (a) and Nb in (b) and (c) for the doped films under study. An arrow indicates the growth direction.

Figure 4.11 (a) to (c) shows the EDX map for the dopants for the doped films. The Nb K- α signal is weak, resulting in a noisy map. The dopant concentration seems well homogeneous throughout the film for both Nb and Fe. A slightly higher intensity near the top of each RTA layer in the Nb signal could possibly indicate a concentration gradient for this dopant; however the low signal-to-noise ratio makes this observation ambiguous. A basic quantitative analysis of the EDX spectrum of the full layer showed that the actual dopant concentration was close to the nominal concentration, *i. e.* 1 at.% for Fe and 2 at.% for Nb; a more accurate quantitative analysis was not attempted.

4.4 Electrical and piezoelectric response characterization

We have performed systematic large and small signal characterization for the 5 films under study. Four samples with different gap distances were measured for each film, for 3 annealing treatments: as-fabricated, after annealing at 550 °C and after annealing at 650 °C. The annealing steps were done in an RTA tool where the temperature was maintained for 10 min under 100 sccm O₂ flow. The samples were measured in a sequence, and otherwise have a similar prehistory. The recorded curves are usually an average of a number of subsequent measurements. A pre-polarization wave was always applied before any large-signal measurement; it is identical to the triangle wave used for recording the measurement. A waiting time of 1 s was observed between the end of the pre-polarization wave and the measurement wave, as is customary. This allows to compare the retention performance of our films between one another and with measurements found in the literature. The aixACCT® TF2000 setup was used for all the measurements. The large signal measurements (PV loop) were recorded at 20 Hz, and the small-signal measurements (CV and piezoelectric coefficient *vs.* field loop) were recorded with a triangle wave at a frequency of 100 mHz for the large signal, and a sine wave at 1 kHz and amplitude of 5 kV/cm for the small signal. For all measurements of PZT thin films with IDE, the Igreja formula for the electric field was used, and the Igreja formula with the conformal mapping model for the parasitic capacitance of the fingers was employed to obtain the dielectric constant from the capacitance measurement. The large-signal piezoelectric coefficient e ($e_{33, \text{if}}$ for IDE samples and $e_{31, \text{f}}$ for PPE samples) was obtained as $e = \partial \sigma_f / \partial E_3$ as discussed in chapter 2. The stress was obtained using equation 2.9 from chapter 2. Since we have a large number of gaps (199 or 99), it is equivalent to use either g_1 or g_2 in this case (see appendix B). We did not use $a + \Delta a$ as the active zone length, even though we found in chapter 3 that it provides a better overlap between the $e_{33, \text{if}}$ loops for various gap distances. The reason is that the arguments supporting the latter method should be confirmed by proper FE modeling before this method is brought into use; such modeling work has not been performed yet.

Characterization in the IDE configuration requires the knowledge of the actual electrode geometry. Since the final electrode dimensions differ in general from the photolithography mask design, and since these differences vary across the wafer, it is necessary to measure the actual finger distance and finger width for each sample with an optical microscope prior to characterization. A Matlab code was developed by Trygve M. Ræder as part of his master's thesis work [98] to extract the finger distance and finger width from the optical microscope images in an automatic fashion; the obtained dimensions were then averaged over a number of adjacent IDE cells. A typical result from this code is shown in Fig. 4.12. Such an automatic procedure allows for controlled and reproducible precision for the measurement of the IDE dimensions.

The thickness of the films was taken as the average between the thickness measured on the bright field TEM images and the HAADF STEM images, which usually differed by several percent. The film thicknesses were also measured with SEM on cleaved samples, and were

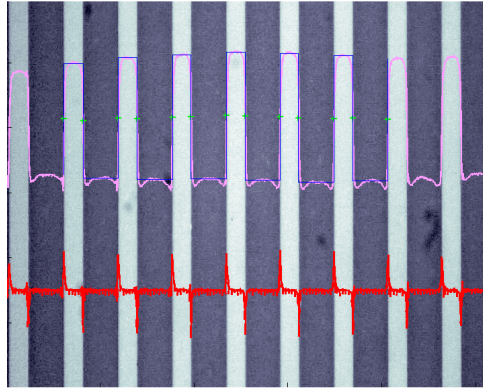


Figure 4.12 – Result image from the image processing routine. The red channel of the original RGB optical microscope image is used as it offers better contrast. The pink curve is the average of each pixel column. The red curve is the derivative of the pink curve. The peaks of the derivative correspond to the edges of the electrode fingers, whose extension as computed by the routine is shown as the blue curve. Knowing the scale of the image, this curve is used to return the finger width and gap distance.

used when TEM imaging was not performed. The SEM thicknesses were found to be systematic underestimates of the TEM thicknesses (when available), sometimes up to 10 % lower. This could be due to the varying orientation of the cross-section profile. Although it is certainly never facing the microscope column orthogonally, the deviation is difficult to judge from the angle under which the cross-section is imaged in the SEM, and can be mistakenly considered as negligible while it is actually significant. Another possible cause is the sample charging by the scanning electron beam, which can stretch or shrink the apparent thickness of the film depending on the charge distribution building up on the sample cross-section — since all the layers in the vicinity of the zone of interest (PZT, MgO, SiO₂) are insulators. This can lead to a 10 % overestimate of the piezoresponse, because the $e_{33,if}$ coefficient is inversely proportional to the film thickness. In the PPE configuration where $e_{31,f}$ is independent of the film thickness, this is not a source of error.

4.4.1 Effect of annealing

Figure 4.13 shows the typical change of behavior of the PZT film with IDE after each annealing step. The main features are :

1. The switchable polarization increases.
2. The coercive field increases.
3. The PV loop becomes more square.
4. The dielectric constant decreases.
5. The piezoelectric response increases, particularly at low fields.

These features are more or less pronounced depending on the composition and the doping

4.4. Electrical and piezoelectric response characterization

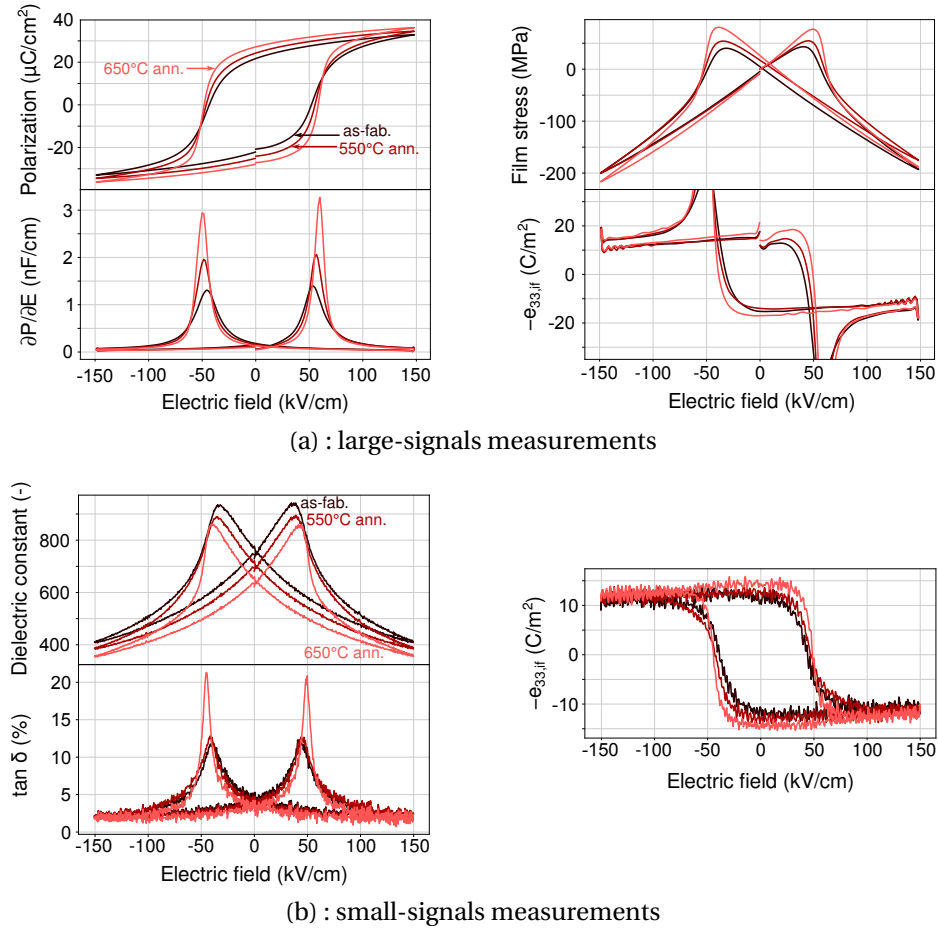


Figure 4.13 – Evolution of the electric and piezoelectric response upon various annealing treatments for the undoped PZT 43/57 film with IDE. (a) : large-signals measurements. (b) : small-signals measurements.

conditions. An important consequence for energy harvesting (and more generally for small-field operations) is the significant improvement in retention and remanent polarization after each annealing step for all investigated films; both are a consequence of the higher coercive field and the reduction of the PV loop slanting. The evolution the piezoelectric response at high fields for the undoped films and for the Fe-doped PZT 43/57 sample is not significantly affected by annealing; however, there is a significant increase of its remanent value, as a consequence of the improved polarization remanence and retention. For both Nb-doped films only, we found a significant increase of the piezoelectric response at all fields after annealing at 650 °C. Figure 4.13 also shows that the losses slightly decrease after each annealing step (away from the coercive field); this effect was also observed for all compositions and dopants tested, and is also beneficial for energy harvesting.

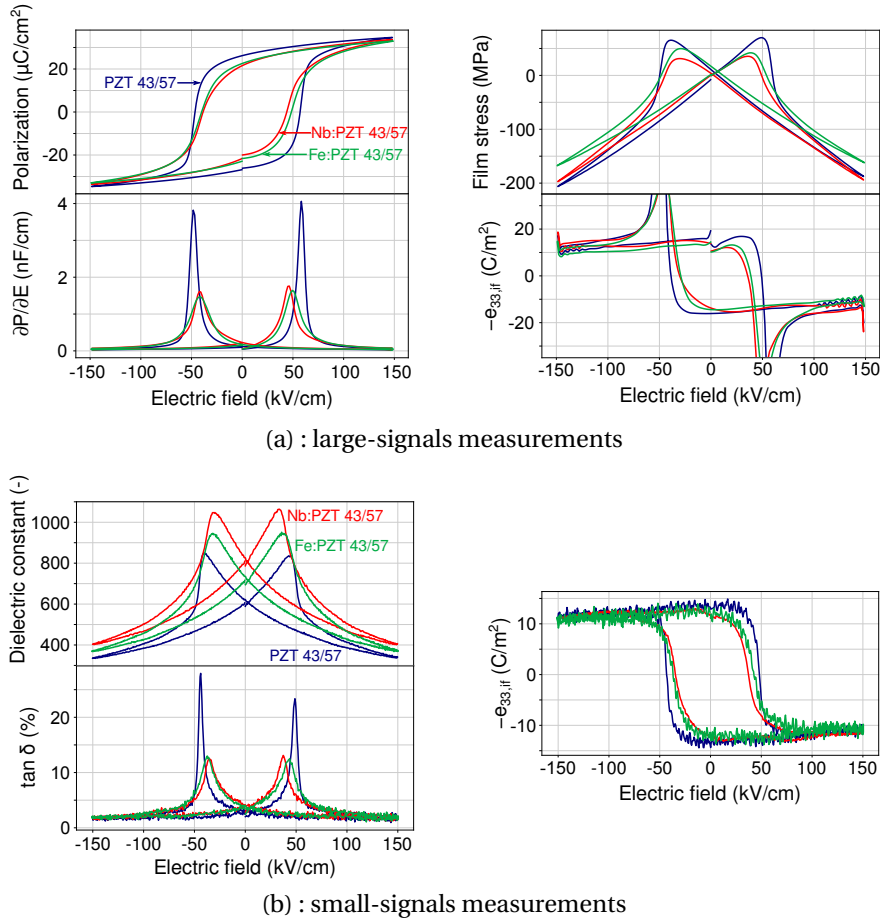


Figure 4.14 – Electric and piezoelectric response for PZT 43/57 films with IDE for three doping conditions, after annealing at 650 °C. (a) : large-signals measurements. (b) : small-signals measurements.

4.4.2 Effect of doping for the tetragonal composition

Figure 4.14 shows a comparison of the loops for all the tetragonal films after annealing at 650 °C. The PV loop of the undoped tetragonal film is impressively square and displays a higher coercive field, a larger switchable polarization and a larger piezoelectric response than either of the doped films. As expected, the Nb-doped film shows a more slanted PV loop, a reduced coercive field, and a higher dielectric constant. Its piezoelectric response at high fields is comparable to the undoped case, but is lower at low fields, due to reduced retention. The Fe-doped film, unexpectedly, shows features close to the Nb-doped film, albeit in a more moderate way. It has a higher coercive field, a lower dielectric constant, and less slanting of the PV loop than the Nb-doped film; but those features are still closer to the Nb-doped film response than to the undoped film response. In particular, its dielectric constant is significantly larger than that of the undoped film. This is surprising given the fact that Fe-doping is expected to make the PZT film harder, *i. e.* with a higher coercive field, a lower

dielectric constant, and less losses. However, we observe the opposite.

One cause for the behavior of the Fe-doped film could be the presence of a passive layer near the electrode fingers. Even though the film-electrode interface plays a minor role in the response of PZT thin film with IDE (see chapter 6), the change of properties upon annealing suggests that this influence, however reduced, may be present nonetheless. The significant porosity observed at the top surface of the Fe-doped film, as a zone of lower effective dielectric constant, could contribute to such an effect. Indeed, passive layers at the film-electrode interface are well-known for causing a slanting of the PV loop in PPE devices [99]. This is because, in this case, the voltage drop across the ferroelectric layer depends on the current net polarization of that layer. However, this does not explain the larger dielectric constant of the Fe-doped film. If anything, the porosity, reducing the film density, should also reduce the dielectric constant.

Comparison with Fe-doped ceramics is not straightforward, since the firing temperatures are well above 1000 °C [11], much higher than the film crystallization temperature of 650 °C. In addition, our films are crystallized in a RTA tool, and not in a furnace. These differing conditions have two important consequences: first, the cations (including dopants) are mobile in the amorphous phase only, and their position is frozen in after their incorporation into the perovskite lattice; second, since the cool-down time from the crystallization temperature of 650 °C is of the order of a few minutes, our films can always be considered as quenched from the crystallization temperature, freezing in the movement of oxygen vacancies as well. Using the Kröger-Vink notation for defects, this means that the position of the $V_O^{\bullet\bullet}$ may not be adjusted to that of Fe_{Ti}' , which unlike in ceramics, may exist as a lone defect. The concentration of lone Fe_{Ti}' defects is reported to be below the detection level of modern electron paramagnetic resonance (EPR) techniques [100, 101]. However, Meštrić and coworkers [100] were working with a powder PTO sample, *i. e.* after calcination. The calcination temperature is not reported, but it may either have been large enough to allow cation movement in the perovskite phase, or have been maintained for a sufficiently long time to exhaust the concentration of Fe_{Ti}' by the formation of $(Fe_{Ti}' - V_O^{\bullet\bullet})^{\bullet}$ associates. Eichel [101] does not specify to what type of samples his statement applies, but all the examples reported in his publication come from ceramic samples, either after calcination or after sintering. Warren *et al.* [102] do not report the presence or absence of isolated Fe_{Ti}' centers, but they do report on the presence of other lone centers such as Ti^{3+} and Cu^{2+} , again in PZT ceramics. They do report their presence, however, in BTO single crystals [103] and BTO ceramics [104]. It is not immediately clear whether these latter reports support the presence of lone Fe_{Ti}' centers also in PZT. Jakes *et al.* [105] also report on a PZT ceramic sample, and on PZT powder obtained by milling of this ceramic. To our knowledge, no recent EPR study of as-fabricated sol-gel PZT thin film is available, and such a study may not be possible due to the very small volume of material involved. There is, therefore, no clear experimental evidence in favor or against the existence of lone Fe_{Ti}' centers in such samples. However, prior to the measurement shown in Fig. 4.14, all samples have been annealed at 650 °C for 10 min. At this temperature, $V_O^{\bullet\bullet}$ are mobile, and the anneal time may be sufficiently long for all Fe_{Ti}' and $V_O^{\bullet\bullet}$ to associate.

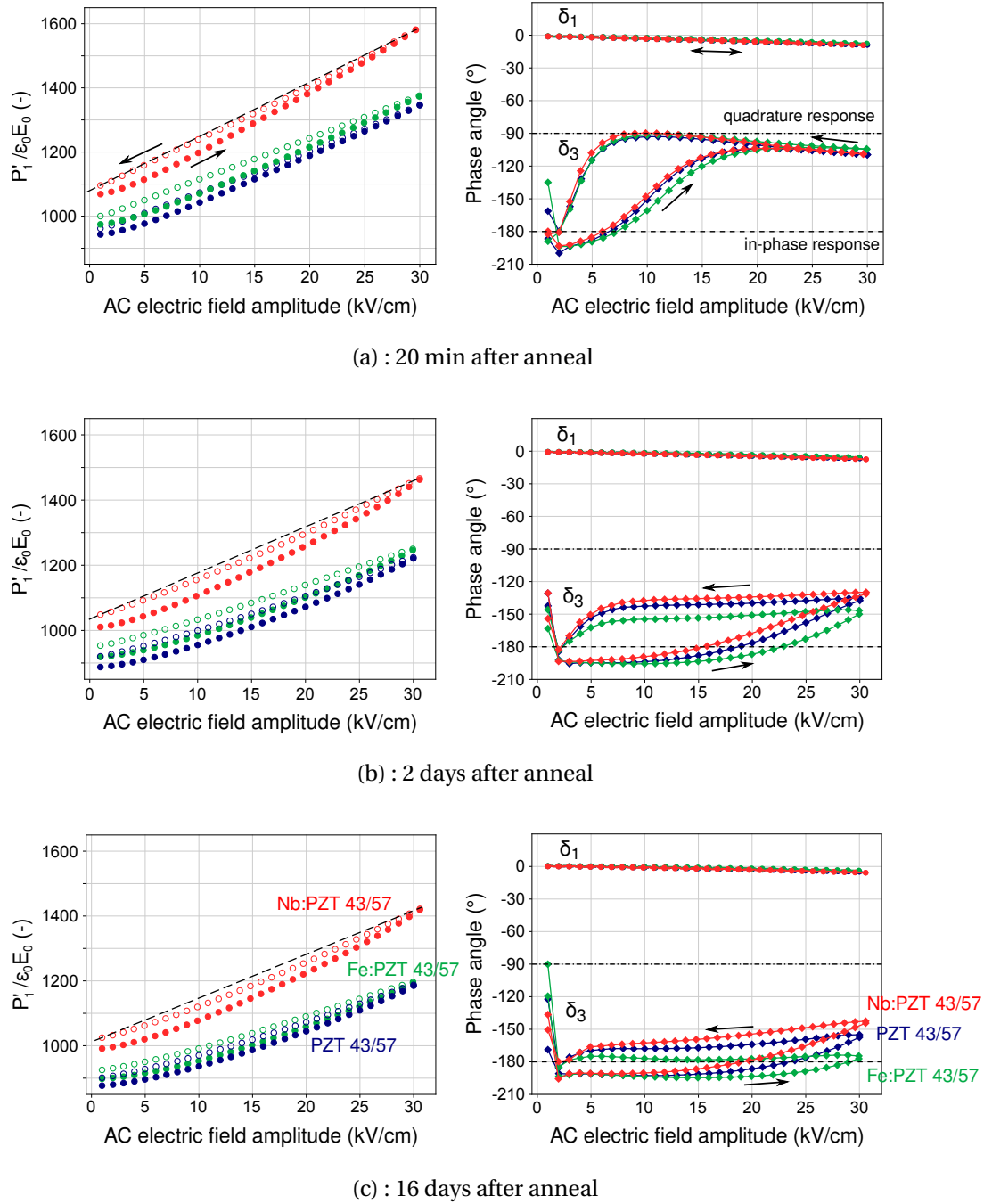


Figure 4.15 – $P'_1/\epsilon_0 E_0$, δ_1 and δ_3 for increasing, then decreasing field amplitude, for undoped and doped PZT 43/57 films, 20 min (a), 2 days (b) and 16 days (c) after the initial annealing step. Arrows indicate the direction of the curves. For the $P'_1/\epsilon_0 E_0$ charts, filled circles indicate the increasing branch and open circles the decreasing branch. The dashed line in the $P'_1/\epsilon_0 E_0$ charts is a guide to the eyes. The color code is shown in (c).

In any case, the existing $(\text{Fe}'_{\text{Ti}} - \text{V}''_{\text{O}})^{\bullet}$ are certainly not aligned with the local polarization, because of the quenching after the end of the annealing time; the alignment of dipolar defect associates would stabilize the domain pattern by a volume effect (see chapter 5 for details). The quenching may explain why the Fe-doped film exhibits properties similar to that of a soft ferroelectric material. The same effect was observed by Morozov and coworkers in a recent publication [106], with a rhombohedral and a tetragonal PZT ceramic doped with 1 at.% of either Fe or Nb. Some Fe-doped samples were quenched to room temperature after a heat treatment at 450 °C, and showed properties qualitatively similar to that of the Nb-doped samples. Unfortunately, the undoped composition was not tested; and this does not explain why the Fe-doped sample has a dielectric constant larger than that of the undoped sample. Note that, since the small-signal frequency used for the measurements shown in Figure 4.14 is 1 kHz, we expect that the dielectric response is dominated by domain wall motion at the exclusion of space-charge contributions, as discussed by Morozov and Damjanovic for rhombohedral ceramics [107].

To investigate further, we have studied the evolution with time of the first 3 harmonics of the polarization response for each of the tetragonal films. The samples were annealed to 550 °C for 10 min under 100 sccm of O₂ flow prior to the measurement. The technique employed is described in chapter 5. We refer the reader to section 5.2.3 of that chapter for the definitions of the regimes we will mention; we will nonetheless provide short definitions here for convenience. We used sub-switching field amplitudes, meaning that the domain pattern should remain unchanged on average over the course of the measurement, and that all sources of non-linearity are attributable to the domain wall contributions. We have performed the same measurement 3 times: the first time, 20 min after the end of the annealing step (Fig. 4.15 (a)); the second time, 2 days after the end of the annealing step (Fig. 4.15 (b)); and the last time, 16 days after the end of the annealing step (Fig. 4.15 (c)). Note that, at the end of each measurement, the samples were totally or partially de-aged; but since all the samples have the same history, it is relevant to compare them. In Fig. 4.15, we show 3 quantities: the real part of a so-called “large-signal permittivity”, meaning the real part of the polarization amplitude of the 1st harmonic, P'_1 , divided by $\epsilon_0 E_0$, where E_0 is the field amplitude; the phase angle δ_1 of the 1st harmonic response; and the phase angle δ_3 of the 3rd harmonic response. The fully unclamped case, where domain walls are moving irreversibly in a random energy landscape, will give a $P'_1/\epsilon_0 E_0$ increasing linearly with E_0 and $\delta_3 = -90^\circ$ (quadrature response); deeply clamped domain walls will give a constant $P'_1/\epsilon_0 E_0$ and $\delta_3 = -180^\circ$ (in-phase response). Intermediate situations correspond to intermediate clamping strengths. The domain walls will become slowly unclamped under the action of the cycling electric field, whose amplitude is first increased and then decreased; the extent to which the response approaches the unclamped case during the measurement is an indication of how much clamped the domain walls were at the start of the measurement [108]. We have not corrected P'_1 for the parasitic capacitance, which behaves purely linearly and therefore, does not contribute to δ_3 . The three samples that we measured have a similar geometry, and as such, the parasitic capacitance should just add about the same constant to P'_1 for all of them; its contribution to δ_1 should be

small, and again, be the same for all samples.

20 min after annealing, all the samples exhibit about the same clamping situation, as seen in Fig. 4.15 (a) : δ_3 starts to deviate from the in-phase response at about the same field amplitude for all samples, and then remains near -90° for decreasing electric field, while at the same time $P'_1/\epsilon_0 E_0$ is a straight line, meaning that the samples have reached the fully unclamped regime at the end of the measurement. This is not achieved 2 days after annealing, as seen in Fig. 4.15 (b); now all samples remain with $\delta_3 = -180^\circ$ until a larger field is reached, and δ_3 does not reach -90° on the return branch; $P'_1/\epsilon_0 E_0$ is not a straight line anymore, and δ_1 has decreased. The same observations are made 16 days after annealing (Fig. 4.15 (c)), except that the domain wall clamping has become stronger, and therefore, the differences with Fig. 4.15 (a) are even more pronounced. This reveals the progress of aging, *i. e.* the progressive reduction of the extrinsic response, with time.

The comparison between the time evolution of the sample responses gives some insight into the behavior of the Fe-doped sample. Also on these charts, the permittivity of the Fe-doped sample is larger than that of the undoped sample, and both are much smaller than that of the Nb-doped sample. However, the progress of aging is faster with the Fe-doped sample. Its permittivity decreases faster than that of the undoped sample, so that after 16 days, they are very close to each other; δ_1 , *i. e.* the dielectric losses, approaches 0 faster than for the other samples; δ_3 does not leave the in-phase response as easily as the other samples, and this becomes more pronounced with time. For all the samples to exhibit the fully unclamped regime as in Fig. 4.15 (a), means that there is some volume within which the domain walls can move along the potential landscape; this means that domain wall motion within the bulk of the grain volume, and not interactions between domain walls and grain boundaries, dominates the overall extrinsic response. The nature of this response alters the fastest for the Fe-doped sample, showing that the mechanisms of aging take place inside the grains, reducing the extrinsic response at the fastest pace. The Nb-doped sample ages the slowest. This behavior is as expected for both dopants [11]. Hence, the dielectric response of the Fe-doped sample behaves qualitatively as expected, only not quantitatively. From this remark, we conclude that the higher dielectric constant of the Fe-doped sample is caused by a higher density of domain walls. Even though the mobility of each wall taken separately is lower in the presence of Fe-doping, the larger number of walls present in the Fe-doped sample overcompensates this fact and results in a larger overall response as compared to the undoped sample. The domain walls responsible for this effect are likely 180° domain walls: indeed, the dielectric response of the Fe-doped samples is much larger than that of the undoped sample, but its piezoelectric response is slightly lower; it would also be larger if a larger number of 90° domain walls was present. Although Arlt and Pertsev mention that a sufficiently small grain size can enhance the domain wall response independently of the domain wall density [109], Figures 4.4 (c) and (e) show that the undoped and Fe-doped PZT 43/57 samples have similar grain sizes. Hence, a larger domain wall density for the Fe-doped PZT 43/57 sample seems the most reasonable explanation.

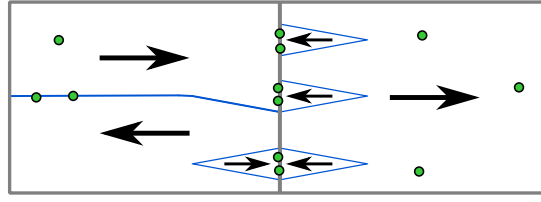


Figure 4.16 – Two adjacent grains are schematically shown. The polarization direction is indicated by black arrows and domain walls are shown in blue. The segregation of Fe^{3+} (green dots) at the grain boundary favors the creation of local domain seeds, which may be misaligned with the predominant polarization direction in the rest of grain. They may also pin domain walls and prevent their disappearance, as shown in the left grain.

The larger number of 180° domain walls in the presence of dopants could be explained considering that the Fe^{3+} ions show some level of segregation in the amorphous phase, since they are impurities. Segregation in the amorphous phase would be passed on to the perovskite phase since the cations are not mobile in the perovskite lattice at the temperatures involved. In particular, segregation at grain boundaries could result in local charges, favoring specific polarization orientations which may exist as small reverse domain seeds, like that proposed to explain polarization fatigue [110]. This would promote the creation of additional domain walls, in order to accommodate these domains. This is schematically shown in Fig. 4.16. Such a mechanism is made possible by the fact that the polarization vector is orthogonal to the grain boundaries in $\{100\}$ -textured tetragonal films after poling. The small thickness of the grain boundaries may prevent this segregation from being observed in the EDX maps of Fig. 4.11. Fe'_{Ti} , $\text{V}_\text{O}^{\bullet\bullet}$ and $(\text{Fe}'_{\text{Ti}} - \text{V}_\text{O}^{\bullet\bullet})^\bullet$ in the bulk of the grains are all domain wall pinning centers [111], and may prevent the disappearance of 180° domain walls at large fields. This is also schematically shown in Fig. 4.16 in the left grain. In the absence of such micro-domains, the undoped sample would exhibit a reduced 180° domain wall density as compared to the Fe-doped sample. The presence of these pinning centers could also lead to a more inhomogeneous coercive field, and explain as well the slanting of the PV loop of the Fe-doped sample.

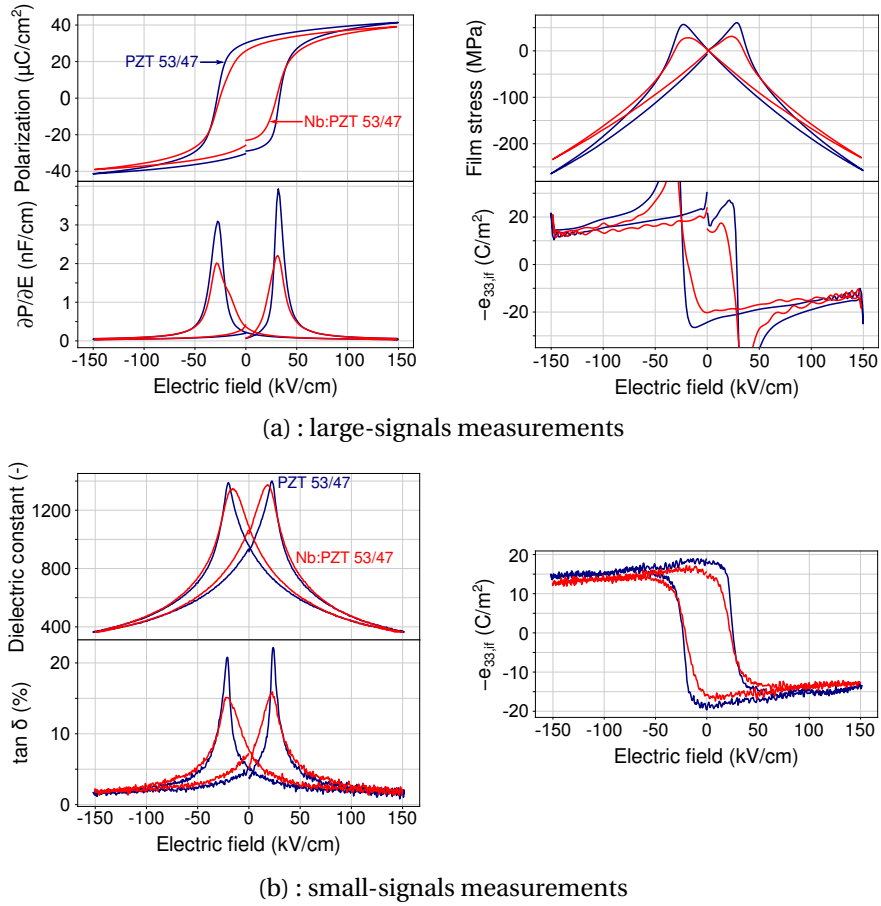


Figure 4.17 – Electric and piezoelectric response for PZT 53/47 films with IDE for two doping conditions, after annealing at 650 °C. (a) : large-signals measurements. (b) : small-signals measurements.

4.4.3 Effect of doping for the MPB composition

Figure 4.17 shows a comparison of the loops for the two films with the MPB composition. We also observe that the undoped film has higher coercive field, larger piezoelectric response, better retention, a more square PV loop (and hence better remanence) than the Nb-doped film. However, the dielectric constant for both films is comparable at high fields; at low fields, the Nb-doped film shows a higher permittivity. In line with the PV loop slanting, the peaks of the dielectric constant and the losses are more spread out for the Nb-doped film, and their maximum is less. Both films display significantly larger switchable polarization, remanent polarization, dielectric constant and piezoelectric response than their tetragonal counterparts discussed before. For the dielectric constant and piezoelectric response, this is as expected. However, the thermodynamic theory of PZT predicts a larger spontaneous polarization for Ti-rich compositions on the tetragonal side of the MPB [20]. Even though the coercive fields are different, saturation was reached for all films at the maximum field of 150 kV/cm. From chapter 3, the maximum reachable polarization for tetragonal and “soft” MPB films with the

4.4. Electrical and piezoelectric response characterization

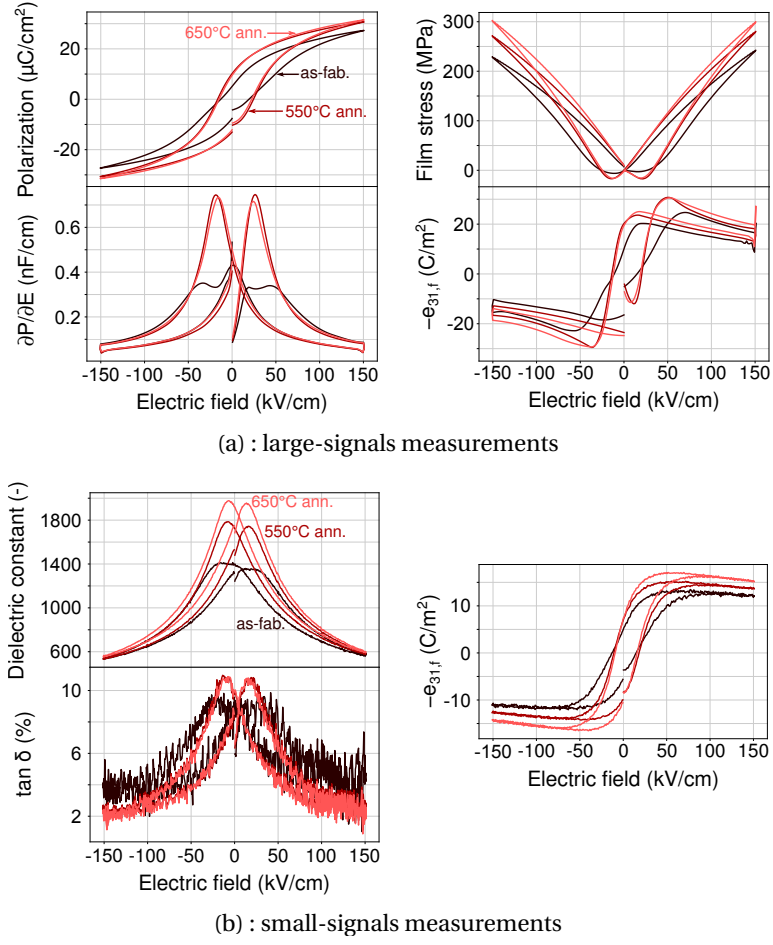


Figure 4.18 – Evolution of the electric and piezoelectric response upon various annealing treatments for a Nb-doped PZT 53/47 film in the PPE configuration. (a) : large-signals measurements. (b) : small-signals measurements.

{100} texture is the same fraction of the spontaneous polarization. The porosity we observed for the undoped and Fe-doped tetragonal films does not seem to be the cause, because the differences listed above include the Nb-doped tetragonal and MPB films which have a similar density. We do not have a reasonable explanation to propose for this observation at present.

4.4.4 Comparison between the IDE and the PPE configurations

Figure 4.18 shows the change of behavior for a Nb-doped PZT 53/47 (MPB) film in the PPE configuration after each annealing step. 5 RTA steps with the gradient-free route were performed to grow this film, with the same precursor solutions as for the PZT thin film with IDE of the same composition and doping presented before. We did not measure the film thickness for this film; however, counting 250 nm per RTA step, we assumed a final PZT thickness of 1.25 μm for extraction of the film stress, the dielectric constant and the electric field. Note that

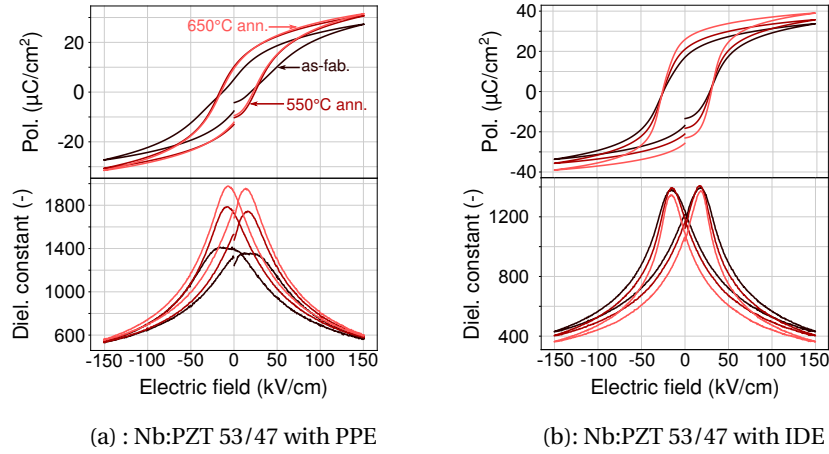


Figure 4.19 – Comparison of the change of electric response upon various annealing treatments for two Nb-doped PZT 53/47 (MPB) films with the PPE (a) and IDE (b) configuration.

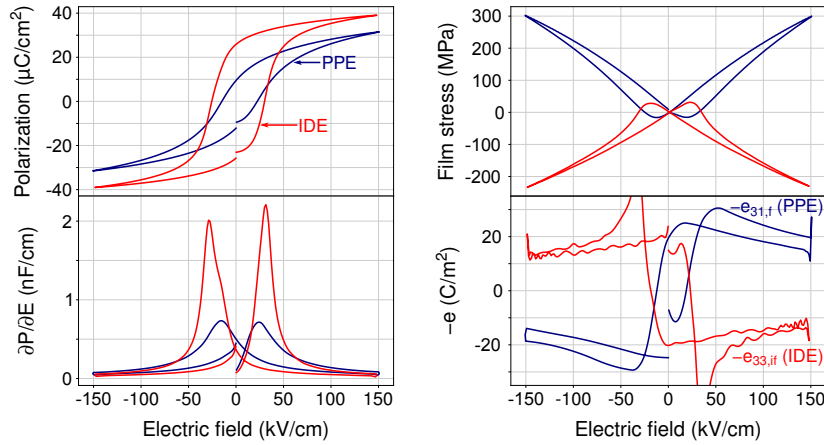
the effective transverse piezoelectric coefficient $e_{31,f}$ does not depend on the film thickness. The main features upon annealing are the following :

1. The switchable polarization increases.
2. The coercive field decreases.
3. The PV loop becomes more square.
4. The dielectric constant increases.
5. The piezoelectric response increases.

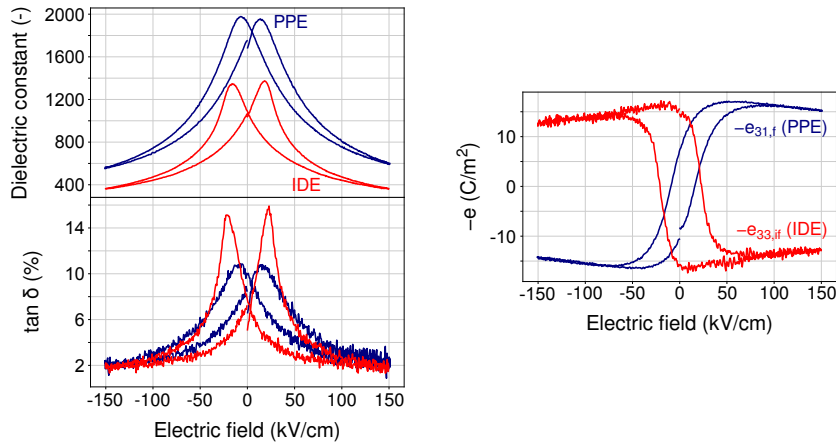
The increase of the piezoelectric response at all fields, not just small fields, is a feature which was also present in Nb-doped PZT films with IDE. The biggest change occur after the 550 °C anneal. The PV loop and the loss loop are almost unchanged after the 650 °C anneal, however the dielectric constant continues to increase and the piezoelectric response significantly improves. The as-fabricated film displayed some imprint and self-poling on the negative poled state side. The imprint remains present after each annealing steps. The as-fabricated sample was measured several weeks after fabrication and shows some aging, with the characteristic pinched PV loop. This aging is entirely canceled by the annealing steps.

Some of the above-listed features differ from the behavior observed in the IDE configuration. Fig. 4.19 compares the two behaviors for the same PZT composition and doping in each electrode configuration. Notably, in the IDE configuration, there is a significant change of the PV loop after the 650 °C anneal, and the dielectric constant decreased after each annealing step (Fig. 4.19 (b)). This decrease is slightly more pronounced at high fields. For the PPE configuration, the dielectric constant at high fields remain unchanged whatever the annealing conditions; it increases only at intermediate and low fields (Fig. 4.19 (a)). Also the dielectric constant of the film with PPE reaches much higher values than the film with IDE; this could however be a consequence of the inferred PPE film thickness. Annealing up to 650 °C should not significantly influence the intrinsic dielectric constant of the perovskite lattice, but each

annealing treatment is expected to change the defect distribution inside the film to some extent, the higher temperature anneal having a larger effect; and therefore, the domain walls clamping and the extrinsic response will change. If the difference in behavior between the two configurations is solely due to the extrinsic dielectric response, then this means that this response increases upon annealing in the PPE configuration, and decreases in the IDE configuration. An increase in the extrinsic response can be caused either by a larger density of domain walls, by a higher mobility of the walls, or both. Damage from the top electrode sputtering deposition in the PPE configuration likely results in a significant clamping of the domain walls, which will be canceled upon subsequent annealing. On the contrary, interfaces are expected to have little influence on the material response of the film with the IDE configuration. The changes observed for the latter case are also less pronounced. Since annealing under oxygen is unlikely to increase domain wall pinning, the decrease in the dielectric constant should rather be attributed to a lower domain wall density reducing the extrinsic response. Since the piezoelectric response increases after annealing, we conclude that the effect of annealing is to reduce the volume of reversed domains, and hence the density of 180° domain walls. This is also consistent with the more abrupt switching observed for all samples with IDE after annealing.



(a) : large-signals measurements



(b) : small-signals measurements

Figure 4.20 – Comparison of the electric and piezoelectric response for two Nb-doped PZT 53/47 (MPB) films with the PPE and IDE configuration, after annealing at 650 °C. (a) : large-signals measurements. (b) : small-signals measurements.

Figure 4.20 compares the Nb-doped PZT 53/47 (MPB) films in the IDE and PPE configurations, after annealing at 650 °C. The switchable polarization is considerably larger for the IDE film, while the large-signal piezoelectric e coefficients are comparable (Figure 4.20 (a)). The maximum field stress at 150 kV/cm appears larger for the PPE film, but the reliability of this conclusion is limited by the fact that we do not know the PPE film thickness with precision. The dielectric constant is much larger for the PPE film, but here also there is uncertainty on the PPE film thickness. Losses are smaller for the IDE film except at the switching field. The coercive field for the IDE film appears larger on both PV and CV loop, and no imprint is present. This is consistent with the fact that the IDE film is in a perfectly symmetrical configuration, since both IDE top electrodes were deposited at the same time on the same surface, so that both electrode/film interfaces are the same. On the contrary, in the PPE configuration, the

top and bottom electrode do not have the same thermal history, since the bottom electrode experienced one or several crystallization anneal at 650 °C that the top electrode has not. Besides, the electric field is directed along the PZT growth direction, which should show a property gradient, because the bottom layers are expected to have a microstructure different from the top layers; and because of the gradient of Zr/(Ti+Zr) ratio, which is never fully compensated even in the gradient-free route [47]. Finally, the top electrode deposition process can cause some damage at the top of the PZT layer, which may be only partially cured after annealing at 650 °C. The larger coercive field for the IDE sample is particularly visible on the small-signal e coefficient loop in Figure 4.20 (b). The IDE film shows excellent retention and remanence as compared to the PPE film. $e_{33,if}$ is about 14.5 C/m² at remanence, close to its maximum value of about 17 C/m², whereas the remanent $e_{31,f}$ is only -8 C/m² for a maximum also of about -17 C/m². This low remanence of $e_{31,f}$ is mostly the consequence of pronounced back-switching at low DC electric field and significant retention loss upon removal of the voltage. The IDE film suffers very little from either of these problems. A similar discussion can be made for the PV loops and the large-signal e loops. Interestingly, the IDE sample shows only a small hysteresis on the return branch, whereas the large-signal $e_{31,f}$ drops by nearly 20 % when the field starts to diminish after the maximum field was reached. This feature could be interesting for large field operations of IDE samples, if high precision is needed.

Those remarks are very similar to the observations made by Chidambaram and coworkers when comparing undoped MPB PZT films with the IDE and PPE configurations [35] (note that, however, the parasitic capacitance was not corrected for in the electrical measurements of the IDE sample they present). In particular, we also observe that, on the tip-to-remanence branch, $e_{31,f}$ and $e_{33,if}$ are about the same. This is different from the effective coefficients we estimated for standard PZT ceramic grades as seen in chapter 4, where we found $e_{33,if} > |e_{31,f}|$. Both elastic and piezoelectric coefficients enter in the formula of each effective e coefficients, and they are likely different for thin films and for bulk samples. It is therefore difficult to draw any firm conclusion from this observation, without a more precise knowledge of the material parameters of the thin films involved. That being said, we note in Fig. 4.20 (a) that the large-signal $e_{31,f}$ is larger than the large-signal $e_{33,if}$ for most of the electric field range. Consequently, a larger stress is generated in the PPE sample than between the IDE fingers. This suggests that the extrinsic contribution to $e_{31,f}$ is larger than that to $e_{33,if}$. This is consistent with the different stress situations of the two samples: the residual tensile stress is aggravated after poling in the PPE configuration, resulting in a larger driving force for the formation of ferroelastic domain walls; on the contrary, the residual tensile stress is partly relieved along one direction after poling in the IDE configuration: hence, a lower quantity of ferroelastic domain walls is expected to be present.

Table 4.2 – Summary of the performances of the samples tested after annealing at 650 °C. ΔP_R is the difference between the initial and final polarization on the PV loop. ϵ_f is taken at remanence (rem.). For $e_{33, \text{if}}$, we took the small-signal (s.-s.) value at remanence. For the PPE sample, the same with $e_{31, \text{f}}$ is shown.

Sample	Rem. s.-s. $e_{33, \text{if}}$ (C/m ²)	$-\sigma_{\text{max}}/E_{\text{max}}$ (C/m ²)	Rem. ϵ_f (-)	P_R (μC/cm ²)	$\Delta P_R/P_R$ (%)
PZT 43/57	12.5	14	590	27.1	3
Nb:PZT 43/57	11	13.3	790	20	8.5
Fe:PZT 43/57	11	11.3	700	21.6	6
PZT 53/47	17.5	17.3	920	28.9	5.2
Nb:PZT 53/47	14.5	15.3	1050	23.1	11.7
Nb:PZT 53/47 PPE	-8	-20	1680	9.4	28.7

4.5 Conclusion

We have performed systematic characterizations of PZT thin films with IDE for several compositions and dopings. The optimized process which we employed yields a good texture control for sol-gel PZT growth on an insulating MgO layer. All the films from a single batch had more than 90 % of the crystallites with the {100} out-of-plane orientation under certain circumstances. A dense and columnar microstructure was obtained for all films, similar to the state-of-the-art sol-gel PZT thin films grown on Pt bottom electrodes. The composition gradient along the growth direction was satisfactorily limited by the gradient-free sol-gel route, and the dopant concentration was well homogeneous within the resolution limit of the STEM EDX tool. We observed that the MgO buffer layer that we used to promote the {100} texture, did not fully prevent lead interdiffusion between the PZT film and the SiO₂ underlayer; however, this appears to have no influence on the device behavior.

Table 4.2 shows a summary of the performances of the tested samples, after the 650 °C anneal. We took the small-signal e coefficient at remanence as representative of small-field and direct mode operations; $-\sigma_{\text{max}}/E_{\text{max}}$ is representative of the large-signal performance. ϵ_f is taken at remanence and $\Delta P_R/P_R$ is a measure of the retention capability of the sample, where ΔP_R is the difference between the initial and final polarization on the (open) PV loop. Large $\Delta P_R/P_R$ means poor retention.

Table 4.3 – Figure of merit for energy harvesting calculated as $e^2/\epsilon_0\epsilon_f$, where $e = e_{33, \text{if}}$ or $(1 - \nu_s)e_{31, \text{f}}$ (for IDE and PPE resp.) is the small-signal value at remanence and ϵ_f is taken at remanence. For IDE samples, we show both the material value $e_{33, \text{if}}^2/\epsilon_0\epsilon_f$ and the engineering value $(1 - \eta)e_{33, \text{if}}^2/\epsilon_0\epsilon_f$. For PPE samples, these two values are the same.

Sample	Material figure of merit $e^2/\epsilon_0\epsilon_f$ (GJ/m ³)	Engineering figure of merit $(1 - \eta)e^2/\epsilon_0\epsilon_f$ (GJ/m ³)
PZT 43/57	29.9	17.9
Nb:PZT 43/57	17.3	10.4
Fe:PZT 43/57	19.5	12.1
PZT 53/47	37.6	22.6
Nb:PZT 53/47	22.6	13.6
Nb:PZT 53/47 PPE	4.3	4.3

Table 4.3 shows the energy harvesting figure of merit (FOM) calculated as $e^2/\epsilon_0\epsilon_f$, where $e = e_{33, \text{if}}$ or $(1 - \nu_s)e_{31, \text{f}}$ (for IDE and PPE resp.) is the small-signal value at remanence and ϵ_f is taken at remanence. The IDE design was not optimized and we had $1 - \eta = 0.6$ for all IDE samples. We observe that, in spite of its larger dielectric constant, the undoped MPB film has the best FOM thanks to its much larger piezoelectric response. The improvement in lower dielectric constant when choosing the undoped tetragonal film is lost in terms of FOM, because of the large decrease in piezoelectric response. In all cases, doped films have a lower FOM than any of the undoped films, and the PPE sample has the lowest FOM of all, due to a poor $e_{31, \text{f}}$ and a large dielectric constant at remanence. Note that hot-poling the films should result in an improved FOM for all samples, since the piezoelectric response should increase and the dielectric constant should decrease.

For all the compositions and dopings tested, the best performances were obtained after annealing at 650 °C, and were a significant improvement over the properties after annealing at the lower temperature of 550 °C, due to a reduction in the number of 180° domain walls. The undoped compositions showed the best performances, because both Nb and Fe doping reduced retention, remanence, and induced a larger dielectric constant. The latter increases the capacitance of the device, which is detrimental for the voltage output of the PEH. The Fe doping of the tetragonal composition resulted in a soft PZT film behavior similar to the properties of the Nb-doped film of the same composition. This was unexpected, and was explained by the larger number of 180° domain walls induced by the Fe dopant as compared to the undoped sample. In short, doping is detrimental for the harvesting performance for both investigated compositions. Undoped compositions should be chosen.

Even though the undoped tetragonal film exhibited the best retention properties of all the composition and dopant combinations we tested, this came at the expense of a significantly reduced piezoelectric response. The latter was partly compensated by the lower dielectric

constant, so that this film showed the second largest FOM. The undoped MPB film showed the largest piezoelectric response, with somewhat reduced retention properties and a significantly larger dielectric constant, and the best FOM. This is an incentive to investigate films with a $\text{Zr}/(\text{Zr}+\text{Ti})$ ratio between 53 % and 43 %, where a better trade-off between retention, piezoelectric response, and dielectric constant may be achieved. We have not studied rhombohedral compositions; the properties on that side of the MPB may also be interesting for piezoelectric energy harvesting applications.

5 Aging and imprint in PZT thin films with IDE

5.1 Introduction

Aging is most generally the change of properties of a material with time in the absence of any external electrical or mechanical load [112]. In ferroelectrics such as BaTiO_3 (BTO) and PZT ceramics or thin films, it results in a decrease of the dielectric constant, the piezoelectric response, and the mechanical and electrical losses; it also manifests itself by a constricted or pinched PV hysteresis loop (in acceptor-doped materials) or an offset of the loop along the voltage axis building up with time (for poled samples) [113]. Aging in the poled state is also called imprint, a term originating from the field of ferroelectric random access memories (Fe-RAM) where this effect can lead to a reading error [114].

It is widely accepted, and supported by a large body of evidence, that the change of properties during aging is related to a stabilization of the domain pattern (even in the single domain state [113]), or, in other words, to a decrease in the mobility of domain walls [112]. Jonker [115] performed a revealing experiment in this respect in 1972: he experimented with ceramics composed of a solid solution of 95 at.% BaTiO_3 and 5 at.% BaZrO_3 , which show a tetragonal to orthorhombic phase transition at 30 °C. Both phases are ferroelectric but with different polar axes. He let the sample age in the unpoled state at 50 °C, that is in the high temperature tetragonal phase, observing the pinched hysteresis. When cooling down below the phase transition temperature and recording the PV loop, the constriction was absent. When the sample was heated up again above the phase transition temperature, returning to the tetragonal phase, the pinched loop reappeared. A symmetric experiment with aging the sample in the orthorhombic phase yielded the symmetric result. This experiment is schematically shown in Fig. 5.1. Jonker found that the constriction of the PV loop was less pronounced after returning to the aged phase if the sample was left longer in the unaged phase, showing that the “memory” of the stabilized state disappears over time. He concluded that aging consists in the stabilization of the current domain pattern by a diffusion process taking place within the sample, and that the memory effect is the consequence of the resulting “diffusion pattern”. A visual evidence of such a stabilization process was more recently provided by Zhang and Ren [116], who observed

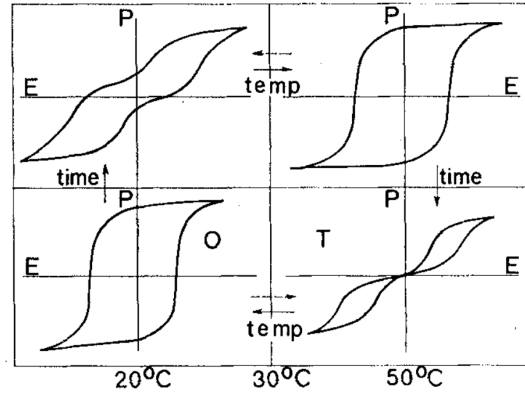


Figure 5.1 – Evolution of the shape of the PV loop for $\text{BaTi}_{0.95}\text{Zr}_{0.05}\text{O}_3$ with time and temperature-induced phase changes. From Ref. [115].

in situ the domain pattern of an aged sample of Mn-doped BTO single crystal during a slow hysteresis PV loop. They witnessed the nearly identical reproduction of the same *ac*-domain pattern every time the electric field reached zero, either from the ascending or descending branch, at the PV loop constriction — showing that the crystal kept a very precise memory of the position of each domain, even after their complete disappearance at the tip of the PV loop.

Several underlying mechanisms were proposed to explain aging and, to this day, it remains unclear which one is dominant. They fall in one of the following three categories [117–119] :

1. A volume effect, in which the domain pattern is stabilized because the polarization within the bulk of the domain is stabilized. This can be achieved by the local alignment, along an energetically favorable direction, of polar defect associates such as $(\text{Fe}'_{\text{Ti,Zr}} - \text{V}_\text{O}^{\bullet\bullet})^\bullet$ — to locally minimize the electrostatic or elastic energy, which depends on the orientation of the associates.
2. A domain wall effect, in which point defects diffuse towards domain walls and fix their positions. The driving force for this process can be the reduction of internal stresses and electrostatic forces caused by charged domain walls, or piezoelectric charges related to local deformations.
3. An interface effect, in which a second phase at grain boundaries or at the material-electrode interface, or a polarization mismatch at grain boundaries, causes local uncompensated bound charges to appear. These charges are then compensated over time by the drift of free charges (electronic or charged defects) driven by the local depolarization field thus created.

The volume effect necessitates very local drift of charges or elastic point defects, unlike the domain wall and interface effects which imply defect diffusion over longer distances — depending on the relative density of defects and domain walls. One or more of these

mechanisms could be active at the same time, possibly with comparable contributions to the total effect. Dopants, composition, microstructure, domain pattern or processing conditions could all influence the relative weight of the three processes.

The aging process can be studied in various ways, and we will describe the two routes which are the most popular in the literature. The first possibility is to monitor the change of properties with the progress of aging, under different experimental conditions such as composition, doping, or temperature, as was done for instance by Arlt and Neumann [120]. The relative speeds at which each property is changing for each experimental condition usually allows to draw some conclusion regarding the processes involved. The main difficulty involved in employing this route, is that the performed measurements will influence the aging process, hence, possibly falsifying the experiment. In addition, the rate of aging does not always allow a convenient monitoring procedure: the properties evolve as the logarithm of time [112], *i. e.* the rate of change greatly varies, from very fast at short time scales to very slow at long time scales; so much so that saturation may not be reached within a reasonable time frame. This is the reason why studying the de-aging process is preferred by some researchers: starting from an aged state, the change of properties upon *de-aging* of the samples is monitored. This was the route followed *e. g.* by Carl and Härdtl [117]. De-aging is achieved by cycling the sample with an AC electric field of a sufficiently large amplitude over a sufficiently long period of time. As before, the relative speed of the property change gives some insight into the de-aging process, revealing what caused aging in the first place. The properties evolve according to an exponential time law in de-aging experiments [117], which makes them much more practical to monitor, and time constants can easily be extracted. Since the same AC electric field can be used for both the de-aging and the measurements, even both at the same time as done by Morozov and Damjanovic [118], the monitoring process does not interfere with the progress of de-aging. However, if a well-defined de-aged state is easy to prepare for aging experiments, typically by annealing above the Curie temperature, this is not the case for de-aging experiments, where the extent of aging in a given sample may only be discovered destructively by de-aging it. For this reason, caution must be exercised to compare results across samples in de-aging experiments. One possibility is to let all samples age in the same conditions prior to the experiment. Another one is to use as-fabricated samples, if the samples are naturally aged after the fabrication process; this is typically the case for ceramic samples.

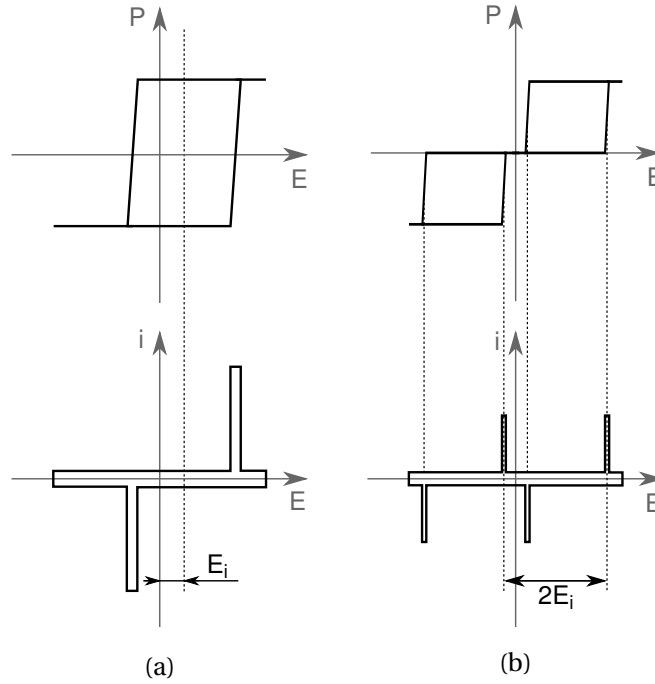


Figure 5.2 – Definition of the internal bias E_i for (a) shifted PV loops and (b) constricted PV loops. For the constricted loop in (b), the distance shown is two times the internal bias. After Carl and Härdtl [117].

The extent of aging is often quantified by an internal bias field E_i , both for constricted PV loops and loops with an offset. This internal bias is geometrically defined as shown in Fig. 5.2. Constricted loops are here considered as the superposition of two PV loops, one having an internal bias E_i and the other an internal bias $-E_i$, corresponding microscopically to the concurrent stabilization of parallel and antiparallel domains. The internal bias is not an electric field which exists in the material, but the macroscopic manifestation of the energy difference between the two poling directions [120]. During the aging process, one direction, say 1, is made more stable than the other, say 2, and the internal bias appearing in the PV loop is the consequence of going from state 1 to state 2 and then back to state 1. This process is schematically shown in Figure 5.3. Writing the spontaneous polarization within a domain P_s , we may write [120]:

$$E_i P_s = \Delta G_{\text{aging}}(t) \quad (5.1)$$

where $\Delta G_{\text{aging}}(t) < 0$ is the volumetric free energy difference between state 1 aged during a time t and state 1 at $t = 0$. This energy becomes more negative with time during aging, and decreases in absolute value with time during de-aging experiments.

The internal bias is immediately available in the current-field loop obtained during a PV measurement, and is for this reason often chosen to monitor the aging and the de-aging process, as was done in Ref. [120] and [117] for example. Note that in the above equation, E_i

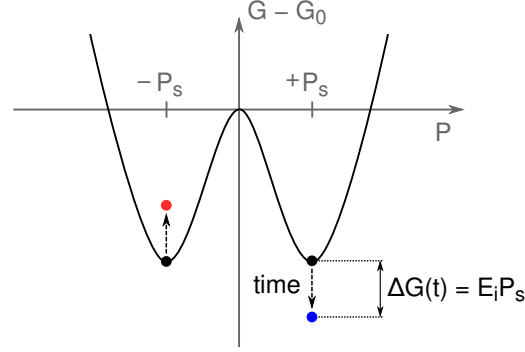


Figure 5.3 – Schematic depiction of the aging process on the free energy G vs. polarization P diagram. During aging, the free energy of the $+P_s$ state gradually decreases, whereas it increases for the $-P_s$ state. After Arlt and Neumann [120].

and P_s are taken with their signs, so that the stabilization of the negative polarization state gives a positive E_i , as in Fig. 5.2 (a).

There are other ways to monitor the progress of aging and de-aging. Dielectric spectroscopy is one of them. It allows to probe the regime of domain wall motion in the sample; aged samples exhibit specific types of domain wall response which are different from the fully de-aged case. It can also be used as a tool to distinguish precise geometrical features of the PV loop, which are related to the aging process. Finally, we mention the Preisach formalism, which can be used to construct a “map” of internal bias fields inside the sample. Before describing the aging process in more details, we will present these other techniques, some of which were employed in this work.

5.2 Harmonic analysis of the polarization response

Ferroelectric materials in general exhibit a pronounced nonlinear and hysteretic behavior [121]. Under some circumstances, the analysis of this behavior can reveal precious information on the microscopic processes taking place in the sample. This can prove very helpful to elucidate the processes of aging, which are still not fully understood. The principal technique which we will discuss for this purpose is the harmonic analysis of the polarization response of the sample, under sub-coercive (or subswitching) electric fields and under switching electric fields. We first present the harmonic description of a response signal; we will show how, from this response, information on the nature of the domain wall motion can be obtained; and we will present the Preisach formalism, which underlies some of the interpretations of the harmonic analysis results, and which can also be used for the analysis of the sample macroscopic response.

5.2.1 Description of the harmonic response

The defining property of ferroelectric materials is the possibility to switch between two stable polarization states. This implies the existence of coercive fields and the hysteresis PV loop. However, hysteresis is not restricted to the polarization reversal of domains. Hysteresis is widely present at all electric field ranges in piezoelectric ceramics — which are polycrystalline compounds of ferroelectric grains poled along their polar axis — in both the dielectric and piezoelectric response [121]. The hysteresis behavior is typically studied in the looping formalism, *i. e.* the response of the sample under the action of a periodic excitation wave (voltage or stress) is recorded. For linear systems, the response $R(t)$ to a sine wave of the form $F(t) = F_0 \sin(\omega t)$, where F_0 is the amplitude of the unspecified driving field F at frequency $f = \omega/(2\pi)$, will be :

$$R(t) = R_0 \sin(\omega t + \varphi) \quad (5.2)$$

where R_0 is the amplitude of the response and φ is the phase angle between the response and the driving field. φ is a measure of the hysteresis of the system : the response is anhysteretic if $\varphi = 0$. In general, R_0 is proportional to F_0 and the proportionality factor is a material parameter. R_0 and φ are sufficient for completely describing the hysteretic response. A linear response for a dielectric (resp. piezoelectric) material means that the dielectric constant (resp. the piezoelectric coefficient of interest) does not depend on the oscillating electric field or stress amplitude, because they are the material parameters mediating the driving field and the material response — the latter being the electric displacement or the strain, depending on the effect under investigation.

In a typical PZT thin film, the shape of the (saturating) CV loops shows that the response cannot be considered as linear. In non-linear systems, the response to an oscillating sine field $F(t) = F_0 \sin(\omega t)$ is the sum of the response at the base frequency f and the responses at all the higher harmonics of f , forming a Fourier series :

$$R(t) = \sum_{n=1}^{+\infty} (R'_n \sin(n\omega t) + R''_n \cos(n\omega t)) \quad (5.3)$$

The sine components $R'_n \sin(n\omega t)$ are said to be “in-phase” with the exciting wave $F(t)$ while the cosine components $R''_n \cos(n\omega t)$ are said to be in “quadrature” or sometimes “out-of-phase” with the driving field. R'_n (resp. R''_n) is called the amplitude of the in-phase (resp. quadrature) component of the n^{th} harmonic of the response $R(t)$. The response is non-linear as soon as any one of those components is non-zero for $n > 1$. The response is anhysteretic if all $R''_n = 0$ for all n . The sum can also be written in terms of amplitudes and phase angles :

$$R(t) = \sum_{n=1}^{+\infty} R_n \sin(n\omega t + \varphi_n) \quad (5.4)$$

$R_n > 0$ is called the amplitude of the n^{th} harmonic of the response $R(t)$ and φ_n is the phase

angle of the n^{th} harmonic. The response is non-linear as soon as there exists one non-zero amplitude for $n > 1$. As before, if $\varphi_n = 0$ for all n , the response is anhysteretic. The various variables are related as follows :

$$\begin{cases} R_n = \sqrt{(R'_n)^2 + (R''_n)^2} \\ \varphi_n = \tan^{-1} \left(\frac{R''_n}{R'_n} \right) \\ R'_n = R_n \cos \varphi_n \\ R''_n = R_n \sin \varphi_n \end{cases} \quad (5.5)$$

5.2.2 Intrinsic and extrinsic contributions

The single domain state cannot be achieved in PZT ceramics or thin films, because of the multiple electrical and mechanical constraints brought about by the polycrystalline structure and the random direction of the polar axes of each crystallite after poling. As such, some ferroelectric and ferroelastic domain walls are always present. They contribute to the macroscopic material response as extrinsic contributions [122]. Both ferroelectric and ferroelastic domain walls contribute to the dielectric response, so that the macroscopic dielectric constant can be written as the sum of the lattice (also called intrinsic) contribution, and the extrinsic contribution:

$$\varepsilon_r = \varepsilon_{\text{int}} + \varepsilon_{\text{ext}} \quad (5.6)$$

Only ferroelastic domain walls contribute to the piezoelectric coefficient of interest, say e , which we write as:

$$e = e_{\text{int}} + e_{\text{ext}} \quad (5.7)$$

The magnitude of the extrinsic contribution can be estimated by comparing the material response at the bias field of interest and the response at very high electric fields, where much less domain walls are expected to be present, while their contribution is limited by the strong field restricting their motion [23]. Another possibility is to measure the response at cryogenic temperatures, where the extrinsic contribution is frozen and only the lattice contributes to the overall response [123, 124]. In the latter case, the room temperature lattice contribution can be extrapolated from a thermodynamic model of the ferroelectric phase [124]. The magnitude of the extrinsic contribution depends on the microstructure of the ceramic or thin film [125] as well as the composition in the case of PZT [126], and can be comparable or larger in magnitude to the intrinsic contribution [23, 126, 127]. The grain size in ceramics was found by several authors to have a significant influence on the domain wall density [128] or on the reduction of the domain wall irreversible movement [126], and hence on the macroscopic response through the extrinsic contribution. Figure 5.4 shows the extent of the extrinsic contribution to

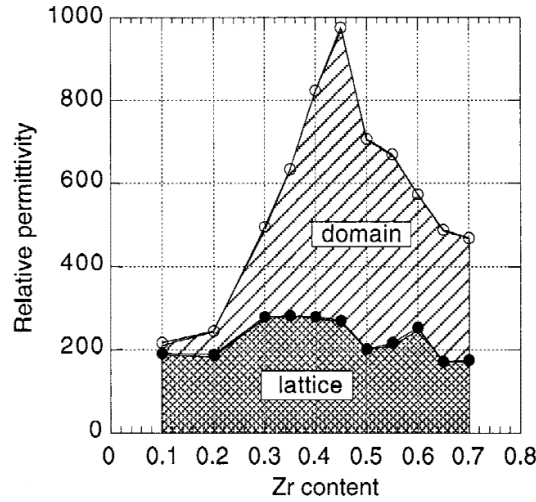


Figure 5.4 – Intrinsic and extrinsic contributions to the relative permittivity for various Zr/(Ti+Zr) ratios in PZT, obtained by comparing the material response with and without a large superimposed DC electric field. From Ref. [23].

the relative permittivity for various Zr/(Ti+Zr) ratios in PZT, as computed by Hiboux *et al.* [23]. Note the peak of the extrinsic contribution near the MPB, showing enhanced mobility or a higher domain wall density at this composition, or both.

Another important factor for the magnitude of the extrinsic contribution is the use of dopants, which in practical PZT samples are generally aliovalent substituents. They fall into two main categories [11]:

1. Acceptor dopants such as Fe^{3+} or Mn^{2+} on the Ti^{4+} site, which have a lower valence than the cation they replace, and are compensated by charged oxygen vacancies;
2. Donor dopants such as Nb^{5+} on the Ti^{4+} site or La^{3+} on the Pb^{2+} site, which have a higher valence than the cation they replace, and are compensated by charged lead vacancies thanks to the volatility of PbO . The incorporation of those dopants can also be compensated by the consumption of oxygen vacancies [129].

The incorporation reactions for Fe and Nb dopants into the PTO lattice can be written as follows [101]:



Because lead oxide is volatile, some lead and oxygen vacancies are spontaneously produced

during processing, according to the reaction [130]:



As a consequence, Nb incorporation can also be compensated by the consumption of oxygen vacancies already present in the crystal, as follows [101, 129]:



Acceptor doping leads to a so-called hardening of the material properties, that is lower dielectric constant, lower losses, higher coercive field, lower piezoelectric response, moderately higher conductivity as compared to the undoped composition. Donor doping leads to material softening giving the opposite change: larger dielectric constant, higher losses, lower coercive field, higher piezoelectric response, lower conductivity as compared to the undoped composition. The difference is attributed to the facilitated (resp. impeded) domain wall movement in soft (resp. hard) compositions [11]. The aging is more (resp. less) pronounced in hard (resp. soft) compositions.

5.2.3 Subswitching driving fields

Two regimes can be identified for the excitation of ferroelectric samples: subswitching driving fields and switching driving fields. If the sample is driven by an electric field $E(t) = E_0 \sin(\omega t)$ such that $E_0 < E_c$ where E_c is the coercive field, then the excitation is said to be subswitching. The domain walls are moving around some equilibrium position and the domain structure is considered as being unchanged on average upon cycling [121]; creation and annihilation of domain walls, nucleation of new domains or merging of neighboring domains are assumed to play a minor role. In this regime, the main source of non-linearity is the extrinsic contribution which is mostly due to the domain wall movement about the rest position [131, 132]. Hence, the analysis of the subswitching response provides direct information on the mobility of domain walls in the system.

The Preisach formalism

A number of mathematical formalisms, along with their microscopic interpretation, are available to describe the hysteresis of non-linear systems. A quite complete review is given by Morozov in his PhD thesis [133]. Here we will present selected elements relevant for this work. A natural approach to hysteresis processes is to describe the macroscopic hysteresis loop as the sum of the response of a collection of microscopic switching units, each possessing its own coercive field E_c and internal bias field E_i (see Fig. 5.5 (a)). Both E_c and E_i are randomly distributed and each microscopic switching unit contributes to the polarization by the same amount P_u . E_i can be either positive or negative and E_c must be positive. The half-plane defined by the set of the possible (E_i, E_c) values is called the Preisach plane. The system is

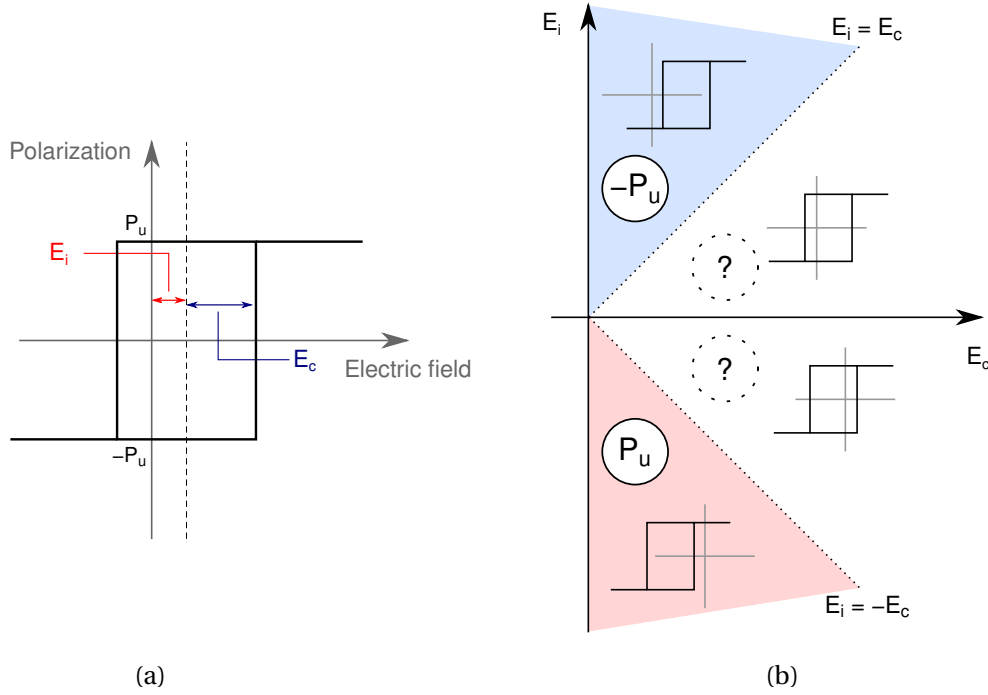


Figure 5.5 – (a) : Hysteresis loop of a single switching unit, showing the geometrical definition of the coercive field E_c and the bias field E_i . (b) : The Preisach plane at zero external bias. The switching units outside of the dashed cone have well-defined states because their bias field is larger than their coercive field. Their contribution to the total polarization is shown in a circle. The switching units within the cone do not and their state depends on the prehistory of the system.

fully described by the probability density $f : E_i, E_c \rightarrow f(E_i, E_c)$; the number of switching units whose coercive field and internal bias field are respectively in $[E_i, E_i + dE_i]$ and in $[E_c, E_c + dE_c]$ is given by $f(E_i, E_c)dE_idE_c$. Under zero bias, the units for which $E_c < |E_i|$ are in a well-defined polarization state, while the state of the units for which $E_c > |E_i|$ is not defined unless the prehistory is known, as shown in Fig. 5.5 (b); after cool-down from the paraelectric phase, they can be assumed to be in either state with equal probability, defining a cone in the Preisach plane.

The switching can be geometrically obtained from the Preisach plane as follows. If a cycling field $E(t)$ with oscillation amplitude E_0 is applied, only the switching units such that $E_0 > E_c + E_i$ and $-E_0 < E_c - E_i$ will contribute to the hysteresis in the steady state (the others will either never change their state, or change their state during the first cycle only). These units are below the line defined by $-E_0 = E_c - E_i$ and above the line defined by $E_0 = E_c + E_i$; this defines a triangle of toggling units in the Preisach plane as shown in Fig. 5.6 (where the line equations were rewritten to put E_i on the left-hand side). When the field reaches $-E_0$, all units have the $-P_u$ state. When the field starts to increase again, all units for which the current field $E(t) > E_c + E_i$ will switch to the P_u state. This defines a new line, parallel to the $E_0 = E_c + E_i$

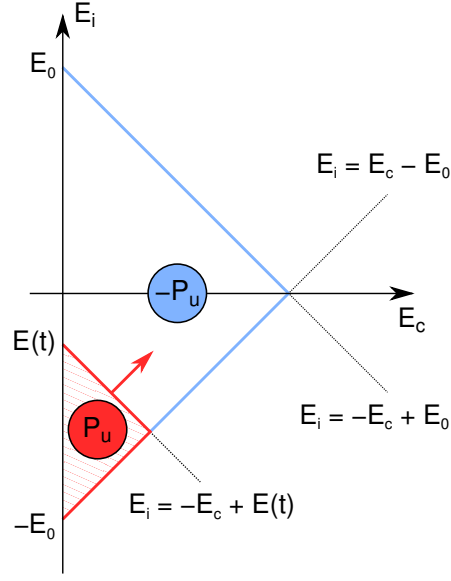


Figure 5.6 – Geometrical representation of the switching process for the electric field increasing from its minimum value. The striped red triangle is growing in the direction indicated by an arrow and the switching units switch from $-P_u$ to P_u when they pass inside it.

line and crossing the y-axis at $E(t)$, below which all the units have the P_u state, which is represented by the red triangular zone in Fig. 5.6. This zone increases, as indicated by the red arrow, until $E(t)$ reaches E_0 and all units have switched to the P_u state. The decreasing part of the cycle then proceeds in a symmetrical manner. The macroscopic polarization change is given by the integration of the number of switched units at each infinitesimal time step dt , which is known from the function f .

Frequency does not enter into consideration for systems which can be described by the Preisach formalism, because as we can see from the previous description, the knowledge of the shape of $E(t)$ alone is sufficient to obtain the switching behavior — the period of the signal does not need to be specified. It was shown that a system obeys the Preisach formalism if and only if the two following conditions are satisfied [134]:

1. Wiping-out property : for a given field profile, the final state of the system depends only on the highest extrema of the profile;
2. Congruency property : stationary hysteresis loops between two given field extrema are geometrically superimposable, irrespective of the previous history of the system.

The wiping-out property condition is unlikely to be fulfilled in practice, because of the well-known memory effect of ferroelectrics. Nevertheless, the formalism can be successfully applied to real systems in a number of situations [134–136].

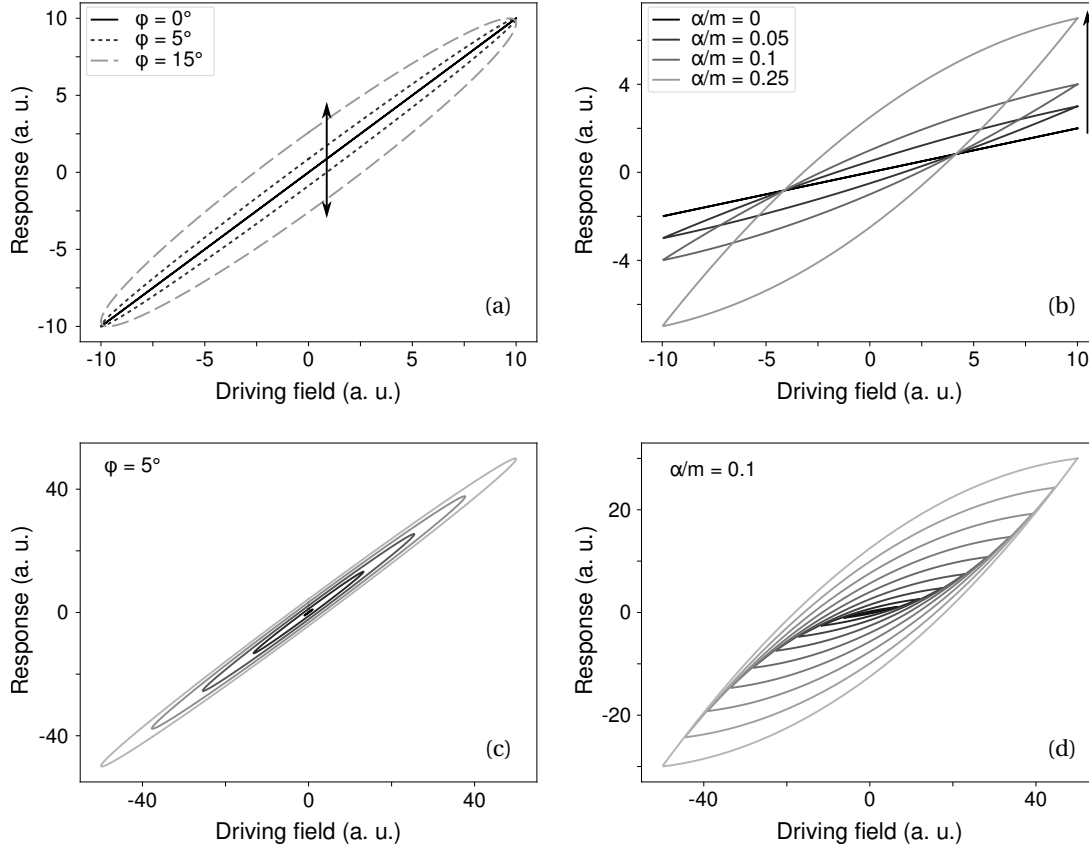


Figure 5.7 – Hysteresis loops for various systems. (a) : For a linear system with a fixed amplitude but various phase angle under the same driving field; arrows indicate how the curve is changing for increasing phase angles. (b) : For a Rayleigh system with various α/m_{init} ratios under the same driving field; an arrow indicate how the curve is changing for increasing α/m_{init} ratio. (c) : For a linear system with phase angle $\phi = 5^\circ$ under increasing driving field amplitude. (d) : For a Rayleigh system with $\alpha/m_{\text{init}} = 0.1$ under increasing driving field amplitude.

The two regimes of domain wall motion

The polarization response of PZT thin films at subswitching fields [108] and the piezoelectric response d_{33} of PZT ceramics under low pressure loads [137] are two examples of systems where the Preisach formalism is applicable. In many circumstances, the response for both systems is well-described by the Rayleigh relation [138] for the hysteresis loop R vs. F :

$$R(F) = (m_{\text{init}} + \alpha F_0)F \pm \frac{1}{2}(F_0^2 - F^2) \quad (5.12)$$

where m is either the permittivity ϵ_r (for polarization-field loops) or the piezoelectric coefficient d_{33} (for charge-pressure loops). m_{init} describes the linear, anhysteretic part of the response, while the coefficient α quantifies the hysteresis of the system. In other words, they describe the reversible and irreversible part of the response, respectively. The “+” and “−”

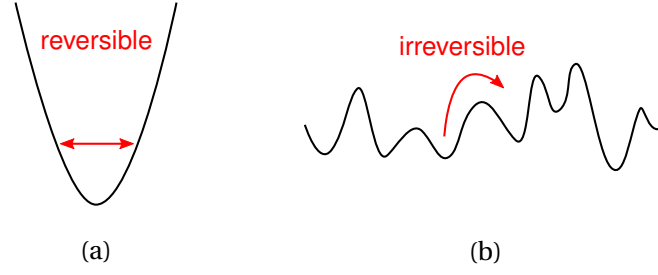


Figure 5.8 – Schematic representation of the energy landscape for the domain wall motion: (a): in the fully clamped state; (b): in the random landscape corresponding to the Rayleigh-like response.

signs are used for increasing and decreasing F , respectively. Note that α also quantifies the non-linearity of the system, since for $\alpha = 0$, the response is linear. This is the central feature of the Rayleigh relation: non-linearity and hysteresis have the same origin and both properties share the same coefficient [121]. Figure 5.7 (a) shows a linear response for a fixed amplitude and various values for the phase angle. It is visible that higher phase angles increase the hysteretic character of the response. The same can be said for increasing α/m_{init} ratio in Fig. 5.7 (b), where the response is nonlinear as described by Eq. 5.12; however, unlike in the linear case, increased hysteresis is accompanied by a larger total response, due to the reversible and the irreversible parts of the response adding up to form the total response. For $\alpha = 0$, the response is linear without loss. Fig. 5.7 (c) shows the behavior for a given linear system with increasing driving field; the total response scales linearly with the field. Fig. 5.7 (d) shows the same with a Rayleigh system, where in this case, the maximum of the response increases with the square of the driving field. This is qualitatively different from the linear system.

The Rayleigh equation can be obtained with the Preisach approach by setting the distribution function to the constant value $f(E_i, E_c) = \alpha$. A microscopic interpretation was provided by Néel as magnetic domain walls moving in a random energy landscape [139] and by Kronmüller as magnetic walls moving in a field of force due to lattice defects [140]. In analogy to these interpretations, this type of response in ferroelectrics is associated with the irreversible motion of domain walls in a random potential landscape created by pinning centers [108, 137, 141]; this is schematically shown in Figure 5.8 (b). Deviation from this response beyond a threshold excitation range was observed and indicates a departure from this microscopic picture [142].

In accordance with its microscopic interpretation, the Rayleigh relation is not accurate in describing systems in which domain walls are expected to be clamped, *e. g.* in hard PZT compositions. A number of explanations have been proposed to explain domain wall clamping and will be discussed in more details later in the text. Clamped domain walls are expected to move at the bottom of a potential well, as schematically shown in Figure 5.8 (a). Robels and Arlt [143] have proposed a V-shaped potential to describe the response of domain walls clamped by electric or elastic dipolar defects, building on the description of the domain wall dynamic developed in previous publications [109, 144, 145]. The steepness of the potential

well increases with time to account for aging, assumed to be the consequence of an increasing number of dipolar defects locally aligned with the polarization. This model presents the response of clamped domain wall as linear and nonhysteretic. To account for their observation of the non-linearity of the response, modified equations were introduced by Li *et al.* [132]. A smearing out of the bottom of the V-shaped potential was in addition proposed to capture the linear and anhysteretic movement of the wall near its rest position [121, 133]. The PV loop obtained by this analytical model is shown next to an experimental PV loop taken on a hard ceramic in Fig. 5.9. A non-linear and anhysteretic behavior is clearly not compatible with the Rayleigh law, which describes a process which is also non-linear but hysteretic.

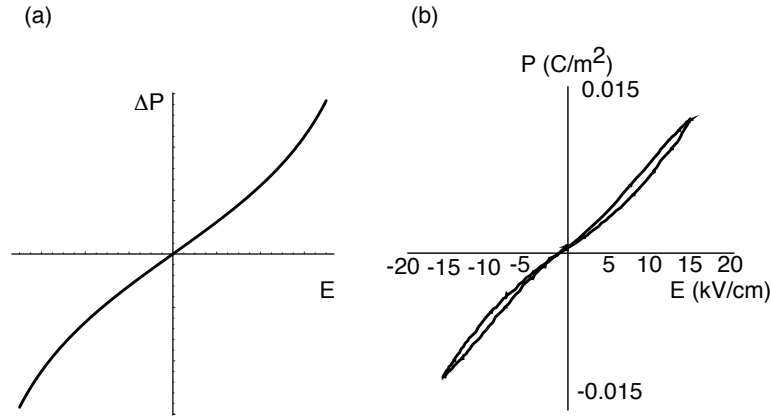


Figure 5.9 – (a) : PV loop calculated with the modified V-shaped potential model proposed in Ref. [121, 133]; (b) : an experimental PV loop from a hard ceramic sample. From Ref. [121]. Courtesy Prof. D. Damjanovic.

In the extreme case, the harmonic polarization response of clamped domain walls to an oscillating electric field $E(t) = E_0 \sin(\omega t)$ should be described by a purely anhysteretic response of the general form :

$$P(t) = \sum_{n=1}^{+\infty} P_n \sin(n\omega t + \delta_n) \quad (5.13)$$

where $\delta_n = 0^\circ$ or 180° for all n , and in case of non-linearity, there exists $P_n \neq 0$ for at least one $n > 1$. By contrast, the Rayleigh relation describe the response of fully unclamped domain walls. The corresponding Fourier series is [108, 146] :

$$P(t) = (\epsilon_{\text{init}} + \alpha E_0) E_0 \sin(\omega t) - \frac{4\alpha E_0^2}{3\pi} \cos(\omega t) - \frac{4\alpha E_0^2}{15\pi} \cos(3\omega t) + \frac{4\alpha E_0^2}{105\pi} \cos(5\omega t) + \dots \quad (5.14)$$

Note how all hysteretic terms (with cosine) and all non-linear terms contain the Rayleigh coefficient α . In addition, there are only odd harmonics and they are all in quadrature with the driving field $E(t)$, meaning that the phase angle $\delta_n = \pm 90^\circ$ for all $n > 1$. The presence

of only odd harmonics is the consequence of the half-wave symmetry postulated by the Rayleigh response, *i. e.* the increasing and decreasing branches of the PV loop having the exact same shape. If the response is plotted against time, the two half-periods of the response are symmetrical with reference to the time axis. Half-wave symmetry is not restricted to the Rayleigh case, but should be present whenever the system responds symmetrically to a symmetrical excitation. Any deviation from such a symmetric response (*e. g.* for poled samples measured along the poling axis as in Ref. [132]) will give rise to non-zero even harmonics.

Experimental approach

This difference between the harmonic response of the fully clamped situation and the Rayleigh behavior allows to qualitatively estimate the magnitude of the domain wall clamping in the sample. The polarization harmonics can be obtained thanks to dielectric spectroscopy measurements. The lowest harmonic for which an unambiguous qualitative difference exists between the two responses is the third harmonic. Therefore, at minimum the 1st and 3rd harmonics should be recorded, under the application of an increasing driving field amplitude. If the dielectric constant changes linearly with the electric field amplitude E_0 and $\delta_3 = \pm 90^\circ$, then the response is Rayleigh-like and the domain walls are presumably moving in a random potential, which is the fully unclamped situation. If the dielectric constant remains constant with increasing field amplitude and $\delta_3 = 0^\circ$ or 180° (or if $P_3 = 0$), then the domain walls are moving at the bottom of a potential well in a non-linear, nonhysteretic fashion (or linearly if $P_2 = P_3 = 0$, neglecting higher harmonics). All other results are the consequence of some intermediate situation, and the proximity to one of the two limiting responses indicates whether the domain walls are rather clamped or rather free in response to the external field, as depicted in Fig. 5.10. As shown there, domain walls become clamped because of aging, and can be de-clamped by the continuous application of an AC electric field (see the two next paragraphs). As soon as the latter is removed, aging sets in again. Because the increasing amplitude of the cycling field is expected to modify the current pinning state of the domain walls, it is usually informative to monitor the harmonic response for an ascending and then descending electric field amplitude, to reveal the disordering action of the driving field.

Figure 5.11 shows the result of a dielectric spectroscopy measurement. The amplitude of the driving field increases, then decreases, in a step-like manner. At each step, the 1st, 2nd and 3rd harmonics of the polarization response are recorded (the 2nd harmonic is not shown here). Arrows indicate the increasing and decreasing branch. At the start of the experiment, the phase angle of the 3rd harmonic δ_3 is close to -180° , and then starts increasing towards -90° above a threshold field. On the returning branch, it remains close to -90° until the field amplitude drops below about 7 kV/cm. The relative permittivity shows a more than linear increase with the field amplitude on the increasing branch, and decreases in a nearly linear fashion on the decreasing branch. δ_1 shows very little hysteresis and increases with the electric

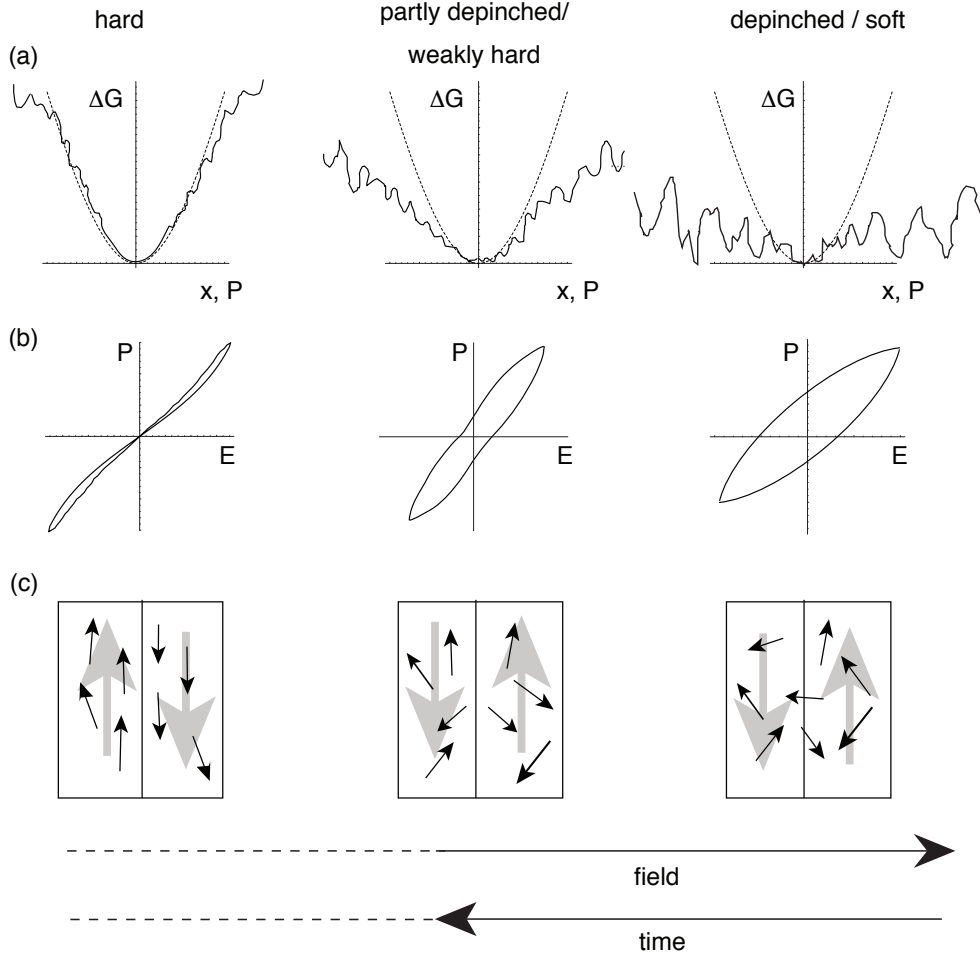


Figure 5.10 – The reversed effects of time and AC electric field on the domain wall potential landscape (a), the shape of the PV loop (b) and the ordering of the microscopic defects inside domains (c). From Ref. [121]. Courtesy Prof. D. Damjanovic.

field; the latter is consistent with the Rayleigh response for which we have:

$$\tan \delta_1 = \frac{4}{3\pi} \left(1 + \frac{\epsilon_{\text{init}}}{\alpha E_0} \right)^{-1} \quad (5.15)$$

The interpretation of this measurement was given by Taylor and Damjanovic [108]: at the start of the first cycle, the domain walls are deeply pinned, as indicated by the in-phase 3rd harmonic response with $\delta_3 \approx -180^\circ$. As the field increases, the response deviates from this state and moves closer to the fully unclamped case, which is finally reached and retained on the decreasing branch, showing a hysteretic behavior. A similar discussion can be made for the behavior of the permittivity, where the linear dependence on the electric field is like the Rayleigh response. This suggests that the domain walls were irreversibly unclamped under the action of the driving field, similarly to de-aging experiments, where the loop pinching

5.2. Harmonic analysis of the polarization response

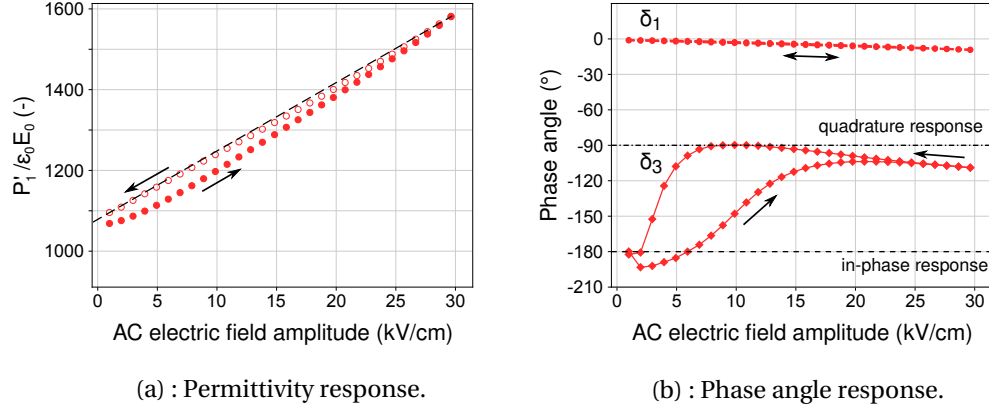


Figure 5.11 – $P'_1/\epsilon_0 E_0$ (a), δ_1 (b) and δ_3 (b) for increasing, then decreasing field amplitude, for an unpoled, Nb-doped PZT 43/57 film with IDE, 20 min after annealing above the Curie temperature. Arrows indicate the direction of the curves. In (a), filled circles indicate the increasing branch and open circles the decreasing branch. The dashed line in (a) is a guide to the eye.

can be relieved by a sufficiently large number of switching cycles [117]. Subsequently, the sample ends up in the de-aged state, and aging sets in again immediately once the driving field is removed [118]. Hence, the measurement is a competition between the aging processes and the de-aging action of the measuring field, as pictured by the bottom arrows pointing in opposite directions in Fig. 5.10. Comparing samples measured in the same conditions, but in different initial states, therefore offers a qualitative way to assess the extent of the initial domain wall clamping in each sample. This is a destructive measurement: as we have seen, the clamping is either reduced or fully destroyed at the end of the measurement.

Within this framework, as pictured in Fig. 5.10, hardening can be understood as the local ordering of microscopic defects — irrespective of their nature — according to the local polarization direction, and, in essence, is thus a manifestation of the aging process [106, 118]. The de-aging process is then the disordering of these defects, which wipes out the memory of the aged domain pattern by allowing irreversible domain wall motion away from their original positions. Conversely, softening and the absence of aging are related properties. This view is supported by the soft-like behavior of quenched ceramics doped with Fe [106]: Aging was not allowed to set in because of the sudden drop of temperature from above the Curie point. This shows that the presence of defects alone does not induce hard properties; only their local ordering does so. We also observed in chapter 4 an Fe-doped film displaying features of a soft sample, which we explained by the rapid cool-down from the high temperature phase during the annealing process in an RTA tool. After a sufficiently long time had passed, this sample started to exhibit a response typical of that due to clamped domain wall motion, *i. e.* it became to harden. We refer the reader to this chapter for a detailed discussion.

5.2.4 Switching driving fields

If the sample is driven by an electric field $E(t) = E_0 \sin(\omega t)$ such as $E_0 > E_c$, the excitation is said to be switching. Polarization reversal within domains occur and the domain structure is erased or greatly changed within each period of the cycle. The complex interplay between domain wall movement and the nucleation and growth of new domains makes this regime difficult to analyze. In particular, the role of domain wall mobility is not evident. Indeed, it was shown that the switching kinetics can be well described in terms of a nucleation-limited process involving independent regions, each characterized by a local waiting time, after which the entirety of the region reverses polarization [147, 148]. The distribution of waiting times was explained for thin films by an inhomogeneous material-electrode coupling coefficient aiding nucleation [149], and by the random distribution of local bias fields for ceramics [150]. This contrasts greatly with the subswitching regime, where domain wall motion is the principal source of the response. Hence, it is not immediately clear how the mechanisms of aging, as understood above within the frame of clamped domain wall motion, can be accommodated within this description, even though the effect of aging is well visible in switching PV loops as well, for instance in the form of constricted loops. Nonetheless, valuable phenomenological information can be extracted from saturating PV loops. The internal bias as defined in Fig. 5.2 is the most widely reported example [117, 120, 151–153]. We will give a few other examples which are relevant for the study of the aging process. These examples will not be restricted to harmonic analysis which has seldom been employed for switching fields, because of the mentioned complexity. But these examples and their discussion involve some of the points we have introduced above, and are for this reason treated in this section.

Morozov and Damjanovic observed that the kinetics of the aging process could be followed by monitoring the evolution with time of δ_3 for saturating PV loops [118]. δ_3 displays a sharp transition from -240° to -60° (in logarithmic time scale) during the progress of de-aging of unpoled samples. This conspicuous feature can be used as a landmark to extract time constants for de-aging, instead of employing the merging of the current peaks as done by Carl and Härdtl [117], which can be ambiguous. Another possibility is the reconstruction of the probability density function of the Preisach plane. This can be accomplished by recording a well-designed sequence of partial PV loops, both saturating and subswitching, yielding first order reversal curve diagrams, or FORCs [154, 155]. This gives a “map” of the distribution of internal bias fields inside the sample, which allows to treat cases which are more complex than the simple example schematically pictured in Fig. 5.2, for instance if multiple current peaks are present. It has been recently employed to analyze the so-called “wake-up” behavior in ferroelectric doped HfO_2 thin films, *i. e.* the opening of the PV loop of as-fabricated samples upon AC field cycling, which shows similarities with the de-aging process in hard PZT thin films [156]. Doped HfO_2 thin films recently received much attention as they could provide ferroelectric properties in a material which is fully compatible with the CMOS process [157]. A more straightforward approach is to directly study the current *vs.* field curve, as proposed by Schenk and coworkers [158], which readily restricts the number of the possible underlying mechanisms. One disadvantage of using FORCs, is that the repeated cycling

necessary to construct them may induce some de-aging and hence, partly falsify the result of the experiment. Therefore their use should be restricted to deeply aged samples. Our samples did not fall into this category. Since we have mostly focused on aging in the poled state, we did not use the technique proposed by Morozov and Damjanovic [118] which was employed for unpoled samples. Indeed, samples aged in the poled state are characterized by an offset of the PV loop, and not by a constriction at 0 electric field. However, since the response of the aged poled samples is asymmetric because of the imprint, it should display a non-zero 2nd harmonic response, which should gradually disappear during de-aging till a perfectly symmetrical PV loop, with no offset, is obtained. Note that, in reality, all samples show some 2nd harmonic response, so that a control sample, possessing as high a degree of symmetry as is experimentally achievable, should be used as a reference point; a PZT thin film with IDE, with both polarity patterned in a single fabrication step (like for the samples measured in chapter 4), and freshly annealed above the Curie temperature, can be used for this purpose. This approach has not been attempted in our work; we have restricted our study of the switching field regime to the evolution of the internal bias.

5.3 Aging mechanisms

After having reviewed the measurement techniques relevant for the study of the aging phenomenon, we will present by which mechanisms aging can proceed. We remind the 3 categories of mechanisms proposed for aging:

1. The volume effect : the bulk of the domains is stabilized by the aging process;
2. The domain wall effect : some defects migrate to domain walls, or domain walls migrate towards defects, to fix their positions;
3. The interface effect : the compensation of bound charges present at interfaces makes one polarization state more stable than the other.

The volume effect is the most discussed in the literature, and the most likely candidates for its accomplishment are dipolar defect associates such as $(\text{Fe}'_{\text{Ti,Zr}} - \text{V}_\text{O}^{\bullet\bullet})^\bullet$, as discussed by many authors [100, 101, 105, 111, 120, 143, 159–164]. Fe can be replaced by any acceptor dopant substituting on the B-site, such as Mn [162] or Cu [101]. According to this mechanism, dipolar defect associates have their direction initially randomized by the high processing temperature during fabrication, as pictured in Fig. 5.12 (a). They then slowly aligns along a preferential, low energy direction which depends on the local direction of the polarization, as shown in Fig. 5.12 (b) where the alignment is complete, illustrating the end of the aging process. If an electric field is applied, domain walls will move, and formerly aligned defects will become misaligned with the new local polarization direction, increasing the free energy of the system, as pictured in Fig. 5.12 (c). This is because the alignment process is much slower than the frequencies at which domain wall motion and polarization switching typically occur during experiments

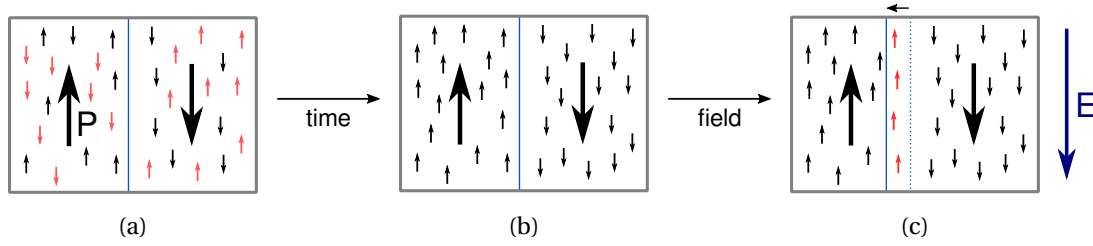


Figure 5.12 – Single crystal with two domains with various prehistories; misaligned dipoles (small arrows) are shown in red; they have larger energy than the well-aligned dipoles, shown in black. (a) : Just after cool-down from the Curie temperature, the dipolar defect associates are randomly oriented. (b) : At the end of aging, all dipolar defect associates are aligned with the local polarization. (c) : An external electric field makes one domain grow; the original position of the middle 180° domain wall is shown with a dotted line. Due to the domain wall displacement, some dipoles are now misaligned, increasing the free energy of the system.

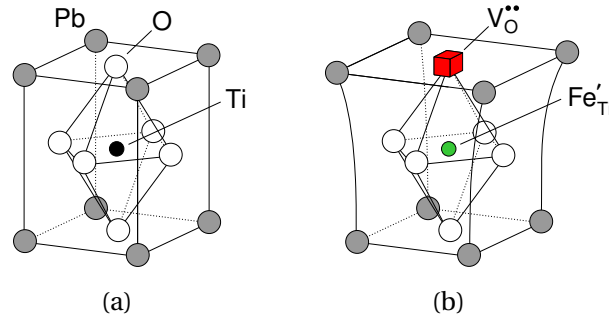


Figure 5.13 – Tetragonal unit cell of PTO free of defect (a) and containing a dipolar defect associate (b). The lattice strain in (b) is exaggerated for clarity. Dimensions are not to scale. After T. M. R  der [98].

or device operations [101]. The orientation of dipolar defect associates may be changed by the hopping of the oxygen vacancy about the acceptor ion to the neighboring positions of the oxygen octahedron, by thermal activation [120, 159]. The cations are not expected to move at temperatures lower than 1000°C , because they have no nearest-neighbor cation-sites, whereas the oxygen sites form a continuous lattice in the perovskite structure [101]. The driving force for this process may be the minimization of the elastic or electrostatic energy [143]: The deformation of the unit cell by the presence of an oxygen vacancy makes it behave like a so-called elastic dipole [120]. This is schematically pictured in Fig. 5.13. Different de-aging behavior of 180° and non- 180° domain walls in Fe-doped PZT ceramics [165] suggests that both the elastic and electrostatic energy minimization routes may coexist.

This mechanism explains well the aging process in the single domain state, in which no domain walls are present to become clamped [162]. In addition, the presence of dipolar defect associates and their alignment with an external electric field has been observed by numerous electron paramagnetic resonance (EPR) studies in Mn-doped BTO single crystals [166] and ceramics of BTO, SrTiO_3 (STO), PZT and $(\text{Pb},\text{La})(\text{Zr},\text{Ti})\text{O}_3$ (PLZT) [102, 104, 163]. Even undoped

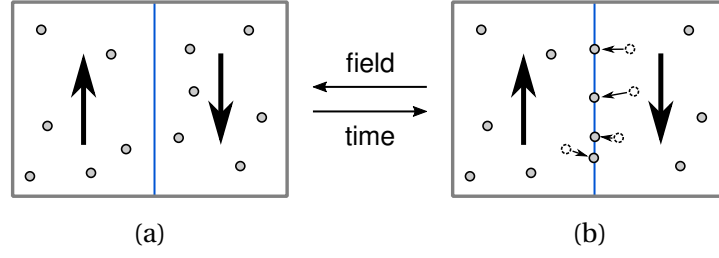


Figure 5.14 – Domain wall effect : (a) initially, some concentration of defects (gray dots) is randomly distributed in the sample. (b) : after enough time, some of those defects migrate to the 180° domain wall position (in blue), pinning it. The defects may be redistributed again, and the domain wall unclamped, under the action of a sufficiently large AC electric field, going back to the situation pictured in (a).

PZT samples showed a non-zero concentration of Fe^{3+} in a concentration of 10^{16} – 10^{17} cm^{-3} [102]. This is generally attributed to the fact that those elements are of a high relative natural abundance [167]. The stable orientation for the associate $(\text{Fe}'_{\text{Ti,Zr}} - \text{V}_\text{O}^{\bullet\bullet})^\bullet$ is along the local polarization direction [100], and isolated Fe'_{Ti} centers (*i. e.* without ancillary $\text{V}_\text{O}^{\bullet\bullet}$) have a concentration below the detection limit of EPR [100, 101]. This means that virtually all Fe^{3+} dopants are associated as $(\text{Fe}'_{\text{Ti,Zr}} - \text{V}_\text{O}^{\bullet\bullet})^\bullet$. Ref. [104] finds an activation energy of about 0.9 eV for the movement of the V_O around the oxygen octahedron for the defect associate alignment in BTO. This is close to the value of 0.84 eV obtained by density functional theory (DFT) by Erhart *et al.* in PTO [168].

The domain wall effect, pictured in Figure 5.14, is less discussed, but there is some evidence that it can contribute in addition to the volume effect. DFT simulations show that many defects have a lower formation energy at the domain wall, such as $\text{V}_\text{O}^{\bullet\bullet}$ in PTO [169], and V_{Pb}'' , $\text{La}_{\text{Pb}}^\bullet$, and $\text{Nb}_{\text{Ti}}^\bullet$ as well [111]; which implies a tendency to migrate there and have a pinning effect. Chandrasekaran and coworkers [111] found that V_O had the strongest pinning effect among the lone defects, and that the associates $(\text{Fe}'_{\text{Ti}} - \text{V}_\text{O}^{\bullet\bullet})^\bullet$ and $(\text{V}_{\text{Pb}}'' - \text{V}_\text{O}^{\bullet\bullet})^\times$ are several times stronger. The defects responsible for the volume effect could therefore have a physical pinning action on the domain wall, in addition to the volumetric pinning action described before. The motion of domain walls under the action of a small electric field, such as the one used for typical dielectric measurements, may also bring them into physical contact with defects which do not contribute to the volume effect (such as isolated $\text{V}_\text{O}^{\bullet\bullet}$), which could from then on locally pin them at this new location. From an experimental point of view, the superposition of the clamping due to a volume and a domain wall effects may be difficult to separate. The former type of clamping, where the wall enters a region of higher potential energy, is called random field defect clamping; the local drop of potential energy at the site of an isolated point defect is called a random bond defect clamping [170]. In a recent publication, Mokry and Sluka [171] showed that it was possible to monitor the progress of the pinning of 180° domain walls during aging by studying their non-linear response under very weak electric fields. In this regime, the domain wall movement is purely reversible and the pinning defects

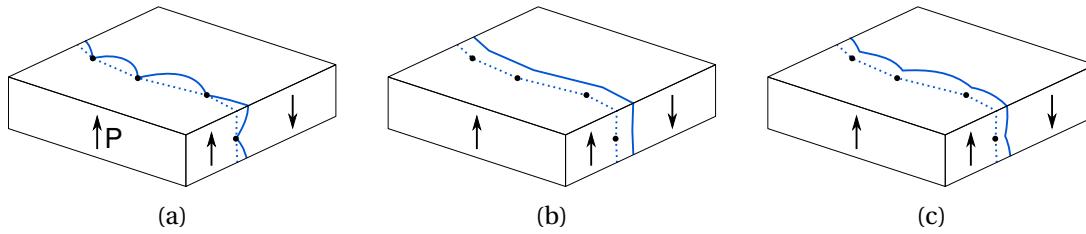


Figure 5.15 – Various modes for 180° domain wall motion. The original wall position is shown as a dotted line and the current position as a solid line. (a) : pure bending mode; (b) : pure planar mode; (c) : superposition of the bending and planar modes. After Ref. [172] and [171].

should not be disturbed, unlike the dielectric spectroscopy experiments described above. Two modes of non-ferroelastic 180° domain wall reversible motion may be distinguished: The planar mode is the oscillation of the domain wall around the pinning center, maintaining its planar shape; the bending mode is the oscillation of the domain wall as a free membrane bending between pinning points. The two modes can be superimposed; Fig. 5.15 pictures each separate mode and the superposition. The authors propose a method to identify the dominant oscillation mode by monitoring the evolution of the non-linear dielectric response with time. This is only possible under certain circumstances, but if applicable, it makes it possible to tell whether the pinning progresses through the uniform accumulation of pinning centers at the walls, or because of the redistribution of the pinning centers along specific directions. The latter process is consistent with the alignment of anisotropic defects such as dipolar defect associates, whereas the former process should not involve them, suggesting an aging process dominated by the migration of isolated defects to the wall. This method is only applicable to 180° domain walls aging, however. It was unfortunately not possible to test it within the frame of our work, but a weaker version of this method was successfully applied to a sol-gel PZT film in an earlier publication by Mokry and coworkers [172]; if further confirmed, this could open up an additional route for investigating the mechanisms of aging.

Finally, we will discuss the interface effect. In a polycrystalline, polydomain sample, it is expected that polarization mismatch at grain boundaries or at charged domain walls may exist, and the resulting local depolarization fields can be the driving force for the redistribution of free charge carriers inside the system, whatever they may be, with the same consequence of a stabilized domain pattern and reduced domain wall motions. This redistribution is schematically shown in Fig. 5.16 (a) and (b). After 180° switching, the charge situation at the grain boundaries is unfavorable, as pictured in Fig. 5.16 (c), and therefore requires more energy to be reached.

There is experimental and theoretical support for this type of mechanisms. Lupascu *et al.* argue that the orientation of dipolar associates is insufficient to explain the sometimes very large bias fields encountered in aged samples, and that the drift of charge carriers to screen local depolarization fields at the grain boundaries can provide much more clamping pressure on domain walls, making it likely to be the predominant aging mechanism [173]. Genenko

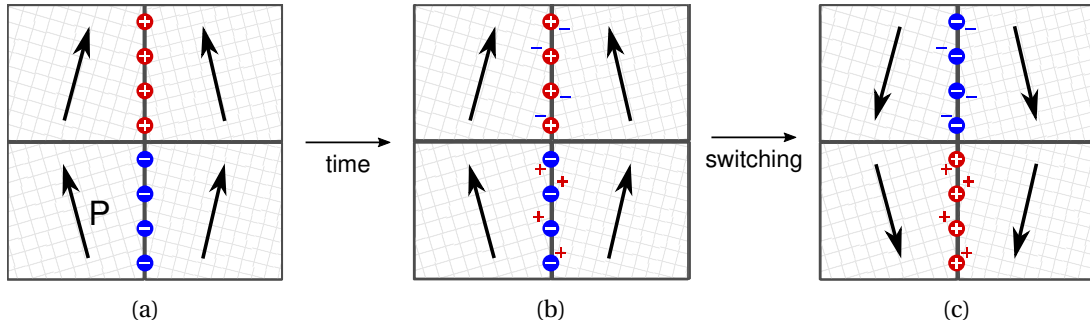


Figure 5.16 – A polycrystalline sample composed of 4 grains, for which the orientation of the grains results in a polarization mismatch at the vertical grain boundaries. (a) : the polarization mismatch causes that uncompensated bound charges (circled charges) are present at the grain boundaries. (b) : at the end of aging, free charges (undecorated charges) have migrated to the grain boundaries to compensate for the bound charges. (c) : after 180° switching of the aged state.

and coworkers [153] could well reproduce the time evolution of the internal bias field in PZT ceramics with increasing Fe-doping concentrations, from undoped to 1 at.% doping, by assuming that oxygen vacancies migrate to the grain boundaries to compensate for the bound charges present there. The diffusion activation energy of oxygen atoms in the bulk of the grains was estimated at 0.9 eV in epitaxial thin films and ceramics of tetragonal PZT, unaffected by Nb doping up to 4 at.%, with help of the depth profiling of the density of a ^{18}O tracer after an exchange anneal [174]. It is, unfortunately, about the same as the activation energy estimated for the vacancy jumps along the oxygen octahedron for the alignment of the $(\text{Fe}'_{\text{Ti}} - \text{V}_\text{O}^\bullet)^\bullet$ associate, so that it does not seem possible to discriminate between the volume and interface effects only on the basis of an activation energy value alone. Diffusion was found faster along the grain boundaries with an activation energy of 0.7 eV; however, it is not clear whether the density of oxygen vacancies at the grain boundaries can be sufficiently large for the aging process to proceed predominantly along this route. Charge separation within a non-ferroelectric layer near the film-electrode interface, to compensate the strong depolarization field which is expected to be present in such cases, has also been investigated as a possible mechanism [152, 175], also yielding good agreement with experimental data. However, in the IDE system, the film-electrode interface appears to play only a minor role, as discussed in chapter 6; for this reason, such a process is unlikely to be predominant in our case.

Maybe more interesting from an experimental point of view, are the experimentations with bandgap light illumination performed by Dimos and coworkers [176]. By applying a sub-coercive voltage on a poled sample under monochromatic UV light illumination, they could suppress the switching polarization to an important degree, for PZT and PLZT ceramics and thin films. The maximum suppression occurs by application of a bias near the coercive voltage. The original PV loop can be reversibly restored by the appropriate combination of light and voltage. Dimos *et al.* [176] interpret this results as the freezing-in of domains due

to the compensation of local depolarization fields by the electron-hole pairs generated by the UV light. This novel instance of domain pattern stabilization can be interpreted as an extreme case of a restoring force to a memorized state: since a fraction of the sample volume is frozen-in and do not participate in the polarization switching any more, the restoring force can be considered as infinitely large. They report an increase in switchable polarization when switching is performed under illumination, suggesting a larger domain wall mobility in this case. This is consistent with the previous description; the continuous compensation of bound charges by the supply of photo-induced carriers would facilitate the switching process, while this same supply as a pulse of fixed duration can stabilize the static domain pattern by the local trapping of the generated charges. The latter mechanism has been proposed as a candidate for ferroelectric fatigue in thin film capacitors [110, 177]. Formally, this can also be regarded as a domain wall effect, since the photogenerated carriers can also compensate bound charges present at domain walls. These observations are not satisfactorily explained by the volume effect, however. Since the bandgap of PZT is quite large (3.4 eV according to Scott *et al.* [178]), it is expected that these mechanisms cannot be observed in regular experimental conditions, where bandgap light should be absent; PZT is a *p*-type semiconductor for which a significant amount of holes are trapped [179], and thereby cannot contribute much to any compensation mechanism in the absence of photogeneration. However, the experiments of Dimos *et al.* [176] strongly support the existence of uncompensated bound charges in the material, and these can also be compensated by ionic defects (*i. e.* charged oxygen vacancies) instead of by electronic charge carriers. Oxygen vacancies should always be positively charged as $V_O^{\bullet\bullet}$ in PZT [111]. Note that uncompensated bound charges at domain walls are not restricted to the case where the neighboring polarization vectors meet head-to-head or tail-to-tail; a 180° domain wall which is not perfectly parallel to the polarization vectors of the domains it separates would bear a net uncompensated bound charge as well [110].

There is experimental evidence that several mechanisms are indeed active at the same time. Morozov and Damjanovic [107] extracted, from impedance spectroscopy data from an Fe-doped rhombohedral PZT ceramic, the activation energy for AC conductivity and DC conductivity, at 0.6–0.8 eV and about 1 eV, respectively. The conductivity process was attributed to hopping conductivity; higher energy barriers must be overcome for long-range drift in this case [180], explaining the energy difference. Earlier de-aging experiments by the same authors [118] showed that the activation energy for the de-aging process was field dependent, at 0.64 eV for low fields and 0.92 eV at higher fields. This strongly suggests that two separate mechanisms for aging are active, one involving short-range motion and one involving long-range motion of charges. The de-aging process then proceeds separately for each, with only the short-range relaxation being active at low fields, whereas larger fields are needed for the long-range relaxation — consistently with the larger activation energy required for long-range drift of charges.

We are therefore presented with the picture of an aging process where several mechanisms are likely to be active at the same time, making their experimental separation very challenging. From the previous enumeration, we can make the following remarks in order to attempt this separation nonetheless:

1. The volume effect is also a local effect; the alignment of dipolar defect associates with the local direction of the polarization should not be sensitive to mesoscopic or macroscopic quantities, such as the domain wall density, the unpoled or poled state of the sample, or the polarization mismatch at grain boundaries.
2. The interface effect should be sensitive to the unpoled or poled state of the sample, since the shape of the (local) depolarizing field should be different in each case, unless domains are very wide in the unpoled sample.
3. UV light illumination may reveal the existence of uncompensated bound charges, *i. e.* of local depolarization fields, by the effects reported by Dimos *et al.* [176]. If their compensation is the main mechanism of aging, this compensation may be fully achieved by the photogeneration of free carriers. In other words, the sample may be fully aged in a short time with the appropriate illumination treatment, after which no aging should take place anymore.
4. Apart from using the method proposed by Mokry and Sluka [171], it does not seem possible to experimentally separate between the volume effect and the domain wall effect. Even though charges are expected to travel over larger distances in the domain wall effect, separation would be possible in this case only if the activation energies for AC and DC conductivity significantly differ, and provided that the domain wall density is not too large, so that the drift distance is sufficiently large to require DC processes to be crossed.

5.4 Goals of this chapter

As we have seen in the above discussions, the topic of aging and imprinting remains controversial and in-depth investigations into this topic is beyond the scope of this work. However, there is great practical interest into the question of aging. For devices operated with small fields or used as energy harvesters, depolarization of the poled state is very detrimental and can turn the device inoperable. Thermodynamical stabilization of the poled state, even at the expense of some partial loss of the piezoresponse, is therefore a precious property. In addition, the reduction of hysteresis after aging is also an advantage for various kinds of applications. To our knowledge, the aging of PZT thin films with IDE is not documented yet, and this chapter is a first attempt at quantifying this process for that configuration.

Besides, there were little investigations on the effect of bandgap light illumination after the publication of the work of Dimos and coworkers [176] mentioned above. They also report

Table 5.1 – Evolution of the remanent ε_f , remanent small-signal $e_{33, \text{if}}$, and material figure of merit $e_{33, \text{if}}^2/\varepsilon_0\varepsilon_f$ after 8 weeks of aging at room temperature after the initial poling event on the day of anneal. The sample is an undoped PZT 53/47 film with IDE.

Time	Rem. ε_f (-)	Rem. s.-s. $e_{33, \text{if}}$ (C/m ²)	$e_{33, \text{if}}^2/\varepsilon_0\varepsilon_f$ (GJ/m ³)
Day of anneal	930	18	39
8 weeks after anneal	710	16.5	43

that the combination of a voltage and UV light illumination aids the poling process. This treatment is therefore very interesting from both a scientific and application point of view, since it potentially provides not only improved stability but also a better poling.

The most interesting situation for energy harvesting is an asymmetric aging process which pins ferroelectric domain walls but not ferroelastic domain walls. This could be the case if the driving force for aging is principally of an electrostatic nature. Such a process would reduce ε_{ext} , thereby lowering the capacitance of the device, while the piezoelectric response is retained because e_{ext} does not change. This would increase the FOM, since it is equal to:

$$(1 - \eta) \frac{e^2}{\varepsilon_0\varepsilon_f} = \frac{1 - \eta}{\varepsilon_0} \frac{(e_{\text{int}} + e_{\text{ext}})^2}{\varepsilon_{\text{int}} + \varepsilon_{\text{ext}}} \quad (5.16)$$

In this case, the aging process would bring two benefits: improved stability of the poled state, and larger harvesting efficiency. Such a process seems to occur naturally, as shown in table 5.1: after 8 weeks of aging at room temperature, the material figure of merit has slightly improved. It is therefore very desirable to gain some control over this process by appropriate material design and treatments.

5.5 Methods

All the samples measured in this study were fabricated with the gradient-free sol-gel route and patterned by photolithography and lift-off following the route described in chapter 4. Unless otherwise mentioned, two RTA steps were performed to grow the PZT films, yielding a thickness between 500 nm and 650 nm in all cases. XRD showed that the films were all fully in the perovskite phase; some of the films had the {100} texture while others were randomly oriented. If not mentioned otherwise, when two films are compared they possessed the same texture. The microstructure of all the films was similar to what is presented in chapter 4. Two PZT compositions were used, PZT 53/57 (MPB) and PZT 43/57 (tetragonal). The concentration of the dopants are 1 at.% for the Fe-doped samples and 2 at.% for the Nb-doped samples — all the doped films are the same as those studied in chapter 4.

The aixACCT[®] TF2000 setup was used for all the standard electrical measurements, and a triangle wave was used to record the PV loops. For dielectric spectroscopy measurements, we used an SR830 DSP lock-in amplifier (Stanford Research Systems) as the voltage source

and for recording the polarization harmonics. A sine wave was used as the driving field. A wide-band power amplifier of model 7602M (Krohn-Hite Corporation) was used to amplify the voltage of the lock-in amplifier. Details on this setup are presented in appendix G. For UV light illumination, we used a 100 W mercury arc lamp (Ushio Inc.) with a 6281 power supply (Oriel Instruments), or a UV laser diode of wavelength 375 nm and optical output power of 70 mW (model RLU4116E, Roithner LaserTechnik GmbH). A fiber optic cable was used to direct the UV light from the Hg arc lamp towards the samples, which were located inside a cylindrical white cardboard case for illumination; both samples and case were standing on an alumina ceramic disc a few mm thick. No filter was used. If not otherwise specified, all the samples were annealed at 550 °C for 10 min under 100 sccm of oxygen flow prior to each measurement, to provide for an identical unaged state of reference for all samples at the start of the experiment.

As seen in chapter 3, it is necessary to apply a number of corrections for electrical measurements of PZT thin films with IDE. If not otherwise specified, the electric field shown in the figures is always obtained with the Igreja model, and the parasitic capacitance was estimated with the conformal mapping model, and subtracted.

For monitoring the progress of imprint, we recorded PV loops (with no prepolarization pulses) at fixed time intervals and at the same maximum field for all samples. The initial poling was accomplished by the first PV measurement. After each measurement, the sample is left in the same poled state. For practical reasons, the electrodes were short-circuited between measurements only for times lower than 10^4 s, after which the samples were left to age in open circuit conditions. With this limitation in mind, we still present the results for times after the short-circuit condition was lifted.

Unlike aging studies on ceramics, where the state after the slow cool-down from the sintering temperature can be used as a reference aged state for all samples, we do not have a convenient reference aged state for sol-gel PZT thin films. Cool-down from the crystallization temperature of 650 °C in the RTA tool takes only a few minutes, and none of the investigated samples showed any pinching when measured immediately afterwards. The pinching appears after several days (resp. weeks) at room temperature for samples with the tetragonal (resp. the MPB) composition and is erased after only a few saturating PV cycles at 20 Hz. On the contrary, the time evolution of the poled state was very fast : after poling, the PV loop offset typically reached half the coercive field after only 1 day at room temperature. For this reason, we have monitored the progress of imprint rather than attempting de-aging experiments; and we have also compared the effect of various treatments on the aged state of the sample.

The internal bias field E_i is a measure of the energy difference between the two poled states [120]. We calculate it as the field offset of the coercive fields, which are given by the position of the peaks of the $\partial P/\partial E$ loop, as :

$$E_i = \frac{E_c^+ + E_c^-}{2} \quad (5.17)$$

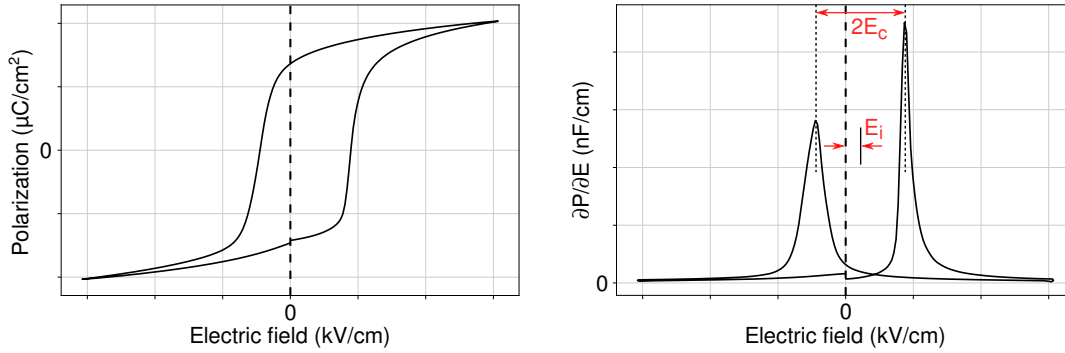


Figure 5.17 – Definition of the PV loop field offset on the PV loop of an aged undoped MPB film with IDE.

where the positive and negative coercive fields E_c^+ and E_c^- are taken with their sign. This is geometrically shown in Fig. 5.17. For the IDE configuration, this method depends on the model used to calculate the true electric field from the applied voltage. Unless specified otherwise, this model is the Igreja formula.

In the following we will use the terms “aging” and “imprint” interchangeably when we investigate aging in the poled state. The term “imprint” will be preferred when referring to features specific to the process of aging in the poled state, while “aging” shall be used whenever we mean the general process.

For all our measurements of aging in the poled state, we have initially poled the sample in the negative polarization state, so that it is always this state which is stabilized by the aging process, and the internal bias is always positive, *i. e.* the PV loop is shifted towards the right side of the chart. Therefore, the switching from the aged state to the other state will occur upon application of a positive electric field, and the switching from the other state to the aged state will occur with a negative electric field. In the following, in order to provide polarity-independent terms, we will refer to the former switching event as the “up-step” switching event (going to a state with larger free energy) and to the latter as the “down-step” switching event (going to a state with lower free energy). Note that, for either switching event, a potential barrier must be overcome in any case. The back-switching upon voltage removal is always the back-switching from the aged state, *i. e.* the “up-step” back-switching.

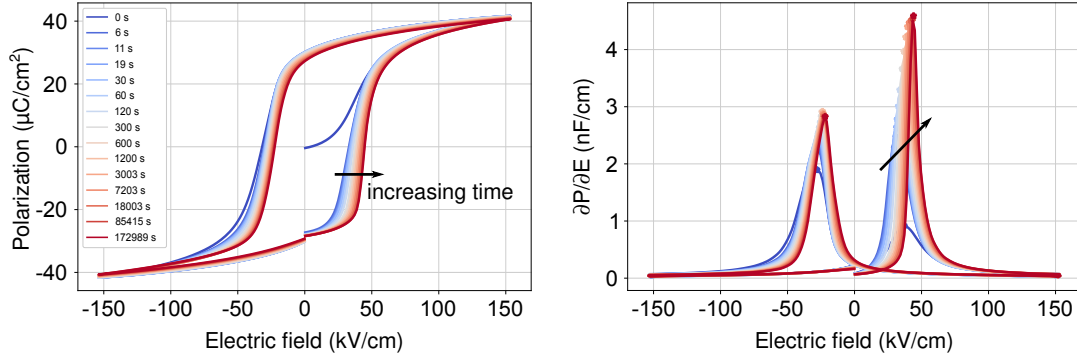


Figure 5.18 – Sequence of PV and the corresponding $\partial P/\partial E$ loops during an imprint experiment of an undoped MPB film with IDE. The color scale is given in the inset in the left chart. The position of the calculated coercive field is indicated by a star in the $\partial P/\partial E$ loop. The time elapsed between the first loop and last loop shown is 48 h and 3 min.

5.6 Experimental results

5.6.1 General observations and UV light exposure

Figure 5.18 shows a typical sequence of PV loops measured over a period of 2 days from initial poling in the negative polarity state. The triangle wave starts at 0 electric field and increases first to the positive field values. We can make the following observations regarding the progress of imprint :

1. The PV loop field offset increases with time.
2. The PV loop becomes more square, with higher $\partial P/\partial E$ peaks at switching.
3. The switchable polarization decreases. Note that, since the current integration constant is arbitrary, the PV loops are centered by the measurement software such as $P(E_{\max}) = -P(-E_{\max})$.
4. The “up-step” $\partial P/\partial E$ peak shifts more quickly towards the right side of the chart than the “down-step” peak does.
5. The backswitching decreases with time.

The increasing asymmetry of the two $\partial P/\partial E$ peaks, and the difference in speed at which they shift, could be the consequence of aging in the poled state, but also of the asymmetry of the measurement, since we do not measure closed loops. The asymmetry of the two peaks is not always as pronounced as the example shown in Fig. 5.18; for some samples, it is the “down-step” peak which becomes the highest in the course of aging; however, the “up-step” peak is always more shifted than the “down-step” peak. At present, we do not have an explanation for this observation. The decrease in switchable polarization is presumably due to the fact that one polarity is less saturated than the other (the aged polarity is slightly more saturated after each cycle), and this lower saturation is not compensated by the increased saturation for the other polarity. This is suggested by the shape of the $\partial P/\partial E$ loop at high fields: At highly positive fields, the derivative is larger than at highly negative fields. That is a consequence of

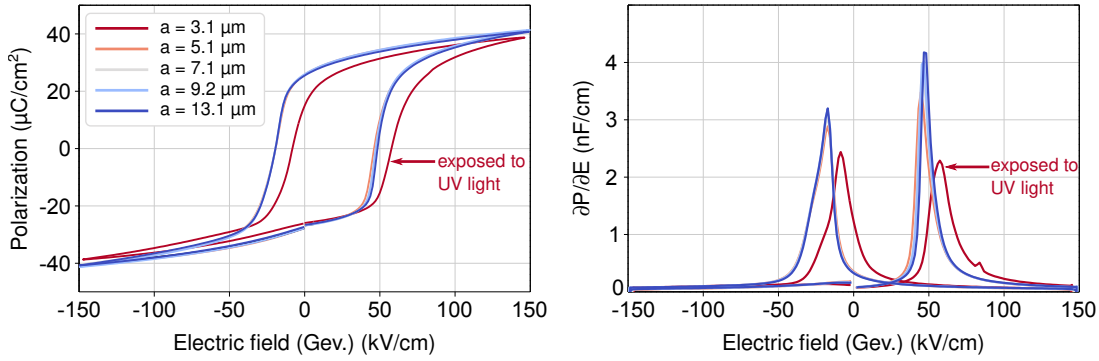


Figure 5.19 – PV loops for the same PZT thin film with various IDE gap distance and the same finger width recorded two weeks after the initial poling. One sample was in addition exposed to UV light with the Hg arc lamp. The electric field was obtained with the Gevorgian model.

the shift of the $\partial P / \partial E$ peaks towards the positive side of the electric field axis. The increased squareness of the loop is very likely the consequence of aging. Aging in the poled state can be regarded geometrically as the pinching of the PV loop near saturation instead of near zero electric field, resulting in a larger slope on the branch leading towards the stabilized state. It is not clear however, why the “up-step” transition also becomes more abrupt. Since aging is related to the relaxation of internal stresses and charges, an aged sample may display a much more homogeneous coercive field for both “up-step” and “down-step” switchings, resulting in a squarer loop.

Figure 5.19 shows the PV loops of the same PZT film with various finger distance and the same finger width, measured two weeks after initial poling. One of the samples was in addition exposed to UV light with the Hg arc lamp prior to the PV measurement. The PV loops of the aged samples which were not illuminated superimpose very well. The trend for the $\partial P / \partial E$ peak height, which is larger for larger gaps, follows that observed for unaged samples in chapter 3. Hence, we conclude that the aging process is gap-independent, in the range of gap values investigated. UV light illumination has a significant effect on the PV loop. Our observations are the following:

1. The PV loop is significantly more offset.
2. The switchable polarization is further decreased.
3. The back-switching from the aged polarization state is further reduced, so that it is virtually absent.
4. The PV loop is more slanted.

The reduction in switchable polarization was also observed by Dimos *et al.* [176]. The fact that the PV loop becomes more slanted instead of more square — which translates in reduced height for both $\partial P / \partial E$ peaks — suggests that the effect of UV light illumination is not the continuation of the imprinting process, but the consequence of a different process which adds up to the progress of imprint already accomplished.

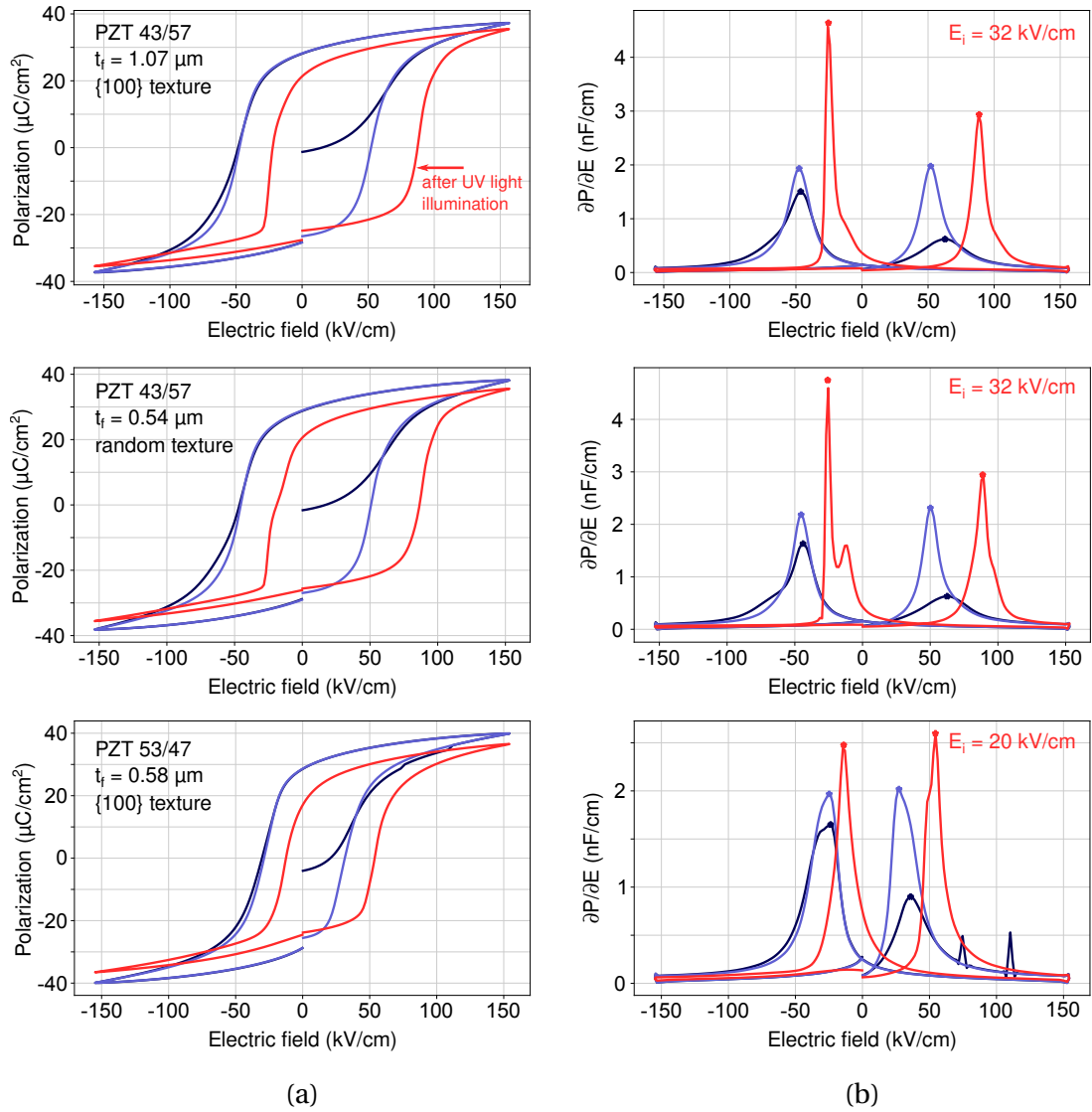


Figure 5.20 – Series of sample exposed to the Hg arc lamp for 1 hour. (a) : the first two PV loops and the loop measured after UV light exposure. Details on the film is shown in the top-left corner of each chart. (b) : corresponding $\partial P/\partial E$ loop. The value of E_i after UV light exposure is shown in the top right corner of each chart.

Figure 5.20 shows the result of 1 h exposure to the Hg arc lamp immediately after poling, for films of various compositions, thickness and texture. Two PV loops were recorded on the unpoled samples (blue curves in Fig. 5.20), which were then exposed all at the same time; after that, a single PV loop was recorded (red curve in Fig. 5.20). We can make the same observations as above, except that, this time, the PV loops do not appear more slanted after illumination. This could be because previously, we compared the effect of UV illumination for aged samples, while we now show fresh samples, whose PV loops are less square than the aged curves. The value of E_i after illumination is the same for both tetragonal samples, and

is significantly lower for the sample with the MPB composition. Another film was treated in the same way, also of the MPB composition, and with similar thickness and texture as the MPB film shown in Fig. 5.20; it displayed $E_i = 17 \text{ kV/cm}$ after the treatment. Lastly, we observe some degree of peak splitting in the $\partial P/\partial E$ curve for the tetragonal samples. This suggests that different parts of the films are being imprinted at different rates. This was also observed on poled samples left to age for a long time, without any illumination. We do not have an explanation for this observation at present.

Apart from the small differences that we reported, neither the texture nor the film thickness appears to have an influence on the resulting offset. It is not clear whether the aging process continues undisturbed in parallel to the effect of illumination; if it does, it can account however for only at most half of the total E_i , comparing with the offset obtained 1 h after the initial poling event without illumination (see Fig. 5.22 for the tetragonal sample and Fig. 5.23 for the MPB sample). The lower offset of the second MPB film tested can then be explained by the observation that this film showed a slightly lower aging rate (see light blue curve in Fig. 5.23). We also observe that the shift of the “up-step” $\partial P/\partial E$ peak is larger than that for the “down-step” peak. In Fig. 5.19, the exposed sample had aged for two weeks, after which time the rate of evolution of the offset has dropped dramatically; thus we can safely assume that the imprint did not progress during the illumination time, and we can state that the additional shift after exposure is entirely due to the effect of UV light. This additional shift is, in this case, the same for both peaks. This is qualitatively different from illumination immediately after the first poling event.

To confirm this latter observation, we have performed an additional illumination experiment on a sample aged for 1 month in the poled state. The sample was illuminated with the Hg arc lamp on the day of initial poling, and then left to age for 31 days. After this time has elapsed, the aging rate is practically zero. The sample was then illuminated for 10 min, and then 30 min, with the UV laser diode, and a PV loop was recorded just before the first illumination step and after each illumination steps. The measurements are shown in Fig. 5.21. Dashed lines indicate the position of the coercive fields on the $\partial P/\partial E$ loops, and the gray scale bars are of the same dimensions for the “down-step” and “up-step” peaks. Here also, the induced shift is the same for both peaks, and the loop also becomes more slanted. Note that the laser diode provides a much larger radiative energy per unit area, because there is direct line of sight between the source and the sample, and because the beam is collimated; this permits a significant shifting of the PV loop in a fraction of the time that would be required with the Hg arc lamp. After a total of 40 min of exposure, E_i has doubled, and the “down-step” coercive field has almost reached 0.

Therefore, UV light illumination does not seem to have the same effect when applied to freshly poled samples instead of aged samples. With the present set of data, we cannot provide evidence that the aging process and the effect of UV light are independent and occurring in parallel. This may be the case only if aging, within the time frame of the experiment, is mostly due to a volume effect, or a domain wall effect involving the diffusion of uncharged defects,

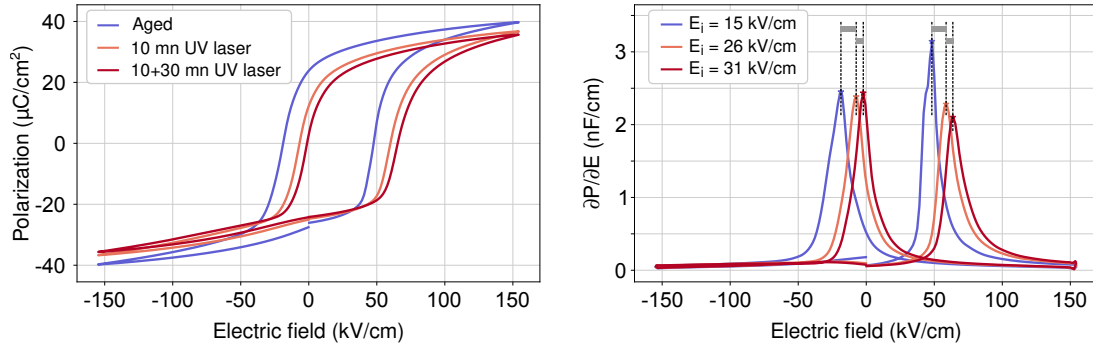


Figure 5.21 – PV loop of an aged, undoped, {100}-textured PZT 53/47 sample with IDE, exposed to the UV laser diode. The color code is shown in the PV loop chart, and the field offset for each curve is shown in the $\partial P/\partial E$ chart.

such as elastic, non-electrostatic dipoles. Both interface effect and domain wall effect, which rely on the drift of charged defects, would be affected by photogenerated carriers. The very fast offset build-up during illumination is due to the fact that the carriers are generated everywhere in the sample, and in particular in the vicinity of the uncompensated bound charges, so that they do not need to travel long distances to reach them. Note that, in the IDE configuration, the active PZT volume is not covered by electrodes and is therefore directly exposed to external radiations; thus, it is not surprising that it is so sensitive to bandgap light.

We observed that repeated illumination continues to increase the offset of the PV loop, but this effect becomes less and less pronounced with cumulative illumination time. This is visible in Fig. 5.21 where the offset increase after 30 min of exposure is only a fraction of the offset produced by the previous 10 min of exposure. This may be due to the decreasing intensity of the local depolarization fields, which are further compensated after each illumination step. There is a competition between bound charges compensation and recombination of photogenerated charge carriers. The latter is prevented by the presence of depolarization fields, which separate electrons and holes upon their creation; however, this separation mechanism becomes less effective after the intensity of these fields have decreased.

UV illumination offers an interesting tool to tune the stability of the poled state. It can be used as an “aging accelerator”, *i. e.* as a treatment to fully age samples, so that they do not age anymore in the rest of the device life. It can also be employed simply to improve the stability of the poled state, when this stability is critical for operations. Further investigations are needed to better understand the action of UV light on the films, and in particular to verify their influence on the piezoelectric properties, a point which has not been treated in this work.

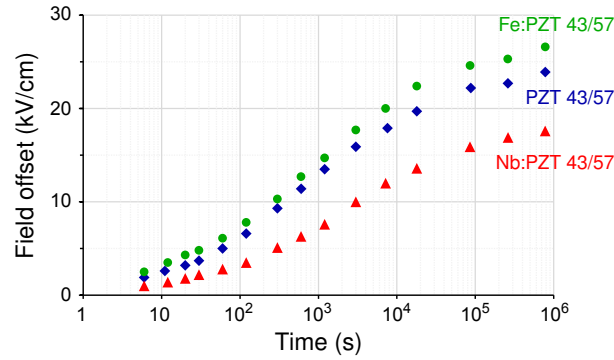


Figure 5.22 – Offset evolution with time for {100}-textured tetragonal PZT thin films with IDE, with various dopants. The color code is given in the chart.

5.6.2 Rate of imprint

In this section we present experimental results showing the rate of imprint for various sample compositions and doping. We recorded PV loops at specific time intervals; the initial poling was accomplished by the first PV loop. The driving field was a triangle wave at 20 Hz with a maximum electric field of 150 kV/cm. This measurement routine results in a competition between aging and the voltage cycle, which partially de-ages the sample at every measurement. We expect that this competition will not greatly influence the aging process if the measurements are performed at sufficiently long time intervals. This is not the case for the beginning of the curves where measurements are performed only several seconds apart. However, since all the samples were measured in the same conditions, we can still compare the time evolution of the PV loop offset between them.

Figure 5.22 shows the influence of two kinds of doping for {100}-textured tetragonal films. As expected, the Fe-doped film is aging at the fastest rate and the Nb-doped film is aging at the slowest rate. Even though we did not reach saturation within the presented time frame, the evolution of the curves suggests that the saturating offset follows the same trend as the aging rate. Nb-doping has significant effect over the aging rate and extent, but does not cancel the effect of aging altogether, which is still significant. This is somewhat surprising considering that donor-doped PZT samples are often credited with small aging in the literature on ceramic samples [11, 107]. It may be the consequence of the small atomic content of the dopant used, which was 2 at.% for Nb. If the effect of donor doping merely compensates for the acceptor impurities naturally present in undoped compositions [11], then a small atomic content of the donor dopant may be insufficient to counterbalance the effect of those impurities, which may be more abundant in thin films than in ceramics due to the different processing conditions. The effect of acceptor doping is less pronounced, consistently with a lower atomic content of only 1 at.%. The dielectric spectroscopy experiments discussed in chapter 4 showed that, for aging in the unpoled state, the trend is the same.

Figure 5.23 shows the influence of Nb doping for {100}-textured PZT films with the MPB

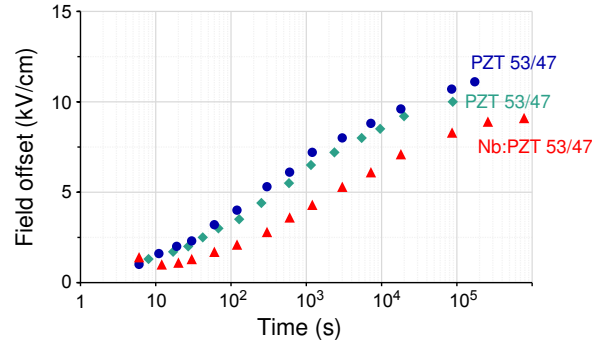


Figure 5.23 – Offset evolution with time for {100}-textured MPB PZT thin films with IDE, with and without Nb doping. The color code is given in the chart.

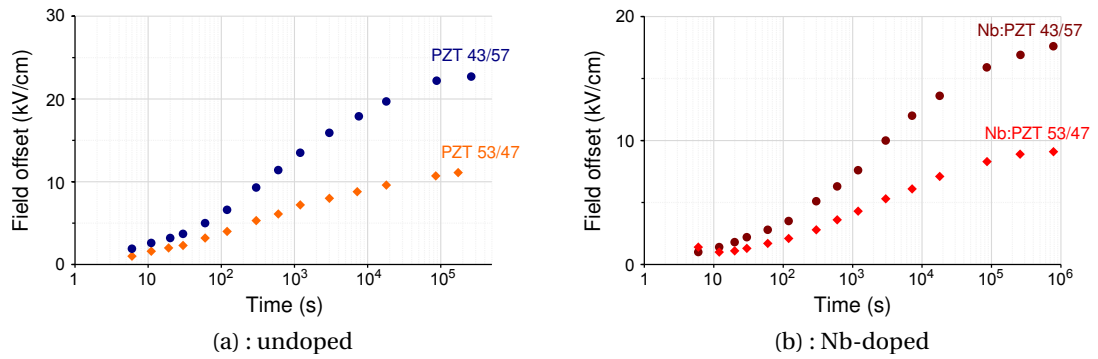


Figure 5.24 – Offset evolution with time for {100}-textured MPB and tetragonal PZT thin films with IDE, undoped (a) and with Nb doping (b). The color code is given in the chart.

composition. Two different undoped films with a similar texture and thickness were tested for comparison, and they show a very similar time evolution. As for tetragonal samples, Nb-doping reduces the aging rate and the saturating offset, and the effect is proportionally less pronounced than for the tetragonal composition, even though the atomic content is the same at 2 at.%. Fig. 5.24 (a) and (b) compare the offset build-up rate for the tetragonal and MPB composition. The MPB composition shows a drastically reduced aging rate as compared to the tetragonal composition, both with and without Nb doping.

Figure 5.25 compares the aging rate for two samples with the same composition and doping, one with the IDE configuration and the other one with the PPE configuration. The PPE sample is the same PZT film studied in chapter 4. This film shows some imprint even in the unaged state due to the presence of self-poling. Both the aging rate and the apparent saturating offset of the PPE sample are significantly lower than that of the IDE sample. This suggests that the aging process in samples with the IDE configuration may be qualitatively different from samples with the PPE configuration. A major difference between the two is the important role of the electrode-film interface in the PPE case, and the in-plane polarization vector, orthogonal to grain boundaries in sol-gel films, in the IDE case. Each could be a critical part of the aging process for each configuration. Further work is needed to fully determine this point. This

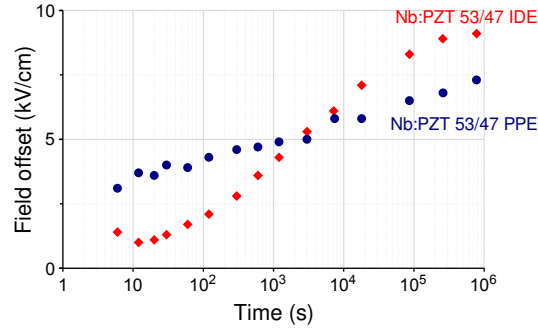


Figure 5.25 – Offset evolution with time for {100}-textured MPB PZT thin films with Nb doping, in the PPE and in the IDE configuration. The color code is given in the chart.

already means that, in addition to better retention and remanence properties, as seen in chapter 4, IDE samples also display a more pronounced stabilization of the poled state with time, and are therefore ideally suited for applications where depolarization leads to device failure.

Because Nb doping reduces the concentration of $V_O^{\bullet\bullet}$ [101] as well as the sample conductivity [11], and since Nb_{Ti}^{\bullet} does not form an associate with its compensation defect V_{Pb}'' [111], it is expected to reduce aging for the three classes of mechanisms. Conversely, because it increases the concentration of $V_O^{\bullet\bullet}$ [101], associates with them to form a dipolar defect which can align with the local polarization [111], and increases the conductivity [11], Fe doping can contribute to all three mechanisms of aging. Therefore, since the doped samples behave as expected from these remarks, doping alone does not allow to distinguish between the aging mechanisms. The small difference in aging rate between the two undoped MPB films is not pronounced enough to be really significant.

The difference in aging rate between tetragonal and MPB samples is more delicate to interpret. For the same doping (Nb doping or no dopant), the defect nature and concentration should not be significantly different between the two compositions. Therefore, the dipolar defect associates content should be about the same. Eichel [101] mentions the presence of reduced Ti on the B-site, Ti_{Ti}' , which can be formed in compounds containing BTO processed under low oxygen partial pressures. They are found to associate with $V_O^{\bullet\bullet}$, which are formed along them in reducing conditions, creating the dipolar defect associate $(Ti_{Ti}' - V_O^{\bullet\bullet})^{\bullet}$, which can contribute to aging like $(Fe_{Ti}' - V_O^{\bullet\bullet})^{\bullet}$ in PZT [101]. The presence of Ti^{3+} ions is reported in lead titanate doped with La and Cu [181], but only at temperatures below 160 K. If it exists in PZT, Ti_{Ti}' may have a larger concentration for Ti-rich compositions; however, our samples are processed in oxidizing conditions, hence it is not likely that its concentration exceeds that of the naturally occurring impurities. Indeed, Warren *et al.* [102] report a concentration (obtained by EPR) of Ti^{3+} comparable to that of Cu^{2+} and Fe^{3+} , at 10^{16} – 10^{17} cm⁻³, in undoped PZT ceramics with the MPB composition. Hence, the more pronounced aging of the tetragonal samples cannot be satisfactorily explained by the larger Ti content alone. After Arlt and Neumann, the internal

bias E_i at time t is given by [120]:

$$E_i = \frac{\Delta n(t) \Delta W}{P_s} \quad (5.18)$$

where P_s is the spontaneous polarization within a domain, $\Delta n(t)$ the density of defects aligned in excess along the lowest energy direction, and ΔW the free energy difference between the highest and lowest energy directions. P_s should be lower for the MPB composition as compared to our tetragonal composition [20]. As discussed above, we expect that $\Delta n(t)$ is similar for the two compositions. However, estimating the change of the ΔW value is problematic; at the MPB composition, the polarization can take additional directions as compared to the tetragonal composition. This is also true in our sol-gel films, for which only a fraction of the film volume actually has the MPB composition, whereas the rest should be evenly distributed between the tetragonal and the rhombohedral phase due to the small composition gradient which remains even in the gradient-free route [47]. It is not clear whether the difference in ΔW alone can explain the large difference of aging rate between the MPB and the tetragonal compositions. Since dipolar defect associates of the type $(\text{Fe}'_{\text{Ti}} - \text{V}_\text{O}^{\bullet\bullet})^\bullet$ have a tetragonal symmetry, we could presume that ΔW should be larger for the tetragonal composition; as such, the ratio $\Delta W/P_s$ could be similar for both compositions. In this case, according to equation 5.18, E_i should have a similar time evolution for both compositions. This would exclude the volume effect as the dominant process of aging. Note that, however, elastic effects such as the ones described by Robels and Arlt [143] were ignored. The elastic properties of defects, as well as the film stress, may differ for the two compositions, resulting in different aging rates as well. This additional complication is, unfortunately, seldom mentioned in the literature, which mostly focus on the electrostatically driven aging mechanisms (elastic effects are for instance absent from the review by Genenko and coworkers [119]). Even though, on the macroscopic scale, the stress situation of the film should be the same after the polarization is switched by 180°, local stress relief processes may exist and hinder domain wall motion upon switching. It is beyond the scope of this thesis work to further discuss these effects. These considerations illustrate well the complexities of the aging process, and we cannot unambiguously exclude the volume effect from the information of Figure 5.24 alone.

Table 5.2 shows the remanent polarization after the initial poling step for a selection of the investigated samples. Note that the remanent polarization increases in the course of the experiment, since, after every PV loop measurement, the aged state (which is the negative polarity side in our experiments) is slightly more saturated. Hence the value shown in Table 5.2 may not be valid at the end of the aging process. We still use them for the purpose of a qualitative discussion. The fact that they do not differ much between different compositions, for a given dopant concentration, excludes interface effects of the type proposed by Grossmann *et al.* [152, 175], for which the offset buildup should be driven by the net polarization of the film.

Table 5.2 – Remanent polarization after initial poling for some of the investigated films.

Film	Remanent pol. ($\mu\text{C}/\text{cm}^2$)
PZT 43/57	25
Nb:PZT 43/57	17
PZT 53/47	27
Nb:PZT 53/47	17
Nb:PZT 53/47 PPE	9

At this stage, we also cannot exclude the contribution of both a domain wall effect and an interface effect due to the polarization mismatch at the grain boundaries. The domain pattern is likely very different in the poled MPB and tetragonal films, since much less polarization direction are allowed in the tetragonal phase. It is difficult to discuss further how this could enhance the aging properties without more knowledge about the actual domain pattern after poling. Piezoforce microscopy (PFM) has been attempted on our samples. The small grain size, the absence of a counter-electrode at the bottom of the PZT film, combined to the much lower signal-to-noise ratio of the lateral mode of the PFM tip used to obtain the contrast for the in-plane components of the polarization vector, resulted in systematic failure to image the in-plane domain pattern of the films with the MPB composition. As a consequence, the two patterns could not be compared. The imaging was more successful for tetragonal compositions. Figures 5.26 (b) and (d) show in-plane PFM amplitude images of the same {100}-textured PZT 43/57 film with IDE, respectively unpoled and after a 30 s-long DC voltage pulse at 50 kV/cm. The topography images are also shown for both. The contrast in the amplitude image is given by the orientation of the in-plane component of the polarization vector inside the grain: out-of-plane components and in-plane components oriented along the PFM cantilever axis, as well as domain walls, appear black. We observe a relatively complex pattern inside large grains, while the pattern inside the small grains is barely discernible. This is not very informative, since the large grains are shallow and as such, are not representative of the sample volume. We imaged the film after increasingly larger poling voltages, and we could qualitatively observe that the domain pattern was becoming less complex, showing larger zones with the same pattern and favoring one specific direction for the domain walls rather than forming cross-hatched patterns. The domain size, even after poling, was of the order of 10 nm whenever visible, and it was not possible to observe domains inside small grains, so that we do not know with certainty whether they were in a polydomain or in a single domain state. Therefore, even this qualitative evolution of the domain pattern upon poling does not bring clear material to our discussion.

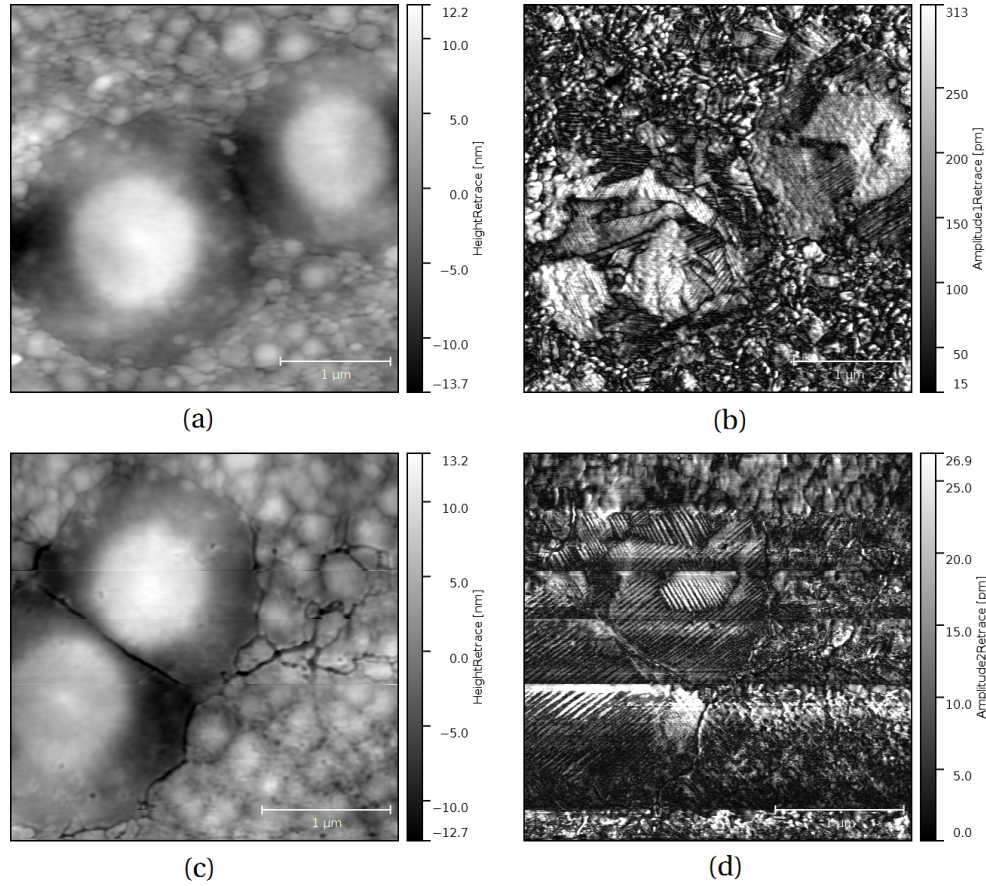


Figure 5.26 – Topography image (a) and in-plane PFM amplitude image (b) of an unpoled {100}-textured PZT 43/57 film with IDE. (c) and (d) show the same, respectively, after a 30 s-long DC voltage pulse at 50 kV/cm. Note that a different zone has been imaged in (c)-(d).

However, the polarization mismatch at the grain boundary can be studied in more detail. In sol-gel PZT films with IDE, the in-plane component of the polarization vector, after alignment with the electric field following poling, is always orthogonal to the grain boundaries, because of the columnar grain growth during the crystallization anneal. This is an immediate source of polarization mismatch at the boundaries between adjacent grains, since the textured growth means that the in-plane orientation of the grains is random. If this mismatch is the driving force of the aging process, then a larger polarization mismatch at the grain boundaries should result in a faster aging rate and a larger value for the saturating internal bias. To qualitatively estimate the extent of the polarization mismatch for a tetragonal and an MPB sample, we have used a simple geometry with square grains with sides parallel to the electrode fingers, as pictured in Fig. 5.27 (a). We used calculations similar to those shown in appendix F in order to determine the polarization mismatch for an arbitrary relative orientation of two neighboring grains. Then we calculated the mismatch 10^6 times for relative orientations chosen at random, yielding histograms for the grain boundaries orthogonal to the poling field direction, and for

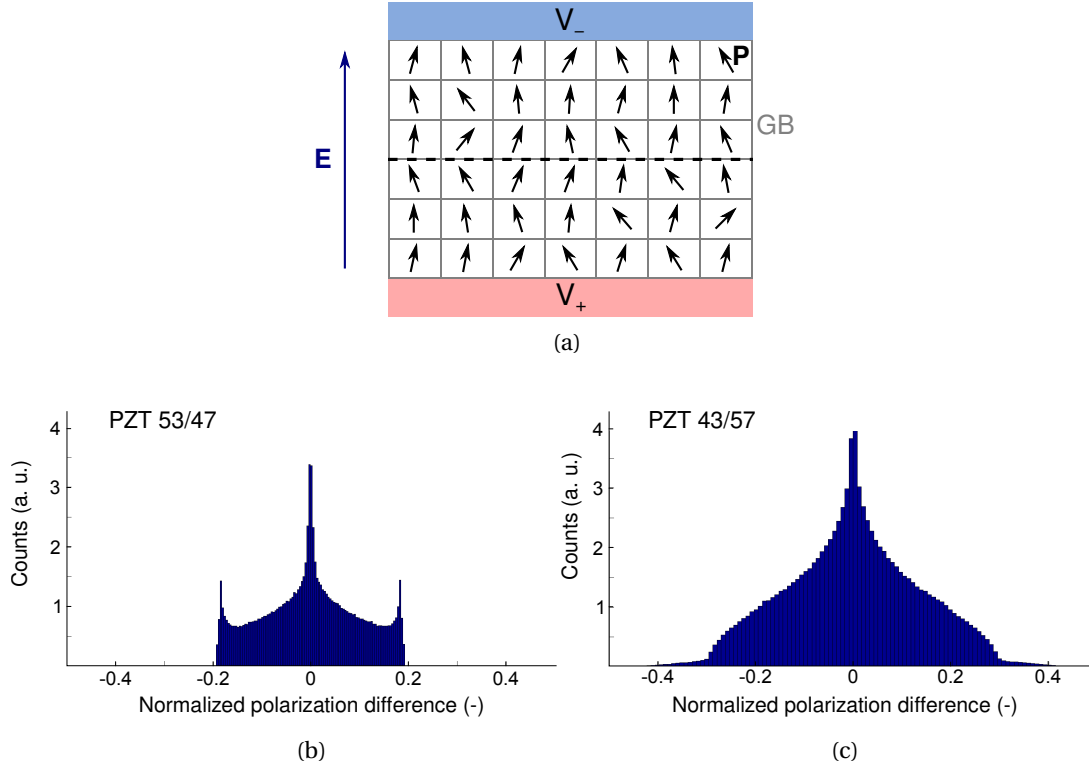


Figure 5.27 – (a): simple model with square grains to estimate the polarization mismatch at the grain boundaries. Each grain has a random in-plane orientation and is shown after poling. (b): histogram of the normalized polarization mismatch at the horizontal grain boundaries for the undoped PZT 53/47. (c): same for the undoped PZT 43/57.

those parallel to the poling field direction. The histograms for the polarization mismatch at grain boundaries orthogonal to the poling field direction (shown as a dashed line in Fig. 5.27 (a)) are shown in Fig. 5.27 (b) for the undoped PZT 53/47 and in Fig. 5.27 (c) for the undoped PZT 43/57. Table 5.3 gives the average of the absolute value and the standard deviation of the polarization mismatch distribution ΔP as function of the spontaneous polarization P_s , for the MPB and the tetragonal film. For the MPB film we have used the “soft” approximation, *i. e.* the polarization vector can take the polar axis of either the rhombohedral or the tetragonal phase to minimize $\mathbf{P} \cdot \mathbf{E}$. ΔP_{\parallel} denotes the polarization mismatch parallel to the poling direction, *i. e.* at the grain boundaries orthogonal to the poling direction; ΔP_{\perp} denotes the polarization mismatch in the orthogonal direction. We observe that, for both sets of grain boundaries, the average mismatch and the standard deviation are significantly less for the MPB composition. Qualitatively, this means that the depolarization fields will be reduced, and that there are less charges to be compensated for; therefore, the aging rate should be lower, and the internal bias field should saturate at lower values for the MPB film than for the tetragonal film. This is in agreement with our observations.

Table 5.3 – Normalized polarization mismatch (in absolute value) and standard deviation for the model shown in Fig. 5.27 (a).

Direction and film	$\langle \Delta P \rangle$	$\sigma_{\Delta P}$
ΔP_{\parallel} PZT 53/47	$0.08P_s$	$0.10P_s$
ΔP_{\perp} PZT 53/47	$0.36P_s$	$0.44P_s$
ΔP_{\parallel} PZT 43/57	$0.11P_s$	$0.14P_s$
ΔP_{\perp} PZT 43/57	$0.49P_s$	$0.60P_s$

The importance of the grain boundaries in the aging process is further supported by our observation that the field offset increases much more slowly, and saturates at a much lower value, for an epitaxial undoped PZT 53/47 film with IDE, with the $\{100\}$ out-of-plane orientation and grown on an SrTiO_3 substrate, than for the $\{100\}$ -textured, polycrystalline films of the same composition shown in Figure 5.23. The time evolution for all three films is displayed in Figure 5.28. Neglecting elastic effects, this last observation seems to exclude the volume effect as the dominant process of aging in polycrystalline films, since this local process takes place within the bulk of the domains and should not be sensitive to the presence or absence of grain boundaries. Unfortunately, we face the same difficulty as before, *i. e.* the experimental impossibility to observe the domain pattern of the two kinds of samples. This means that we cannot determine whether the absence of any grain boundary in the epitaxial PZT film lowers the aging rate because it influences the domain pattern, or because there is no polarization mismatch to be compensated for, and hence no local depolarization field. Further investigations with other experimental procedures may allow to separate the two effects and to determine which one is predominant.

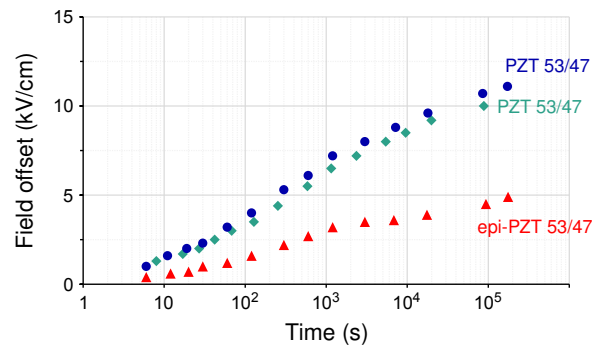


Figure 5.28 – Offset evolution with time for two $\{100\}$ -textured polycrystalline MPB PZT thin films and for one epitaxial PZT thin film of the same composition, all in the IDE configuration. The color code is given in the chart.

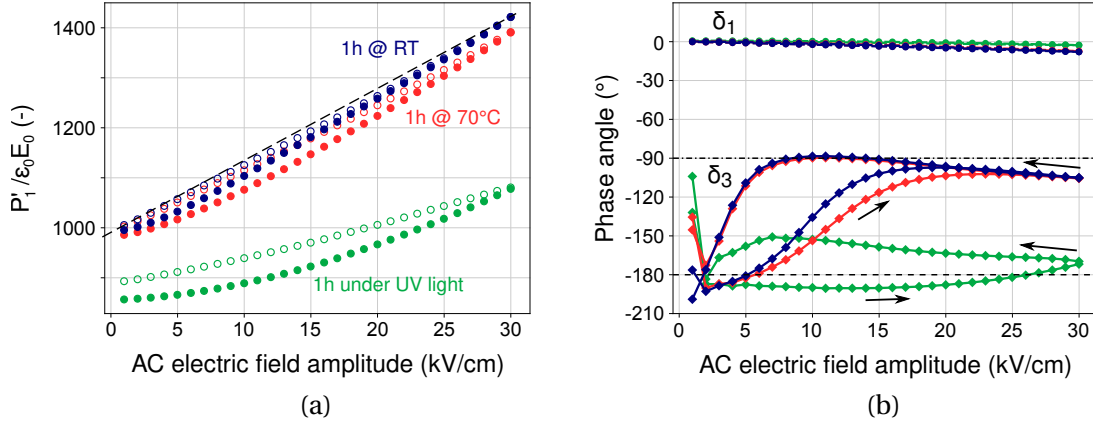


Figure 5.29 – $P'_1 / \epsilon_0 E_0$ (a), δ_1 (b) and δ_3 (b) for increasing, then decreasing field amplitude, for an unpoled, undoped PZT 43/57 film with IDE, after various aging treatments. The color code is given in (a). In (a), filled circles indicate the increasing branch and open circles the decreasing branch. The dashed line in (a) is a guide to the eye. Arrows indicate the direction of the δ_3 curves in (b).

5.6.3 Subswitching dielectric spectroscopy

To complement our study of the aging process by monitoring the time evolution of the internal bias, we have conducted subswitching dielectric spectroscopy on an undoped PZT 43/57 sample, which experienced various treatments, to compare the extent of domain wall clamping thereby introduced. For all experiments, we proceeded in the following way: the sample was annealed at 550 °C for 10 min under 100 sccm of O₂ flow. After that, a 20 min waiting time was observed, after which a 1 h-long treatment was applied. The reference treatment against which we compare the effects of the other treatments, is aging at room temperature during 1 h, *i. e.* this is simply an additional waiting time. In this way, all the samples start in the same unpoled state aged for 20 min, and the applied treatment can be compared to the case where nothing is performed. Note that we have not corrected P'_1 for the parasitic capacitance; this is not important for comparison, because the same sample was used for all the spectroscopy measurements of this section. The parasitic capacitance behaves purely linearly and therefore, does not contribute to δ_3 . Its contribution to δ_1 should be small.

Figure 5.29 compares various aging treatments during which the sample was in the unpoled state. The behaviors with increasing electric field amplitude of the samples aged at room temperature and at 70 °C are similar and correspond to the case already described in section 5.2.3. The only difference is that the sample aged at high temperature displays a more pronounced pinning of the domain walls, as revealed by a reduced $P'_1 / \epsilon_0 E_0$ and a change of δ_3 from –180° to –90° which is more gradual on the increasing branch. On the decreasing branch, δ_3 is the same as for the sample aged at room temperature, and $P'_1 / \epsilon_0 E_0$ joins the decreasing curve of the sample aged at room temperature. This shows that the cycling electric field could remove all the additional clamping due to the time spent at higher temperature rather than

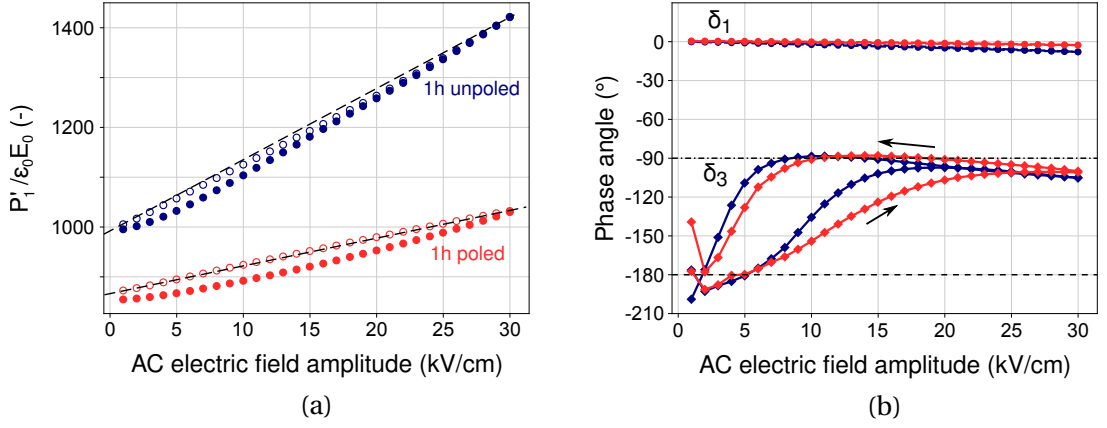


Figure 5.30 – $P'_1 / \epsilon_0 E_0$ (a), δ_1 (b) and δ_3 (b) for increasing, then decreasing field amplitude, for an unpoled and a poled undoped PZT 43/57 sample with IDE, after 1 h aging at room temperature. The color code is given in (a). In (a), filled circles indicate the increasing branch and open circles the decreasing branch. The dashed lines in (a) is a guide to the eye. Arrows indicate the direction of the δ_3 curves in (b).

room temperature. This is likely a coincidence, and the two samples may not have ended in a similar state if the hot treatment had lasted longer. Figure 5.29 also shows the effect of UV light illumination on the unpoled sample. This treatment results in a drastic decrease of $P'_1 / \epsilon_0 E_0$, which becomes much less field-dependent, and in a significant increase of δ_1 towards 0° ; δ_3 can only very partially be increased towards -90° . This shows the strong clamping effect of the UV light on the domain walls; the hysteresis as well as the non-linearity are significantly suppressed after illumination. This is an interesting property for applications, where hysteresis and non-linearity are often undesired. It suggests that uncompensated bound charges are present also in the unpoled state — either at interfaces such as grain boundaries, at domain walls, or both — and are compensated by the photogenerated carriers, similarly to what was discussed for the poled state in section 5.6.1.

Figure 5.30 compares the response of the same undoped PZT 43/57 sample after 1 h of aging spent in the unpoled or in the poled state. The poled state was achieved by the cycling of two PV loop at 20 Hz at a maximum field of 150 kV/cm, *i. e.* under the same conditions as for the monitoring of the internal bias. The response after poling is much less hysteretic, as revealed by the value of δ_1 very close to 0° , and much less non-linear, as seen in the significant reduction of the dependence of $P'_1 / \epsilon_0 E_0$ on the electric field. This is attributed to the reduced number of domain walls inside the film after poling. On the decreasing branch, δ_3 has nearly reached -90° and the decreasing branch of $P'_1 / \epsilon_0 E_0$ is nearly a straight line, showing that we have attained a Rayleigh-like regime. However, the increase of δ_3 from -180° to -90° is much more gradual for the poled case than for the unpoled case. This suggests a larger clamping of the domain walls in the poled case after 1 h. Thus, the aging appears to proceed faster in the poled state. This is likely the consequence of larger depolarization fields, as discussed in the previous section for explaining the aging rate of tetragonal and MPB samples.

Depolarization fields for the unpoled samples are expected to be much smaller and localized, because minimizing the depolarization fields is one of the driving force for domain splitting after cool-down below the Curie temperature. This is an interface effect. However, the domain pattern is likely greatly changed between the unpoled and the poled state, and this difference could explain the faster aging rate for poled samples as well, *i. e.* with a domain wall effect. As was discussed when commenting the PFM studies shown in Figure 5.26, we could not make any definitive conclusion about the change of the domain pattern between the poled and the unpoled state. As such, we cannot decide which effect, between the interface and the domain wall effects, is the main mechanism behind the faster aging rate of the poled state. However, as a local phenomenon, the volume effect should not be sensitive to the poled or unpoled state of the sample, and should therefore result in the same domain wall clamping situation after an identical time has elapsed. This is not what we observe in Figure 5.30; therefore, we conclude that the volume effect is not predominantly responsible for the faster aging rate of the poled state. Note that, as in section 5.6.2, we did not discuss elastic effects, even though the stress situation of the film should be different in the poled and unpoled state.

5.7 Conclusion

We have reviewed the possible mechanisms for aging in PZT thin films. Aging can be caused by so-called volume effects, domain wall effects, or interface effects. The results from several studies indicate that in the general case, more than one mechanism is active. However, their experimental separation is not straightforward. As such, the combination of several experimental techniques is an approach of choice to exclude inconsistent mechanisms and to obtain mutually supporting results. The time evolution of the sample response can be probed either by switching or by subswitching fields. The former allows access to macroscopic properties which reveal the global behavior of the system, and is usually closest to device operation conditions. The latter provides rich information on the behavior of the domain walls on the local scale, and on their interactions with the defects which cause aging.

The study of aging on our PZT thin films with IDE did not provide an unambiguous answer as to the predominant mechanism in this case. Volume effects could be excluded, but we could not determine whether a domain wall effect or an interface effect is more likely. Volume effects of the elastic type could possibly play a role, but were not investigated further. The discussion of the domain wall effect is hindered by the experimental difficulty of imaging the domain pattern of PZT thin films with IDE. It was not possible to realize it with the samples with the MPB composition. In the absence of an effective visualization technique, studying the time evolution of the small-signal response with the method developed by Mokřý and Sluka [171] could prove helpful to discriminate between the two effects. Another route for investigations would be the analysis of additional samples with different microstructures, *e. g.* epitaxial samples with the tetragonal compositions, or polycrystalline samples with a different grain size distribution or a different texture. Epitaxial samples of various Zr/(Ti+Zr) ratio could help to evaluate the contribution of a volume effect and, in the absence of grain boundaries,

should reveal the extent of the domain wall effect as well, for a range of compositions and phases.

UV light illumination offers interesting opportunities to adjust the sample response and the polarization stability. With sufficiently long exposure time, we managed to offset the PV loop to the point that the “down-step” coercive field was nearly 0, which should drastically improve the stability of the poled state. Without UV light exposure, the offset saturated at about half of the initial coercive field value. Further investigations should be pursued to fully understand the effect of bandgap irradiations on the sample behavior, and to evaluate its potential for applications in commercial devices. The IDE configuration is particularly well-suited for this kind of study, since no special, transparent electrode is needed in this case, because the active volume is not covered.

6 PZT thin films with asymmetric electrodes

6.1 Introduction

In the PPE configuration, the interface between the ferroelectric thin film and the electrode plays a very important role for the properties of the ferroelectric capacitor [99]. For instance, it was speculated that the preferential trapping of charges at one of the film-electrode interfaces may induce self-poling in the as-fabricated sample [182]. Self-poling denotes the partially poled state of an as-fabricated ferroelectric thin film, before any poling treatment is performed [102, 183, 184]. Self-poling is a desirable property for some of the applications of ferroelectric thin films, since, if sufficiently pronounced, it can remove the necessity for poling the film. This concerns applications where a low or even no voltage at all is applied, such as for piezoelectric sensors and energy harvesters as well as for pyroelectric detectors. Self-poled films usually also exhibit a more stable polarization than the ones poled by an external field. This then leads in addition to a more stable operation characteristics of the sensors. The presence of a non-zero net polarization state, which is spontaneously stable, solves thus a number of problems. Unlike aging where the properties of the sample change with time, self-poling may not involve degradation of properties. Self-poling can be very stable, to the point of still being present after annealing above the Curie temperature [185]; mastering such a mechanism would provide an excellent stability to the poled state at room temperature, and thereby excellent reliability of the sensor or harvester. This also prevents depolarization caused by the application of a reverse bias in bipolar operations.

Many studies attempted to address the question of the origin of self-poling. Local interface bias field between the film and the electrode [186], strain gradients [187, 188], damage from the top electrode deposition by sputtering deposition processes [189], have all been proposed as an explanation for the presence of self-poling. Baek *et al.* [190] report a record internal bias field accompanied by self-poling in a 1 μm -thick $\text{Pb}(\text{Mg}_{1/3}\text{Nb}_{2/3})\text{O}_3\text{--PbTiO}_3$ (PMN-PT) thin film, which shifts the PV loop so much that both coercive fields are negative, providing spontaneous stability to the poled state at zero external bias. They attributed this behavior to the asymmetry of the electrode they employed, namely Pt/PMN-PT/SrRuO₃. Unfortunately, in the PPE

configuration, the asymmetries introduced by the growth of the film, by the different thermal budget between the top and bottom film-electrode interfaces, and by different mechanical stresses at the two interfaces, does not allow to unambiguously conclude that the internal bias field is an effect of the different electrode materials only.

In this chapter, we studied the influence of electrodes made of dissimilar materials using the IDE configuration, and also the PPE geometry for comparison. In the IDE design, both electrode types are grown on the same surface of the ferroelectric material. Inhomogeneities along the growth direction should play a very much smaller role, because the field lines are mostly perpendicular to the growth direction. Therefore, the comparison of the behavior of the IDE and the PPE sample should allow to separate the effects due to the asymmetry of the materials alone, and those due to the processing route. We then proposed a design which induced self-poling in samples with the IDE geometry.

This chapter is adapted from the following publication:

- R Nigon, N Chidambaram, TM Raeder, and P Muralt. Influence of asymmetric electrodes on the switching of PZT thin films. In *Applications of Ferroelectric, International Symposium on Integrated Functionalities and Piezoelectric Force Microscopy Workshop (ISAF/ISIF/PFM), 2015 Joint IEEE International Symposium on the*, pages 193–196. IEEE, 2015

and from the master thesis work of Trygve M. Ræder under our supervision:

- T. M. Ræder. Self-poling and ageing in PZT thin films with interdigitated electrodes. Master's thesis, NTNU, Norway, 2015

6.2 Sample fabrication

We followed the same fabrication route as described in chapter 4. Three 500 nm-thick undoped PZT 43/57 thin films were deposited by sol-gel with the gradient-free route on Si wafers with 2 μm wet oxide buffered with an evaporated 100 nm-thick MgO layer. 2 crystallization anneals at 650 °C for 1 min under 100 sccm of O₂ flow were performed to obtain the desired thickness. A PTO seed layer was deposited first for seeding the perovskite phase. XRD scans showed that the films had a random texture. In all other respects, their structure is similar to the undoped MPB film shown in chapter 4, with dense, columnar grains with a smooth surface. The asymmetric IDE were prepared by photolithography and lift-off like described in chapter 4. Two photolithography steps were performed, one per electrode side. The first set of electrode structures to be deposited was always Pt, and after deposition this set was annealed at 550 °C for 10 min under 100 sccm of O₂ flow before the fabrication process was resumed. For one of the tetragonal films, both sets of Pt electrodes were deposited in a single step and then annealed at 550 °C as described above. This provided a symmetrical electrode situation which served as a reference. Pd and indium tin oxide (ITO) were chosen as electrode materials for the

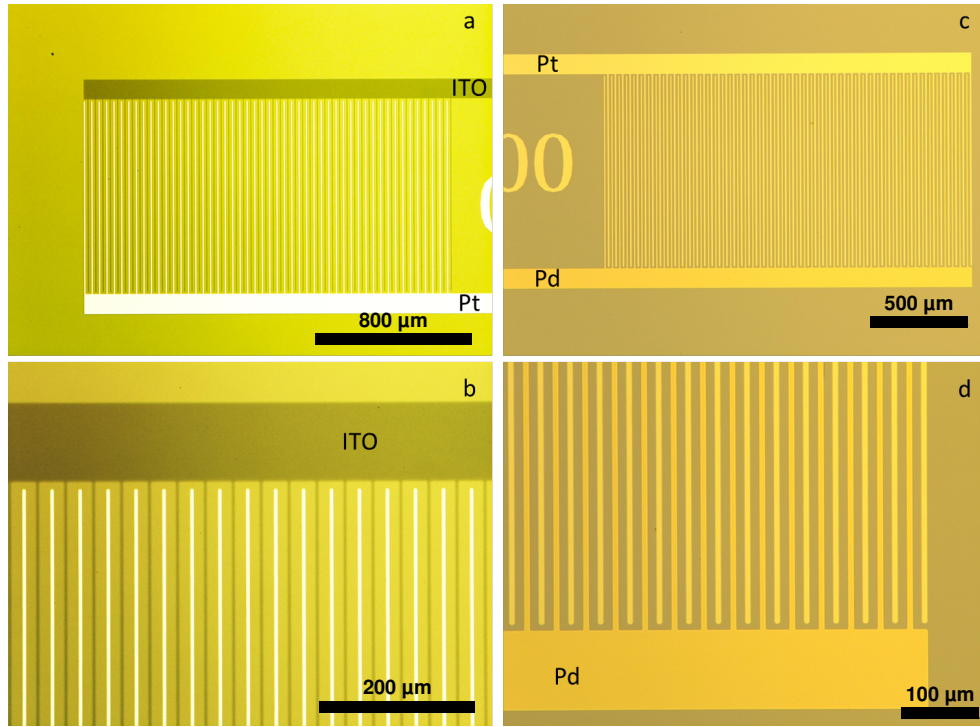


Figure 6.1 – (a): Pt-ITO IDE structures, shown at higher magnification in (b). (c): Pt-Pd IDE structures, shown at higher magnification in (d).

second polarity electrode for the remaining two tetragonal films. These materials were chosen because of their availability in our cleanroom facility, and because they provide a varied set of work functions: The work function is 5.9 eV for Pt [191], 5.4 eV for Pd [191], and 4.4–4.5 eV for ITO [192]. All electrodes were 50 nm thick. Figure 6.1 shows optical microscope images of the final structures; as can be seen, excellent alignment of the second mask was achieved. The structures were then diced into $1.5\text{ mm} \times 15\text{ mm}$ cantilevers.

In addition to the IDE devices, PPE devices have been fabricated. One 500 nm-thick undoped PZT 43/57 film was deposited on a Pt/TiO₂/Ti-buffered Si wafer with 500 nm wet oxide, following the same gradient-free sol-gel route as above. XRD scans showed that this film was fully in the perovskite phase and {100}-textured, as expected. The microstructure was similar to that of the films grown on the MgO underlayer. After deposition and patterning of a photoresist by photolithography, a 50 nm-thick Pt layer was sputtered on half of the wafer to serve as top electrode. The other half was screened by a piece of dummy wafer. A 50 nm-thick ITO layer was then sputtered on the other half of the wafer in the same fashion, while the Pt layer was screened by the dummy. We proceeded to lift-off in one step, for both electrodes at the same time. The PZT film was then wet-etched to access the bottom Pt electrode. The etched zones were patterned by photolithography. Finally, the wafer was diced into $1.5\text{ mm} \times 15\text{ mm}$ cantilevers, with were therefore of two kinds but with the same PZT film: Pt/PZT/Pt or ITO/PZT/Pt. No annealing of the top electrodes was performed in this case, in order to study the effect of

the sputter deposition.

In this chapter, the Gevorgian model with the empirical parasitic capacitance model was used for the correction of the PV loops. The reader is referred to chapter 3 for details on this model.

6.3 Results

6.3.1 IDE structures

We used the same setups and measurement conditions as the ones presented in chapter 4. Figure 6.2 (a) shows the PV loops for Pt-Pt, Pt-ITO and Pt-Pd IDE structures on undoped PZT 43/57, as fabricated. This means that the Pt electrodes have all been annealed at 550 °C, whereas the Pd and ITO electrodes are as-deposited. In case of asymmetric electrodes, the samples were always cycled with the Pt electrode grounded and the driving voltage applied to the Pd or ITO electrode. We observe that the Pt-ITO and Pt-Pd loops show a lower maximum polarization, more slanting, and lower coercive fields than the Pt-Pt loop. The slanting is more pronounced for the as-fabricated Pt-ITO sample. Figure 6.2 (b) shows the same as Fig. 6.2 (a), but after annealing all the samples at 650 °C for 10 min under 100 sccm of O₂ flow. After this anneal, all samples reach the same switchable polarization and become more square. However the Pt-ITO and Pt-Pd sample loops still retained some slanting, and, interestingly, the Pt-Pd IDE sample is this time the most slanted. It also has a larger coercive field than before annealing, unlike the other samples for which the coercive field remains essentially unchanged. TEM cross-section of the Pt-Pd sample revealed the partial oxidation of the Pd electrode by oxygen exchange with the underlying PZT, which may explain the slanting of this loop by the presence of a dead layer at the film-electrode interface [99]. In chapter 4, we also observed that the loop becomes more square, along with a moderate increase of the coercive field and of the switchable polarization, after annealing as-deposited symmetric Pt-Pt electrodes. This indicates that at least part of the above observations are related to the deposition process rather than to the electrode materials.

The offset of the PV loop which may be observed in Fig. 6.2 (a) and (b) is the consequence of imprint in the poled state. Figure 6.3 shows the aging rate for the 3 samples. All samples have been annealed at 550 °C for 10 min under 100 sccm of O₂ flow prior to the aging measurement. The aging rates are comparable for all the samples. The Pt-ITO sample appears to age at a slightly lower rate, but to saturate at about the same value as the other samples. It is not clear whether the random texture could explain the variation of aging rate. It is expected to have some influence if the aging mechanism involves the compensation of depolarizing fields caused by the polarization mismatch at the grain boundaries, as discussed in chapter 5.

We could not observe a PV loop without an offset: Indeed, the onset of the aging process after the poling action of the PV loop is very fast, reaching several kV/cm within seconds as seen in Fig. 6.3. As a consequence, it may be masking any internal bias present in the samples because of the use of asymmetric electrodes. However, as seen from Fig. 6.3, if any internal

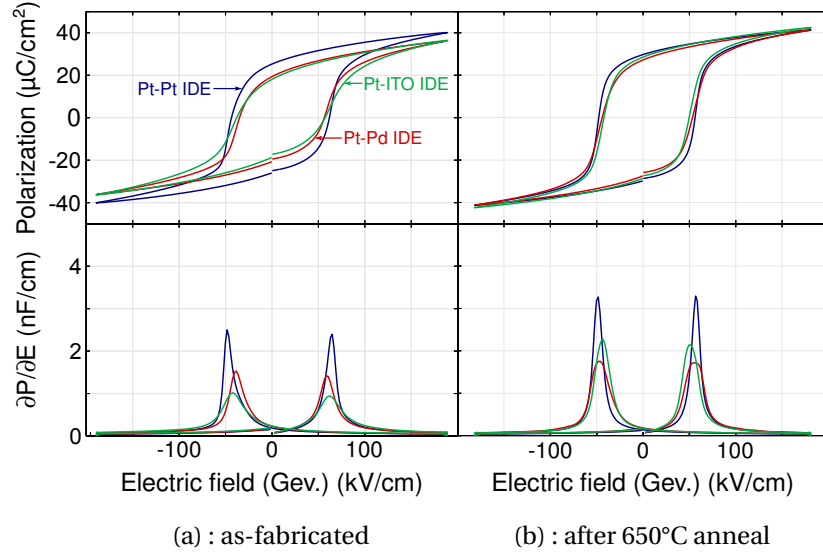


Figure 6.2 – (a) : PV loops of as-fabricated IDE samples with PZT 43/57. The Pt electrodes (both in the Pt-Pt version and in the asymmetric versions) were annealed at 550 °C, whereas the ITO and Pd electrodes are as-deposited. (b) : PV loops after annealing at 650 °C under 100 sccm O₂ flow for 10 min. The color legend is the same for (a) and (b).

bias exists in addition to the internal bias caused by the aging process, it must be smaller than 2 kV/cm for the asymmetric samples. In addition, all the samples display the same offset *vs.* time evolution at low times. This rather suggests that, if any internal bias is present due to the asymmetry of the electrode materials, its effect is negligible.

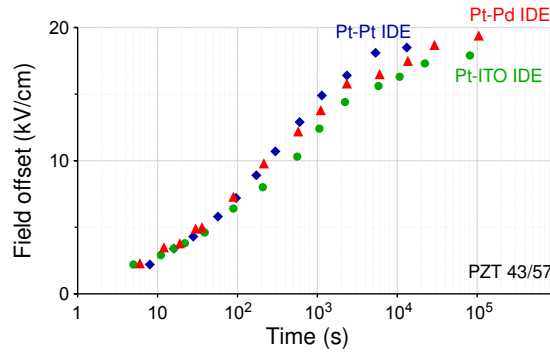


Figure 6.3 – Offset evolution with time for randomly oriented, tetragonal PZT thin films with symmetric and asymmetric electrodes. The electrode materials is indicated in the chart.

6.3.2 PPE structures

The behavior of the PPE structures was quite different from that of the IDE structures. As explained above, two PPE configurations were prepared on the same PZT 43/57 film: Pt/PZT/Pt and ITO/PZT/Pt. The PZT film with the PPE structures has a similar thickness and microstructure as the films with the IDE structures. As-deposited, none of the PPE samples could be switched below 100 kV/cm (we did not try to cycle the samples at higher fields since the breakdown field was about 120 kV/cm); in addition, all displayed some self-poling. The latter was estimated by measuring the $e_{31,f}$ piezoelectric coefficient in direct mode [39]. This is a non-destructive measurement. $e_{31,f}$ is non-zero if and only if the sample is already poled to some extent. For as-deposited samples, we found $e_{31,f} = -4.9 \text{ C/m}^2$ for Pt/PZT/Pt and $e_{31,f} = -1.2 \text{ C/m}^2$ for ITO/PZT/Pt. The latter is not a very large value, but the former is more than 25 % of the best value reported for PZT by Baek *et al.* [190]. This is, therefore, a significant value which may even be used as such for some applications.

To probe the stability of the self-poling of our PPE structures, we have performed a sequence of annealing treatments in an RTA tool, during which the temperature was maintained for 10 min under 100 sccm of O₂ flow. After each treatment, a PV loop was recorded and the value of $e_{31,f}$ was tested. We starting the sequence at 150 °C, and increased the annealing temperature by step of 100 °C until reaching 750 °C. The PV loops and the values of $e_{31,f}$ after each treatment and for each type of sample are shown in Fig. 6.4. Above a threshold temperature of 300–400 °C, the self-polarization was lost and the samples became switchable. The switchable polarization increased with increasing annealing temperatures. Below the threshold temperature, the self-polarization was pointing downward, consistently with positive charge accumulation at the top electrode and contrary to similar studies on sputtered PZT films [185, 193]. Its disappearance after annealing under oxygen flow suggests that an accumulation of oxygen vacancies below the top electrode, due to the sputter deposition process, may be causing it. The fact that the as-fabricated Pt/PZT/Pt samples displayed higher $e_{31,f}$ values than the ITO/PZT/Pt samples, and that the self-polarization direction is in both cases the same and opposite to the electric field induced by the work function difference between ITO and Pt, suggests that the work function difference between the top and bottom electrodes plays a very minor role.

6.3.3 Discussion

In contrast to the PPE configuration, none of the IDE samples showed any piezoelectric activity prior to electrical measurements, even though the Pt and ITO electrodes were deposited with the same tools for both IDE and PPE samples. Therefore, the same type of sputter damage should be present at the top-electrode/PZT interface in both cases. All IDE samples could readily be switched, albeit with a slightly slanted PV loop, immediately after fabrication and without any annealing treatment. The same was true for the as-deposited, symmetric Pt-Pt IDE electrodes studied in chapter 4. It appears that any asymmetry in switching with the

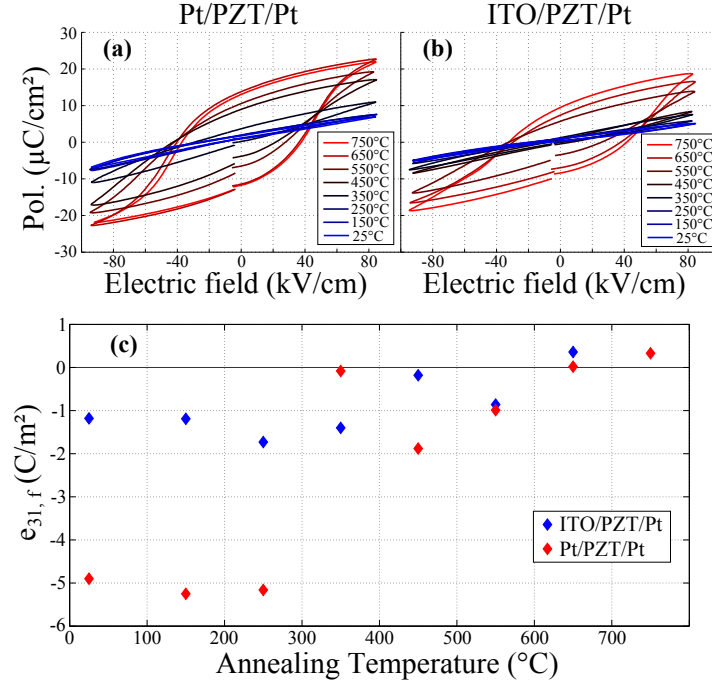


Figure 6.4 – Third PV loop for Pt/PZT/Pt (a) and ITO/PZT/Pt (b) PPE samples after annealing treatments at various temperatures under 100 sccm O_2 flow for 10 min. (c) : $e_{31,f}$ of virgin samples after annealing treatments at various temperatures under 100 sccm O_2 flow for 10 min. An annealing temperature of 25 $^{\circ}\text{C}$ means that no annealing treatment was performed. We gave $e_{31,f}$ a negative sign for self-polarization pointing downward (positive poling with reference to top electrode), and positive for pointing upward (negative poling).

asymmetric IDE is predominantly due to a rapid imprinting when the sample stays in a poled state, so that the influence of using asymmetric electrodes has a negligible impact on the switching process. This shows that the electrode/film interface has a only a minor influence on the behavior of the IDE system. This supports the IDE switching scenario where the nucleation of reverse domains occurs within the field concentration region at the edge of the fingers (covered by photoresist during electrode sputter deposition), while the majority of the electrode/PZT interface experiences no electric field at all, as seen in chapter 3. We attribute the difference of loop slope, coercive field and maximum polarization between the Pt-Pt IDE samples and the Pt-ITO and Pt-Pd samples on tetragonal PZT, to the defects introduced during top electrode sputter deposition. These defects can be completely or almost completely cured by annealing under oxygen flow. It is therefore believed that these defects are mainly oxygen vacancies and dislocations. It is not clear whether the impossibility to reach steeper switching slopes for Pt-ITO and Pt-Pd samples on tetragonal PZT, is due to incomplete curing of the sputtering damage, to another kind of defect which cannot be cured at the temperature involved, such as a lower dielectric layer due to an imperfect ferroelectric-metal interface, or to some influence of the electrode/film interface, which, albeit minor, may still manifest itself. We performed TEM examination of the Pt/PZT, Pd/PZT and the ITO/PZT interfaces to

further investigate these points. Unfortunately, this did not reveal any clear evidence in favor of any of the proposed scenarios, apart from the partial oxidation of the Pd electrode which we discussed earlier.

The loss of self-poling for PPE samples after annealing above a threshold temperature, in addition to a self-polarization direction opposite to what we could expect given the work function difference between the top and bottom electrode, shows that the work function difference has no significant impact. Besides, the largest self-poling effect was observed in Pt/PZT(43/57)/Pt capacitors, thus in the version with identical contact metals. The self-poling of the PPE samples is more likely due to the difference in thermal and processing history of the contacts. The bottom film/electrode interface has repeatedly been annealed at 650 °C during the crystallization step of the sol-gel process, whereas the top-electrode/film interface was processed at room temperature. The damage from the top electrode sputtering, therefore, can be a primary cause for self-poling in the PPE configuration. The difference in the self-poling experienced by the two stack designs can be due to the fact that a different sputtering tool was used for the deposition of the Pt and the ITO top electrode, with different processing conditions: the Pt film was deposited by DC sputtering whereas the ITO film was deposited by RF sputtering. This is different from the results of Kwok *et al.*, who observed strong self-poling of their sol-gel PZT film with RF-sputtered RuO₂ top electrodes, but none at all with DC-sputtered RuO₂ top electrodes [189]. These apparently contradictory results simply show that the top electrode/film interface is very sensitive to the processing route. Type of bias, chamber pressure and gas mix in the plasma for top electrode sputtering deposition may all have some influence on the final properties of the PPE capacitor, through ion bombardment and UV light absorption. Further investigations on this topic are needed to properly assess their impact and their role in self-poling. Self-poling aided by the flexoelectric effect could also occur at non-relaxed interface layers at the bottom of the film, particularly if epitaxial growth with some lattice mismatch is possible on the bottom electrode. We finally note that, even if sputtering defects can be a primary cause for self-poling in the PPE configuration, such defects could also be the cause for the observed low breakdown field. The impossibility to switch the as-fabricated films suggests the presence of a non-ferroelectric layer at the top-electrode/film interface [99], induced by the sputtering damage. The interface layer having a lower dielectric constant, it is subject to larger electric fields, and as the material is less dense or more defective, this allows for more detrimental conduction paths. This low breakdown field is detrimental for the reliability of the device during operations.

6.4 Introduction of self-poling into the IDE system

From the above discussion, it appears that sputtering damage from the top electrode deposition is a convenient way to induce a significant amount of self-poling into a PPE sample. Since the direction of self-poling observed in this case is consistent with the presence of oxygen vacancies near the top-electrode/film interface, where the sputter deposition took place, it is also possible that a gradient of oxygen vacancy density can also be used to cause or promote

the self-poling of the sample. In order to introduce some amount of self-poling into the IDE system, it is however not sufficient to limit this sputtering damage or vacancy gradient to the vicinity of the electrodes, as we observed. For this reason, we have fabricated additional IDE devices in an effort to obtain self-poled IDE systems. In this section, we will describe the processing and testing of these devices.

6.4.1 Fabrication

We deposited a 500 nm-thick sol-gel PZT film with the MPB composition following the same route as in section 6.2. Symmetrical, 50 nm-thick Pt-Pt IDE electrodes were patterned on top by photolithography, sputtering and lift-off in a single fabrication step. A 2 nm-thick Ti-layer was deposited on top of the Pt electrodes to provide adhesion with the next layer. These electrodes were not annealed. We then patterned, on top of the Pt IDE structures, a SiO₂ layer by photolithography, sputtering and lift-off. The SiO₂ layer was 150 nm thick. This layer did not lift-off very well, and for this reason we performed an additional dry etching step with fluoride chemistry to remove the SiO₂ remaining in the contact pad area; after that, remover was used to dissolve the underlying photoresist (PR) and lift-off (LOR) resist. The wafer was patterned with a PR layer during the dry etching step, so that only the contact pad area were exposed to the etching gas during processing; this PR layer was dissolved in the remover solution along with the PR and LOR layers which were still present below the SiO₂ parts which did not lift-off. At the end of the patterning process, the wafer was diced into 1.5 mm × 15 mm cantilevers for testing.

Figure 6.5 presents the two types of cantilever designs which were used. In design “H” (standing for “half”), the SiO₂ layer covers one IDE finger and extends on both sides until it reaches midgap. This design corresponds to Fig. 6.5 (a) and (c). In design “F” (standing for “full”), the SiO₂ layer covers one IDE finger and covers the gap on each side completely, stopping only at the start of the IDE finger of opposite polarity. This design corresponds to Fig. 6.5 (b) and (d).

A mask-less aligner MLA150 (Heidelberg Instruments GmbH) was used for the direct patterning of the PR for the SiO₂ layer deposition. This technique was favored since it allowed more precise alignment as compared with a traditional mask aligner operated manually. Optimization of this process step allowed the positioning of the edges of the SiO₂ layer within 200 nm of their intended location. Figure 6.6 shows a view of the patterned SiO₂ layer on the Pt electrodes as an illustration.

6.4.2 Results

We measured the direct mode piezoelectric coefficient e_{IDE} of as-fabricated samples for both designs H and F for various gap distances. The results are shown in Fig. 6.7. All the samples tested displayed some self-poling, whose extent was gap-dependent. The highest e_{IDE} are obtained for the smallest gap values. For small gaps, the H design consistently displays larger

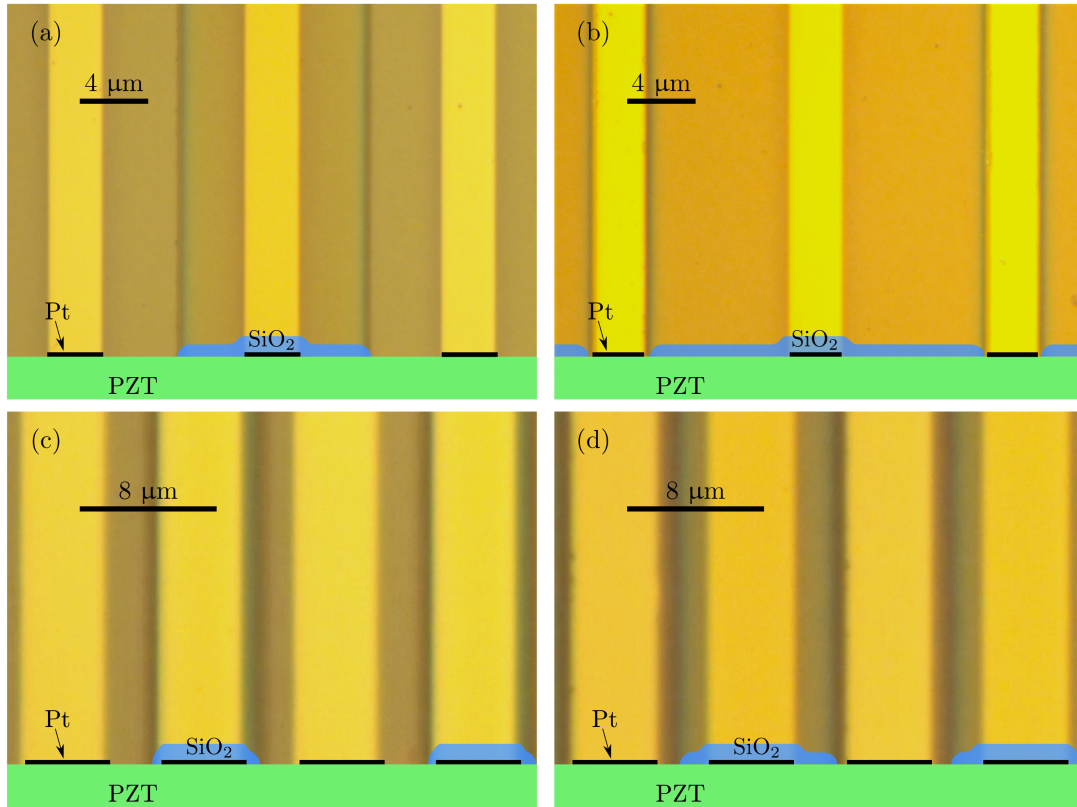


Figure 6.5 – (a) and (c): optical microscope images of the interdigitation zone for design H (half), for a large gap in (a) and a small gap in (c). (b) and (d): optical microscope images of the interdigitation zone for design F (full), for a large gap in (b) and a small gap in (d). An overlay at the bottom of each image shows the corresponding cross-section view.

e_{IDE} values than the F design. At large gap values, this trend seems to reverse, but the e_{IDE} values do not differ much. The maximum e_{IDE} was obtained for a sample with design H at 1.65 C/m^2 ; this represents nearly 20 % of the e_{IDE} value obtained after poling the sample with a triangle pulse of frequency 20 Hz and maximum field of 150 kV/cm, after annealing the sample at 550°C for 10 minute under 100 sccm of O_2 flow. The annealing treatment was found to destroy the self-poling of all the samples. For all samples, the net polarization was directed away from the covered Pt electrode and towards the uncovered Pt electrode, as schematically shown in Fig. 6.8. This is, to our knowledge, the first instance of self-poling reported for PZT thin films with IDE structures.

In an effort to introduce oxygen vacancies in a localized way, we have annealed the samples in forming gas (FG, 5 at.% H_2 in N_2), which has a strong reducing power. Oxygen exchange with the atmosphere should only take place in exposed PZT area and at the edge of the Pt electrode fingers, which may serve as a catalyst for the oxygen exchange reaction. In this way, we expect to introduce oxygen deficiency over half the gap distance in design H, and in the vicinity of the electrode finger only in design F. All anneals were performed at 650°C for 10 minute under

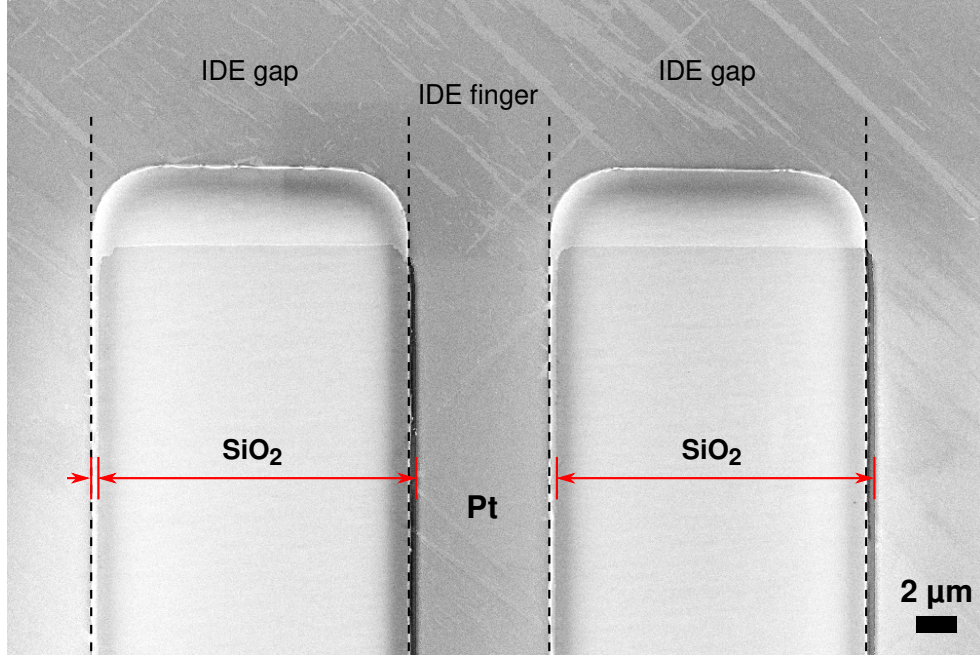


Figure 6.6 – SEM image of the patterned SiO_2 layer on the Pt electrodes obtained on a wafer used for the calibration of the process. The zone corresponding to the IDE gaps and the IDE fingers are separated by dashed lines. The misalignment between the SiO_2 and the Pt patterns is shown in red on the left of the image.

200 sccm of FG flow. One set of samples was annealed for 20 min to assess the influence of the annealing time. We also annealed some samples under 100 sccm of O_2 flow instead as a control group. The e_{IDE} measured after these treatments are shown in Fig.6.9. For all types of samples, they are greatly lower than the as-fabricated value, and not much larger than values corresponding to the samples annealed in oxygen. Since no self-poling is expected in the latter case, a value of 0.2 C/m^2 for e_{IDE} , which the highest value obtained after such a treatment, can be considered as the noise floor for this measurement. Hence, some self-poling is present only below a threshold gap value, and for these samples, the value of e_{IDE} is again larger for the H design than for the F design. The polarization direction in all cases is the same as that shown in Fig. 6.8. Increasing the annealing time seems to slightly increase the e_{IDE} value.

6.4.3 Discussion

The FG anneal is not effective as a poling treatment. The obtained value of e_{IDE} are too small to be of any practical interest. The direction of the net polarization may be explained by the diffusion of the generated $\text{V}_{\text{O}}^{\bullet\bullet}$ away from the exposed surface, since they should be mobile at 650°C , leaving behind two electrons e' (or one lead vacancy V_{Pb}'' , if oxygen exits the sample as lead oxide) to compensate for the introduced doubly positive charge. This creates an electric field pointing towards the exposed area, which can pole this volume during cool-down below

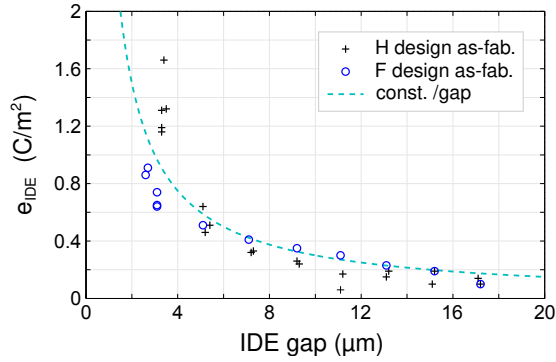


Figure 6.7 – e_{IDE} values measured for the H and F designs, on as-fabricated samples, for various IDE gap values. A curve of the form B/a , where B is a constant and a is the gap, is shown as a dashed line.

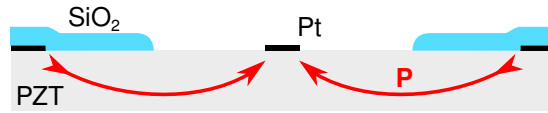


Figure 6.8 – Direction of self-poling indicated on a sample with design H.

the Curie temperature. This field must be quite small, given the small e_{IDE} values we measured.

The as-fabricated self-poling is more interesting. Unfortunately, the small gap geometry for which it is the most pronounced, is also the geometry where the footprint of the electrodes on the PZT film is the largest. This yields a small active-to-passive-volume ratio, because the PZT volume below the IDE fingers is not active, as we saw in chapter 3. The gap-dependence of e_{IDE} is close to a function of the form B/a , where B is a constant and a is the IDE gap, as shown in Fig. 6.7. This suggests the presence of some built-in voltage dropping across the gap distance. The interesting feature is that the self-poling appeared at room temperature during fabrication, when the coercive field is about 25 kV/cm for the tested composition;

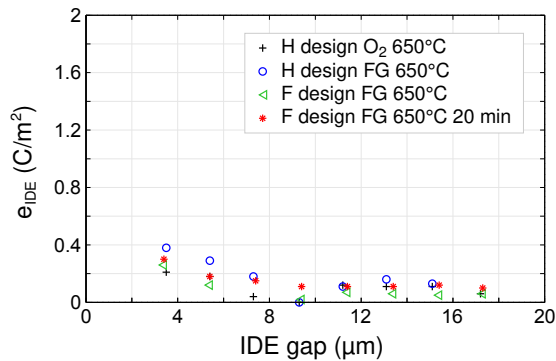


Figure 6.9 – e_{IDE} values measured for the H and F designs, after various annealing treatments, for various IDE gap values.

indeed, no anneal was performed after the crystallization step of the sol-gel film. The built-in polarization was visible when recording a PV loop on as-fabricated samples, which possessed a pinched shape. No such polarization or shape were observed for films with un-annealed, as deposited symmetrical Pt-Pt IDE electrodes. This suggests the presence of an electric field sufficiently strong to partially pole the sample at room temperature, which originated during the fabrication process after the patterning of the Pt IDE structures.

Unfortunately, the origin of such an electric field remains obscure. Sputtering damage is a likely candidate for the presence of this field. For this reason, we have experimented with the deposition of an additional SiO₂ layer on top of the sample. The patterned SiO₂ layer behaves as a hard mask, so that any damage can only be introduced where the PZT is originally exposed. Depositing an additional layer of SiO₂ on top of an as-fabricated sample had no significant influence on the value of e_{IDE} . This is not unexpected, since in this way we simply make the sample symmetrical, *i. e.* we bring any field which may be present to 0; the poling should be retained, because no counter-voltage is applied against it. On the contrary, if, prior to the additional SiO₂ deposition, the sample is annealed at 550 °C for 10 minute under 100 sccm of O₂ flow (which destroys the self-poling), e_{IDE} remains zero after deposition. This shows that the asymmetric sputtering damage introduced by the deposition of the SiO₂ layer cannot alone explain the presence of self-poling. The presence of sputtering damage originating from both the Pt and SiO₂ depositions seems to be necessary.

Another physical explanation exists for the observed B/a dependence of the self-poled e_{IDE} . If a volume within the gap is self-poled, and if this volume is the same independently of the sample geometry, then the amount of charge per gap ΔQ_g generated during actuation should be the same for all samples. From equation 2.16 in chapter 2, e_{IDE} is of the form:

$$e_{IDE} = D \frac{\Delta Q_g}{l - (a + b)N_g} \quad (6.1)$$

where D is a constant which depends on the geometry of the setup, the film thickness and the finger length, which are the same for all samples; l is the distance between the clamp and the actuating tip, which is also the same for all samples; a is the gap distance; b is the finger width; and N_g is the number of gaps. This expression is qualitatively of the same form as the observed dependence. Our samples have $N_g = 200$ for small gaps and $N_g = 100$ for large gaps, hence a regime change should be observed. This is not immediately apparent in Fig. 6.7, but this could be due to the very low value of e_{IDE} for large gaps, close to the noise floor of the experiment. The presence of a self-poled volume independent of the geometry can be explained by the presence of some built-in voltage, but this time dropping across an identical distance for all samples, *e. g.* between some point below the SiO₂-covered Pt electrode up to some point a fixed distance away, outside of the electrode finger area and still below the SiO₂ coating.

Another possibility could be the flexoelectric effect. The wafer is expected to reach about 100 °C during the sputtering process. This could induce local thermal mismatch between the

Pt, SiO₂ and PZT layers after cool-down to room temperature, generating strain gradients. The electric field generated by the flexoelectric effect is of the form $g \partial \epsilon / \partial x$, where g is the flexoelectric coefficient and ϵ is the strain. Since the coercive field of the samples is 25 kV/cm, the product $g \partial \epsilon / \partial x$ must be of the order of 10 kV/cm = 10⁶ V/m to pole some volume of PZT. Since g is of the order of 1 V, $\partial \epsilon / \partial x$ must be of the order of 10⁶ m⁻¹. This is realized if ϵ varies by 10⁻³ over a distance of 1 nm. Such a strain gradient is plausible only over a very short distance, so that the total strain remains reasonable, *i. e.* over a few nm. Therefore, the electric field is present only in an extremely small volume; it is unrealistic that such a small volume may produce a e_{IDE} value reaching 20 % of the poled case in the small gap samples. The flexoelectric effect is therefore not a satisfying explanation of the observed self-poling.

Local exposure to UV light during the PR exposure step should not cause any field to appear in the sample. Indeed, charge separation of the photogenerated carrier could occur, leading to charge accumulation in some regions and therefore electric field build-up, but only if there already exists an electric field to separate the charges — which otherwise simply recombine. Hence, the exposure step may enhance the effect of an already present electric field, but may not generate one. The moderate dose of 130 mJ/cm² is used in the mask-less aligner, and a large portion of this energy should be absorbed by the PR layer which lies between the PZT surface and the UV light source. Hence, UV light likely plays a minor role in the self-poling process, if it plays a role at all. The most likely explanation for the self-poling of our IDE structures is some interaction between the sputter damage caused by the sputter deposition of the Pt and the SiO₂ layers, or by a combination of effects provoked by the two deposition processes performed in a sequence. The exact nature of those effects remains unfortunately elusive.

6.5 Conclusion

The use of dissimilar electrode materials had no observable influence on both self-poling and switching asymmetries, in both PPE and IDE samples. Self-poling of PPE samples could be attributed to a difference in thermal and processing history of the contacts. In the IDE configuration, it can reasonably be assumed that any asymmetry in switching is exclusively due to a rapid imprinting when the sample stays in a poled state, and no self-poling was observed. The use of dissimilar electrode materials only has a modest influence on the dielectric and aging properties.

A specific sample design was developed in an effort to introduce some self-poling into the IDE system. A SiO₂ layer was patterned in an asymmetrical fashion on top of symmetrical Pt IDE structures. As-fabricated samples displayed some amount of self-poling, which was larger for shorter gap distances. The maximum piezoelectric coefficient measured on self-poled samples reached nearly 20 % of the poled value; still, the absolute value was too small to be really interesting for any practical application. From the dependence observed in Fig. 6.7, a gap of less than 0.7 μm would be required to reach above 50 % of the piezoelectric

activity of a poled sample, assuming that the scaling rule remains valid in this gap range. Such small structures would require advanced photolithography tools to be fabricated. In addition, designs with small gaps also have a smaller active-to-passive-volume ratio, which results in a lower amount of charges generated in direct mode for a given device size, and thus a lower output power for energy harvesting.

Therefore, the costs for reaching a sufficiently large extent of self-poling in IDE systems do not seem to be compensated by the gains. A control over the aging process is more promising in this respect to ensure the reliability of the device by improving the stability of the poled state.

7 Applications and design rules for PZT thin films with IDE

7.1 Introduction

The previous chapters gave many insight into the behavior of the IDE system. From the investigations we have performed, we will review in this chapter the possible applications for which this system is particularly suited, and more attractive than the PPE configuration. We will then propose a set of design rules for optimal performance of PZT thin films with IDE.

7.2 Applications for PZT thin films with IDE

First, we remark that none of the IDE samples investigated in chapter 4 is well-suited for large-field operation. Even though both IDE and PPE configurations have the same effective piezoelectric coefficient at large fields, tens to hundreds of volts are needed to reach saturation in the IDE configuration, because the IDE gap is of the order of several μm . For similar electric fields, PPE devices can reach the same excursion at a fraction of the voltage necessary to drive IDE samples, because the voltage is dropping across the PZT film thickness instead of across the gap distance. The PZT film thickness is typically 1–2 μm for PPE devices with sol-gel films, much less than the gap distance realized in our devices.

In addition, for IDE samples, the tip end excursion does not solely depend on the material piezoelectric coefficient e_{33} , if and on the size of the interdigitation zone (as would be the case for PPE samples), but also on the metalization ratio $\eta = b/(a + b)$, where a is the gap distance and b is the electrode finger width. This is the consequence of the electric field distribution inside the ferroelectric layer. As we saw in chapter 3, there is no electric field below the electrode fingers; this volume of material is therefore inactive and does not contribute to the cantilever bending through the converse piezoelectric effect, nor does it participate to the charge generation through the direct piezoelectric effect. Consequently, the tip excursion will be dictated by an averaged curvature, so that the overall bending is described by an effective

Table 7.1 – Comparison between a Nb-doped PZT 53/47 film in the IDE and PPE configurations, for the small-signal remanent (rem.) e coefficient and an effective large-signal coefficient.

Sample	Rem. small-sig. e coeff. (C/m ²)	Large-sig. $-\sigma_{\max}/E_{\max}$ (C/m ²)
IDE material value	14.5	15.3
IDE engineering value	8.7	9.2
PPE value	−8	−20

or engineering stress $\overline{\sigma}_f$, which is given by:

$$\overline{\sigma}_f = (1 - \eta)\sigma_f \quad (7.1)$$

where σ_f is the ferroelectric film stress developed between the IDE fingers. Table 7.1 compares the two Nb-doped PZT 53/47 samples shown in Fig. 4.20 in chapter 4. One film is a 640 nm-thick film with IDE, and the other one is a 1.25 μm -thick film in the PPE configuration. Table 7.1 shows the small-signal e coefficient ($e_{31, f}$ for the PPE sample and $e_{33, if}$ for the IDE sample) at remanence, which is representative of small-field operations, and the large-signal maximum stress σ_{\max} reached at the maximum field $E_{\max} = 150\text{kV/cm}$ (the same for both samples) divided by E_{\max} , which is representative of large-field actuation. The IDE sample has $\eta = 0.4$. We observe that the engineering value is much reduced as compared to the material response for both large and small-signal, because of the large value of η . The fact that the remanent small-signal $e_{33, if}$ and the large signal $e_{33, if}$ are close for the IDE sample, shows its excellent retention properties. On the contrary, for the PPE sample, the remanent small-signal $e_{31, f}$ is less than half of its large-signal value. However, the large-signal $e_{31, f}$ is significantly larger than the large-signal $e_{33, if}$ — not only for the engineering value, but also for the material value. This shows that IDE samples are less suited for large field operations also from a material response point of view. The difference may be explained by larger extrinsic contributions to $e_{31, f}$ than to $e_{33, if}$: because of the residual tensile stress in the PPE sample, more ferroelastic domain walls are expected to be present, unlike in the IDE case where the poled state is more elastically stable, reducing the driving force for ferroelastic domain wall formation.

Hence, for large-field operations, the PPE configuration is more advantageous, for three reasons:

1. The driving voltage is much lower for PPE samples.
2. For a given sample size, the active volume is larger for PPE samples, because IDE samples must have $\eta > 0$ to be operated.
3. The larger extrinsic contributions to $e_{31, f}$ means that the material response in large-field operations is larger in the PPE configuration.

However, the excellent remanence and retention properties of the IDE samples make them ideal for energy harvesting or sensor applications, where the stability of the poled state and a high sensitivity at low fields are critical. The lower capacitance of IDE devices, as compared to

PPE devices, allows a larger voltage output for the same amount of generated charges, which is essential for good rectification efficiency. Provided that the larger remanence compensates for the lower excursion, actuation for small displacements could be also envisioned. One advantage of IDE for large-field operations, however, is the reduced hysteresis and larger linearity at high fields. This is an interesting feature if precise actuation is more important than a large displacement or a large force, in particular for open loop configurations. Since the stress developed in the film is compressive, the active layer will also be less sensitive to mechanical failure.

Due to lower remanence and retention properties, doped compositions always have a lower piezoelectric response at low fields, while the response at high fields is comparable or slightly inferior. In addition, they all increased the dielectric constant of the film, increasing the capacitance of the device. Undoped compositions should therefore be preferred. Although the undoped tetragonal composition has the best retention of all the 5 compositions and dopings investigated in chapter 4, the largest remanence, switchable polarization, and piezoelectric response was obtained with the undoped MPB film, showing a record small-signal $e_{33,if}$ of 17.5 C/m^2 at remanence. The tetragonal compositions show a nearly field-independent $e_{33,if}$ on the return branch whatever the doping employed, for both large and small signals. Consequently, this composition should provide very little hysteresis and nearly perfect linear behavior under unipolar excitation. Although the MPB composition also shows little hysteresis, its behavior is less linear. The remanent small-signal $e_{33,if}$ of the undoped tetragonal film is significantly lower, at 12.5 C/m^2 ; a more advantageous compromise between linearity and piezoelectric response may be obtained by choosing a tetragonal composition closer to the MPB. We have not explored the rhombohedral side of the PZT phase diagram, where better trade-offs could also exist. The excellent remanence and retention properties of IDE samples are likely due to the more stable stress situation of the poled state, as discussed above. Unfortunately, this also reduces the extrinsic contributions to $e_{33,if}$ and means that PPE samples are more competitive at large fields.

The fabrication of IDE is more challenging than that of PPE structures. One difficulty resides in the fact that periodic patterns with a small feature size should occupy a significant area; this makes the quality of the finished structures more sensitive to defects, even localized ones, in the photoresist coating (in particular for lift-off processes, in which the lift-off resist layers are more likely to have these kinds of defects than most types of photosensitive resists), or to any damage occurring during resist development after UV exposure. Their fabrication therefore requires a good quality control over the whole patterning process. Moreover, efficient poling of the ferroelectric layer requires geometrical dimensions not too much larger than the film thickness (see next section for more details), that is, of the order of $10 \mu\text{m}$ at the maximum. Photolithography techniques must therefore be employed; it is not possible to use a hardmask for patterning the structures, making them more expensive and more complex to produce than PPE devices.

7.3 Design rules

The design rules for ferroelectric thin films with IDE naturally appear when considering the regime in which they have the lowest performance, *i. e.* large-field operations. Studying how the performance could be improved for this regime will provide golden rules for all types of operations.

The driving voltage can be reduced for IDE by reducing the gap distance, and the η factor can be made smaller by reducing the electrode finger width while keeping the gap distance constant. However, FE simulations show that when the finger width b becomes comparable to or less than the PZT film thickness t_f , the electric field is unevenly distributed within the gap region and can even polarize zones below the electrode fingers. The latter is detrimental, because the effect of the $e_{31,f}$ coefficient below the fingers opposes that of the $e_{33,if}$ coefficient within the gap. Thus, disadvantages for small b values are twofold:

1. Only a fraction of the PZT volume within the gap region is active;
2. The tensile stress generated by the polarization of the PZT volume below the electrode fingers cancels out a fraction of the compressive stress generated within the gap region.

This limits the downscaling of the finger width b to at least 2 times the film thickness t_f , as a rule of thumb — precise FE analysis could predict a different lower threshold.

Keeping b constant, a compromise must be found between minimizing η — which by reducing the footprint of the electrode fingers, increases the active volume to inactive volume ratio — and minimizing a — to keep the driving voltage reasonably low. An additional motivation for keeping a low is the observation that the piezoelectric response shows a weak gap dependence and is larger for small gaps, as seen in chapter 3. Furthermore, if a conductive substrate such as Si is used, the electric field between the electrode fingers will dramatically drop for large gaps, due to the substrate behaving as a floating electrode, as seen in chapter 3. This can be avoided for a Si substrate by employing a thick SiO_2 insulation layer, much thicker than the 2 μm -thick layer used in this study. Orders of magnitude estimates show that even commercially available highly resistive Si wafers are not resistive enough to prevent their behaving as a floating potential — for frequencies of the order of the kHz or less, which are typical frequencies for operation. If it is not possible to use an insulating substrate (*e. g.* for mechanical performance reasons), nor to increase the insulating layer thickness to sufficiently large values, then an upper limit for the gap distance a will exist, above which complete poling of the PZT volume within the gap region cannot be realized below the breakdown voltage. This places a lower threshold for the reduction of η by the increase of a . The drop of electric field at midgap is avoided if $C_{\text{PZT}}^{\text{gap}} \gg C_{\text{fing}}$, which is realized if the following criterium is fulfilled:

$$\frac{\varepsilon_f t_f}{a} \gg \frac{\varepsilon_u b}{t_u} \quad (7.2)$$

where the subscript f refers to the ferroelectric layer (PZT in our case) and the subscript u

Table 7.2 – Effect of geometrical parameters on the IDE system. The condition on the driving voltage can also be read as a condition on the poling voltage.

Parameter	a	η	r_a & r_b	c
Effect for high value	high driving voltage, low capacitance	response-per-area ratio is small	low field uniformity within layer	constant field across gap
Effect for low value	low driving voltage, high capacitance	response-per-area ratio is large	high field uniformity within layer	drop of field at midgap

refers to the insulating layer (SiO_2 in our case). We write c as the ratio of those two capacitances:

$$c = \frac{\epsilon_f t_f t_u}{\epsilon_u ab} \quad (7.3)$$

The criterium is fulfilled if $c \gg 1$.

Lastly, lower a values result in a larger capacitance, which is detrimental for the voltage output. But, for application when a voltage output is desired, no driving is necessary; therefore, there is no competition between keeping the capacitance low, and keeping the driving voltage low. However, one should keep in mind that samples with large a value require a larger voltage to be poled; even more so if the IDE structures are patterned on a conductive substrate, as discussed. A large poling voltage involves a risk of electrical breakdown, so that a compromise is to be found if a low capacitance is also desired.

Table 7.2 sums up the various trade-offs that must be addressed for optimized IDE design. We wrote $r_a = t_f/a$ and $r_b = t_f/b$. Minimizing both r_a and r_b and maximizing c ensures efficient poling between the IDE fingers, while minimizing η allows more force and displacement, or charge generation, for a given sample size. As seen in chapter 3, the condition for good field uniformity within the ferroelectric layer is the same as for the validity for the simplification of the Gevorgian and Igreja formulas; it is satisfied as soon as both a and b are several times larger than t_f , *i. e.* both r_a and r_b should be at least lower than $1/2$.

7.4 Conclusion

The excellent remanence and retention properties of IDE samples make them very attractive for energy harvesting, sensors, and possibly small-fields operations. They display much less hysteresis, in particular for the tetragonal composition, which could be an advantage for some large-field operations where a large stroke is less important than precision. We reviewed the trade-offs involved by the IDE design and proposed design rules to maximize the performance of such devices.

The IDE configuration opens a new area for studying the behavior of ferroelectric thin films. The stress situation in IDE samples after poling is very different from that of poled PPE samples, because the in-plane polarization can relieve some of the tensile stress often present in sol-gel-prepared PZT films. In PPE devices, there is a competition between the electrostatic energy, which is minimized when the polarization is aligned with the out-of-plane electric field, and the elastic energy, which is minimized when the polarization remains in-plane if a residual tensile stress is present. Comparing the behavior of IDE and PPE devices offers the opportunity to better understand the interplay between electrostatic and elastic energies in ferroelectric thin films, which is beneficial for optimizing the poling process and improving the remanence and retention properties.

Note, however, that the present investigation was presented for PZT thin films on Si substrate. Other substrates, such as metal sheets, may have thermal expansion coefficient larger than that of Si, resulting in a residual compressive stress in the PZT film. Since we attributed the fact that $|e_{31, f}| > e_{33, if}$ to the larger number of ferroelastic domain walls in the PPE configuration, due to tensile stress relief, we expect that, in case of residual compressive stress, the situation should be reversed, and that we have $e_{33, if} > |e_{31, f}|$ and better retention for the PPE configuration instead of the IDE configuration.

Finally, the in-plane orientation of the polarization in poled IDE samples, orthogonal to the grain boundaries in the common case of columnar grain growth, also makes it possible to investigate the influence of the grain boundaries on the overall properties of the film, as well as the properties of the grain boundaries themselves, in a novel way.

8 Conclusion and outlook

In this PhD work, we have investigated and explained a number of aspects of the properties of PZT thin films with interdigitated electrodes for use in piezoelectric energy harvesters.

We have proposed an analytical model for extracting the effective material properties from standard characterization measurements. This model is well supported by FE simulations and by the good coincidence of these properties for various IDE geometries. The IDE capacitor behaves like a PPE capacitor with an area given by the sections parallel to the finger electrodes, and with an electrode distance given by $a + \Delta a$, where Δa is derived from conformal mapping transformations according to Igreja and Dias [79] and is proportional to the ferroelectric film thickness. The effective electric field needs to be scaled by $1/(a + \Delta a)$. It also shows that the active region of the PZT thin film with IDE is not limited to the volume located between the IDE fingers, but extends over a slightly larger distance equal to $a + \Delta a$. We demonstrated that the effective area which should be used to obtain the polarization from current integration corresponds to the simple model case, where the IDE fingers traverse through the film. The polarization response is closely related to the local behavior of the film at the middle of the gap. We also found that if the substrate is conductive enough, like is always the case for commercially available Si, it behaves as a floating electrode, causing a parasitic capacitance to be present in parallel to the material response. This parasitic capacitance will greatly reduce the electric field within the active volume when the gap distance is too large, which may lead to insufficient poling if this effect is not accounted for. We have provided a method to subtract the contribution of the parasitic capacitance to the overall sample response, which has an accuracy of better than 4 % in a wide range of IDE geometries as determined by FE simulations. Here again, the obtained experimental data support well the validity of this model. The model is applicable for the geometry range which is relevant for a PEH device, *i. e.* where the finger width and the gap distance are both several times larger than the ferroelectric film thickness. The possibility to accurately extract the effective material coefficients for the IDE configuration — which has a much more complex behavior than the PPE configuration, but is better suited as a piezoelectric energy harvester device — makes material response optimization possible, and permits to design the appropriate structure geometry to maximize

the harvesting performances.

We have thoroughly investigated the performances of doped PZT thin films with IDE, for several combinations of dopant and composition. We have improved an existing fabrication route to obtain textured PZT films on an insulating MgO layer. It was possible to obtain more than 90 % of the crystallites with the {100} texture for all the wafers of a given batch in certain circumstances. Even though the MgO layer did not fully prevent lead interdiffusion between the PZT and the SiO₂ underlayer, this did not have any influence on the properties of the investigated samples. The deposition route yielded a dense and columnar microstructure, similar to state-of-the-art sol-gel PZT thin films grown on Pt bottom electrodes. The composition gradient along the growth direction was satisfactorily limited by the gradient-free sol-gel route, and for the doped films, the dopant concentration was well homogeneous. We found that dopants systematically reduced the performances, so that undoped compositions should be chosen. Dopants always reduced the piezoelectric response and the retention capability of the sample, and increased the dielectric constant of the material. These features indicate that dopants stabilize higher domain wall densities, and seeds or small domains of opposite orientation. All three are detrimental for energy harvesting. Of the two compositions tested, the MPB composition displayed a far better piezoelectric response, but the tetragonal composition showed a better retention and a much lower dielectric constant. It appears that there is a trade-off to be addressed between the piezoelectric response, the stability of the poled state, and the relative permittivity. All are equally important for good harvesting performances, so that the evaluation should be performed on a case-by-case basis.

Finally, we have studied the possibility to improve the stability of the poled state through aging and self-poling. The stability of the poled state is of critical importance in a PEH device, since depolarization of the sample means the loss of the power source of the entire microsystem. Although it seems possible and attractive to exploit self-poling in the PPE configuration, its introduction into the IDE configuration — as a kind of symmetry breaking imposed on the top surface — did not provide sufficiently strong effects to be of real practical interest. The aging process appears more promising, since it may allow to tune the extrinsic contributions to the dielectric and piezoelectric response of the sample. It is desirable to lower the former, in order to decrease the capacitance of the device and reach a larger voltage output. On the contrary, the latter should be prevented from decaying with time, so that the fraction of mechanical energy converted into electrical energy, which is at the heart of the energy harvesting operation, remains constant over the entire lifetime of the device. We could not unambiguously determine the mechanisms of aging in our IDE sample, which prevents us for the moment from fully optimizing this phenomenon. The most likely mechanism is charge compensation of polarization discontinuities at grain boundaries. This would also explain the faster aging of IDE structures as compared to PPE structures. Nonetheless, our observations with UV light exposure are promising, and further investigations should permit to gain some control over the aging process to the benefit of the harvesting performances.

From our investigations, we could deduce and propose golden rules for the design of IDE

structures for typical applications. The main concerns to be addressed are the electric field homogeneity within the film to achieve proper poling and actuation; the reduction of the footprint of the IDE structures to obtain larger performances for a given sample size; the magnitude of the voltage bias necessary to drive the sample; and the capacitance of the device. The excellent retention properties and low capacitance of the IDE samples make them ideally suited for sensors and energy harvesters. Their increased linearity and lower hysteresis could also make them interesting for specific actuation applications. The compressive stress that is generated in the ferroelectric layer may be better suited for some applications than the tensile stress developed in the PPE configuration, and in particular, it should limit the risk of mechanical failure of the ferroelectric film. However, this comes at the cost of a reduced generated stress for a given driving field for the IDE configuration. This is presumably due to a lower number of ferroelastic domain walls, because the poled state shows a more stable stress situation than in the PPE case.

Our investigations have significantly improved the understanding of the IDE system. However, a number of open questions remain. The material values extracted with our analytical model still display some geometry dependence: smaller gap samples show a larger dielectric and piezoelectric response. This could be explained by the particular domain pattern which must exist near the electrode finger's edge, which is a zone presenting two complexities. First, there is a field concentration region near the electrode finger. It is not clear how this region could influence the overall sample behavior. In particular, we speculate that the nucleation of reversed domains during switching takes place at this location. Unfortunately, PFM imaging did not provide evidence in favor or against this assumption. If switching is nucleation-limited, promoting the nucleation of reversed domains by tuning the geometry of the electrode finger edge should allow a more efficient poling process. Further study into the switching dynamics of PZT thin film with IDE could elucidate this point. Second, the polarization direction, which is located in the plane of the film within the gap, must change its direction when approaching the electrode fingers, to be able to transfer to the electrodes the charges generated within the gap by the direct piezoelectric effect. There must, therefore, exist a zone near the electrode finger's edge, where the out-of-plane polarization is not zero — even though it should be zero within the middle of the electrode finger. This zone should extend over some distance into the electrode finger. This fact could explain why the IDE system behaves as if the active volume had a length of $a + \Delta a$, larger than the gap distance a . Phase-field simulations of the domain pattern at the edge of the electrode finger could shed some light on the exact domain configuration at the junction between the active zone and the electroded zone, to understand how the polarization changes its direction by 90° .

The latter discussion also raises the question of how to treat the inhomogeneities which are intrinsic to ferroelectric films with IDE. Because the electric field strength varies within the active region, so do the local dielectric constant, piezoelectric coefficient, and domain configuration. These variations are not limited to the material volume situated near the electrode finger: In the case where the structures are patterned on top of a conductive substrate which behaves as a floating potential, the strength of the electric field will drop at midgap in

some situations. In our model, we have postulated a homogeneous response, which appears to describe well the film behavior; but this assumption does not hold in real samples. Here again, further simulation efforts, taking into account the piezoelectric properties of the material which we have neglected in our simulation work, may provide some insight into the validity and limitations of the homogeneous approach, and help to build a model which could also address the inhomogeneous case.

The sensitivity of the IDE sample to UV light exposure could offer a valuable tool to tune the extrinsic response according to the need of the application. This may be used to lower the dielectric response so that the capacitance of the sample is decreased, providing a larger voltage output. It could also be employed to reinforce the stability of the poled state and, thus, improve the reliability of the device. Finally, it is reported that enhanced poling can be achieved by the simultaneous application of a poling bias and UV radiations. All these features are beneficial for energy harvesting operations.

The principal challenge of piezoelectric energy harvesting with ferroelectric thin films is to provide both a large power output and a large voltage output. The latter can be obtained with the IDE configuration. The former, however, greatly depends on the quality and performance of the ferroelectric active layer. This is the reason why the improvement and tuning of the material properties are of primary importance for the advancement of piezoelectric energy harvesting technology. In this thesis work, we have contributed to that goal through accurate and systematic characterization, and by investigating novel routes to adjust the material behavior.

A PZT thin films by CSD

In this work, we used a 2-methoxyethanol (2MOE) sol-gel route adapted from Blum and Gurkovich [92, 194] and from Budd *et al.* [195]. Not including the precursor solution preparation, the film deposition is a three-step process:

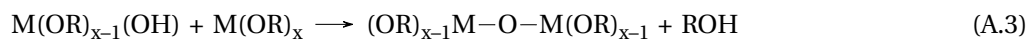
1. Spin-coating of the precursor solution onto the substrate;
2. Pyrolysis at 350 °C for 1 min;
3. Crystallization in a rapid thermal annealing tool (RTA) at 650 °C for 1 min under O₂ flow.

Using a concentration of 0.45 mol L⁻¹ for the precursor solutions, each spin-coating step yields a film thickness of 60–70 nm after pyrolysis. Four spin-coating steps are performed before the wafer is brought to the RTA tool for crystallization. This yields a perovskite film about 250 nm-thick. The sequence is then repeated to reach larger thicknesses. The coating of a 1 μm film requires 16 spinning steps and 4 RTA anneals, and double this amount for reaching a thickness of 2 μm. The final composition of the film is dictated by the stoichiometry of the precursor solutions; lead is always present in excess of 10 at.% to 30 at.% to compensate for lead oxide volatilization during the high temperature steps. The solution preparation procedure is described in detail in Chidambaram's PhD thesis [93].

The pyrolysis step evaporates the solvent and turns the metal alkoxides M(OR)_x from the precursor solution into a gel made of a three-dimensional network of M–O–M bonds [49, 194]. The monomer units form by hydrolysis as follows:



Polymerization then proceeds by condensation through water or alcohol elimination, respectively:



Due to the much larger energy required for the nucleation of the perovskite phase than for its growth [25], the crystalline phase is formed by heterogeneous nucleation on the substrate surface, causing columnar grain growth. After the first RTA step is performed, each new PZT layer nucleates quasi-epitaxially on the previous one [44], yielding a final film with the same thickness as the grains. These films are typically dense and smooth [44], with a similar microstructure for growth on Pt or MgO [35]. The crystallization in an RTA tool reduces the amount of lead loss (because of the shorter duration of the high temperature step) and delays the nucleation of the perovskite phase to higher temperatures, which favors heterogeneous nucleation at the substrate [49]. Heterogeneous nucleation and the quasi-epitaxial growth allows texture control by the use of an appropriate seed layer [25]. PTO is generally used for {100} growth and a thin TiO₂ seed layer is chosen for {111} growth, resulting in more than 90 % of the film volume having the desired orientation for a large range of Zr/(Ti+Zr) ratio [50]. PTO has also been used as a seed layer to obtain {100} films on MgO [35], albeit with limited reproducibility [51].

During growth, the crystalline front progresses from the bottom to the top of the amorphous gel as a flat plane [196]. If only one solution is used for all spinning steps, the final film shows a gradient of composition within each crystallized layer [44]. Ti ions are preferentially incorporated into the perovskite lattice during the crystallization anneal, because the energy required to form PTO is lower than that to form PZO [97]. The ions are quite mobile in the amorphous gel, and not at all inside the perovskite lattice because the sol-gel growth temperature is too low; as a consequence, a Ti flow towards the growth front and a Zr flow away from the growth front are established [13], yielding a Ti-rich composition at the bottom and a Ti-poor composition at the top of the crystallized layer, as compared to the nominal composition of the precursor solution. It is possible to reduce the dispersion around the nominal composition from ± 12 at.% to ± 2.5 at.% by using a set of 4 solutions with compositions opposing the natural Zr/(Zr+Ti) gradient, as shown by Calame and Muralt [47]; this is the so-called gradient-free route. The more homogeneous film they obtained resulted in a 20 %-larger $e_{31, f}$ as compared to a film fabricated with the one-composition route. They worked with the nominal MPB composition, so that the portions of the film whose composition deviates from the MPB is expected to exhibit a significantly lower response. The increase in $e_{31, f}$ may therefore be more marginal if the nominal composition is away from the MPB.

This route requires the preparation of more precursor solutions (4 instead of 2), and therefore is more expensive to pursue, so that the one-composition route remains sometimes preferred even though it results in lower performances. In this work, we have exclusively used the gradient-free route to exclude any possible effect due to the presence of a composition gradient.

B Piezoelectric coefficient for the cantilever beam architecture

In this appendix, we will review how to obtain the piezoelectric coefficient of a ferroelectric thin film for the cantilever beam architecture, with the PPE or the IDE configuration, for both converse and direct mode.

B.1 Piezoelectric coefficient in converse mode

We use beam-shaped 1.5 mm wide and 15 mm long sample for our measurements. This design allows ready electrical and piezoelectric response characterization with the equipment at our disposal, following a technique proposed by Dubois and Muralt [39], for both parallel plate and interdigitated electrode configurations.

An aixACCT[®] TF2000 setup was used to record the PV and CV loops. This setup is combined with a single laser beam interferometer to measure the cantilever tip excursion in order to monitor the stress in the ferroelectric film. In this way, we record the PV, CV and stress-field loops simultaneously. The principle is described in detail by Mazzalai and coworkers [40]. Particularly noteworthy is the fact that a good linear fit is obtained for all top electrode length down to 2 mm, meaning that the clamping has no measurable rigidifying effect as long as the active area extends at least 2 mm from the clamping position. The active area should also occupy a significant fraction of the cantilever width — $2/3$ for all our samples, similarly to the cited work [40].

Figure B.1 pictures the setup configuration for the converse mode measurement for a cantilever with IDE. The cantilever is clamped at the start of the interdigitation zone which is the active zone. When the electrodes are biased, compressive stress builds up between the IDE fingers, which bends the substrate downward. The curvature of the active zone is then amplified by the slope of the cantilever in the inactive zone. The cantilever tip excursion is measured by interferometry by shining a laser beam onto a dedicated reflector at the sample end, or with a photonic sensor placed at the same location [40]. In the PPE cantilever, the beam would bend upward.

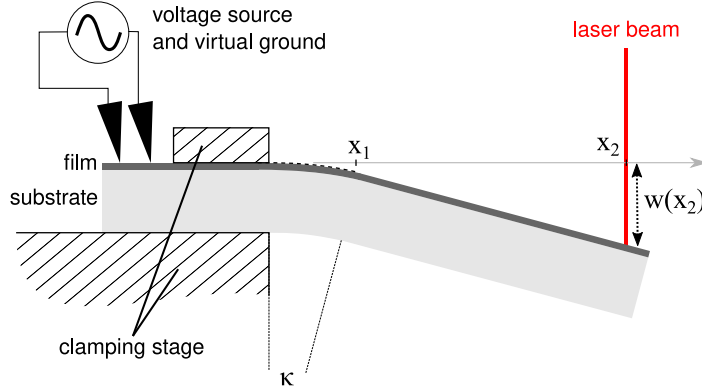


Figure B.1 – Configuration of the clamping stage. The dimensions are not to scale. The cantilever tip excursion $w(x_2)$ is exaggerated for clarity. Samples with IDE will bend downward as pictured; samples with PPE will bend upward.

Figure B.2 shows the geometry of the interdigitated zone and the definition of lengths for the IDE configuration. Note that the polarization vector can only take discrete orientations whereas the electric field lines are curved, and will attempt to locally maximize $\mathbf{P} \cdot \mathbf{E}$ for \mathbf{E} larger than the coercive field. The finger length W is $980 \mu\text{m}$ and the structures either have 100 or 200 fingers (that is 50 or 100 for each polarity, respectively). t_f is the thickness of the PZT layer, a is the IDE gap and b is the finger width.

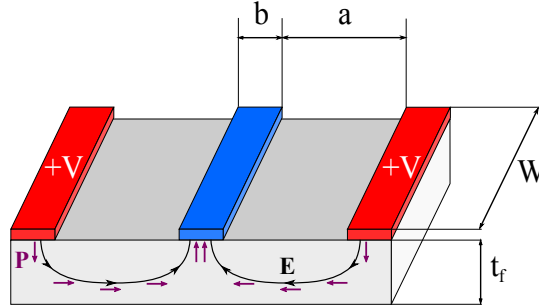


Figure B.2 – Definition of lengths for the IDE configuration. The polarization is pictured as taking discrete orientation to locally align with the electric field.

B.1.1 Cantilever bending geometry

We place the origin of lengths at the start of the unclamped zone, which coincides with the start of the active area. We assume constant curvature in the active area (extending from 0 to x_1), caused by the stress in the PZT film from the transverse piezoelectric coefficient; and zero curvature in the inactive area (which extends from x_1 to the end of the cantilever). We name $w(x)$ the (small) excursion of the point at coordinate x of a fiber along the cantilever axis and situated on the neutral plane of the beam (*i. e.* which experiences no lateral or longitudinal deformation upon bending of the cantilever). The laser spot shines on the point

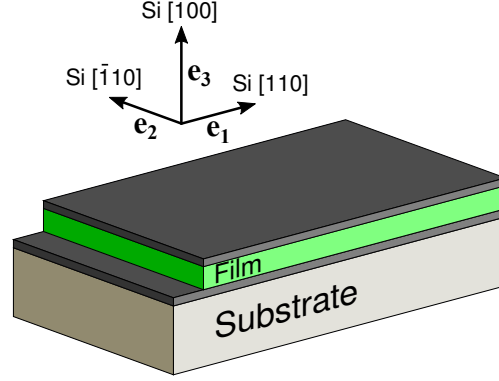


Figure B.3 – Definition of the axes for the PPE case.

of coordinate x_2 . The situation is pictured in Figure B.1. In the PPE configuration, a tensile stress will appear in the film upon biasing, causing the cantilever to bend upward instead of downward as pictured. Downward bending will happen in the IDE configuration, where a compressive stress is developed instead.

From our assumptions, the excursion at x_1 is then given by :

$$w(x_2) = w(x_1) + (x_2 - x_1) w'(x_1) \quad (\text{B.1})$$

And the excursion at $x \in [0, x_1]$ is given by :

$$w(x) = \frac{1}{2} \kappa x^2 \quad (\text{B.2})$$

where κ is the curvature : $\kappa = 1/R$ where R is the radius of curvature. From equations B.1 and B.2 we obtain the curvature in the active zone as function of the excursion :

$$\kappa = \frac{2w(x_2)}{x_1(2x_2 - x_1)} \quad (\text{B.3})$$

B.1.2 Parallel plate electrodes

Figure B.3 shows the definition of the axes. Axis 3 is directed out of the plane of the film while both axes 1 and 2 are situated in the film plane. The ferroelectric film is clamped by the substrate and free to deform in the out-of-plane direction, therefore we assume that the film stress or strain is uniform within the film, and we have $\epsilon_1 = \epsilon_2 = 0$ and $\sigma_3 = 0$. In the parallel plate configuration, the crystallites are randomly oriented within the plane of the film but have all the same out-of-plane direction (textured film), and the film is poled in the out-of-plane direction by the electric field $\mathbf{E} = E_3 \mathbf{e}_3$. It has therefore the ∞/mm symmetry in that direction,

Appendix B. Piezoelectric coefficient for the cantilever beam architecture

and writing the piezoelectric constitutive equations for this symmetry, we obtain:

$$\sigma_1 = c_{13}^E \epsilon_3 - e_{31} E_3 \quad (\text{B.4a})$$

$$\sigma_2 = c_{13}^E \epsilon_3 - e_{31} E_3 \quad (\text{B.4b})$$

$$\sigma_3 = c_{33}^E \epsilon_3 - e_{33} E_3 = 0 \quad (\text{B.4c})$$

$$D_3 = e_{33} \epsilon_3 + \kappa_{33}^e E_3 \quad (\text{B.4d})$$

Thus $\sigma_1 = \sigma_2 = \sigma_f$ and we have :

$$\sigma_f = - \left(e_{31} - e_{33} \frac{c_{13}^E}{c_{33}^E} \right) E_3 = -e_{31,f} E_3 \quad (\text{B.5})$$

where $e_{31,f}$ can also be written as $e_{31,f} = d_{31} / (s_{11}^E + s_{12}^E)$.

Since the film stress σ_f is assumed to be constant across the film thickness t_f , the film exerts a force per unit width $F_f = \sigma_f t_f$ on the substrate. In reaction, the substrate exerts an equal and opposite force $F_s = -F_f$. Since the points of application of these two equal and opposite forces do not coincide (one is applied at the middle of the film, the other one at the middle of the substrate), they generate a moment M_F at a point situated midway between their respective point of application, which is hence given by :

$$M_F = F_f \frac{1}{2} \frac{t_s + t_f}{2} + F_s \frac{1}{2} \frac{t_s + t_f}{2} \quad (\text{B.6a})$$

$$= F_f \frac{t_s + t_f}{2} \quad (\text{B.6b})$$

This moment will be compensated by internal bending moments of the substrate and the film [197] such as $M_F = M_s + M_f$. They are given by, from section 9.3.2 of the cited work [197], for isotropic elastic materials in uniaxial stress and per unit width :

$$M_s = \frac{E_s t_s^3}{12R} \quad (\text{B.7})$$

$$M_f = \frac{E_f t_f^3}{12R} \quad (\text{B.8})$$

where E is Young's modulus and t the thickness, and the subscript s (resp. f) refers to the substrate (resp. the film). Therefore :

$$F_f \frac{t_s + t_f}{2} = \frac{1}{12R} (E_s t_s^3 + E_f t_f^3) \quad (\text{B.9})$$

Neglecting terms in t_f/t_s or in higher orders of this ratio, and knowing that $F_f = \sigma_f t_f$, we obtain the so-called Stoney formula per unit width :

$$\sigma_f = \frac{1}{6R} \frac{E_s t_s^2}{t_f} \quad (\text{B.10})$$

In case of equi-biaxial stress, E_s should be replaced by $E_s/(1 - \nu_s)$ where ν_s is the Poisson's ratio of the substrate material :

$$\sigma_f = \frac{1}{6R} \frac{E_s t_s^2}{(1 - \nu_s) t_f} \quad (\text{B.11})$$

Equation B.10 was first given by Stoney in 1909 [198]. From the assumption that the film thickness t_f is much less than the substrate thickness t_s , it provides a relationship between the film stress and the bow of the substrate, which is independent of the elastic properties of the film.

Mazzalai and coworkers [40] assume equi-biaxial stress under the top electrode and uniaxial stress (along the cantilever axis) outside of the zone covered by the top electrode. The linear fits they obtained in Figure 5 of their work justifies the description of the cantilever bow by a single curvature present within the active area. Because the lateral extension of both the uncovered zone (0.25 mm on each side of the 1 mm-wide electrode) and the electrode-covered zone is much larger than the film thickness (at most 4 μm for sol-gel processed films), it is reasonable to assume uniaxial stress in the uncovered zone. Thus, if we write c_f the electrode width w_{el} to cantilever width w_{ca} ratio, or electrode coverage factor (which is 2/3 for our PPE samples), the film equi-biaxial stress σ_f in the active zone is obtained by :

$$F_f = \sigma_f t_f w_{el} = (w_{ca} - w_{el}) \frac{1}{6R} E_s t_s^2 + w_{el} \frac{1}{6R} \frac{E_s}{1 - \nu_s} t_s^2 \quad (\text{B.12a})$$

$$\sigma_f = \frac{1}{6R} \frac{E_s t_s^2}{(1 - \nu_s) c_f t_f} ((1 - \nu_s)(1 - c_f) + c_f) \quad (\text{B.12b})$$

Thanks to equation B.3 we can now link the tip displacement and the film stress as follows :

$$\sigma_f = \frac{1}{3} \frac{E_s t_s^2}{(1 - \nu_s) c_f t_f} ((1 - \nu_s)(1 - c_f) + c_f) \frac{w(x_2)}{x_1(2x_2 - x_1)} \quad (\text{B.13})$$

Single crystal Si wafers are no isotropic materials. Hence, in equation B.13, orientational Young's modulus and Poisson's ratio must be used. They are given by Hopcroft and coworkers [76] but more generally can be obtained from the elastic stiffness matrix of Si, which is available from various sources (Hopcroft *et al.* give 5 references). Our cantilever long axis is along the Si [110] direction (parallel to the main flat) and the orthogonal axis is along the $[\bar{1}10]$ direction, hence we should use $E_s = 169 \text{ GPa}$ and $\nu_s = 0.064$ [40, 76]. Alternately, equations B.10 and B.11 can be obtained for anisotropic materials by directly using the elastic stiffness matrix as done by Janssen *et al.* [199]. Note that the neutral axis is not situated in the middle of the Si substrate as stated by Mazzalai and coworkers [40], but $2t_s/3$ away from the film/substrate interface, independently of σ_f ; see Janssen *et al.* [199] for a derivation of the position of the neutral axis with mechanical equilibrium equations, and section 2.1 of the book by Freund and Suresh [200] for a derivation through minimization of the elastic energy.

Dividing by the electric field strength in the out-of-plane direction $E_3 = V/t_f$, where V is

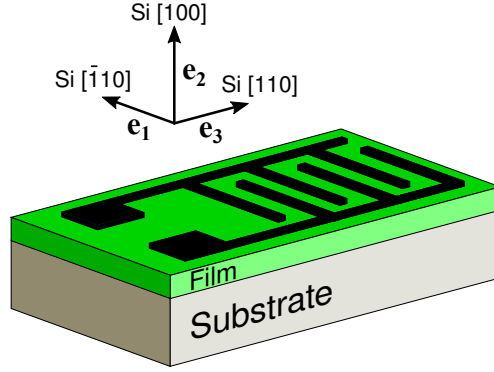


Figure B.4 – Definition of the axes for the IDE case.

the bias across the parallel plate electrodes, we obtain the effective transverse piezoelectric coefficient $e_{31, f}$:

$$e_{31, f} = -\frac{1}{3} \frac{E_s t_s^2}{V(1 - \nu_s)c_f} \left((1 - \nu_s)(1 - c_f) + c_f \right) \frac{w(x_2)}{x_1(2x_2 - x_1)} \quad (\text{B.14})$$

This latter formula is used to obtain $e_{31, f}$ from small-signal measurements; then V is the small-signal amplitude and $w(x_2)$ the tip displacement amplitude. For large signal measurements, one should rather calculate σ_f from equation B.13 and then use $e_{31, f} = d\sigma_f/dE_3$ as discussed by Mazzalai and coworkers [40], to capture both the field and history-dependence of $e_{31, f}$ in ferroelectric thin films.

B.1.3 Interdigitated electrodes

Figure B.4 shows the definition of the axes. The electric field is directed along axis 3, with the electrode fingers along the 1 direction, while axis 2 is pointing out-of-plane. Note that since the PZT is poled by the electric field, even though the electric field changes sign at each gap, it is always in the poled direction. Without loss of generality, we will therefore assume that $E_3 > 0$. Again the film is clamped, causing $\epsilon_1 = \epsilon_3 = 0$ and $\sigma_2 = 0$. Like Chidambaram *et al.* [35] we assume that the crystallites have the same properties along the unpoled directions 1 and 2, even though axis 2 is the film growth direction; this approximation gives similar calculations to the PPE case, and allows ready estimates for effective coefficients using commercial material data of PZT ceramics. As a consequence, the poled film has the ∞/mm symmetry in the 3 direction, and the piezoelectric constitutive equations are:

$$\sigma_1 = c_{12}^E \epsilon_2 - e_{31} E_3 \quad (\text{B.15a})$$

$$\sigma_2 = c_{11}^E \epsilon_2 - e_{31} E_3 = 0 \quad (\text{B.15b})$$

$$\sigma_3 = c_{13}^E \epsilon_2 - e_{33} E_3 \quad (\text{B.15c})$$

$$D_3 = e_{31} \epsilon_2 + \kappa_{33} E_3 \quad (\text{B.15d})$$

Hence, $\epsilon_2 = e_{31} E_3 / c_{11}^E$, and we have :

$$\sigma_1 = - \left(1 - \frac{c_{12}^E}{c_{11}^E} \right) e_{31} E_3 = -e_{31, \text{if}} E_3 \quad (\text{B.16a})$$

$$\sigma_3 = - \left(e_{33} - \frac{c_{13}^E}{c_{11}^E} e_{31} \right) E_3 = -e_{33, \text{if}} E_3 \quad (\text{B.16b})$$

Because $e_{31} < 0$ and the stiffness coefficients are positive, $e_{33, \text{if}} > e_{33} > 0$ and $\sigma_3 < 0$ is compressive when the field is along the poled direction. The sign of $e_{31, \text{if}}$ depends on the value of the ratio c_{12}^E / c_{11}^E ; this ratio is typically less than 1, and thus gives typically tensile stress along the 1 direction since $e_{31} < 0$. Note that, if $c_{12}^E / c_{11}^E < 1$, then $|e_{31, \text{if}}| < |e_{31}|$. For the parallel plate case, we had $|e_{31, \text{f}}| > |e_{31}|$, which was a consequence of the film clamping. In the IDE configuration, the net effect along the poling direction comes from the $e_{33, \text{if}}$ parameter and is a combination of the longitudinal and the transverse piezoelectric coefficients.

Because the stress between the electrode fingers is not equi-biaxial, the bending of the Si substrate cannot be described by a single curvature. Instead, it is described by a curvature of its main axis κ_3 (named after the stress component that causes it) and a curvature of the orthogonal axis κ_1 . Then a reasoning similar to that used to obtain the Stoney formula (Freund and Suresh [200], section 3.7.1) yields , per unit width:

$$\kappa_3 = \frac{6(\sigma_3 t_f - \nu_s \sigma_1 t_f)}{E_s t_s^2} \quad (\text{B.17a})$$

$$\kappa_1 = \frac{6(\sigma_1 t_f - \nu_s \sigma_3 t_f)}{E_s t_s^2} \quad (\text{B.17b})$$

In case of equi-biaxial stress the previous equations reduce to equation B.11. Like before, this is valid for an isotropic substrate. For our cantilevers on Si [100] substrates, axis 1 is along the $[\bar{1}10]$ direction and axis 3 is along the $[110]$ direction, thus in both cases we must use $E_s = 169 \text{ GPa}$ and $\nu_s = 0.064$ [76]. The cantilever tip excursion gives access to κ_3 only, which is nonetheless influenced by σ_1 as shown in equation B.17a. We have, from equations B.16a and B.16b and writing $R_3 = 1/\kappa_3$:

$$\sigma_3 = \frac{1}{6R_3} \frac{E_s t_s^2}{\left(1 - \nu_s \frac{\sigma_1}{\sigma_3}\right) t_f} = \frac{1}{6R_3} \frac{E_s t_s^2}{\left(1 - \nu_s \frac{e_{31, \text{if}}}{e_{33, \text{if}}}\right) t_f} \quad (\text{B.18})$$

Thus in the IDE case, and unlike the PPE case, the bending of the substrate depends on the film piezoelectric properties. Since $e_{31, \text{if}} / e_{33, \text{if}} < 0$, this is a mechanically softening effect. This is because both the effective longitudinal and transverse piezoelectric coefficients contribute to increase the compressive stress along the electric field direction.

Table B.1 shows the values of the effective piezoelectric coefficients encountered so far, for two common commercial PZT ceramic grades. We observe, like Chidambaram and coworkers [35], that $e_{33, \text{if}} > e_{33}$ and $|e_{31, \text{f}}| > |e_{31}|$, that $e_{33, \text{if}} > |e_{31, \text{f}}|$, and finally that $e_{31, \text{if}}$ is much smaller than

Appendix B. Piezoelectric coefficient for the cantilever beam architecture

Table B.1 – Effective piezoelectric coefficients for standard PZT ceramic grades.

PZT grade	e_{31} (C/m ²)	e_{33} (C/m ²)	$e_{31,f}$ (C/m ²)	$e_{31,if}$ (C/m ²)	$e_{33,if}$ (C/m ²)
PZT-4	−5.2	15.1	−15	−2.3	17.9
PZT-5H	−6.55	23.3	−23.3	−2.4	27.7

all the others. Thus, the film clamping increases the response also in the IDE case, but this increase is less pronounced than in the PPE case. The anisotropy in the piezoresponse in the IDE case is very marked, since $e_{31,if}$ is much less than $e_{33,if}$.

Since $\nu_s = 0.064 \ll 1$, the factor $1 - \nu_s e_{31,if}/e_{33,if}$ can be neglected in first approximation, as done by Chidambaram and coworkers [35]; the film is then considered to experience pure uniaxial stress and the formula reduces to equation B.10. We will nonetheless keep this factor in the rest of the derivation for the sake of completeness.

Now we must link the curvature within the gap to the cantilever tip displacement. We assume that the regions below the electrode fingers are inactive and as such, show no stress. We name a the gap distance and b the finger width, and $\eta = b/(a + b)$ the metalization ratio. Then we can assume one of the following [35]:

1. The Si substrate shows a constant, averaged curvature within the interdigitation zone, given by $(1 - \eta)\kappa_3$.
2. The Si substrate shows a step-wise curvature equal to κ_3 within the gaps and 0 below the fingers.

In case 1, the averaged curvature $(1 - \eta)\kappa_3$ and the tip displacement are connected by equation B.3. Case 2 is similar to the thin substrate case treated by Chidambaram *et al.* [35]. It gives the following formula for the tip displacement :

$$w(x_2) = \frac{1}{2} N_g^2 a^2 \kappa_3 \left(1 + \left(1 + \frac{1}{N_g} \right) \frac{b}{a} \right) + N_g a \kappa_3 (x_2 - x_1) \quad (\text{B.19})$$

where N_g is the number of gaps. The active zone extends over a distance $x_1 = N_g(a + b) - b$, assuming that the first electrode finger is clamped. If $N_g \gg 1$, cases 1 and 2 are equivalent. For convenience in the rest of the calculation, we write $w(x_2) = g_i \kappa_3$ where g_i is a geometric factor given by either :

$$g_1 = \frac{1}{2} x_1 (2x_2 - x_1) (1 - \eta) \quad (\text{B.20a})$$

$$g_2 = \frac{1}{2} N_g^2 a^2 \left(1 + \left(1 + \frac{1}{N_g} \right) \frac{b}{a} \right) + N_g a (x_2 - x_1) \quad (\text{B.20b})$$

and the index $i = 1, 2$ corresponds to case 1 and 2 respectively.

Assuming uniaxial stress in the substrate outside of the interdigitation zone and equating the

moments, we obtain :

$$F_f = \sigma_3 t_f w_{el} = (w_{ca} - w_{el}) \frac{\kappa_3}{6} E_s t_s^2 + w_{el} \frac{\kappa_3}{6} \frac{E_s}{1 - \nu_s \frac{e_{31,if}}{e_{33,if}}} t_s^2 \quad (B.21a)$$

$$\sigma_3 = \frac{w(x_2)}{6g_i} \frac{E_s t_s^2}{c_f t_f} \left(1 - c_f + \frac{c_f}{1 - \nu_s \frac{e_{31,if}}{e_{33,if}}} \right) \quad (B.21b)$$

Lastly, dividing by the electric field within the gap region $E_3 = V/a$, we find $e_{33,if}$ as a function of the tip displacement :

$$e_{33,if} = - \frac{w(x_2)}{6g_i} \frac{a E_s t_s^2}{V c_f t_f} \left(1 - c_f + \frac{c_f}{1 - \nu_s \frac{e_{31,if}}{e_{33,if}}} \right) \quad (B.22)$$

Neglecting the ratio $\nu_s e_{31,if}/e_{33,if}$ and using the geometric factor g_1 (resp. g_2), we obtain the same formula as in equations 16 and 18 (resp. 31) of the cited work [35]. As seen in chapter 3, it is more accurate to write $E_3 = V/(a + \Delta a)$ where $a + \Delta a$ is an effective gap for electrical properties. In this case we have :

$$e_{33,if} = - \frac{w(x_2)}{6g_i} \frac{(a + \Delta a) E_s t_s^2}{V c_f t_f} \left(1 - c_f + \frac{c_f}{1 - \nu_s \frac{e_{31,if}}{e_{33,if}}} \right) \quad (B.23)$$

This corresponds to the material coefficient $\widehat{e_{33,if}}$ for g_1 (material coefficient for thick substrate case) or $\widehat{e_{33,if}}$ for g_2 (material coefficient for thin substrate case) of Chidambaram and coworkers [35]. If N_g is large, $g_1 = g_2$ and $\widehat{e_{33,if}} = \widetilde{e_{33,if}}$, *i. e.* it is not possible to distinguish between a step-like curvature and an average curvature solely by monitoring the tip displacement.

B.2 Piezoelectric coefficient in direct mode

B.2.1 Setup description and cantilever bending geometry

For measuring the transverse piezoelectric coefficients through the direct piezoelectric effect, we use a setup first proposed by Dubois and Murali [39]. In this setup a cantilever beam is clamped at one end and a piezoelectric actuator applies an alternating force on the beam free end. Since the piezoelectric film is much thinner than the substrate, it is assumed to experience the same strain as that induced at the surface of the bent substrate. This strain is readily obtained thanks to beam theory formulas [201]. Both the static and oscillating strains must remain small for these formulas to be valid. The electrodes are connected either to a charge amplifier to collect the piezoelectric charges generated by the oscillating strain — the piezoelectric film is then in closed-circuit condition, since the charge amplifier input behaves as a virtual ground; or to a voltage amplifier to measure the voltage difference induced by the oscillating strain — the open-circuit condition is then realized in the film. An oscilloscope is used to visualize the charge amplifier (resp. the voltage amplifier) output and we record the peak-to-peak variation of the charge (resp. the voltage). This allows to obtain the effective

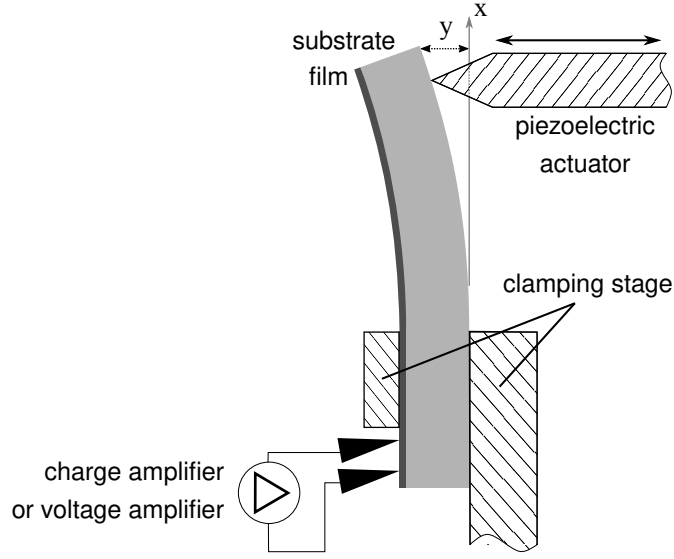


Figure B.5 – Configuration of the clamping stage for direct transverse piezoelectric effect measurements. The dimensions are not to scale. The cantilever excursion y is exaggerated for clarity. The piezoelectric actuator moves back and forth as indicated by arrows, causing a small excursion oscillation around an average excursion value.

transverse e and h coefficients, respectively. The setup is pictured in Figure B.5. The peak-to-peak displacement of the actuator is monitored thanks to a strain gauge and can be adjusted.

We set $x = 0$ at the clamping position and $x = l > 0$ at the point where the actuator is in contact with the substrate at zero excursion. Excursion is denoted as y and counted positive when pointing towards the left in Figure B.5. The excursion is given by [39] :

$$y = \frac{F}{6E_s I_{ca}} (3lx^2 - x^3) \quad (B.24)$$

$$I_{ca} = \frac{w_{ca} t_s^3}{12} \quad (B.25)$$

I_{ca} is the moment of inertia of the cantilever with reference to its neutral axis. In this case the neutral axis is located at the centroid of the cross-sections of the cantilever [201], which have a rectangular shape. The small deformation can be described by a local curvature given by :

$$\kappa = \frac{d^2 y}{dx^2} \quad (B.26)$$

The strain along the cantilever axis at the film/substrate interface then is:

$$\epsilon_i = -\frac{t_s}{2} \kappa = -\frac{t_s}{2} \frac{F}{E_s I_{ca}} (l - x) \quad (B.27)$$

The strain index is $i = 1$ for the PPE configuration and $i = 3$ for the IDE configuration, according to the reference frames previously defined. Here the substrate is in uniaxial stress. Writing the actuator peak-to-peak displacement as Δy_{act} , imposed on the cantilever beam at $x = l$, the peak-to-peak strain is given by, from equations B.24 and B.27:

$$\Delta y_{\text{act}} = \frac{\Delta F l^3}{3E_s I_{\text{ca}}} \quad (\text{B.28a})$$

$$\Delta \epsilon_i = -\Delta y_{\text{act}} \frac{3t_s}{2l^3} (l - x) \quad (\text{B.28b})$$

The maximum strain is reached at $x = 0$, *i. e.* at the end of the clamped region, and is of the order of $t_s \Delta y_{\text{act}} / l^2$. In our setup the piezoelectric actuator induces a peak-to-peak oscillating deflection of $\Delta y_{\text{act}} = 4.5 \mu\text{m}$, t_s is typically 0.5 mm and $l = 9 \text{ mm}$. This gives a maximum peak-to-peak strain close to 3×10^{-5} . Hence the assumption of small strains is justified, as long as the static strain remains small as well. The latter is controlled thanks to a micrometric screw commanding the distance between the actuator tip and the clamping stage; this allows precise positioning of the cantilever beam and hence accurate limitation of the static strain to sufficiently low values. Dubois and Muralet [39] observed a dependence of the $e_{31, \text{f}}$ coefficient on the static strain; in this work we performed all the measurements as close as possible to the zero-strain point, on the compressive side. Chidambaram and coworkers [43] treated the case for the IDE configuration.

Our electrode pattern, both in the PPE and in the IDE case, is designed so that the active zone starts exactly where the clamping ends. If the active zone starts at coordinate x_s from the end of the clamped section, one would need to start the following integrals from x_s instead of 0, but the reasoning is otherwise unchanged. The cited works [39, 43] provide formulas for the case $x_s \neq 0$.

B.2.2 Parallel plate electrodes

Short circuit

Let d be the distance over which the top electrode covers the cantilever along the x direction. As before we name w_{el} the (rectangular) top electrode width. We use the same reference frame as in Figure B.3. The strain state of the film is then the strain state of the substrate surface at the film/substrate interface and is given by, for $x \in [0, d]$ and from equation B.28b:

$$\epsilon_1(x) = -y_{\text{act}} \frac{3t_s}{2l^3} (l - x) \quad (\text{B.29a})$$

$$\epsilon_2(x) = -\nu_s \epsilon_1(x) \quad (\text{B.29b})$$

where y_{act} is the actuator position at any given time, *i. e.* the excursion at $x = d$. $\nu_s = 0.064$ is the Poisson's ratio of Si between the directions $[110]$ and $[\bar{1}10]$.

Appendix B. Piezoelectric coefficient for the cantilever beam architecture

From the constitutive equations we can write, since $\sigma_3 = 0$:

$$\epsilon_1 = s_{11}^E \sigma_1 + s_{12}^E \sigma_2 + d_{31} E_3 \quad (\text{B.30a})$$

$$\epsilon_2 = s_{12}^E \sigma_1 + s_{11}^E \sigma_2 + d_{31} E_3 \quad (\text{B.30b})$$

$$D_3 = d_{13}(\sigma_1 + \sigma_2) + \kappa_{33}^E E_3 \quad (\text{B.30c})$$

In short circuit conditions, $E_3 = 0$ and we have:

$$\sigma_1 + \sigma_2 = \frac{\epsilon_1 + \epsilon_2}{s_{11}^E + s_{12}^E} \quad (\text{B.31})$$

And, using equation B.29b:

$$D_3 = d_{13}(\sigma_1 + \sigma_2) = \frac{d_{13}}{s_{11}^E + s_{12}^E} (1 - \nu_s) \epsilon_1 \quad (\text{B.32a})$$

$$D_3 = (1 - \nu_s) e_{31, f} \epsilon_1 \quad (\text{B.32b})$$

For one strain oscillation cycle, the peak-to-peak charge signal is thus given by:

$$\Delta Q = w_{\text{el}} \int_0^d \Delta D_3(x) dx \quad (\text{B.33a})$$

$$\Delta Q = -e_{31, f} w_{\text{el}} (1 - \nu_s) \Delta y_{\text{act}} \frac{3t_s}{2l^3} \int_0^d (l - x) dx \quad (\text{B.33b})$$

$$\Delta Q = -e_{31, f} w_{\text{el}} (1 - \nu_s) \Delta y_{\text{act}} \frac{3t_s}{2l^3} d \left(l - \frac{d}{2} \right) \quad (\text{B.33c})$$

This gives $e_{31, f}$ as function of the sample geometry, peak-to-peak actuator displacement and recorded peak-to-peak charge signal:

$$e_{31, f} = - \frac{2l^3 \Delta Q}{3 \Delta y_{\text{act}} t_s (1 - \nu_s) w_{\text{el}} d \left(l - \frac{d}{2} \right)} \quad (\text{B.34})$$

If the electrode starts at a distance $x_0 > 0$ from the clamp, the formula becomes [39]:

$$e_{31, f} = - \frac{2l^3 \Delta Q}{3 \Delta y_{\text{act}} t_s (1 - \nu_s) w_{\text{el}} d \left(l - x_0 - \frac{d}{2} \right)} \quad (\text{B.35})$$

Open circuit

For the open circuit case, we will use another set of constitutive equations [43]:

$$\sigma_3 = c_{13}^D (\epsilon_1 + \epsilon_2) + c_{33}^D \epsilon_3 - h_{33} D_3 = 0 \quad (\text{B.36a})$$

$$E_3 = -h_{13} (\epsilon_1 + \epsilon_2) - h_{33} \epsilon_3 + \beta_{33}^E D_3 \quad (\text{B.36b})$$

This is valid at any coordinate x below the top electrode. In open circuit condition, the voltage difference between the electrodes is constant and each electrode bears no charge on average. This means that the product $E_3(x)t_f(x)$ is constant for all x below the top electrode, and $\int D_3(x)dx = 0$ (but $D_3(x)$ is not necessarily 0 at a given x). Thus, if we multiply the previous equations by dx/d and integrate, we obtain:

$$0 = \frac{1}{d} \int_0^d c_{13}^D(x)(\epsilon_1(x) + \epsilon_2(x))dx + \frac{1}{d} \int_0^d c_{33}^D(x)\epsilon_3(x)dx - h_{33} \frac{1}{d} \int_0^d D_3(x)dx \quad (\text{B.37a})$$

$$\frac{1}{d} \int_0^d E_3(x)dx = -h_{13} \frac{1}{d} \int_0^d (\epsilon_1(x) + \epsilon_2(x))dx - h_{33} \frac{1}{d} \int_0^d \epsilon_3(x)dx + \frac{1}{d} \int_0^d \beta_{33}^\epsilon(x)D_3(x)dx \quad (\text{B.37b})$$

The film is free to move in the 3 direction, and $D_3(x)$ is not constant, so that the film thickness and, hence, the electric field, as well as the elastic stiffness coefficients and the dielectric susceptibility should vary with x , and as such should remain within the integral. This would lead to cumbersome calculations. As an approximation, we assume like the cited work [43] that the film thickness and the material coefficients are constant. This approximation is more accurate for short electrodes, that is for a small d/l ratio. As a consequence, E_3 is constant, and since $\int D_3(x)dx = 0$ and $\epsilon_2 = -\nu_s \epsilon_1$, this yields:

$$0 = c_{13}^D(1 - \nu_s)\langle \epsilon_1 \rangle + c_{33}^D\langle \epsilon_3 \rangle \quad (\text{B.38a})$$

$$E_3 = -h_{13}(1 - \nu_s)\langle \epsilon_1 \rangle - h_{33}\langle \epsilon_3 \rangle \quad (\text{B.38b})$$

where $\langle \cdot \rangle$ denotes averaging. We obtain:

$$E_3 = -\left(h_{13} - h_{33} \frac{c_{13}^D}{c_{33}^D}\right)(1 - \nu_s)\langle \epsilon_1 \rangle = -(1 - \nu_s)h_{31,f}\langle \epsilon_1 \rangle \quad (\text{B.39})$$

where we define an effective transverse piezoelectric coefficient $h_{31,f}$ like we did before with $e_{31,f}$. We have, after equation B.29a:

$$\langle \epsilon_1 \rangle = -y_{\text{act}} \frac{3t_s}{2l^3} \left(l - \frac{d}{2}\right) \quad (\text{B.40})$$

Writing $V = E_3 t_f$, we relate the measured peak-to-peak voltage to the effective coefficient $h_{31,f}$:

$$h_{31,f} = \frac{2l^3 \Delta V}{3\Delta y_{\text{act}} t_s (1 - \nu_s) t_f \left(l - \frac{d}{2}\right)} \quad (\text{B.41})$$

B.2.3 Interdigitated electrodes

Short circuit

We use the same reference frame as in Figure B.4. The strain state of the film is:

$$\epsilon_3(x) = -y_{\text{act}} \frac{3t_s}{2l^3} (l - x) \quad (\text{B.42a})$$

$$\epsilon_1(x) = -\nu_s \epsilon_3(x) \quad (\text{B.42b})$$

where y_{act} is the actuator position at any given time. $\nu_s = 0.064$ is the Poisson's ratio of Si between the directions $[110]$ and $[\bar{1}10]$. From the constitutive equations we can write, since $\sigma_2 = 0$ and $E_3 = 0$ in short circuit conditions:

$$0 = c_{12}^E \epsilon_1 + c_{11}^E \epsilon_2 + c_{13}^E \epsilon_3 \quad (\text{B.43a})$$

$$D_3 = e_{31}(\epsilon_1 + \epsilon_2) + e_{33}\epsilon_3 \quad (\text{B.43b})$$

Therefore:

$$\epsilon_2 = \frac{\nu_s c_{12}^E - c_{13}^E}{c_{11}^E} \epsilon_3 \quad (\text{B.44})$$

$$D_3 = \left(e_{31} \left(\frac{\nu_s c_{12}^E - c_{13}^E}{c_{11}^E} - \nu_s \right) + e_{33} \right) \epsilon_3 = e_{\text{IDE}} \epsilon_3 \quad (\text{B.45})$$

Note that e_{IDE} is not a material parameter but depends on the Poisson's ratio of the substrate, as noticed by Chidambaram *et al.* [43]. Notably it is not equal to $e_{33, \text{if}}$ which is the coefficient obtained in the converse effect measurement. We have:

$$e_{\text{IDE}} = e_{33, \text{if}} - \nu_s e_{31, \text{if}} = e_{33, \text{if}} \left(1 - \nu_s \frac{e_{31, \text{if}}}{e_{33, \text{if}}} \right) \quad (\text{B.46})$$

The factor on the right-hand side of $e_{33, \text{if}}$ in equation B.46 was encountered in equation B.18. If the ratio $\nu_s e_{31, \text{if}} / e_{33, \text{if}}$ is small enough to be neglected, then we have $e_{\text{IDE}} = e_{33, \text{if}}$.

For a given gap situated between coordinates x_1 and x_2 , the peak-to-peak dielectric displacement is $1/a \int_{x_1}^{x_2} D_3(x) dx$ where $a = x_2 - x_1$ is the gap distance. The same integral over ϵ_3 yields, from equation B.42a:

$$\frac{1}{a} \int_{x_1}^{x_2} \epsilon_3(x) dx = -\frac{1}{a} y_{\text{act}} \frac{3t_s}{2l^3} \int_{x_1}^{x_2} (l - x) dx \quad (\text{B.47a})$$

$$= -\frac{1}{a} y_{\text{act}} \frac{3t_s}{2l^3} a(l - x_0) \quad (\text{B.47b})$$

$$= -y_{\text{act}} \frac{3t_s}{2l^3} (l - x_0) \quad (\text{B.47c})$$

where $x_0 = (x_2 + x_1)/2$ is the coordinate of the point at the middle of the gap. Therefore the

total electric displacement is, from equation B.45:

$$D_{\text{tot}} = -e_{\text{IDE}} y_{\text{act}} \frac{3t_s}{2l^3} \sum_{\text{gaps}} (l - x_{\text{mid-gap}}) \quad (\text{B.48})$$

Since $x = 0$ at the start of the interdigitation zone, for gap n we have $x_{\text{mid-gap}} = n\lambda/2 - a/2$ where λ is the IDE period. Then:

$$\sum_{\text{gaps}} (l - x_{\text{mid-gap}}) = \sum_{n=1}^{N_g} \left(l + \frac{a}{2} \right) - \frac{\lambda}{2} \sum_{n=1}^{N_g} n \quad (\text{B.49a})$$

$$\sum_{\text{gaps}} (l - x_{\text{mid-gap}}) = N_g \left(l + \frac{a}{2} \right) - \frac{dN_g}{2} \quad (\text{B.49b})$$

where N_g is the number of gaps and $d = \lambda(N_g + 1)/2$ is the length of the interdigitation zone (assuming $d \gg a$, which is reasonable for $N_g \gg 1$). Since $l \gg a$ in our case of micrometric IDE geometry, we obtain:

$$D_{\text{tot}} = -e_{\text{IDE}} y_{\text{act}} \frac{3t_s}{2l^3} N_g \left(l - \frac{d}{2} \right) \quad (\text{B.50})$$

For one cycle, the peak-to-peak charge signal is given by $\Delta Q = w_{\text{el}} t_f \Delta D_{\text{tot}}$, where w_{el} is here the IDE finger active length — the length over which electrode fingers of opposite polarity are facing each other — and t_f is the piezoelectric thin film thickness. Hence:

$$\Delta Q = -e_{\text{IDE}} \Delta y_{\text{act}} \frac{3t_s}{2l^3} w_{\text{el}} t_f N_g \left(l - \frac{d}{2} \right) \quad (\text{B.51})$$

$$e_{\text{IDE}} = - \frac{2l^3 \Delta Q}{3 \Delta y_{\text{act}} t_s w_{\text{el}} t_f N_g \left(l - \frac{d}{2} \right)} \quad (\text{B.52})$$

If we write $A_{\text{eff}} = w_{\text{el}} t_f N_g$ the effective area of the IDE capacitor, we obtain:

$$e_{\text{IDE}} = - \frac{2l^3 \Delta Q}{3 \Delta y_{\text{act}} t_s A_{\text{eff}} \left(l - \frac{d}{2} \right)} \quad (\text{B.53})$$

This is the same equation as equation B.34 for which the capacitor area was $w_{\text{el}} d$. In the present case however the substrate's Poisson's ratio is included in e_{IDE} . If the electrodes start at $x_0 > 0$ from the clamp, the formula becomes [43]:

$$e_{\text{IDE}} = - \frac{2l^3 \Delta Q}{3 \Delta y_{\text{act}} t_s A_{\text{eff}} \left(l - x_0 - \frac{d}{2} \right)} \quad (\text{B.54})$$

Appendix B. Piezoelectric coefficient for the cantilever beam architecture

Open circuit

For the open circuit condition, we use the following set of equations within the gap:

$$0 = c_{12}^D \epsilon_1 + c_{11}^D \epsilon_2 + c_{13}^D \epsilon_3 - h_{13} D_3 \quad (\text{B.55a})$$

$$E_3 = -h_{31}(\epsilon_1 + \epsilon_2) - h_{33} \epsilon_3 + \beta_{33}^e D_3 \quad (\text{B.55b})$$

As for the parallel plate case, we will assume that the thin film material coefficients are constant along the cantilever axis (within each gap and from gap to gap as well), and that the gap distance remains unchanged to its unstrained value a . Then, averaging over all the gaps, we obtain:

$$0 = c_{12}^D \langle \epsilon_1 \rangle + c_{11}^D \langle \epsilon_2 \rangle + c_{13}^D \langle \epsilon_3 \rangle \quad (\text{B.56a})$$

$$E_3 = -h_{31}(\langle \epsilon_1 \rangle + \langle \epsilon_2 \rangle) - h_{33} \langle \epsilon_3 \rangle \quad (\text{B.56b})$$

This is similar to equation B.45, and gives:

$$E_3 = - \left(h_{31} \left(\frac{v_s c_{12}^D - c_{13}^D}{c_{11}^D} - v_s \right) + h_{33} \right) \langle \epsilon_3 \rangle = -h_{\text{IDE}} \langle \epsilon_3 \rangle \quad (\text{B.57})$$

Replacing the superscript E by D we can define $h_{33, \text{if}}$ and $h_{31, \text{if}}$ like $e_{33, \text{if}}$ and $e_{31, \text{if}}$, and:

$$h_{\text{IDE}} = h_{33, \text{if}} \left(1 - v_s \frac{h_{31, \text{if}}}{h_{33, \text{if}}} \right) \quad (\text{B.58})$$

From the previous calculations, we find, for $N_g \gg 1$:

$$\sum_{\text{gaps}} \int_{x_{\text{start}}}^{x_{\text{end}}} (l - x) dx = a N_g \left(l - \frac{d}{2} \right) \quad (\text{B.59})$$

Hence from equation B.42a:

$$\langle \epsilon_3 \rangle = - \frac{1}{a N_g} \Delta y_{\text{act}} \frac{3 t_s}{2 l^3} a N_g \left(l - \frac{d}{2} \right) = - \Delta y_{\text{act}} \frac{3 t_s}{2 l^3} \left(l - \frac{d}{2} \right) \quad (\text{B.60})$$

We note that this is the same average value as for the parallel plate case. Writing $V = E_3 a$:

$$h_{\text{IDE}} = \frac{2 l^3 \Delta V}{3 \Delta y_{\text{act}} t_s a \left(l - \frac{d}{2} \right)} \quad (\text{B.61})$$

As will be seen in a later section, it is more accurate to write $V = E_3(a + \Delta a)$ where $a + \Delta a$ is an effective gap value for electrical properties. The formula then becomes:

$$h_{\text{IDE}} = \frac{2 l^3 \Delta V}{3 \Delta y_{\text{act}} t_s (a + \Delta a) \left(l - \frac{d}{2} \right)} \quad (\text{B.62})$$

B.2. Piezoelectric coefficient in direct mode

Again this formula will be more accurate for a small d/l ratio. This is the same formula as in equation B.41, replacing the film thickness t_f by the effective gap $a + \Delta a$, and including the substrate's Poisson's ratio in h_{IDE} .

C Conformal mapping and elliptic functions

In this appendix we discuss features of conformal mapping techniques and elliptic functions which arise in calculations involving Schwartz-Christoffel transformations.

C.1 Conformal mapping

C.1.1 Definition

Conformal mapping is a section of complex analysis that is resourceful for a number of physical problems. Conformal mapping functions are complex functions of the complex number — therefore, they transform two-dimensional shapes into new two-dimensional shapes — that preserve angles: This means that the image, by a conformal mapping function f , of two curves intersecting at a point z_0 under the angle δ intersect at $f(z_0)$ under the same angle δ , taken with unchanged orientation [84]. Chapter 5 of the cited work by Henrici [84] contains a thorough description of conformal mapping functions and their properties. Unless otherwise specified, this section is based on the general results presented in that chapter.

It can be shown that it is equivalent for a function to be a conformal map and to be holomorphic with non-zero complex derivative. A holomorphic function is a function of the complex variable which is complex-differentiable in its domain of definition. This gives a number of simple examples of conformal maps, such as rational functions (*i. e.* the quotient of two polynomial functions) of the complex variable when the denominator is not zero. Moebius transformations and Schwartz-Christoffel transformations are two important examples of conformal maps for solving boundary-value problems in physics [84]. The latter type will be described in more details in section C.1.3. The interest of working with complex numbers is that we can use the general theorems of complex analysis to solve two-dimensional problems, by interpreting two-dimensional vectors as complex numbers.

C.1.2 Conformal transplants and boundary-value problems

Let D be a region of the complex plane and f a holomorphic function such as $f : D \rightarrow f(D) = E$ is bijective (that is, for any point $w \in E$, there is one and only one point $z \in D$ such as $f(z) = w$). The variable plane of which D is a subset is often called the z -plane, and the image plane containing E the w -plane. Let $\phi : (x, y) \rightarrow \phi(x, y) = \phi(z) \in \mathbf{R}$ be a scalar function defined on D . We use the usual convention that z is identified either as a complex number or a point $(x, y) \in \mathbf{R}^2$ such as $z = x + iy$. ϕ is typically a potential defined in a domain D of the two-dimensional plane. We can then define an image potential ψ in E such as for all $w \in E$, we have:

$$\psi(w) = \phi(f^{-1}(w)) \quad (\text{C.1})$$

If $w_0 = u_0 + iv_0 = f(x_0, y_0)$, then we have $\psi(u_0, v_0) = \phi(x_0, y_0)$, that is the value of ψ at $f(x_0, y_0)$ is equal to the value of ϕ at (x_0, y_0) . ψ is called the conformal transplant of ϕ under the mapping f .

An important property of conformal transplants is the following : If ϕ is harmonic, meaning it satisfies Laplace's equation $\Delta\phi = 0$, then ψ is also harmonic and satisfies the Laplace's equation as well. If we must find the potential function which is the solution of a boundary-value problem in the z -plane, we know that this potential exists and is unique. Choosing an appropriate conformal mapping function f which simplifies the geometry of the problem, we can solve the problem in the w -plane instead. Using the same notations as before, if ψ is the solution of the problem in the w -plane, then $\psi \circ f$ — which is the conformal transplant of ψ under the mapping f^{-1} — is the (unique) solution of the problem in the z -plane. This property can be used to find the field lines in two-dimensional electrostatics or the flow lines in two-dimensional fluid dynamics for complex geometries which can be transformed into simpler ones where the solution is known or easy to derive. The z -plane is then called the physical plane and the w -plane is the model plane. Some examples are given in section 5.7 and 5.8 of the cited work [84].

C.1.3 The Schwartz-Christoffel transformation

The Schwartz-Christoffel transformation is a particular case of conformal map which maps a complex half-plane onto the interior of a polygon. Usually the upper half-plane is chosen, *i. e.* the plane containing all $z \in \mathbf{C}$ such as $\text{Im}(z) > 0$; in that case the pre-image of the corners of the polygon are situated on the real axis, which as a whole is mapped onto the boundary of the resulting polygon (the points at infinity on the real axis can be mapped as finite points on a given side of the polygon). Apart from adding to the list of known transformations, this conformal map is also interesting because it is possible to derive an explicit formula for an arbitrary polygon (see section 7.5 of the book by Saff and Snider [202] for a method). Details and some examples can be found in section 5.12 of the cited work [84].

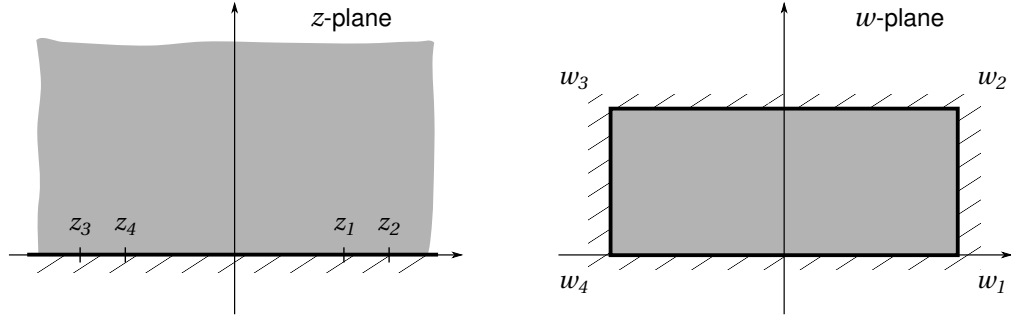


Figure C.1 – Pictures of the z -plane and the w -plane showing the position of the z_i and w_i points. The zones in gray are images of each other by the mapping function or its inverse. The real axis of the z -plane (in bold) is mapped onto the boundary of the rectangle (also in bold).

In the case of layers with interdigitated electrodes, the Schwartz-Christoffel transformation of interest is the one mapping the upper half-plane onto a rectangle [78, 79, 86]. Here we follow the example given by Henrici in section 5.13 of the cited work [84]. We would like to map the z -plane onto the w -plane with a mapping function f .

We use the configuration shown in Figure C.1 where the rectangle is symmetrical with reference to the imaginary axis of the w -plane and has one side on the real axis. The rectangle has width D and height H . We note $w_i = f(z_i)$ for $i = 1 \dots 4$ (all the z_i are situated on the real axis) and we impose $f(0) = 0$ and $z_1 = 1$. In that case, we have $z_4 = -1$ and $z_2 = -z_3 = 1/k$ with $0 < k < 1$. The mapping function is then given by, for $z_0 \in \mathbb{C}$ such as $\text{Im}(z_0) \geq 0$:

$$f(z_0) = C \int_0^{z_0} \frac{dz}{(1-z)^{1/2} (1+z)^{1/2} (1-kz)^{1/2} (1+kz)^{1/2}} \quad (\text{C.2})$$

The integral is evaluated along an arbitrary path in the upper half z -plane such as there is continuity of the branch used to calculate each of the square roots all along the chosen path. The square root branch should be chosen such as it is continuous for $\text{Im}(z) \geq 0$ and equal to 1 for $z = 0$. C in equation C.2 is then a positive real value. It can be shown that k , C , D and H are related by the following equations:

$$D = 2CK(k) \quad (\text{C.3a})$$

$$\frac{D}{H} = \frac{K(k)}{K(k')} \quad (\text{C.3b})$$

where $K: k \rightarrow K(k)$ is the complete elliptic integral of the first kind:

$$K(k) = \int_0^1 \frac{dz}{(1-z^2)^{1/2} (1-k^2 z^2)^{1/2}} \quad (\text{C.4})$$

Equation C.3a is a direct consequence of Equation C.2 for $z_0 = 1$. The derivation of Equation C.3b is more involved and is presented by Henrici [84] in section 5.13. k is called the modulus. Elliptical integrals were given this name in the seventeenth century as mathematicians of the time used them to evaluate arc lengths of ellipses [84]. The modulus k then corresponds to the eccentricity of the ellipse, which is 0 for a circle and approaches 1 for very elongated ellipses. Note that C is only a normalization factor stemming from the fact that we imposed $z_1 = 1$.

C.2 Elliptic functions

C.2.1 Motivations

In the analytical treatment of the capacitance of structures with interdigitated electrodes, the cited authors [78, 79, 86] employ a first transformation mapping a subset of the IDE geometry onto the upper half-plane — which is the inverse of a Schwartz-Christoffel transformation — and a Schwartz-Christoffel transformation mapping the upper half-plane onto an equivalent parallel plate capacitor. In the previous section we gave the Schwartz-Christoffel transformation formulas. If k is known, we can readily calculate the position of an image point. The problem is now to find k from the knowledge of D and H for the inverse transformation. This can be achieved thanks to the elliptic and theta functions.

C.2.2 Jacobi elliptic and theta functions

If $\varphi \in \mathbf{R}$, we define u as:

$$u = \int_0^\varphi \frac{d\theta}{(1 - m \sin^2 \theta)^{1/2}} \quad (\text{C.5})$$

u is the (incomplete) elliptic integral of the first kind (see sections 17.1 to 17.3 of Abramowitz and Stegun [203]). $m \in [0, 1]$ is called the parameter and $\varphi = \text{am } u$ the amplitude. Writing $m = k^2$ and setting $\varphi = \pi/2$, we obtain the complete elliptic integral of the first kind:

$$K(k) = \int_0^1 \frac{dz}{(1 - z^2)^{1/2} (1 - k^2 z^2)^{1/2}} = \int_0^{\pi/2} \frac{d\theta}{(1 - m \sin^2 \theta)^{1/2}} \quad (\text{C.6})$$

The Jacobi elliptic functions can be defined as functions of φ , but a number of other approaches are possible for elliptic functions in general (see section 16.1 of the handbook by Abramowitz and Stegun [203], sections 20.1 and 20.2 of the handbook by Whittaker and Watson [204], or a geometric construction based on Schwartz-Christoffel transformations at the end of section 5.13 in the book by Henrici [84]). Igreja and Dias [79] and Cattaneo [86] use the sine amplitude function $\text{sn}(u, k) = \sin \text{am } u = \sin \varphi$ for the inverse transformation. k must be specified since the result of the elliptic integral depends on the values of both φ and k .

Related to the elliptic functions are the Jacobi theta functions $\vartheta_i(z, q)$ for $i = 1 \dots 4$. $z \in \mathbf{C}$ is the

variable and $q \in \mathbf{C}$ is called the nome, $|q| < 1$. Their definitions as infinite sums and important relations are given in sections 16.27 and 16.28 of the cited book [203]. The sums are:

$$\vartheta_1(z, q) = 2q^{1/4} \sum_{n=0}^{\infty} (-1)^n q^{n(n+1)} \sin(2n+1)z \quad (\text{C.7a})$$

$$\vartheta_2(z, q) = 2q^{1/4} \sum_{n=0}^{\infty} q^{n(n+1)} \cos(2n+1)z \quad (\text{C.7b})$$

$$\vartheta_3(z, q) = 1 + 2 \sum_{n=1}^{\infty} q^{n^2} \cos 2nz \quad (\text{C.7c})$$

$$\vartheta_4(z, q) = 1 + 2 \sum_{n=1}^{\infty} (-1)^n q^{n^2} \cos 2nz \quad (\text{C.7d})$$

If the nome is chosen such as $q = e^{-\pi K'/K}$, where $K = K(k)$ and $K' = K(k')$ for a given modulus k , sections 16.36 and 16.38 of the same work [203] give the expressions of the various variables in terms of theta functions:

$$K = \frac{\pi}{2} \vartheta_3(0)^2 \quad (\text{C.8})$$

$$K' = \frac{\pi}{2} \vartheta_3(0, q_1)^2 \quad (\text{C.9})$$

$$k = \frac{\vartheta_2(0)^2}{\vartheta_3(0)^2} \quad (\text{C.10})$$

$$k' = \frac{\vartheta_2(0)^2}{\vartheta_4(0)^2} \quad (\text{C.11})$$

$$\text{sn } u = \frac{\vartheta_3(0)}{\vartheta_2(0)} \frac{\vartheta_1(v)}{\vartheta_4(v)} \quad (\text{C.12})$$

where $q_1 = q(k')$ and $v = \pi u/(2K) = u\vartheta_3(0)^{-2}$. Here we omitted k and q in the notation of the elliptic and theta functions, respectively, as is sometimes done for brevity when no confusion is to be expected [203, 204]. $\vartheta_i(0, q)$ may also be written ϑ_i . Note that only the ratio K'/K needs to be known to obtain all the above values. This ratio is given by the rectangle dimensions as seen in Equation C.3b.

These relations give a definition of $\text{sn } u$ for $u \in \mathbf{C}$ and we can calculate an inverse mapping of the Schwartz-Christoffel transformation.

The elliptic functions and the theta functions are usually available in most scientific programming languages, and if not they can be evaluated for instance thanks to the definition of theta functions as sums. K is usually available. Note that sometimes the parameter m is used instead of the modulus k , and similarly for the theta functions which can take either the argument v or the argument u . The documentation should be carefully consulted to determine which variables should be used.

D Derivation of the simplified Gevorian model

In section D.1 and D.2 we derive the simplification of k and $K(k)$ and $K(k')$ respectively, in the case where $a, b \gg t_f$, for which k is very close to zero.

D.1 Simplification of k

Defining $A = e^{-\pi a/4t_f}$ and $B = e^{-\pi b/4t_f}$, we have:

$$\sinh\left(\frac{\pi b}{4t_f}\right) = \frac{B^{-1} - B}{2} \quad (\text{D.1a})$$

$$\sinh\left(\frac{\pi(a+b)}{4t_f}\right) = \frac{(AB)^{-1} - AB}{2} \quad (\text{D.1b})$$

$$\cosh\left(\frac{\pi b}{4t_f}\right) = \frac{B^{-1} + B}{2} \quad (\text{D.1c})$$

$$\cosh\left(\frac{\pi(a+b)}{4t_f}\right) = \frac{(AB)^{-1} + AB}{2} \quad (\text{D.1d})$$

Appendix D. Derivation of the simplified Gevorgian model

Now k is given by:

$$k = \frac{\sinh\left(\frac{\pi b}{4t_f}\right)}{\sinh\left(\frac{\pi(a+b)}{4t_f}\right)} \sqrt{\frac{\cosh^2\left(\frac{\pi(a+b)}{4t_f}\right) + \sinh^2\left(\frac{\pi(a+b)}{4t_f}\right)}{\cosh^2\left(\frac{\pi b}{4t_f}\right) + \sinh^2\left(\frac{\pi(a+b)}{4t_f}\right)}} \quad (\text{D.2a})$$

$$= \frac{B^{-1} - B}{(AB)^{-1} - AB} \sqrt{\frac{((AB)^{-1} + AB)^2 + ((AB)^{-1} - AB)^2}{(B^{-1} + B)^2 + ((AB)^{-1} - AB)^2}} \quad (\text{D.2b})$$

$$= A \frac{1 - B^2}{1 - A^2 B^2} \sqrt{\frac{(1 + A^2 B^2)^2 + (1 - A^2 B^2)^2}{A^2(1 + B^2)^2 + (1 - A^2 B^2)^2}} \quad (\text{D.2c})$$

$$= \sqrt{2}A \frac{1 - B^2}{1 - A^2 B^2} \sqrt{\frac{1 + A^4 B^4}{1 + A^2 + A^2 B^4 + A^4 B^4}} \quad (\text{D.2d})$$

$$= \sqrt{2}A \frac{1 - B^2}{1 - A^2 B^2} \sqrt{\frac{1 + A^4 B^4}{(1 + A^2)(1 + A^2 B^4)}} \quad (\text{D.2e})$$

We have $A \xrightarrow{a/t_f \rightarrow +\infty} 0$ and $B \xrightarrow{b/t_f \rightarrow +\infty} 0$, so we can use Taylor series expansion in the neighborhood of 0 to simplify the previous expression.

In the following we use the Landau little- o notation : If f and g are two real and regular enough functions defined on an interval containing $a \in \mathbf{R}$, such as g is not zero near a , then $f(x) \underset{x \rightarrow a}{\simeq} o(g(x))$ is equivalent to $f(x)/g(x) \xrightarrow{x \rightarrow a} 0$.

We have:

$$k = \sqrt{2}A(1 - B^2) \left(1 + A^2 B^2 + o(A^2 B^2)\right) \left(1 + \frac{A^4 B^4}{2} + o(A^4 B^4)\right) \times \left(1 - \frac{A^2}{2} + o(A^2)\right) \left(1 - \frac{A^2 B^4}{2} + o(A^2 B^4)\right) \quad (\text{D.3a})$$

Keeping only second order terms, since $A^2 B^4/2 + o(A^2 B^4) = o(AB)$, and using the rules for multiplication, we obtain:

$$k = \sqrt{2}A(1 - B^2) (1 + o(AB)) (1 + o(AB)) \left(1 - \frac{A^2}{2} + o(A^2)\right) (1 + o(AB)) \quad (\text{D.4a})$$

$$= \sqrt{2}A(1 - B^2) (1 + o(AB)) \left(1 - \frac{A^2}{2} + o(A^2)\right) \quad (\text{D.4b})$$

$$= \sqrt{2}A(1 - B^2) \left(1 - \frac{A^2}{2} + o(A^2) + o(AB)\right) \quad (\text{D.4c})$$

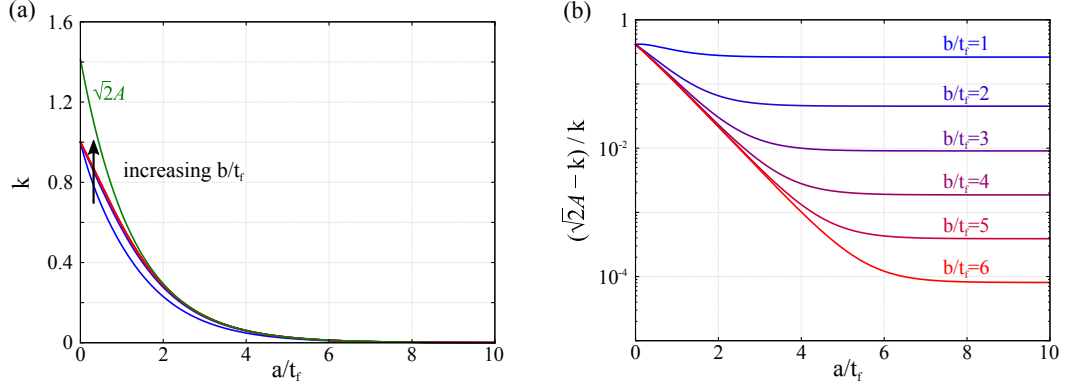


Figure D.1 – (a) k dependency on a and b . For large a/t_f and b/t_f ratio, k quickly drops to 0. In this region, $\sqrt{2}A$ seems to be a good approximation. This is confirmed by (b), which shows that the error is less than 1 % as long as a and b are a few times larger than t_f . The color code is given in (b).

Figure D.1 shows the dependencies of k , as well as an evaluation of the accuracy of the developed approximation. It can be seen that k can be approximated by the first order term with an error lower than 1 % as long as a and b are both a few times larger than t_f .

D.2 Simplification of $K(k)$ and $K(k')$

For this derivation we rely on Taylor series expansion of the elliptic integrals [205] used in the Gevorgian formula, which gives, for k close to 0:

$$K(k) = \frac{\pi}{2} \left(1 + \frac{1}{4}k^2 + o(k^2) \right) \quad (\text{D.5a})$$

$$K'(k) = \frac{2}{\pi} \ln\left(\frac{4}{k}\right) K(k) - \left(\frac{k^2}{4} + o(k^2) \right) \quad (\text{D.5b})$$

where $K'(k) = K(\sqrt{1-k^2}) = K(k')$. Since after equation D.5a, $K(k) > 0$ for k close enough to 0, we can divide by $K(k)$ and expand in Taylor series:

$$\frac{\pi}{2} \frac{K'(k)}{K(k)} = \ln\left(\frac{4}{k}\right) - \frac{\pi}{2} K(k)^{-1} \left(\frac{k^2}{4} + o(k^2) \right) \quad (\text{D.6a})$$

$$= \ln\left(\frac{4}{k}\right) - \left(1 - \frac{k^2}{4} + o(k^2) \right) \left(\frac{k^2}{4} + o(k^2) \right) \quad (\text{D.6b})$$

$$= \ln\left(\frac{4}{k}\right) - \left(\frac{k^2}{4} + o(k^2) \right) \quad (\text{D.6c})$$

$$= \ln(4) - \ln(k) - \frac{k^2}{4} + o(k^2) \quad (\text{D.6d})$$

Appendix D. Derivation of the simplified Gevorgian model

We have:

$$k^2 = 2A^2(1-B^2)^2 \cdot \left(1 - \frac{A^2}{2} + o(A^2) + o(AB)\right)^2 \quad (\text{D.7a})$$

$$= 2A^2(1-2B^2+o(B^2)) \cdot (1-A^2+o(A^2)+o(AB)) \quad (\text{D.7b})$$

$$= 2A^2(1-A^2-2B^2+o(A^2)+o(B^2)+o(AB)) \quad (\text{D.7c})$$

$$= 2A^2 + o(A^2) + o(B^2) + o(AB) \quad (\text{D.7d})$$

As a consequence, $o(k^2)$ can be replaced by $o(A^2)$ in equation D.6d. We can similarly expand $\ln(k)$:

$$\ln(k) = \ln(\sqrt{2}A) + \ln(1-B^2) + \ln\left(1 - \frac{A^2}{2} + o(A^2) + o(AB)\right) \quad (\text{D.8a})$$

$$= \ln(\sqrt{2}A) - B^2 - \frac{A^2}{2} + o(A^2) + o(B^2) + o(AB) \quad (\text{D.8b})$$

Therefore:

$$\frac{\pi}{2} \frac{K'(k)}{K(k)} = \ln(4) - \ln(k) - \frac{k^2}{4} + o(k^2) \quad (\text{D.9a})$$

$$= \ln(4) - \ln(\sqrt{2}A) + B^2 + \frac{A^2}{2} - \frac{A^2}{2} + o(A^2) + o(B^2) + o(AB) \quad (\text{D.9b})$$

$$= \ln(2\sqrt{2}/A) + B^2 + o(A^2) + o(B^2) + o(AB) \quad (\text{D.9c})$$

We know that $A \xrightarrow{a/t_f \rightarrow +\infty} 0^+$, thus $\ln(2\sqrt{2}/A) \xrightarrow{A \rightarrow 0^+} +\infty$, and we can proceed to factorization:

$$\frac{\pi}{2} \frac{K'(k)}{K(k)} = \ln\left(\frac{2\sqrt{2}}{A}\right) \left(1 + \frac{B^2}{\ln\left(\frac{2\sqrt{2}}{A}\right)} + o(A^2) + o(B^2) + o(AB)\right) \quad (\text{D.10a})$$

$$\frac{2}{\pi} \frac{K(k)}{K'(k)} = \frac{1}{\ln\left(\frac{2\sqrt{2}}{A}\right)} \frac{1}{1 + \frac{B^2}{\ln\left(\frac{2\sqrt{2}}{A}\right)} + o(A^2) + o(B^2) + o(AB)} \quad (\text{D.10b})$$

$$= \frac{1}{\ln\left(\frac{2\sqrt{2}}{A}\right)} \left(1 - \frac{B^2}{\ln\left(\frac{2\sqrt{2}}{A}\right)} + o(A^2) + o(B^2) + o(AB)\right) \quad (\text{D.10c})$$

Even at the first order, the approximation is expected to be very accurate since A and B exponentially decrease with increasing a/t_f and b/t_f . Thus we will restrict ourselves to the first order term, and omit the $o(x)$ terms in the rest of the calculation.

Since $A = e^{-\pi a/4t_f}$, we have:

$$\ln\left(\frac{2\sqrt{2}}{A}\right) = \ln(2\sqrt{2}) + \frac{\pi a}{4t_f} \quad (\text{D.11a})$$

$$= \frac{\pi}{4t_f} \left(a + \frac{4t_f \ln(2\sqrt{2})}{\pi} \right) \quad (\text{D.11b})$$

$$= \frac{\pi}{4t_f} (a + \Delta a) \quad (\text{D.11c})$$

where we wrote:

$$\Delta a = \frac{4\ln(2\sqrt{2})}{\pi} t_f \quad (\text{D.12a})$$

$$\approx 1.324 t_f \quad (\text{D.12b})$$

The elliptic integral ratio is therefore given by, in the first order for $a, b \gg t_f$, according to equation D.10c:

$$\frac{K(k)}{K(k')} = \frac{2t_f}{a + \Delta a} \quad (\text{D.13})$$

E Derivation of the simplified Igreja model

In this appendix we derive the simplification of the Igreja formula for $a, b \gg t_f$. We remind $\eta = b/(a+b)$ and $\lambda = 2(a+b)$; therefore, $0 < \eta < 1$. The outline of this derivation was proposed by C. H. Nguyen.

In order to simplify the derivation, we will use the Hilberg approximation [206], which provides a simplified relationship between the modulus k and the value of $K = K(k)$:

$$\begin{cases} \frac{K}{K'} \approx \frac{2}{\pi} \ln \left(2 \sqrt{\frac{1+k}{1-k}} \right) & \text{for } 1 \leq \frac{K}{K'} \leq \infty \text{ and } \frac{1}{\sqrt{2}} \leq k \leq 1 \\ \frac{K}{K'} \approx \frac{\pi}{2} \frac{1}{\ln \left(2 \sqrt{\frac{1+k'}{1-k'}} \right)} & \text{for } 0 \leq \frac{K}{K'} \leq 1 \text{ and } 0 \leq k \leq \frac{1}{\sqrt{2}} \end{cases} \quad (\text{E.1})$$

We wrote, as usual, $k' = \sqrt{1-k^2}$ and $K' = K(k')$. The conditions for the value of the ratio K/K' and the value of k are equivalent. This gives the following formulas for obtaining k and k' :

$$\begin{cases} k \approx \frac{y-4}{y+4} & \text{for } 1 \leq \frac{K}{K'} \leq \infty \text{ and } \frac{1}{\sqrt{2}} \leq k \leq 1 \\ k' \approx \frac{1-4q}{1+4q} & \text{for } 0 \leq \frac{K}{K'} \leq 1 \text{ and } 0 \leq k \leq \frac{1}{\sqrt{2}} \end{cases} \quad (\text{E.2})$$

where we wrote:

$$\begin{cases} q = \exp(-\pi K'/K) \\ y = \exp(\pi K/K') \end{cases} \quad (\text{E.3})$$

Appendix E. Derivation of the simplified Igreja model

In the Igreja model, we have:

$$\frac{K'}{K} = \frac{4t_f}{\lambda} = \frac{2t_f}{a+b} \quad (\text{E.4})$$

Since $a, b \gg t_f$, we are in the case where $K/K' \gg 1$, and therefore:

$$k = \frac{y-4}{y+4} = \left(1 - \frac{4}{y}\right) \left(1 + \frac{4}{y}\right)^{-1} \quad (\text{E.5})$$

$$\approx \left(1 - \frac{4}{y}\right) \left(1 - \frac{4}{y}\right) \quad (\text{E.6})$$

$$\approx 1 - \frac{8}{y} \quad (\text{E.7})$$

at the first order, because $y = \exp(\pi K/K') \gg 1$.

We have $K(0) = \pi/2$, so that, for $k \approx 1$, $K' \approx \pi/2$, and we have, according to equation E.1:

$$\frac{2K}{\pi} = \frac{2}{\pi} \ln \left(\frac{2\sqrt{2}}{\sqrt{1-k}} \right) \quad (\text{E.8})$$

$$K = \ln \left(\frac{4}{\sqrt{1-k^2}} \right) \quad (\text{E.9})$$

multiplying the numerator and denominator inside the logarithm by $\sqrt{1+k} \approx \sqrt{2}$.

Since $k \approx 1$, we have [207]:

$$\text{sn}(K\eta, k) \approx \tanh(K\eta) \quad (\text{E.10})$$

And we can write, for $x \gg 1$:

$$\tanh x = 1 - \frac{2}{e^{2x} + 1} \approx 1 - 2e^{-2x} \quad (\text{E.11})$$

Since $K(k) \xrightarrow[k \rightarrow 1]{} +\infty$, and since in real samples $0 < \eta < 1$ is not infinitesimally small, for k close to 1 we have $K\eta \gg 1$, and hence:

$$\tanh K\eta = 1 - 2 \exp \left(-2\eta \ln \left(\frac{4}{\sqrt{1-k^2}} \right) \right) \quad (\text{E.12})$$

$$\tanh K\eta = 1 - 2 \left(\frac{\sqrt{1-k^2}}{4} \right)^{2\eta} \quad (\text{E.13})$$

According to equation E.7:

$$k^2 = 1 - \frac{16}{y} \quad (\text{E.14})$$

$$\sqrt{1 - k^2} = \frac{4}{y^{1/2}} \quad (\text{E.15})$$

And so:

$$\tanh K\eta = 1 - \frac{2}{y^\eta} \quad (\text{E.16})$$

Defining $\beta = \text{sn}(K\eta, k)$, we can write k_I as follows:

$$k_I = \frac{\beta\sqrt{1 - k^2}}{\sqrt{1 - \beta^2 k^2}} \quad (\text{E.17})$$

According to equations E.15 and E.16, and since $y \gg 1$ and $\eta > 0$, we have:

$$\beta\sqrt{1 - k^2} = \left(1 - \frac{2}{y^\eta}\right) \frac{4}{y^{1/2}} \approx \frac{4}{y^{1/2}} \quad (\text{E.18})$$

Similarly, neglecting higher order terms:

$$\sqrt{1 - \beta^2 k^2} = \left(1 - \left(1 - \frac{4}{y^\eta}\right)\left(1 - \frac{16}{y}\right)\right)^{1/2} \quad (\text{E.19})$$

$$= \left(1 - 1 + \frac{4}{y^\eta} + \frac{16}{y}\right)^{1/2} \quad (\text{E.20})$$

$$= \frac{4}{y^{1/2}} \left(1 + \frac{y^{1-\eta}}{4}\right)^{1/2} \quad (\text{E.21})$$

Finally, we can write:

$$k_I = \frac{\beta\sqrt{1 - k^2}}{\sqrt{1 - \beta^2 k^2}} = \frac{1}{\left(1 + \frac{y^{1-\eta}}{4}\right)^{1/2}} \quad (\text{E.22})$$

Since $0 < \eta < 1$, $1 - \eta > 0$ and thus k_I is close to 0 for $y \gg 1$. In appendix D we saw that, in this

Appendix E. Derivation of the simplified Igreja model

case and at the first order, we have:

$$\frac{\pi}{2} \frac{K'(k_I)}{K(k_I)} = \ln(4) - \ln(k_I) \quad (\text{E.23})$$

$$= \ln(4) + \frac{1}{2} \ln \left(1 + \frac{y^{1-\eta}}{4} \right) \quad (\text{E.24})$$

$$\approx \ln(4) + \frac{1}{2} \ln \left(\frac{y^{1-\eta}}{4} \right) \quad (\text{E.25})$$

$$= \ln(4) + \frac{1}{2} (1 - \eta) \ln(y) - \frac{1}{2} \ln(4) \quad (\text{E.26})$$

$$= \ln(2) + \frac{1}{2} \frac{a}{a+b} \ln(y) \quad (\text{E.27})$$

And from equations E.3 and E.4:

$$\ln(y) = \ln(\exp(\pi K/K')) = \pi \frac{a+b}{2t_f} \quad (\text{E.28})$$

Therefore:

$$\frac{K'(k_I)}{K(k_I)} = \frac{2}{\pi} \ln(2) + \frac{1}{\pi} \frac{a}{a+b} \pi \frac{a+b}{2t_f} \quad (\text{E.29})$$

$$= \frac{2}{\pi} \ln(2) + \frac{a}{2t_f} \quad (\text{E.30})$$

$$= \frac{1}{2t_f} \left(\frac{4\ln(2)}{\pi} t_f + a \right) \quad (\text{E.31})$$

from which we can finally write:

$$C_I = \varepsilon_f \varepsilon_0 \frac{K(k_I)}{K'(k_I)} = \varepsilon_f \varepsilon_0 \frac{2t_f}{a + \Delta a} \quad (\text{E.32})$$

where:

$$\Delta a = \frac{4\ln(2)}{\pi} t_f \quad (\text{E.33})$$

F Derivation of the maximum reachable polarization

In this appendix we calculate explicitly the maximum reachable polarization after poling of a PZT thin film with IDE structures, for tetragonal and rhombohedral symmetry having the {100}, {110} or the {111} out-of-plane orientation of the crystallites.

Since 180° switching is always possible, it is sufficient to consider a misalignment angle θ between the most favorable polarization direction and the poling direction comprised between $-\pi/2$ and $\pi/2$. Therefore, in the following, we always have $\theta \in [-\frac{\pi}{2}, \frac{\pi}{2}]$. We define \mathbf{e}_z as the poling direction, \mathbf{e}_y the orthogonal in-plane direction, and \mathbf{e}_x the out-of-plane direction pointing away from the substrate, such as $(\mathbf{e}_x, \mathbf{e}_y, \mathbf{e}_z)$ is a direct base (a bold font denotes a vector variable). We assume that, in all cases, the crystal chooses the polarization axis and direction closest to the poling direction, independently of any other consideration (notably, neglecting any mechanical clamping). P_s is defined as the saturating polarization, such as $\|\mathbf{P}\| = P_s$, and P_i are the components of \mathbf{P} where i is x , y , or z .

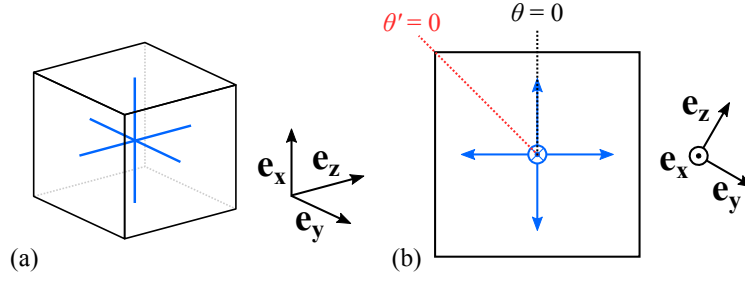


Figure F1 – (a) : Drawing of the tetragonal unit cell with the (100) direction out-of-plane. Here the poling direction \mathbf{e}_z is aligned with one of the principal crystallographic direction. The polar axes are shown in blue. (b) : The structure seen from the out-of-plane direction, with the projection of the allowed polarization vectors in the $(\mathbf{e}_y, \mathbf{e}_z)$ plane, and the origin of the angles. The poling direction \mathbf{e}_z is shown to make a 30° angle with the $\theta = 0$ direction.

F.1 Tetragonal (100)

In that case, one polar axis is directed along \mathbf{e}_x and the two others are in the $(\mathbf{e}_y, \mathbf{e}_z)$ plane. The polarization will be directed along one of the latter. Figure F1 shows the situation and the origin of the angles. We thus have:

$$P_z^{\text{tet}(100)} = \begin{cases} P_s \cos \theta & \text{if } |\theta| \leq \pi/4 \\ P_s \sin \theta & \text{if } \pi/4 \leq |\theta| \leq \pi/2 \end{cases} \quad (\text{F1})$$

Changing the origin of the angles, we can also write the more direct formula:

$$P_z^{\text{tet}(100)} = P_s \cos\left(\frac{\pi}{4} - |\theta'|\right) \quad (\text{F2})$$

By symmetry, the average value of $P_z^{\text{tet}(100)}$ on all possible orientations is given by :

$$\langle P_z^{\text{tet}(100)} \rangle = \int_{-\pi/4}^{\pi/4} \frac{2}{\pi} P_s \cos \theta \, d\theta \quad (\text{F3a})$$

$$= \frac{2\sqrt{2}}{\pi} P_s \quad (\text{F3b})$$

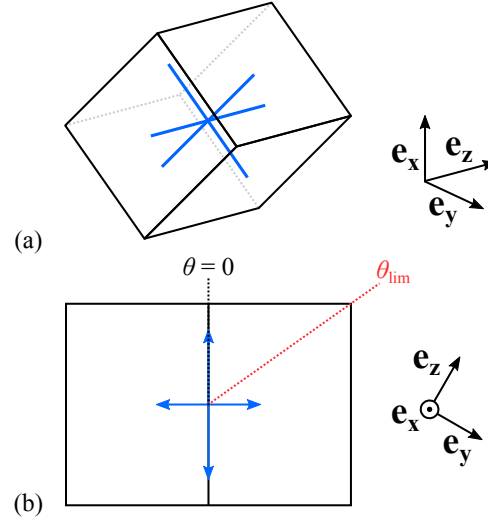


Figure F2 – (a) : Drawing of the tetragonal unit cell with the (110) direction out-of-plane. Here the poling direction \mathbf{e}_z is aligned with one of the principal crystallographic direction. The polar axes are shown in blue. (b) : The structure seen from the out-of-plane direction, with the projection of the allowed polarization vectors in the $(\mathbf{e}_y, \mathbf{e}_z)$ plane, and the origin of the angles. The poling direction \mathbf{e}_z is shown to make a 30° angle with the $\theta = 0$ direction. $\theta_{\text{lim}} = 54.74^\circ$ is also shown.

F.2 Tetragonal (110)

In this case, one polar axis lies in the $(\mathbf{e}_y, \mathbf{e}_z)$ plane and the two others are out of that plane, with two directions being equivalent for our calculation. The polarization can be directed along one of each depending on the in-plane orientation of the grain. Figure F.2 shows the definition of the origin of the angles. We have:

$$P_z^{\text{tet}(110)} = \begin{cases} P_s \cos \theta & \text{if } |\theta| \leq \theta_{\text{lim}} \\ \frac{\sqrt{2}}{2} P_s \sin \theta & \text{if } \theta_{\text{lim}} \leq |\theta| \leq \pi/2 \\ \theta_{\text{lim}} = \arctan(\sqrt{2}) \approx 54.74^\circ & \end{cases} \quad (\text{F4})$$

θ_{lim} is the misalignment angle beyond which it is more favorable for the polarization to be directed along one of the out-of-plane axes. By symmetry, the average value of $P_z^{\text{tet}(110)}$ is given by:

$$\langle P_z^{\text{tet}(110)} \rangle = \int_0^{\pi/2} \frac{2}{\pi} P_z^{\text{tet}(110)}(\theta) d\theta \quad (\text{F5a})$$

$$= \frac{3}{\pi} P_s \sin \theta_{\text{lim}} \quad (\text{F5b})$$

$$= \frac{\sqrt{6}}{\pi} P_s \quad (\text{F5c})$$

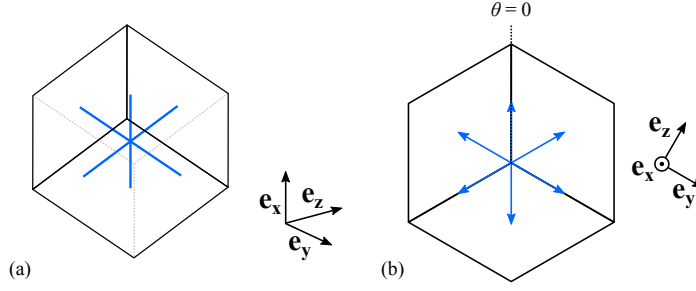


Figure E3 – (a) : Drawing of the tetragonal unit cell with the (111) direction out-of-plane. The polar axes are shown in blue. (b) : The structure seen from the out-of-plane direction, with the projection of the allowed polarization vectors in the (e_y, e_z) plane, and the origin of the angles. The poling direction e_z is shown to make a 30° angle with the $\theta = 0$ direction.

F.3 Tetragonal (111)

In that case all the polar axes are out of the (e_y, e_z) plane, making an angle $\theta_1 = \arctan(\sqrt{2}/2) \approx 35.26^\circ$ with it. Their projection onto this plane are thus of norm $P_s \cos \theta_1$, and are evenly spaced with an angle $\pi/3$. The situation is depicted in Figure E3. Therefore:

$$P_z^{\text{tet}(111)} = \begin{cases} P_s \cos \theta_1 \cos \theta & \text{if } |\theta| \leq \pi/6 \\ P_s \cos \theta_1 \cos(\pi/3 - |\theta|) & \text{if } \pi/6 \leq |\theta| \leq \pi/2 \\ \cos \theta_1 = \sqrt{6}/3 & \end{cases} \quad (\text{E6})$$

Hence, by symmetry, the average value of $P_z^{\text{tet}(111)}$ is given by:

$$\langle P_z^{\text{tet}(111)} \rangle = \int_{-\pi/6}^{\pi/6} \frac{3}{\pi} P_s \cos \theta_1 \cos \theta d\theta \quad (\text{E7a})$$

$$= \frac{3}{\pi} P_s \cos \theta_1 \quad (\text{E7b})$$

$$= \frac{\sqrt{6}}{\pi} P_s \quad (\text{E7c})$$

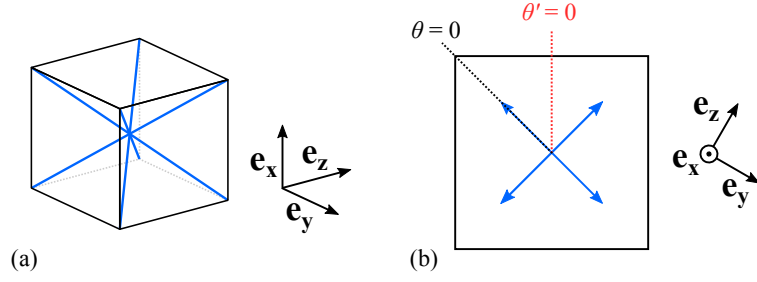


Figure F.4 – (a) : Drawing of the rhombohedral unit cell with the (100) direction out-of-plane. Here the poling direction \mathbf{e}_z is aligned with one of the principal crystallographic direction. The polar axes are shown in blue. (b) : The structure seen from the out-of-plane direction, with the projection of the allowed polarization vectors in the $(\mathbf{e}_y, \mathbf{e}_z)$ plane, and the origin of the angles. The poling direction \mathbf{e}_z is shown to make a 30° angle with the $\theta' = 0$ direction.

F.4 Rhombohedral (100)

In that case, all the polar axes are out of the $(\mathbf{e}_y, \mathbf{e}_z)$ plane, making an angle $\theta_1 = \arctan(\sqrt{2}/2) \approx 35.26^\circ$ with it. Their projection into the $(\mathbf{e}_y, \mathbf{e}_z)$ plane gives the same situation as for the tetragonal (100) case, but with a polarization of norm $P_s \cos \theta_1$ instead (see Figure F.4). Thus:

$$P_z^{\text{rh}(100)} = \begin{cases} P_s \cos \theta_1 \cos \theta & \text{if } |\theta| \leq \pi/4 \\ P_s \cos \theta_1 \sin \theta & \text{if } \pi/4 \leq |\theta| \leq \pi/2 \end{cases} \quad (\text{F.8})$$

Changing the origin of the angles, we can also write the more direct formula:

$$P_z^{\text{rh}(100)} = P_s \cos \theta_1 \cos \left(\frac{\pi}{4} - |\theta'| \right) \quad (\text{F.9})$$

As a consequence, the average value of $P_z^{\text{rh}(100)}$ is given by:

$$\langle P_z^{\text{rh}(100)} \rangle = \frac{2\sqrt{2}}{\pi} P_s \cos \theta_1 \quad (\text{F.10a})$$

$$= \frac{4\sqrt{3}}{3\pi} P_s \quad (\text{F.10b})$$

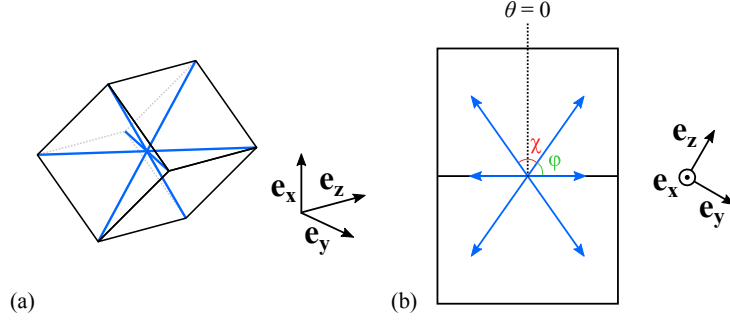


Figure F5 – (a) : Drawing of the rhombohedral unit cell with the (110) direction out-of-plane. Here the poling direction e_z is aligned with one of the principal crystallographic direction. The polar axes are shown in blue. (b) : The structure seen from the out-of-plane direction, with the projection of the allowed polarization vectors in the (e_y, e_z) plane, and the origin of the angles. The poling direction e_z is shown to make a 30° angle with the $\theta = 0$ direction. The angles χ and φ are also shown.

F.5 Rhombohedral (110)

This case is slightly more complex than the tetragonal (110) geometry. We have two axes in the (e_y, e_z) plane, and two axes out of that plane, making an angle φ with it. The two out-of-plane axes are equivalent for the polarization. The in-plane axes are separated by an angle $\chi = \arccos(1/3) \approx 70.53^\circ$; χ gives its name to the 71° domain walls. Similarly, $2\varphi = \pi - \chi \approx 109.47^\circ$ gives its name to the 109° domain walls. See Figure F.5 for a display of the situation. Fortunately, the peculiar geometry of this case allows to write $P_z^{\text{rh}(110)}$ with a simple formula, when choosing the proper origin for the angles as shown in Figure F.5:

$$P_z^{\text{rh}(110)} = P_s \cos\left(\frac{\chi}{2} - |\theta|\right) \quad (\text{F.11})$$

Therefore, the polarization will always be in-plane, unless the electric field is aligned with the projection of the out-of-plane axes into the (e_y, e_z) plane, in which case it is equivalent for the polarization to remain in the plane or to go out-of-plane.

By symmetry, we can integrate between $\theta = 0$ and $\theta = \pi/2$. For easier calculations, we place the origin at $\theta = \chi/2$, and the average value of $P_z^{\text{rh}(110)}$ on all possible orientations is then given by:

$$\langle P_z^{\text{rh}(110)} \rangle = \int_{-\frac{\chi}{2}}^{\varphi} \frac{1}{\varphi + \frac{\chi}{2}} P_s \cos \theta \, d\theta \quad (\text{F.12a})$$

$$= \frac{2P_s}{\pi} \int_{-\frac{\chi}{2}}^{\varphi} \cos \theta \, d\theta \quad (\text{F.12b})$$

$$= \frac{2P_s}{\pi} \left(\sin \varphi + \sin \frac{\chi}{2} \right) \quad (\text{F.12c})$$

$$= \frac{2\sqrt{3}}{3\pi} P_s (1 + \sqrt{2}) \quad (\text{F.12d})$$

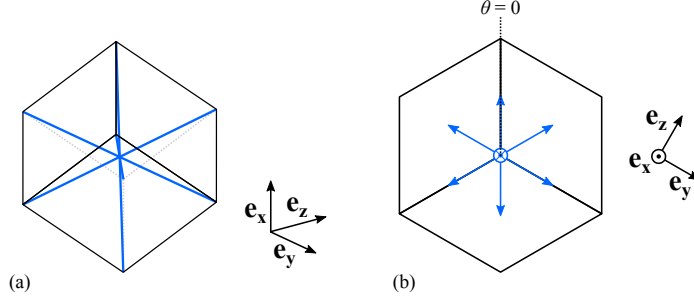


Figure F6 – (a) : Drawing of the rhombohedral unit cell with the (111) direction out-of-plane. The polar axes are shown in blue. (b) : The structure seen from the out-of-plane direction, with the projection of the allowed polarization vectors in the (e_y, e_z) plane, and the origin of the angles. The poling direction e_z is shown to make a 30° angle with the $\theta = 0$ direction.

F.6 Rhombohedral (111)

This case is equivalent to the tetragonal (111) geometry. One polar axis is directed fully out-of-plane and plays no role. The three other polar axes are out of the (e_y, e_z) plane, making an angle $\theta_2 = \arccos(2\sqrt{2}/3) \approx 19.47^\circ$ with it. Their projection onto this plane are thus of norm $P_s \cos\theta_2$, and are evenly spaced with an angle $\pi/3$. The situation is depicted in Figure F6. Therefore:

$$P_z^{\text{rh}(111)} = \begin{cases} P_s \cos\theta_2 \cos\theta & \text{if } |\theta| \leq \pi/6 \\ P_s \cos\theta_2 \cos(\pi/3 - |\theta|) & \text{if } \pi/6 \leq |\theta| \leq \pi/2 \\ \cos\theta_2 = 2\sqrt{2}/3 & \end{cases} \quad (\text{F.13})$$

Hence, we have:

$$\langle P_z^{\text{rh}(111)} \rangle = \int_{-\pi/6}^{\pi/6} \frac{3}{\pi} P_s \cos\theta_2 \cos\theta d\theta \quad (\text{F.14a})$$

$$= \frac{3}{\pi} P_s \cos\theta_2 \quad (\text{F.14b})$$

$$= \frac{2\sqrt{2}}{\pi} P_s \quad (\text{F.14c})$$

G Dielectric spectroscopy

G.1 Experimental setup

The dielectric spectroscopy setup is used to record the harmonics of the polarization response of the sample. Figure G.1 pictures the equivalent circuit of the measurement setup. The ferroelectric film with IDE is modeled by two capacitors in parallel: C_f corresponding to the ferroelectric film, and C_{par} to the parasitic capacitance. A wide-band power amplifier of model 7602M (Krohn-Hite Corporation) is used to amplify the sinusoidal voltage generated by the function generator of a SR830 DSP lock-in amplifier (Stanford Research Systems). The amplified signal V_{applied} is applied to one electrode side by a micromanipulator, while the other electrode side is connected in series to the resistor R . The resistor is connected in parallel to the input of the lock-in amplifier as shown in Fig. G.1, so that the voltage drop across the resistor is measured by the lock-in. V_C is the voltage drop across the IDE sample while V_R is the voltage drop across the resistor, and by construction we have $V_{\text{applied}} = V_C + V_R$. i is the current flowing through the circuit.

The resistance R must be chosen small enough in order to avoid any transient effect in the circuit due to a too large RC time constant. Besides, R must be chosen small enough so that the voltage drops mostly across the capacitor and not at the resistor. Since the signal intensity is proportional to the resistor value, the resistance should however not be too low, to provide a sufficiently large signal-to-noise ratio at the input of the lock-in. As a rule of thumb, the resistor R is therefore chosen such as:

$$RC \leq \frac{1}{100\omega} \quad (\text{G.1})$$

where $\omega = 2\pi f$, f is the frequency of V_{applied} and $C = C_f + C_{\text{par}}$ is the capacitance of the IDE sample. In addition, it should not be chosen too much below this value. This condition is straightforward to verify *a posteriori*, since:

$$\frac{V_1}{V_{\text{applied}}} = RC\omega \quad (\text{G.2})$$

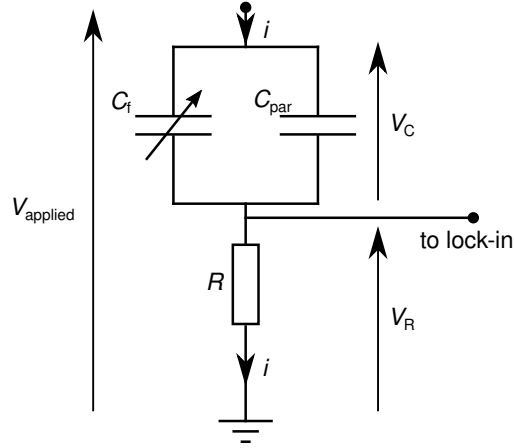


Figure G.1 – Electrical circuit of the situation.

where V_1 is the amplitude of the first harmonic of the voltage signal at the resistor V_R . Hence, the above conditions on R are satisfied if $V_1 / V_{\text{applied}} \leq 0.01$ for all values of V_{applied} during the measurement.

A charge amplifier may be used instead of a resistor, for instance if a great change of the capacitance of the sample is expected in the course of the measurement. The treatment of this case is very similar and will not be shown.

G.2 Derivation of the polarization harmonics

V_{applied} is a sinusoidal signal such as $V_{\text{applied}} = V_0 \sin(\omega t)$. Any variable of time $X(t)$ can be written as a Fourier series of in-phase (denoted X'_n) and out-of-phase or quadrature (denoted X''_n) terms in the following way (neglecting the DC component):

$$X(t) = \sum_{n=1}^{+\infty} (X'_n \sin(n\omega t) + X''_n \cos(n\omega t)) \quad (\text{G.3})$$

The sum can also be written in terms of amplitudes and phase angles:

$$X(t) = \sum_{n=1}^{+\infty} X_n \sin(n\omega t + \varphi_n) \quad (\text{G.4})$$

The various variables are related as follows:

$$\begin{cases} X_n = \sqrt{(X'_n)^2 + (X''_n)^2} \\ \varphi_n = \tan^{-1} \left(\frac{X''_n}{X'_n} \right) \\ X'_n = X_n \cos \varphi_n \\ X''_n = X_n \sin \varphi_n \end{cases} \quad (\text{G.5})$$

The parasitic capacitance C_{par} of the IDE structures will contribute to the charges flowing through the measurement apparatus when cycling with a sinusoidal field, as given by the following formula:

$$Q_{\text{sample}} = Q_{\text{ferroelectric charges}} + Q_{\text{par}} \quad (\text{G.6})$$

$$= AP + Q_{\text{par}} \quad (\text{G.7})$$

where $A = (2N - 1)Wt_f$ is the effective area for deriving the polarization of the PZT layer with IDE structures from the integrated current, and Q_{par} is the additional charge coming from the polarization of the parasitic capacitance. Because Q_{par} does not scale linearly with the area of the IDE structure, it is not straightforward to decompose as the product of an area and a polarization, in the form $Q_{\text{par}} = A_{\text{par}}P_{\text{par}}$. It should be evaluated separately, by recording the harmonic response of the IDE structures with the interdigitation cleaved away. This gives the contribution of the contact pads and the bus line to Q_{par} , but the contribution from the interdigitation zone remains unknown. The conformal mapping technique proposed in chapter 3 cannot be applied for the loss part (*i. e.* the quadrature component) of Q_{par} . The only possibility to estimate it, is to fabricated IDE structures directly on a SiO_2 layer. This has not been done. For this reason, at the present time, we can correct for the parasitic contributions from the contact pad and bus lines, but not for the parasitic contributions of the SiO_2 underlayer within the interdigitation zone. In the rest of the text, we will keep the Q_{par} term in the equations, for the purpose of allowing the correction whenever a full model will be available.

Since $RC \leq 1/100\omega$, that is $RC \ll 1/\omega$, there is no transient effect. We have $V_R(t) = Ri(t)$ from Ohm's law. In addition, since the IDE sample is much more resistive than R (typical values for R are in the range of 1 to 10 k Ω), most of the voltage V_{applied} drops across the IDE sample. Therefore, $V_{\text{applied}}/(a + \Delta a)$ is an accurate evaluation of the electric field within the PZT layer, where a is the IDE gap and Δa the gap correction for the drop of electric field within the gap (see chapter 3). The harmonics of $V_R(t)$ are measured by the lock-in amplifier (amplitude and phase).

Neglecting all leakage currents through the capacitors, the current is solely due to the change of polarization of the capacitors, and we have:

$$\begin{cases} i(t) \approx \frac{\partial Q}{\partial t} = A \frac{\partial P}{\partial t} + \frac{\partial Q_{\text{par}}}{\partial t} \\ i(t) = \frac{V_R(t)}{R} \end{cases} \quad (\text{G.8})$$

with Q_{par} the polarization charges of the parasitic capacitance under the action of V_{applied} .

Appendix G. Dielectric spectroscopy

We write:

$$V_R(t) = \sum_{n=1}^{+\infty} (V_n \sin(n\omega t) \cos \varphi_n + V_n \cos(n\omega t) \sin \varphi_n) \quad (\text{G.9})$$

$$P(t) = \sum_{n=1}^{+\infty} (P'_n \sin(n\omega t) + P''_n \cos(n\omega t)) \quad (\text{G.10})$$

$$Q_{\text{par}}(t) = \sum_{n=1}^{+\infty} (Q'_{\text{par}_n} \sin(n\omega t) + Q''_{\text{par}_n} \cos(n\omega t)) \quad (\text{G.11})$$

V_n is the amplitude and φ_n the phase of the n^{th} harmonic $V_n \sin(n\omega t + \varphi_n)$ of $V_R(t)$. V_n and φ_n are the values measured by the lock-in amplifier. In practice the output of the lock-in amplifier is a root-mean-square (rms) amplitude and needs to be multiplied by $\sqrt{2}$ to obtain V_n . Note that the Fourier components are mixing V_n and φ_n because $\sin(n\omega t + \varphi_n) = \sin(n\omega t) \cos \varphi_n + \cos(n\omega t) \sin \varphi_n$, since $\sin(a+b) = \sin a \cos b + \sin b \cos a$. φ_n is always given between -180° and 180° by the lock-in amplifier.

The time derivative is given by:

$$\frac{\partial P}{\partial t} = \sum_{n=1}^{+\infty} (P'_n n\omega \cos(n\omega t) - P''_n n\omega \sin(n\omega t)) \quad (\text{G.12})$$

$$\frac{\partial Q_{\text{par}}}{\partial t} = \sum_{n=1}^{+\infty} (Q'_{\text{par}_n} n\omega \cos(n\omega t) - Q''_{\text{par}_n} n\omega \sin(n\omega t)) \quad (\text{G.13})$$

And from G.8 we have:

$$\frac{V_R(t)}{R} = A \frac{\partial P}{\partial t} + \frac{\partial Q_{\text{par}}}{\partial t} \quad (\text{G.14})$$

We can identify term by term, and we obtain for all n :

$$\begin{cases} \frac{V_n}{R} \cos \varphi_n = -An\omega P''_n - n\omega Q''_{\text{par}_n} \\ \frac{V_n}{R} \sin \varphi_n = An\omega P'_n + n\omega Q'_{\text{par}_n} \end{cases} \quad (\text{G.15})$$

$$\begin{cases} -An\omega P''_n = \frac{V_n}{R} \cos \varphi_n + n\omega Q''_{\text{par}_n} \\ An\omega P'_n = \frac{V_n}{R} \sin \varphi_n - n\omega Q'_{\text{par}_n} \end{cases} \quad (\text{G.16})$$

$$\begin{cases} P_n'' = -\frac{V_n}{An\omega R} \cos \varphi_n - \frac{Q_{\text{par}_n}''}{A} \\ P_n' = \frac{V_n}{An\omega R} \sin \varphi_n - \frac{Q_{\text{par}_n}'}{A} \end{cases} \quad (\text{G.17})$$

Following Equation G.5, the phase angle δ_n and the amplitude P_n of the n^{th} harmonic of the polarization P of the ferroelectric is given by :

$$\delta_n = \tan^{-1} \left(\frac{P_n''}{P_n'} \right) \quad (\text{G.18})$$

$$P_n = \sqrt{(P_n')^2 + (P_n'')^2} \quad (\text{G.19})$$

The harmonic response of a cleaved sample can be measured to obtain Q_{par_n}' and Q_{par_n}'' for the harmonics of interest, as a function of the dimensions of the structures — which are essentially the length of the bus lines, since all the contact pads have the same size. The uncleaved bus line contribution can then be extrapolated for each sample geometry. For a cleaved sample without any interdigitation, the PZT plays no role, and we have:

$$\begin{cases} Q_{\text{par}_n}'' = -\frac{V_n}{n\omega R} \cos \varphi_n \\ Q_{\text{par}_n}' = \frac{V_n}{n\omega R} \sin \varphi_n \end{cases} \quad (\text{G.20})$$



Bibliography

- [1] John Frederick Nye. *Physical properties of crystals: their representation by tensors and matrices*. Oxford university press, 1985.
- [2] Michel Brissaud. *Matériaux piézoélectriques: caractérisation, modélisation et vibration*. Presses Polytechniques et Universitaires Romandes, 2007.
- [3] Robert E Newnham. *Properties of materials: anisotropy, symmetry, structure*. Oxford University Press, 2005.
- [4] AH Meitzler, HF Tiersten, AW Warner, D Berlincourt, GA Couquin, and FS Welsh III. IEEE standard on piezoelectricity, 1988.
- [5] Rich Ruby. Review and comparison of bulk acoustic wave FBAR, SMR technology. In *Ultrasonics Symposium*, pages 1029–1040. IEEE, 2007.
- [6] Nicola A Spaldin. A beginner’s guide to the modern theory of polarization. *Journal of Solid State Chemistry*, 195:2–10, 2012.
- [7] Malcolm E Lines and Alastair M Glass. *Principles and applications of ferroelectrics and related materials*. Oxford university press, 1977.
- [8] Dragan Damjanovic. Ferroelectric, dielectric and piezoelectric properties of ferroelectric thin films and ceramics. *Reports on Progress in Physics*, 61(9):1267, 1998.
- [9] G Arlt. Twinning in ferroelectric and ferroelastic ceramics: stress relief. *Journal of Materials Science*, 25(6):2655–2666, 1990.
- [10] G Arlt and P Sasko. Domain configuration and equilibrium size of domains in BaTiO₃ ceramics. *Journal of Applied Physics*, 51(9):4956–4960, 1980.
- [11] Bernard Jaffe, Willam R Cook Jr., and Hans Jaffe. *Piezoelectric ceramics*. Academic Press Inc. (London) Ltd., 1971.
- [12] Anthony J Moulson and John M Herbert. *Electroceramics: materials, properties, applications*. John Wiley & Sons, 2003.
- [13] Paul Muralt. Recent progress in materials issues for piezoelectric MEMS. *Journal of the American Ceramic Society*, 91(5):1385–1396, 2008.

Bibliography

- [14] DA Berlincourt, C Cmolik, and H Jaffe. Piezoelectric properties of polycrystalline lead titanate zirconate compositions. *Proceedings of the IRE*, 48(2):220–229, 1960.
- [15] RJ Nelmes and WF Kuhs. The crystal structure of tetragonal PbTiO_3 at room temperature and at 700K. *Solid State Communications*, 54(8):721–723, 1985.
- [16] MJ Haun, E Furman, SJ Jang, and LE Cross. Thermodynamic theory of the lead zirconate-titanate solid solution system, part I: Phenomenology. *Ferroelectrics*, 99(1):13–25, 1989.
- [17] MJ Haun, E Furman, HA McKinstry, and L Eric Cross. Thermodynamic theory of the lead zirconate-titanate solid solution system, part II: Tricritical behavior. *Ferroelectrics*, 99(1):27–44, 1989.
- [18] MJ Haun, ZQ Zhuang, E Furman, SJ Jang, and L Eric Cross. Thermodynamic theory of the lead zirconate-titanate solid solution system, part III: Curie constant and sixth-order polarization interaction dielectric stiffness coefficients. *Ferroelectrics*, 99(1):45–54, 1989.
- [19] MJ Haun, E Furman, TR Halemane, and LE Cross. Thermodynamic theory of the lead zirconate-titanate solid solution system, part IV: Tilting of the oxygen octahedra. *Ferroelectrics*, 99(1):55–62, 1989.
- [20] MJ Haun, E Furman, SJ Jang, and LE Cross. Thermodynamic theory of the lead zirconate-titanate solid solution system, part V: Theoretical calculations. *Ferroelectrics*, 99(1):63–86, 1989.
- [21] Dragan Damjanovic. Contributions to the piezoelectric effect in ferroelectric single crystals and ceramics. *Journal of the American Ceramic society*, 88(10):2663–2676, 2005.
- [22] Nicolas Ledermann, Paul Muralt, Jacek Baborowski, Martin Forster, and Jean-Paul Pel-laux. Piezoelectric $\text{Pb}(\text{Zr}_x, \text{Ti}_{1-x})\text{O}_3$ thin film cantilever and bridge acoustic sensors for miniaturized photoacoustic gas detectors. *Journal of Micromechanics and Microengineering*, 14(12):1650, 2004.
- [23] Stephane Hiboux, Paul Muralt, and Thomas Maeder. Domain and lattice contributions to dielectric and piezoelectric properties of $\text{Pb}(\text{Zr}_x, \text{Ti}_{1-x})\text{O}_3$ thin films as a function of composition. *Journal of materials research*, 14(11):4307–4318, 1999.
- [24] Susan Trolier-McKinstry and Paul Muralt. Thin film piezoelectrics for MEMS. *Journal of Electroceramics*, 12(1):7–17, 2004.
- [25] Paul Muralt. PZT thin films for microsensors and actuators: Where do we stand? *IEEE transactions on ultrasonics, ferroelectrics, and frequency control*, 47(4):903–915, 2000.
- [26] P Muralt, M Kohli, T Maeder, A Kholkin, K Brooks, N Setter, and R Luthier. Fabrication and characterization of PZT thin-film vibrators for micromotors. *Sensors and Actuators A: Physical*, 48(2):157–165, 1995.

- [27] R Bruchhaus, D Pitzer, R Primig, M Schreiter, W Wersing, N Neumann, N Hess, J Vollheim, R Köhler, and M Simon. A 11×6 element pyroelectric detector array utilizing self-polarized PZT thin films grown by sputtering. *Integrated Ferroelectrics*, 17(1-4):369–376, 1997.
- [28] Paul Muralt, Nicolas Ledermann, J Paborowski, Abdolghaffar Barzegar, Sandrine Gentil, Brahim Belgacem, Sylvain Petitgrand, Alain Bosseboeuf, and Nava Setter. Piezoelectric micromachined ultrasonic transducers based on PZT thin films. *Ultrasonics, Ferroelectrics and Frequency Control, IEEE Transactions on*, 52(12):2276–2288, 2005.
- [29] Eiji Fujii, Ryoichi Takayama, Kouji Nomura, Akiko Murata, Taku Hirasawa, Atsushi Tomozawa, Satoru Fujii, Takeshi Kamada, and Hideo Torii. Preparation of (001)-oriented $\text{Pb}(\text{Zr}, \text{Ti})\text{O}_3$ thin films and their piezoelectric applications. *Ultrasonics, Ferroelectrics and Frequency Control, IEEE Transactions on*, 54(12):2431–2431, 2007.
- [30] Utku Baran, Dean Brown, Sven Holmstrom, Davide Balma, Wyatt O Davis, Paul Muralt, and Hakan Urey. Resonant PZT MEMS scanner for high-resolution displays. *Microelectromechanical Systems, Journal of*, 21(6):1303–1310, 2012.
- [31] Yoshihisa Fujisaki. Review of emerging new solid-state non-volatile memories. *Japanese Journal of Applied Physics*, 52(4R):040001, 2013.
- [32] P Muralt, M Marzencki, B Belgacem, F Calame, and S Basrour. Vibration energy harvesting with PZT micro-device. *Procedia Chemistry*, 1(1):1191–1194, 2009.
- [33] P. Muralt. Ferroelectric thin films for micro-sensors and actuators: a review. *Journal of Micromechanics and Microengineering*, 10(2):136, 2000.
- [34] Han Geun Yu, L Zou, K Deng, R Wolf, S Tadigadapa, and S Trolier-McKinstry. Lead zirconate titanate MEMS accelerometer using interdigitated electrodes. *Sensors and Actuators A: Physical*, 107(1):26–35, 2003.
- [35] N Chidambaram, D Balma, R Nigon, A Mazzalai, R Matloub, CS Sandu, and P Muralt. Converse mode piezoelectric coefficient for lead zirconate titanate thin film with interdigitated electrodes. *Journal of Micromechanics and Microengineering*, 25(4):045016, 2015.
- [36] Paul Muralt. Piezoelectric thin films for MEMS. *Integrated Ferroelectrics*, 17(1-4):297–307, 1997.
- [37] Yuichi Tsujiura, Saneyuki Kawabe, Fumiya Kurokawa, Hirotaka Hida, and Isaku Kanno. Comparison of effective transverse piezoelectric coefficients $e_{31,f}$ of $\text{Pb}(\text{Zr}, \text{Ti})\text{O}_3$ thin films between direct and converse piezoelectric effects. *Japanese Journal of Applied Physics*, 54(10S):10NA04, 2015.
- [38] P Muralt, RG Polcawich, and S Trolier-McKinstry. Piezoelectric thin films for sensors, actuators, and energy harvesting. *MRS bulletin*, 34(9):658–664, 2009.

- [39] Marc-Alexandre Dubois and Paul Muralt. Measurement of the effective transverse piezoelectric coefficient $e_{31,f}$ of AlN and $\text{Pb}(\text{Zr}_x, \text{Ti}_{1-x})\text{O}_3$ thin films. *Sensors and Actuators A: Physical*, 77(2):106–112, 1999.
- [40] Andrea Mazzalai, Davide Balma, Nachiappan Chidambaram, Ramin Matloub, and Paul Muralt. Characterization and fatigue of the converse piezoelectric effect in PZT films for MEMS applications. *Journal of Microelectromechanical Systems*, 24(4):831–838, 2015.
- [41] Klaus Prume, Paul Muralt, Florian Calame, Thorsten Schmitz-Kempen, and Stephan Tiedke. Piezoelectric thin films: Evaluation of electrical and electromechanical characteristics for MEMS devices. *IEEE transactions on ultrasonics, ferroelectrics, and frequency control*, 54(1), 2007.
- [42] Rudeger HT Wilke, Paul J Moses, Pierre Jousse, Charles Yeager, and Susan Trolier-McKinstry. Wafer mapping of the transverse piezoelectric coefficient $e_{31,f}$ using the wafer flexure technique with sputter-deposited Pt strain gauges. *Sensors and Actuators A: Physical*, 173(1):152–157, 2012.
- [43] Nachiappan Chidambaram, Andrea Mazzalai, and Paul Muralt. Measurement of effective piezoelectric coefficients of PZT thin films for energy harvesting application with interdigitated electrodes. *Ultrasonics, Ferroelectrics and Frequency Control, IEEE Transactions on*, 59(8):1624–1631, 2012.
- [44] Nicolas Ledermann, Paul Muralt, Jacek Baborowski, Sandrine Gentil, Kapil Mukati, Marco Cantoni, Andreas Seifert, and Nava Setter. {100}-textured, piezoelectric $\text{Pb}(\text{Zr}_x, \text{Ti}_{1-x})\text{O}_3$ thin films for MEMS: integration, deposition and properties. *Sensors and Actuators A: Physical*, 105(2):162–170, 2003.
- [45] Nachiappan Chidambaram, Andrea Mazzalai, Davide Balma, and Paul Muralt. Comparison of lead zirconate titanate thin films for microelectromechanical energy harvester with interdigitated and parallel plate electrodes. *Ultrasonics, Ferroelectrics and Frequency Control, IEEE Transactions on*, 60(8), 2013.
- [46] F Tyholdt, F Calame, K Prume, H Raeder, and P Muralt. Chemically derived seeding layer for {100}-textured PZT thin films. *Journal of Electroceramics*, 19(4):311–314, 2007.
- [47] F Calame and P Muralt. Growth and properties of gradient free sol-gel lead zirconate titanate thin films. *Applied physics letters*, 90(6):062907–062907, 2007.
- [48] Andrea Mazzalai. *PZT thin films for MEMS devices: From in-situ sputter deposition to energy harvesting device*. PhD thesis, EPFL, 2014.
- [49] Robert W Schwartz. Chemical solution deposition of perovskite thin films. *Chemistry of Materials*, 9(11):2325–2340, 1997.
- [50] Andreas Seifert, Nicolas Ledermann, Stephane Hiboux, Jacek Baborowski, Paul Muralt, and Nava Setter. Processing optimization of solution derived $\text{PbZr}_{1-x}\text{Ti}_x\text{O}_3$ thin films for piezoelectric applications. *Integrated Ferroelectrics*, 35(1-4):159–166, 2001.

- [51] Nachiappan Chidambaram. Private communication.
- [52] Paul D Mitcheson, Eric M Yeatman, G Kondala Rao, Andrew S Holmes, and Tim C Green. Energy harvesting from human and machine motion for wireless electronic devices. *Proceedings of the IEEE*, 96(9):1457–1486, 2008.
- [53] Jerome P Lynch and Kenneth J Loh. A summary review of wireless sensors and sensor networks for structural health monitoring. *Shock and Vibration Digest*, 38(2):91–130, 2006.
- [54] KY Koo, JMW Brownjohn, DI List, and R Cole. Structural health monitoring of the tamar suspension bridge. *Structural Control and Health Monitoring*, 20(4):609–625, 2013.
- [55] Dominique Siegert and Michael Peigney. Study of energy harvesting from traffic-induced bridge vibrations. In *11th World Conference on Computational Mechanics, 5th European Conference on Computational Mechanics, 6th European Conference on Computational Fluid Dynamics (WCCM XI-ECCM V-ECFD VI)*, pages 643–654, 2014.
- [56] Liya Zhao, Lihua Tang, and Yaowen Yang. Comparison of modeling methods and parametric study for a piezoelectric wind energy harvester. *Smart materials and Structures*, 22(12):125003, 2013.
- [57] Dewei Jia and Jing Liu. Human power-based energy harvesting strategies for mobile electronic devices. *Frontiers of Energy and Power Engineering in China*, 3(1):27–46, 2009.
- [58] Shad Roundy, Paul K Wright, and Jan Rabaey. A study of low level vibrations as a power source for wireless sensor nodes. *Computer communications*, 26(11):1131–1144, 2003.
- [59] Tom Sterken, Paolo Fiorini, Kris Baert, R Puers, and G Borghs. An electret-based electrostatic μ -generator. In *Transducers, Solid-State Sensors, Actuators and Microsystems, 12th International Conference on, 2003*, volume 2, pages 1291–1294. IEEE, 2003.
- [60] CB Williams and Rob B Yates. Analysis of a micro-electric generator for microsystems. *Sensors and Actuators A: Physical*, 52(1-3):8–11, 1996.
- [61] Rajeevan Amirtharajah and Anantha P Chandrakasan. Self-powered signal processing using vibration-based power generation. *IEEE journal of solid-state circuits*, 33(5):687–695, 1998.
- [62] Shad Roundy and Paul K Wright. A piezoelectric vibration based generator for wireless electronics. *Smart Materials and structures*, 13(5):1131, 2004.
- [63] Alperen Toprak and Onur Tigli. Piezoelectric energy harvesting: State-of-the-art and challenges. *Applied Physics Reviews*, 1(3):031104, 2014.
- [64] Alper Erturk and Daniel J Inman. Issues in mathematical modeling of piezoelectric energy harvesters. *Smart Materials and Structures*, 17(6):065016, 2008.

- [65] Alper Erturk and Daniel J Inman. A distributed parameter electromechanical model for cantilevered piezoelectric energy harvesters. *Journal of vibration and acoustics*, 130(4):041002, 2008.
- [66] A Erturk and Daniel J Inman. An experimentally validated bimorph cantilever model for piezoelectric energy harvesting from base excitations. *Smart Materials and Structures*, 18(2):025009, 2009.
- [67] Jeong Woo Yi, Wan Y Shih, and Wei-Heng Shih. Effect of length, width, and mode on the mass detection sensitivity of piezoelectric unimorph cantilevers. *Journal of applied physics*, 91(3):1680–1686, 2002.
- [68] YB Jeon, R Sood, J-H Jeong, and S-G Kim. MEMS power generator with transverse mode thin film PZT. *Sensors and Actuators A: Physical*, 122(1):16–22, 2005.
- [69] R Matloub, Mahmoud Hadad, Andrea Mazzalai, Nachiappan Chidambaram, Gilles Moulard, CS Sandu, Th . Metzger, and Paul Muralt. Piezoelectric $\text{Al}_{1-x}\text{Sc}_x\text{N}$ thin films: A semiconductor compatible solution for mechanical energy harvesting and sensors. *Applied Physics Letters*, 102(15):152903, 2013.
- [70] R Elfrink, M Renaud, TM Kamel, C De Nooijer, M Jambunathan, M Goedbloed, D Hohlfeld, S Matova, V Pop, L Caballero, et al. Vacuum-packaged piezoelectric vibration energy harvesters: Damping contributions and autonomy for a wireless sensor system. *Journal of Micromechanics and Microengineering*, 20(10):104001, 2010.
- [71] M Defosseux, M Allain, E Defay, and S Basrour. Highly efficient piezoelectric micro-harvester for low level of acceleration fabricated with a CMOS compatible process. *Sensors and Actuators A: Physical*, 188:489–494, 2012.
- [72] Huicong Liu, Chengkuo Lee, Takeshi Kobayashi, Cho Jui Tay, and Chenggen Quan. A new S-shaped MEMS PZT cantilever for energy harvesting from low frequency vibrations below 30 Hz. *Microsystem technologies*, 18(4):497–506, 2012.
- [73] Martin Deterre, Elie Lefevre, Yanan Zhu, Marion Woytasik, Bertrand Boutaud, and Renzo Dal Molin. Micro blood pressure energy harvester for intracardiac pacemaker. *Journal of Microelectromechanical Systems*, 23(3):651–660, 2014.
- [74] Huidong Li, Chuan Tian, and Z Daniel Deng. Energy harvesting from low frequency applications using piezoelectric materials. *Applied physics reviews*, 1(4):041301, 2014.
- [75] Michele Pozzi and Meiling Zhu. Plucked piezoelectric bimorphs for knee-joint energy harvesting: modelling and experimental validation. *Smart Materials and Structures*, 20(5):055007, 2011.
- [76] Matthew A Hopcroft, William D Nix, and Thomas W Kenny. What is the Young's Modulus of Silicon? *Journal of microelectromechanical systems*, 19(2):229–238, 2010.

- [77] R Nigon, N Chidambaram, TM Raeder, and P Muralt. Influence of asymmetric electrodes on the switching of PZT thin films. In *Applications of Ferroelectric, International Symposium on Integrated Functionalities and Piezoelectric Force Microscopy Workshop (ISAF/ISIF/PFM), 2015 Joint IEEE International Symposium on the*, pages 193–196. IEEE, 2015.
- [78] Spartak S Gevorgian, Torsten Martinsson, Peter LJ Linner, and Erik Ludvig Kollberg. CAD models for multilayered substrate interdigital capacitors. *Microwave Theory and Techniques, IEEE Transactions on*, 44(6):896–904, 1996.
- [79] Rui Igreja and CJ Dias. Analytical evaluation of the interdigital electrodes capacitance for a multi-layered structure. *Sensors and Actuators A: Physical*, 112(2):291–301, 2004.
- [80] R Nigon, TM Raeder, and P Muralt. Characterization methodology for lead zirconate titanate thin films with interdigitated electrode structures. *Journal of Applied Physics*, 121(20):204101, 2017.
- [81] CH Nguyen, R Nigon, TM Ræder, U Hanke, E Halvorsen, and P Muralt. Extraction of properties of ferroelectric thin films in interdigitated electrode systems. In preparation.
- [82] OG Vendik and MA Nikolskii. Nonlinearity of a ferroelectric layer described using a planar capacitor model. *Technical Physics Letters*, 29(3):184–187, 2003.
- [83] OG Vendik, SP Zubko, and MA Nikolskii. Modeling and calculation of the capacitance of a planar capacitor containing a ferroelectric thin film. *Technical Physics*, 44(4):349–355, 1999.
- [84] Peter Henrici. *Applied and computational complex analysis. Volume 1: Power series, integration, conformal mapping, location of zeros*. John Wiley & Sons, Inc., 1974.
- [85] KF Young and HPR Frederikse. Compilation of the static dielectric constant of inorganic solids. *Journal of Physical and Chemical Reference Data*, 2(2):313–410, 1973.
- [86] Paolo Walter Cattaneo. Capacitances in micro-strip detectors: A conformal mapping approach. *Solid-State Electronics*, 54(3):252–258, 2010.
- [87] AK Tagantsev. The role of the background dielectric susceptibility in uniaxial ferroelectrics. *Ferroelectrics*, 69(1):321–323, 1986.
- [88] Alexander K Tagantsev. Landau expansion for ferroelectrics: which variable to use? *Ferroelectrics*, 375(1):19–27, 2008.
- [89] Vladimir O Sherman, Alexander K Tagantsev, Nava Setter, David Iddles, and Tim Price. Ferroelectric-dielectric tunable composites. *Journal of applied physics*, 99(7):074104, 2006.

Bibliography

- [90] AK Tagantsev, VO Sherman, KF Astafiev, J Venkatesh, and N Setter. Ferroelectric materials for microwave tunable applications. *Journal of electroceramics*, 11(1-2):5–66, 2003.
- [91] CJ Dias and R Igreja. A method of recursive images to obtain the potential, the electric field and capacitance in multi-layer interdigitated electrode (IDE) sensors. *Sensors and Actuators A: Physical*, 256:95–106, 2017.
- [92] John B Blum and SR Gurkovich. Sol-gel-derived PbTiO_3 . *Journal of Materials Science*, 20(12):4479–4483, 1985.
- [93] Nachiappan Chidambaram. *Advanced sol-gel processing of PZT thin films for piezoelectric MEMS structures*. PhD thesis, EPFL, 2014.
- [94] National Center for Biotechnology Information. PubChem Compound Database; CID=14792, <https://pubchem.ncbi.nlm.nih.gov/compound/14792>. Last accessed on Oct. 31, 2017.
- [95] Z Jin. ICDD Grant-in-Aid. Testing & Analysis Centre, Suzhou Univ., PR China, 1998. PDF card 00-050-0346.
- [96] H.E. Swanson and E. Tatge. PDF card 00-004-0829. *Standard X-Ray Diffraction Powder Patterns, Natl. Bur. Stand. (U.S.), Circular 539*, I:37–39, 1953.
- [97] Paul Muralt. Texture control and seeded nucleation of nanosize structures of ferroelectric thin films. *Journal of applied physics*, 100(5):051605, 2006.
- [98] T. M. Ræder. Self-poling and ageing in PZT thin films with interdigitated electrodes. Master's thesis, NTNU, Norway, 2015.
- [99] AK Tagantsev and G Gerra. Interface-induced phenomena in polarization response of ferroelectric thin films. *Journal of applied physics*, 100(5):051607, 2006.
- [100] Hrvoje Meštrić, R-A Eichel, T Kloss, K-P Dinse, So Laubach, PC Schmidt, KA Schönauf, M Knapp, H Ehrenberg, et al. Iron-oxygen vacancy defect centers in PbTiO_3 : Newman superposition model analysis and density functional calculations. *Physical Review B*, 71(13):134109, 2005.
- [101] Rüdiger-A Eichel. Structural and dynamic properties of oxygen vacancies in perovskite oxides-analysis of defect chemistry by modern multi-frequency and pulsed EPR techniques. *Physical Chemistry Chemical Physics*, 13(2):368–384, 2011.
- [102] WL Warren, GE Pike, K Vanheusden, D Dimos, BA Tuttle, and J Robertson. Defect-dipole alignment and tetragonal strain in ferroelectrics. *Journal of applied physics*, 79(12):9250–9257, 1996.

-
- [103] William L Warren, Duane Dimos, Bruce A Tuttle, and Donald M Smyth. Electronic and ionic trapping at domain walls in BaTiO₃. *Journal of the American Ceramic Society*, 77(10):2753–2757, 1994.
- [104] William L Warren, Karel Vanheusden, Duane Dimos, Gordon E Pike, and Bruce A Tuttle. Oxygen vacancy motion in perovskite oxides. *Journal of the American Ceramic Society*, 79(2):536–538, 1996.
- [105] Peter Jakes, Emre Erdem, Rüdiger-A Eichel, Li Jin, and Dragan Damjanovic. Position of defects with respect to domain walls in Fe³⁺-doped Pb[Zr_{0.52}Ti_{0.48}]O₃ piezoelectric ceramics. *Applied Physics Letters*, 98(7):072907, 2011.
- [106] Maxim I Morozov, Mari-Ann Einarsrud, Julian R Tolchard, Philipp T Geiger, Kyle G Webber, Dragan Damjanovic, and Tor Grande. In-situ structural investigations of ferroelasticity in soft and hard rhombohedral and tetragonal PZT. *Journal of Applied Physics*, 118(16):164104, 2015.
- [107] MI Morozov and D Damjanovic. Charge migration in Pb(Zr, Ti)O₃ ceramics and its relation to ageing, hardening, and softening. *Journal of Applied Physics*, 107(3):034106, 2010.
- [108] DV Taylor and D Damjanovic. Domain wall pinning contribution to the nonlinear dielectric permittivity in Pb(Zr, Ti)O₃ thin films. *Applied Physics Letters*, 73(14):2045–2047, 1998.
- [109] G Arlt and NA Pertsev. Force constant and effective mass of 90° domain walls in ferroelectric ceramics. *Journal of Applied Physics*, 70(4):2283–2289, 1991.
- [110] AK Tagantsev, I Stolichnov, EL Colla, and N Setter. Polarization fatigue in ferroelectric films: Basic experimental findings, phenomenological scenarios, and microscopic features. *Journal of Applied Physics*, 90(3):1387–1402, 2001.
- [111] Anand Chandrasekaran, Dragan Damjanovic, Nava Setter, and Nicola Marzari. Defect ordering and defect–domain-wall interactions in PbTiO₃: A first-principles study. *Physical Review B*, 88(21):214116, 2013.
- [112] Walter A Schulze and Kiyoshi Ogino. Review of literature on aging of dielectrics. *Ferroelectrics*, 87(1):361–377, 1988.
- [113] PV Lambeck and GH Jonker. The nature of domain stabilization in ferroelectric perovskites. *Journal of Physics and Chemistry of Solids*, 47(5):453–461, 1986.
- [114] J Lee, R Ramesh, VG Keramidas, WL Warren, GE Pike, and JT Evans Jr. Imprint and oxygen deficiency in (Pb, La)(Zr, Ti)O₃ thin-film capacitors with La-Sr-Co-O electrodes. *Applied physics letters*, 66(11):1337–1339, 1995.
- [115] GH Jonker. Nature of aging in ferroelectric ceramics. *Journal of the American Ceramic Society*, 55(1):57–58, 1972.

Bibliography

- [116] LX Zhang and X Ren. In situ observation of reversible domain switching in aged Mn-doped BaTiO₃ single crystals. *Physical Review B*, 71(17):174108, 2005.
- [117] K Carl and KH Hardtl. Electrical after-effects in Pb(Ti,Zr)O₃ ceramics. *Ferroelectrics*, 17(1):473–486, 1977.
- [118] Maxim I Morozov and Dragan Damjanovic. Hardening-softening transition in Fe-doped Pb(Zr,Ti)O₃ ceramics and evolution of the third harmonic of the polarization response. *Journal of Applied Physics*, 104(3):034107, 2008.
- [119] Yuri A Genenko, Julia Glaum, Michael J Hoffmann, and Karsten Albe. Mechanisms of aging and fatigue in ferroelectrics. *Materials Science and Engineering: B*, 192:52–82, 2015.
- [120] G Arlt and H Neumann. Internal bias in ferroelectric ceramics: origin and time dependence. *Ferroelectrics*, 87(1):109–120, 1988.
- [121] Dragan Damjanovic. Hysteresis in piezoelectric and ferroelectric materials. *The science of hysteresis*, 3:337–465, 2006.
- [122] L Eric Cross. Ferroelectric ceramics: tailoring properties for specific applications. *Ferroelectric ceramics*, pages 1–86, 1993.
- [123] XL Zhang, ZX Chen, Leslie E Cross, and WA Schulze. Dielectric and piezoelectric properties of modified lead titanate zirconate ceramics from 4.2 to 300K. *Journal of Materials Science*, 18(4):968–972, 1983.
- [124] ZQ Zhuang, MICHAEL J Haun, S-J Jang, and LESLIE E Cross. Composition and temperature dependence of the dielectric, piezoelectric and elastic properties of pure PZT ceramics. *IEEE transactions on ultrasonics, ferroelectrics, and frequency control*, 36(4):413–416, 1989.
- [125] G Arlt, D Hennings, and G De With. Dielectric properties of fine-grained barium titanate ceramics. *Journal of applied physics*, 58(4):1619–1625, 1985.
- [126] Dragan Damjanovic and Marlyse Demartin. Contribution of the irreversible displacement of domain walls to the piezoelectric effect in barium titanate and lead zirconate titanate ceramics. *Journal of Physics: Condensed Matter*, 9(23):4943, 1997.
- [127] QM Zhang, H Wang, N Kim, and LE Cross. Direct evaluation of domain-wall and intrinsic contributions to the dielectric and piezoelectric response and their temperature dependence on lead zirconate-titanate ceramics. *Journal of Applied Physics*, 75(1):454–459, 1994.
- [128] Clive A Randall, Namchul Kim, John-Paul Kucera, Wenwu Cao, and Thomas R Shrout. Intrinsic and extrinsic size effects in fine-grained morphotropic-phase-boundary lead zirconate titanate ceramics. *Journal of the American Ceramic Society*, 81(3):677–688, 1998.

-
- [129] Sanjeev Aggarwal and R Ramesh. Point defect chemistry of metal oxide heterostructures. *Annual review of materials science*, 28(1):463–499, 1998.
- [130] DM Smyth. Charge motion in ferroelectric thin films. *Ferroelectrics*, 116(1):117–124, 1991.
- [131] Don Berlincourt and Helmut HA Krueger. Domain processes in lead titanate zirconate and barium titanate ceramics. *Journal of Applied Physics*, 30(11):1804–1810, 1959.
- [132] Shaoping Li, Wenwu Cao, and LE Cross. The extrinsic nature of nonlinear behavior observed in lead zirconate titanate ferroelectric ceramic. *Journal of applied physics*, 69(10):7219–7224, 1991.
- [133] Maxim Morozov. *Softening and hardening transitions in ferroelectric Pb(Zr, Ti)O₃ ceramics*. PhD thesis, EPFL, 2005.
- [134] G Robert, D Damjanovic, N Setter, and AV Turik. Preisach modeling of piezoelectric nonlinearity in ferroelectric ceramics. *Journal of Applied Physics*, 89(9):5067–5074, 2001.
- [135] G Robert, D Damjanovic, and N Setter. Preisach modeling of ferroelectric pinched loops. *Applied Physics Letters*, 77(26):4413–4415, 2000.
- [136] G Robert, D Damjanovic, and N Setter. Preisach distribution function approach to piezoelectric nonlinearity and hysteresis. *Journal of applied physics*, 90(5):2459–2464, 2001.
- [137] Dragan Damjanovic and Marlyse Demartin. The Rayleigh law in piezoelectric ceramics. *Journal of Physics D: Applied Physics*, 29(7):2057, 1996.
- [138] Lord Rayleigh. XXV. - Notes on electricity and magnetism - III. On the behaviour of iron and steel under the operation of feeble magnetic forces. *The London, Edinburgh, and Dublin Philosophical Magazine and Journal of Science*, 23(142):225–245, 1887.
- [139] Louis Néel. Théories des lois d'aimantation de Lord Rayleigh. *Cahiers de physique*, 12:1–20, 1942.
- [140] H Kronmüller. Statistical theory of Rayleigh's law. *Z. Angew. Phys.*, 30:9–13, 1970.
- [141] DV Taylor and D Damjanovic. Evidence of domain wall contribution to the dielectric permittivity in PZT thin films at sub-switching fields. *Journal of Applied Physics*, 82(4):1973–1975, 1997.
- [142] Dragan Damjanovic. Stress and frequency dependence of the direct piezoelectric effect in ferroelectric ceramics. *Journal of Applied Physics*, 82(4):1788–1797, 1997.
- [143] U Robels and G Arlt. Domain wall clamping in ferroelectrics by orientation of defects. *Journal of applied physics*, 73(7):3454–3460, 1993.

Bibliography

- [144] G Arlt and H Dederichs. Complex elastic, dielectric and piezoelectric constants by domain wall damping in ferroelectric ceramics. *Ferroelectrics*, 29(1):47–50, 1980.
- [145] G Arlt, H Dederichs, and R Herbiet. 90°-domain wall relaxation in tetragonally distorted ferroelectric ceramics. *Ferroelectrics*, 74(1):37–53, 1987.
- [146] Maxim Morozov, Dragan Damjanovic, and Nava Setter. The nonlinearity and sub-switching hysteresis in hard and soft PZT. *Journal of the European Ceramic Society*, 25(12):2483–2486, 2005.
- [147] Alexander K Tagantsev, Igor Stolichnov, Nava Setter, Jeffrey S Cross, and Mineharu Tsukada. Non-Kolmogorov-Avrami switching kinetics in ferroelectric thin films. *Physical Review B*, 66(21):214109, 2002.
- [148] Yuri A Genenko, Sergey Zhukov, Sergey V Yampolskii, Jörg Schütrumpf, Robert Dittmer, Wook Jo, Hans Kungl, Michael J Hoffmann, and Heinz von Seggern. Universal polarization switching behavior of disordered ferroelectrics. *Advanced Functional Materials*, 22(10):2058–2066, 2012.
- [149] G Gerra, AK Tagantsev, and N Setter. Surface-stimulated nucleation of reverse domains in ferroelectrics. *Physical review letters*, 94(10):107602, 2005.
- [150] Sergey Zhukov, Yuri A Genenko, and Heinz von Seggern. Experimental and theoretical investigation on polarization reversal in unfatigued lead-zirconate-titanate ceramic. *Journal of Applied Physics*, 108(1):014106, 2010.
- [151] WL Warren, D Dimos, GE Pike, BA Tuttle, MV Raymond, R Ramesh, and JT Evans Jr. Voltage shifts and imprint in ferroelectric capacitors. *Applied physics letters*, 67(6):866–868, 1995.
- [152] M Grossmann, O Lohse, D Bolten, U Boettger, T Schneller, and R Waser. The interface screening model as origin of imprint in $\text{PbZr}_x\text{Ti}_{1-x}\text{O}_3$ thin films. I. Dopant, illumination, and bias dependence. *Journal of applied physics*, 92(5):2680–2687, 2002.
- [153] Yu A Genenko, J Glaum, O Hirsch, H Kungl, MJ Hoffmann, and T Granzow. Aging of poled ferroelectric ceramics due to relaxation of random depolarization fields by space-charge accumulation near grain boundaries. *Physical Review B*, 80(22):224109, 2009.
- [154] Lionel Cima, Eric Laboure, and Paul Muralt. Characterization and model of ferroelectrics based on experimental Preisach density. *Review of scientific instruments*, 73(10):3546–3552, 2002.
- [155] Liliana Mitoseriu, Laurentiu Stoleriu, Alexandru Stancu, Carmen Galassi, and Vincenzo Buscaglia. First order reversal curves diagrams for describing ferroelectric switching characteristics. *Processing and Application of Ceramics*, 3(1-2):3–7, 2009.

- [156] Franz PG Fengler, Milan Pešić, Sergej Starschich, Theodor Schneller, Christopher Küneth, Ulrich Böttger, Halid Mulaosmanovic, Tony Schenk, Min Hyuk Park, Robin Nigon, Paul Muralt, et al. Domain pinning: Comparison of hafnia and PZT based ferroelectrics. *Advanced Electronic Materials*, 3(4), 2017.
- [157] TS Böske, J Müller, D Bräuhäus, U Schröder, and U Böttger. Ferroelectricity in hafnium oxide thin films. *Applied Physics Letters*, 99(10):102903, 2011.
- [158] T Schenk, E Yurchuk, S Mueller, U Schroeder, S Starschich, U Böttger, and T Mikolajick. About the deformation of ferroelectric hystereses. *Applied physics reviews*, 1(4):041103, 2014.
- [159] U Robels, L Schneider-Störmann, and G Arlt. Domain wall trapping as a result of internal bias fields. *Ferroelectrics*, 133(1):223–228, 1992.
- [160] U Robels, JH Calderwood, and G Arlt. Shift and deformation of the hysteresis curve of ferroelectrics by defects: An electrostatic model. *Journal of applied physics*, 77(8):4002–4008, 1995.
- [161] Xiaobing Ren. Large electric-field-induced strain in ferroelectric crystals by point-defect-mediated reversible domain switching. *Nature materials*, 3(2):91, 2004.
- [162] Lixue Zhang and Xiaobing Ren. Aging behavior in single-domain Mn-doped BaTiO₃ crystals: Implication for a unified microscopic explanation of ferroelectric aging. *Physical Review B*, 73(9):094121, 2006.
- [163] WL Warren, D Dimos, GE Pike, K Vanheusden, and R Ramesh. Alignment of defect dipoles in polycrystalline ferroelectrics. *Applied physics letters*, 67(12):1689–1691, 1995.
- [164] Paul Erhart, Rüdiger-Albert Eichel, Petra Träskelin, and Karsten Albe. Association of oxygen vacancies with impurity metal ions in lead titanate. *Physical Review B*, 76(17):174116, 2007.
- [165] Julia Glaum, Yuri A Genenko, Hans Kungl, Ljubomira Ana Schmitt, and Torsten Granzow. De-aging of Fe-doped lead-zirconate-titanate ceramics by electric field cycling: 180°-vs. non-180° domain wall processes. *Journal of Applied Physics*, 112(3):034103, 2012.
- [166] Lixue Zhang, Emre Erdem, Xiaobing Ren, and Rüdiger-A Eichel. Reorientation of $(\text{Mn}^{2+}-\text{V}_{\text{O}}^{\bullet})^{\times}$ defect dipoles in acceptor-modified BaTiO₃ single crystals: An electron paramagnetic resonance study. *Applied Physics Letters*, 93(1):1, 2008.
- [167] N-H Chan, RK Sharma, and Donald M Smyth. Nonstoichiometry in undoped BaTiO₃. *Journal of the American Ceramic Society*, 64(9):556–562, 1981.
- [168] Paul Erhart, Petra Träskelin, and Karsten Albe. Formation and switching of defect dipoles in acceptor-doped lead titanate: A kinetic model based on first-principles calculations. *Physical Review B*, 88(2):024107, 2013.

Bibliography

- [169] Lixin He and David Vanderbilt. First-principles study of oxygen-vacancy pinning of domain walls in PbTiO_3 . *Physical Review B*, 68(13):134103, 2003.
- [170] Alexander Kirillovich Tagantsev, L Eric Cross, and Jan Fousek. *Domains in ferroic crystals and thin films*. Springer, 2010.
- [171] Pavel Mokřý and Tomáš Sluka. Identification of defect distribution at ferroelectric domain walls from evolution of nonlinear dielectric response during the aging process. *Physical Review B*, 93(6):064114, 2016.
- [172] Pavel Mokřý, Yongli Wang, Alexander K Tagantsev, Dragan Damjanovic, Igor Stolichnov, and Nava Setter. Evidence for dielectric aging due to progressive 180° domain wall pinning in polydomain $\text{Pb}(\text{Zr}_{0.45}\text{Ti}_{0.55})\text{O}_3$ thin films. *Physical Review B*, 79(5):054104, 2009.
- [173] Doru C Lupascu, Yuri A Genenko, and Nina Balke. Aging in ferroelectrics. *Journal of the American Ceramic Society*, 89(1):224–229, 2006.
- [174] S Gottschalk, H Hahn, S Flege, and AG Balogh. Oxygen vacancy kinetics in ferroelectric $\text{PbZr}_{0.4}\text{Ti}_{0.6}\text{O}_3$. *Journal of Applied Physics*, 104(11):114106, 2008.
- [175] M Grossmann, O Lohse, D Bolten, U Boettger, and R Waser. The interface screening model as origin of imprint in $\text{PbZr}_x\text{Ti}_{1-x}\text{O}_3$ thin films. II. Numerical simulation and verification. *Journal of applied physics*, 92(5):2688–2696, 2002.
- [176] D Dimos, WL Warren, MB Sinclair, BA Tuttle, and RW Schwartz. Photoinduced hysteresis changes and optical storage in $(\text{Pb},\text{La})(\text{Zr},\text{Ti})\text{O}_3$ thin films and ceramics. *Journal of applied physics*, 76(7):4305–4315, 1994.
- [177] WL Warren, D Dimos, BA Tuttle, GE Pike, and HN Al-Shareef. Relationships among ferroelectric fatigue, electronic charge trapping, defect-dipoles, and oxygen vacancies in perovskite oxides. *Integrated ferroelectrics*, 16(1-4):77–86, 1997.
- [178] JF Scott, K Watanabe, AJ Hartmann, and RN Lamb. Device models for PZT/Pt, BST/Pt, SBT/Pt, and SBT/Bi ferroelectric memories. *Ferroelectrics*, 225(1):83–90, 1999.
- [179] MV Raymond and DM Smyth. Defect chemistry and transport properties of $\text{Pb}(\text{Zr}_{1/2}\text{Ti}_{1/2})\text{O}_3$. *Integrated Ferroelectrics*, 4(2):145–154, 1994.
- [180] Jeppe C Dyre. The random free-energy barrier model for ac conduction in disordered solids. *Journal of Applied Physics*, 64(5):2456–2468, 1988.
- [181] O Bidault, M Actis, and M Maglione. Stabilization of Ti^{3+} in reduced $(\text{Pb},\text{La})(\text{Ti},\text{Cu})\text{O}_3$ ceramics: An EPR study. *Solid state communications*, 95(12):845–849, 1995.
- [182] IP Pronin, E Yu Kaptelov, EA Tarakanov, LM Sorokin, VP Afanasjev, and AV Pankrashkin. Self-polarization and migratory polarization in thin-film ferroelectric capacitor. *Integrated Ferroelectrics*, 49(1):285–294, 2002.

- [183] Ryoichi Takayama and Yoshihiro Tomita. Preparation of epitaxial $\text{Pb}(\text{Zr}_x\text{Ti}_{1-x})\text{O}_3$ thin films and their crystallographic, pyroelectric, and ferroelectric properties. *Journal of Applied Physics*, 65(4):1666–1670, 1989.
- [184] Shan Sun, Yongmei Wang, Paul A Fuierer, and Bruce A Tuttle. Annealing effects on the internal bias field in ferroelectric PZT thin films with self-polarization. *Integrated Ferroelectrics*, 23(1-4):25–43, 1999.
- [185] R Bruchhaus, D Pitzer, R Primig, M Schreiter, and W Wersing. Sputtering of PZT thin films for surface micromachined IR-detector arrays. *Integrated ferroelectrics*, 25(1-4):1–11, 1999.
- [186] J Lee, CH Choi, BH Park, TW Noh, and JK Lee. Built-in voltages and asymmetric polarization switching in $\text{Pb}(\text{Zr}, \text{Ti})\text{O}_3$ thin film capacitors. *Applied physics letters*, 72(25):3380–3382, 1998.
- [187] J Karthik, RVK Mangalam, JC Agar, and LW Martin. Large built-in electric fields due to flexoelectricity in compositionally graded ferroelectric thin films. *Physical Review B*, 87(2):024111, 2013.
- [188] M Boota, EP Houwman, M Dekkers, M Nguyen, and G Rijnders. Epitaxial $\text{Pb}(\text{Mg}_{1/3}\text{Nb}_{2/3})\text{O}_3\text{—PbTiO}_3$ (67/33) thin films with large tunable self-bias field controlled by a $\text{PbZr}_{1-x}\text{Ti}_x\text{O}_3$ interfacial layer. *Applied Physics Letters*, 104(18):182909, 2014.
- [189] Kin Wing Kwok, Bing Wang, Helen Lai Wah Chan, and Chung Loong Choy. Self-polarization in PZT films. *Ferroelectrics*, 271(1):69–74, 2002.
- [190] SH Baek, J Park, DM Kim, VA Aksyuk, RR Das, SD Bu, DA Felker, J Lettieri, V Vaithyanathan, SSN Bharadwaja, et al. Giant piezoelectricity on Si for hyperactive MEMS. *Science*, 334(6058):958–961, 2011.
- [191] William M Haynes. *CRC handbook of chemistry and physics*. CRC press, 2014.
- [192] Y Park, V Choong, Y Gao, BR Hsieh, and CW Tang. Work function of indium tin oxide transparent conductor measured by photoelectron spectroscopy. *Applied Physics Letters*, 68(19):2699–2701, 1996.
- [193] Stephane Hiboux and Paul Muralt. Origin of voltage offset and built-in polarization in in-situ sputter deposited PZT thin films. *Integrated Ferroelectrics*, 36(1-4):83–92, 2001.
- [194] SR Gurkovich and JB Blum. Crystallization of amorphous lead-titanate prepared by a sol-gel process. *Ferroelectrics*, 62(1):189–194, 1985.
- [195] KD Budd, SK Dey, and DA Payne. Sol-gel processing of PbTiO_3 , PbZrO_3 , PZT, and PLZT thin films. In *British Ceramic Proceedings*. Inst of Ceramics, 1985.

Bibliography

- [196] Florian Calame. *PZT thin film growth and chemical composition control on flat and novel three-dimensional micromachined structures for MEMS devices*. PhD thesis, EPFL, 2007.
- [197] Milton Ohring. *Materials science of thin films*. Academic press, 2001.
- [198] G Gerald Stoney. The tension of metallic films deposited by electrolysis. *Proceedings of the Royal Society of London. Series A, Containing Papers of a Mathematical and Physical Character*, 82(553):172–175, 1909.
- [199] GCAM Janssen, MM Abdalla, F Van Keulen, BR Pujada, and B Van Venrooy. Celebrating the 100th anniversary of the Stoney equation for film stress: Developments from polycrystalline steel strips to single crystal silicon wafers. *Thin Solid Films*, 517(6):1858–1867, 2009.
- [200] Lambert Ben Freund and Subra Suresh. *Thin film materials: stress, defect formation and surface evolution*. Cambridge University Press, 2004.
- [201] Stephen Timoshenko and Gleason Harvey MacCullough. *Elements of strength of materials*. Van Nostrand, 1949.
- [202] Edward B Saff and Arthur David Snider. *Fundamentals of complex analysis for mathematics, science, and engineering*. Prentice-Hall, 1976.
- [203] Milton Abramowitz and Irene A Stegun. *Handbook of mathematical functions: with formulas, graphs, and mathematical tables*, volume 55. Courier Corporation, 1964.
- [204] Edmund Taylor Whittaker and George Neville Watson. *A course of modern analysis*. Cambridge university press, 1996.
- [205] WC Hassenpflug. Elliptic integrals and the Schwarz-Christoffel transformation. *Computers & Mathematics with Applications*, 33(12):15–114, 1997.
- [206] Wolfgang Hilberg. From approximations to exact relations for characteristic impedances. *IEEE Transactions on Microwave Theory and techniques*, 17(5):259–265, 1969.
- [207] Wolfram Mathworld. <http://mathworld.wolfram.com/JacobiEllipticFunctions.html>. Last accessed on August 21, 2017.

Robin Nigon

French citizen
robin.nigon@m4x.org

MSc in Materials Science and Engineer

Education

10.2013 – present
Lausanne, Switzerland

EPFL: *PhD Student in Materials Science and Engineering*
Ceramics Laboratory, supervisor: Prof. Paul Muralt.

09.2011 – 05.2013
Lausanne, Switzerland

EPFL: *Master of Science in Materials Science and Engineering*

09.2008 – 05.2011
Palaiseau, France

Ecole Polytechnique: *Engineer's Degree*

09.2006 – 06.2008
Paris, France

Lycée Henri IV: *Intensive undergraduate program in Mathematics and Physics*

Research and Industry Experience

10.2013 – present
Lausanne, Switzerland

EPFL: *PhD Student in Materials Science and Engineering*
Piezoelectric and ferroelectric thin film characterization. Microfabrication, cleanroom and thin film processing. Finite element modeling.
Supervisor: Prof. Paul Muralt (EPFL).

10.2012 – 04.2013
Leuven, Belgium

Imec: *master thesis*
Electrical characterization of Resistive Random Access Memory (RRAM) designs.
Supervisors: Prof. Paul Muralt (EPFL), Dr. Ludovic Goux (Imec).

09.2011 – 07.2012
Lausanne, Switzerland

EPFL Institute of Materials: *research assistant*
Experimental work in composite, cementitious and polymeric materials in three laboratories at EPFL Institute of Materials.
Supervisors: Prof. Andreas Rossoll (LMM), Cheng Yu (LMC), Roman Marty (LMOM).

05.2011 – 08.2011
Munich, Germany

MTU Aero Engines GmbH: *research intern*
Mechanical fatigue modeling for nickel-based super alloys.
Supervisors: Prof. Habibou Maitournam (Ecole Polytechnique), Dr. Andreas Fischersworring-Bunk and Frank Vöse (MTU).

Languages

French
English

native speaker
fluent

German

fluent

Computer skills

Programming

Matlab, Python, Visual Basic for Applications (VBA), Labview.

Softwares

Microsoft Office suite, Comsol Multiphysics, photolithography mask design.

Publications

F. Fengler et al., "Analysis of performance instabilities of hafnia based ferroelectrics using modulus spectroscopy and thermally stimulated depolarization currents", in preparation.

C. H. Nguyen et al., "Extraction of properties of ferroelectric thin films in interdigitated electrode systems", in preparation.

R. Nigon et al., "Characterization methodology for lead zirconate titanate thin films with interdigitated electrode structures", *J. Appl. Phys.* **121**, 204101 (2017)

F. Fengler et al., "Domain pinning: Comparison of hafnia and PZT based ferroelectrics", *Advanced Electronic Materials*, **3**(4) (2017)

R. Nigon et al., "Influence of asymmetric electrodes on the switching of PZT thin films", in *2015 Joint IEEE International Symposium on the Applications of Ferroelectric (ISAF), International Symposium on Integrated Functionalities (ISIF), and Piezoelectric Force Microscopy Workshop (PFM). IEEE*, 2015. p. 193-196

N. Chidambaram et al., "Converse mode piezoelectric coefficient for lead zirconate titanate thin film with interdigitated electrodes", *Journal of Micromechanics and Microengineering*, **Volume 25**, Number 4, 2015

R. Marty et al., "Two-Fold Odd–Even Effect in Self-Assembled Nanowires from Oligopeptide-Polymer-Substituted Perylene Bisimides", *J. Am. Chem. Soc.*, **2014**, **136** (10), pp 3919–3927

L. Goux et al., "On the bipolar resistive-switching characteristics of Al₂O₃- and HfO₂-based memory cells operated in the soft-breakdown regime", *J. Appl. Phys.* **116**, 134502 (2014)

L. Goux et al., "Understanding of the intrinsic characteristics and memory trade-offs of sub- μ A filamentary RRAM operation", in *2013 Symposium on VLSI Technology Digest of Technical Papers*, 2013.

